




Universitat Autònoma de Barcelona

**ADVERTIMENT.** L'accés als continguts d'aquesta tesi queda condicionat a l'acceptació de les condicions d'ús establertes per la següent llicència Creative Commons:  [http://cat.creativecommons.org/?page\\_id=184](http://cat.creativecommons.org/?page_id=184)

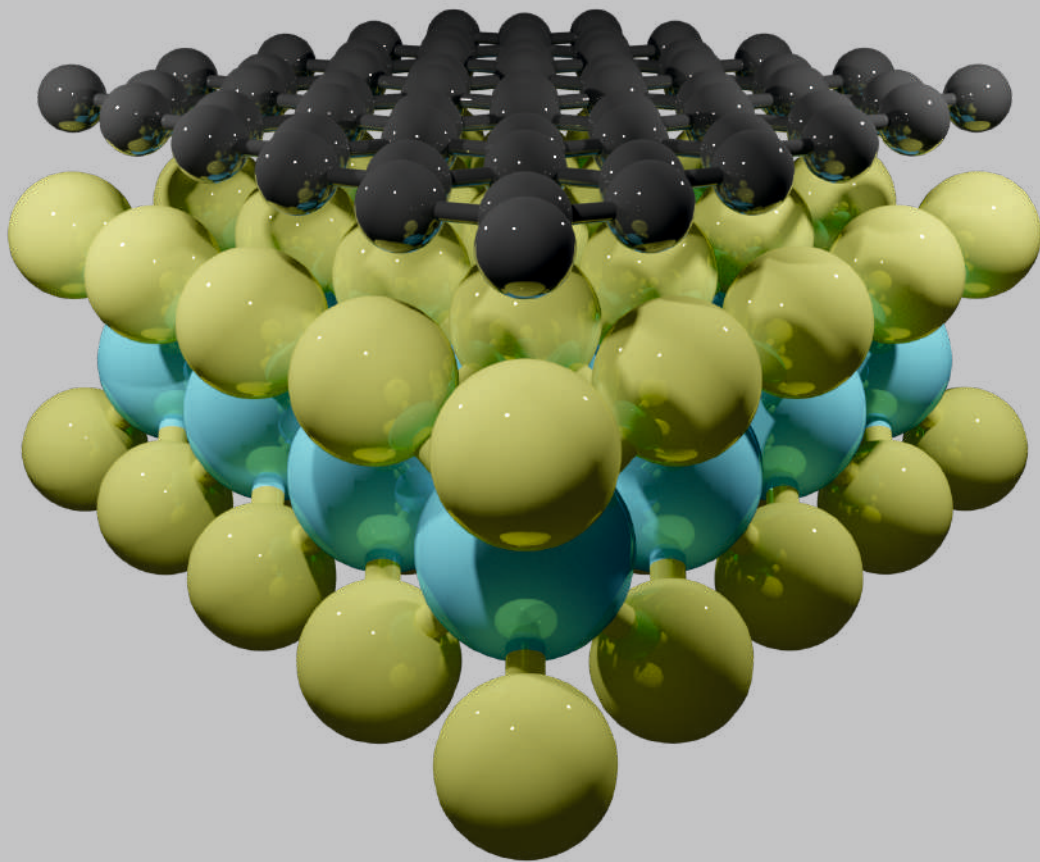
**ADVERTENCIA.** El acceso a los contenidos de esta tesis queda condicionado a la aceptación de las condiciones de uso establecidas por la siguiente licencia Creative Commons:  <http://es.creativecommons.org/blog/licencias/>

**WARNING.** The access to the contents of this doctoral thesis it is limited to the acceptance of the use conditions set by the following Creative Commons license:  <https://creativecommons.org/licenses/?lang=en>

# SPIN-ORBIT COUPLING IN GRAPHENE/TRANSITION METAL DICHALCOGENIDES DEVICES

---

L. ANTONIO BENÍTEZ



UNIVERSITAT AUTÒNOMA DE BARCELONA

DOCTORAL THESIS IN PHYSICS

---

**Spin-orbit coupling in graphene/transition  
metal dichalcogenides devices**

---

Luis Antonio BENÍTEZ MORENO

*Supervisor:*

Prof. Dr. Sergio O. VALENZUELA

*Co-supervisors:*

Prof. Dr. Stephan ROCHE

Dr. Marius V. COSTACHE

*Tutor:*

Dr. Jordi Mompart

Submitted to The Doctoral School of the Autonomous University of  
Barcelona at Bellaterra, in partial fulfillment of the requirements for the  
degree of Doctor of Philosophy

Bellaterra, Barcelona

October 19, 2020

## Declaration of Authorship

I, Luis Antonio BENÍTEZ MORENO, declare that this thesis titled, “Spin-orbit coupling in graphene/transition metal dichalcogenides devices” and the work presented in it are my own. I confirm that:

- This work was done wholly or mainly while in candidature for a research degree at this University.
- Where any part of this thesis has previously been submitted for a degree or any other qualification at this University or any other institution, this has been clearly stated.
- Where I have consulted the published work of others, this is always clearly attributed.
- Where I have quoted from the work of others, the source is always given. With the exception of such quotations, this thesis is entirely my own work.
- I have acknowledged all main sources of help.
- Where the thesis is based on work done by myself jointly with others, I have made clear exactly what was done by others and what I have contributed myself.

Signed:

---

Date:

---

*“¡Qué gran tónico sería para el novel observador el que su maestro, en vez de asombrarlo y desalentarlo con la descripción de las cosas acabadas, le expusiera el pasado embrionario de cada invención científica, la serie de errores y tanteos que le precedieron, y los cuales constituyen, desde el punto de vista humano, la verdadera explicación de cada descubrimiento, es decir, lo único que puede persuadirnos de que el descubridor, con ser un ingenio esclarecido y una poderosa voluntad, fue al fin y al cabo un hombre como todos! ”*

Santiago Ramón y Cajal.

# Abstract

The presented work is within the fields of spintronics and spin-orbitronics, whose final aim is to control the electron's spin degree of freedom via the spin-orbit coupling (SOC) in solid-state systems. The quest for greater control of the electron's spin has taken an exciting direction with the isolation and later demonstration of spin injection in graphene. Because of the graphene intrinsic low SOC, spins can travel over long distances through its crystal lattice, resulting in an ideal channel for the spin transport. But at the same time, the graphene's low SOC inhibits the manipulation and the generation of spin currents, which are the cornerstone for implementing spin-based devices successfully. We can get over this limitation by enhancing graphene's SOC by proximity with transition metal dichalcogenides (TMDCs) in van der Waals heterostructures. TMDCs are two-dimensional semiconductors that possess a strong intrinsic SOC. In this thesis, using spin transport measurements, we investigate the induced SOC in graphene by the proximity to TMDCs to achieve two main objectives:

- Obtain signatures of an enhanced spin-orbit and spin-valley coupling in graphene by proximity to a semiconducting TMDC using spin transport measurements.
- Study the possibility to generate spin currents using the induced SOC in graphene, which would be a building block for spin generation and detection free from magnetic materials.

To achieve such objectives, many efforts have been devoted to fabricating carefully designed samples, adapting and proposing experimental protocols based on spin precession measurements, and in the analysis and modeling of the signals. As a result, several relevant contributions to the understanding of spin-orbit phenomena in graphene/TMDCs have been achieved, which summarized according to the objectives are:

- The unambiguous demonstration of anisotropic spin dynamics in heterostructures comprising graphene,  $WS_2$ ,  $MoS_2$ , and  $WSe_2$ . Using out-of-plane and oblique spin precession measurements, we show that the spin lifetime is largest when the spins point out of the graphene plane. We observe that the spin lifetime changes over an order of magnitude depending on the spin orientation, indicating that the strong spin-valley coupling of the TMDC is imprinted in the graphene and felt by the propagating spins. Moreover, we show that such anisotropic spin relaxation can be electrically controlled, changing from a highly anisotropic to a nearly isotropic regime. These findings provide a rich platform to explore coupled spin-valley phenomena and offer novel spin manipulation strategies based on spin relaxation anisotropy in two-dimensional materials.

- The demonstration of strongly enhanced room-temperature spin-to-charge interconversion in graphene driven by the proximity of  $WS_2$ . By performing spin precession experiments in Hall bars, we separate the contributions of the spin Hall and the spin galvanic effects. Remarkably, their corresponding conversion efficiencies can be tailored by electrostatic gating in magnitude and sign, peaking nearby the charge neutrality point with an equivalent magnitude that is comparable to the largest efficiencies reported to date. Such an electric-field tunability provides a building block for a spin-generation free from magnetic materials, and for ultra-compact magnetic memory technologies.

# Resumen

El presente trabajo se encuentra dentro de los campos de la espintrónica y la espín-orbitrónica, cuyo objetivo final es controlar el grado de libertad de espín del electrón mediante el acoplamiento espín-órbita (SOC) en sistemas de estado sólido. La búsqueda de un mayor control del espín del electrón ha tomado una dirección emocionante con el aislamiento y la posterior demostración de la inyección de espín en grafeno. Debido al bajo SOC intrínseco del grafeno, los espines pueden viajar largas distancias a través de su red cristalina, lo que convierte al grafeno en un canal ideal para el transporte de espines. Pero al mismo tiempo, el bajo SOC del grafeno inhibe la manipulación y la creación de dichas corrientes de espín, fundamentales para implementar con éxito dispositivos basados en el espín del electrón. Sin embargo, podemos superar esta limitación aumentando el SOC del grafeno mediante los efectos de proximidad con los dicalcogenuros de metales de transición (TMDC) en estructuras de van der Waals heterogéneas. Los TMDC son semiconductores bidimensionales que poseen un SOC intrínseco fuerte. En esta tesis, utilizando medidas de transporte de espín, investigamos el SOC inducido en el grafeno por la proximidad a los TMDC para lograr dos objetivos principales:

- Obtener indicios de un aumento en el acoplamiento espín-órbita y espín-valle en el grafeno modificado por la proximidad a un dicalcogenuro de metal de transición semiconductor utilizando medidas de transporte de espín.
- Estudiar la posibilidad de generar corrientes de espín utilizando el acoplamiento espín-órbita inducido en el grafeno, herramienta fundamental para la generación y detección de espines sin usar materiales magnéticos.

Para lograr tales objetivos, se han dedicado muchos esfuerzos a la fabricación de muestras cuidadosamente diseñadas, a adaptar y proponer protocolos experimentales basados en medidas de precesión de espín, y a el análisis y modelado de las señales. Como resultado, se han logrado varias contribuciones relevantes para la comprensión de los fenómenos de espín-órbita en heteroestructuras de grafeno y dicalcogenuros de metales de transición, las cuales resumidas acorde a los objetivos son:

- La demostración inequívoca de una dinámica de espín anisotrópica en heteroestructuras que comprenden grafeno,  $WS_2$ ,  $MoS_2$  y  $WSe_2$ . Utilizando mediciones de precesión de espín oblicua y fuera del plano, mostramos que el tiempo de vida del espín es mayor cuando los espines apuntan fuera del plano del grafeno. Observamos, además, que el tiempo de vida del espín varía en un orden de magnitud dependiendo de su orientación, lo que indica que el fuerte acoplamiento espín-valle del dicalcogenuro de metal de transición se imprime en el grafeno y es percibido por los espines que se propagan. Además, mostramos que dicha relajación anisotrópica de espín se puede controlar eléctricamente,



cambiando de un régimen altamente anisotrópico a uno casi isotrópico. Estos hallazgos proporcionan una plataforma para explorar fenómenos de acoplamiento espín-valle, y ofrecen nuevas estrategias para la manipulación de espín basadas en la anisotropía de relajación de espín en materiales bidimensionales.

- La demostración de una conversión de corrientes de espín a corrientes de carga, y viceversa, en grafeno. Dicha conversión es medida a temperatura ambiente y mediada por la proximidad del grafeno a un  $WS_2$ . Realizando experimentos de precesión de espín en estructuras tipo Hall, separamos las contribuciones del efecto Hall y galvánico de espín. Sorprendentemente, sus correspondientes eficiencias de conversión se pueden ajustar tanto en magnitud y signo mediante una compuerta electrostática, siendo máximas cerca del punto de neutralidad de carga del grafeno. La eficiencia medida de estos efectos es comparable a las eficiencias más grandes reportadas hasta la fecha. Tal grado de control alcanzado mediante campos eléctrico proporciona una herramienta para la generación de corrientes de espín sin usar materiales magnéticos, y para tecnologías de memorias magnéticas ultra compactas.

# Resum

Aquest treball s'emmarca dins els camps de l'espintrònica i la spin-orbitrònica, l'objectiu final del qual és controlar el grau de llibertat de l'espín de l'electró mitjançant l'acoblament spin-òrbita (SOC) en sistemes d'estat sòlid. La recerca d'un major control de l'espín ha pres una direcció emocionant amb l'aïllament i posterior demostració de la injecció d'espín en grafè. Degut al baix SOC intrínsec del grafè, els espins poden viatjar distàncies llargues a través de la seva xarxa cristal·lina, la qual cosa fa del grafè un canal ideal per al transport d'espins. Tanmateix, el SOC feble del grafè inhibeix la manipulació i la creació de les corrents d'espín mencionades, fonamentals per tal d'implementar amb èxit dispositius basats en l'espín de l'electró. Aquesta limitació pot ser superada augmentant el SOC a través d'efectes de proximitat amb els dicalcogenurs de metalls de transició (TMDC) en estructures de van der Waals heterogènies. Els TMDC són semiconductors bidimensionals que posseeixen un SOC intrínsec fort. En aquesta tesi, utilitzant mesures de transport d'espín, investiguem el SOC induït en el grafè per la proximitat dels TMDC per aconseguir dos objectius principals:

- Obtenir indicis d'un augment en l'acoblament spin-òrbita i espín-vall en el grafè modificat per la proximitat amb un TMDC semiconductor utilitzant mesures de transport d'espín.
- Estudiar la possibilitat de generar corrents d'espín utilitzant l'acoblament espín-òrbita induït en el grafè, una fonamental per a la generació i detecció d'espins sense utilitzar materials magnètics.

Per aconseguir aquests objectius, s'han dedicat molts esforços a la fabricació de mostres acuradament dissenyades, a adaptar i proposar protocols experimentals basats en mesures de precessió d'espín, i a l'anàlisi i modelatge de les senyals. Com a resultat, s'ha aconseguit fer diverses contribucions rellevants per a la comprensió dels fenòmens de spin-òrbita en heteroestructures de grafè i TMDCs, que resumides d'acord amb els objectius són:

- La demostració inequívoca d'una dinàmica d'espín anisotròpica en heteroestructures que comprenen grafè,  $WS_2$ ,  $MoS_2$  i  $WSe_2$ . Utilitzant mesures de precessió d'espín obliqua i fora del pla, demostrem que el temps de vida de l'espín és més gran quan els spins apunten fora del pla del grafè. Observem que el temps de vida de l'espín varia en un ordre de magnitud depenent de la seva orientació, indicant que el fort acoblament espín-vall de l'TMDC s'imprimeix en el grafè i és percebut pels espins que es propaguen. A més, mostrem que aquesta relaxació anisotròpica d'espín es pot controlar elèctricament, canviant d'un règim altament anisotròpic a un de gairebé isotròpic. Aquestes troballes proporcionen una plataforma per explorar fenòmens d'acoblament espín-vall, i ofereixen noves estratègies per a la manipulació d'espín basades en l'anisotropia de relaxació d'espín en materials bidimensionals.

- La demostració d'una conversió de corrents d'espín a corrents de càrrega, i viceversa, en grafè. Aquesta conversió facilitada per la proximitat de l'grafè amb un WS<sub>2</sub> i mesurada a temperatura ambient. Realitzant experiments de precessió d'espín en estructures tipus Hall, separem les contribucions de l'efecte Hall i galvànic de spin. Sorprenentment, les eficiències de conversió d'espín corresponents a cadascun dels mecanismes es poden ajustar tant en magnitud com en signe mitjançant una comporta electrostàtica, essent màximes prop del punt de neutralitat de càrrega del grafè. L'eficiència mesurada d'aquests efectes és comparable a les eficiències més grans publicades fins ara. Aquest grau de control assolit mitjançant camps elèctric proporciona una eina per a la generació de corrents d'espín sense utilitzar materials magnètics, i per a tecnologies de memòries magnètiques ultra compactes.

## *Acknowledgements*

First of all, I want to thank my supervisor, Sergio Valenzuela, for allowing me to explore experimental physics in his group. Thank you, Sergio, for your great support, and for the long fruitful physics talks we had during these years. I was lucky to work with such a great scientist. In fact, you have the Argentine style of doing science that I genuinely admire. Without a doubt, you were one of the people who contributed the most to this project to conclude successfully.

Thanks to my co-supervisor Marius Costache for guiding me through the details of experimental physics early on in my Ph.D. and later on for being willing to help when I needed it. You are a great experimental physicist. Thank you for your advice, friendship, and for the generous support you gave me when I was looking for a research stay. Thanks to my co-supervisor Stephan Roche for your advice, networking, and theoretical perspective. Thank you also for the friendly talks we had every day during lunchtime, and for motivating me to go to Singapore.

Many thanks to Juan Sierra for becoming my main support in the laboratory and a very good friend. Thanks for teaching me so many things about nanofabrication, measurements, and above all, for being so present in my work, motivating me when I needed it. For trusting me so much and for supporting me in each idea and step.

Thanks to Williams Savero for his support, friendship, patience, and knowledge. It was great to work with you. Thanks to Aloïs Arrighi for teaching me what you knew about heterostructures' fabrication early on my Ph. D. You were very kind and helpful always. To Matias Timmermans, who is no longer in the group, it was nice working with you. To Fred, Zewdu, Regina, Adriana, Iván, Josef, Carmen, Lorenzo, Marc, Aleandro, Aron, José, Pablo, Carlos, Ainhoa, Rafa, for their kind help and the fun shared.

Special thanks to Rocío Rodríguez for her unconditional support, for her love, for lighting me up with her enthusiasm, discipline, knowledge, joy, and many moments of infinite happiness.

I want to express my deepest gratitude to my family, especially to my father, mother, and brother, for their endless affection and great trust, for supporting me no matter what.

And last but not least, to the Spanish Ministry of Economy and Competitiveness (MINECO) for the economical support through the FPI fellowship. To the nanofabrication division staff at ICN2 and IMB-CNM, the competitive funding, the finance departments at ICN2. I probably left behind many people I have to thank; please forgive me and accept my gratitude.

L. Antonio Benítez.  
Cerdanyola del Vallès, Barcelona.  
September 2020.

# Contents

<b>Declaration of Authorship</b>	<b>i</b>
<b>Abstract</b>	<b>iii</b>
<b>Resumen</b>	<b>v</b>
<b>Resum</b>	<b>vii</b>
<b>Acknowledgements</b>	<b>ix</b>
<b>Contents</b>	<b>x</b>
<b>List of Figures</b>	<b>xiii</b>
<b>List of Abbreviations</b>	<b>xv</b>
<b>1 Introduction</b>	<b>1</b>
1.1 Spintronics . . . . .	1
1.2 Two-dimensional materials . . . . .	3
1.3 Spin-orbit coupling . . . . .	4
1.4 Thesis outline . . . . .	6
References . . . . .	6
<b>2 Theoretical background</b>	<b>13</b>
2.1 Electronic properties of graphene . . . . .	13
2.1.1 Density of states of graphene . . . . .	15
2.2 Two-dimensional transition metal dichalcogenides . . . . .	17
2.3 Spin-orbit coupling in graphene . . . . .	18
2.4 Spin relaxation in graphene . . . . .	20
2.4.1 Elliot-Yafet spin relaxation mechanism . . . . .	20
2.4.2 Dyakonov-Perel spin relaxation mechanism . . . . .	21
2.4.3 Specific spin relaxation mechanisms in graphene . . . . .	22
2.5 Proximity effects in graphene/TMDC heterostructures . . . . .	23
2.5.1 Anisotropic spin relaxation in graphene/TMDCs . . . . .	25
2.5.2 Spin to charge interconversion . . . . .	27
Spin Hall effect . . . . .	28
Intrinsic contribution to the SHE . . . . .	28
Extrinsic contribution to the SHE . . . . .	29

Spin galvanic effect . . . . .	30
References . . . . .	32
<b>3 Measurements protocols, device fabrication and characterization.</b>	<b>37</b>
3.1 Spin injection and detection in graphene lateral devices . . . . .	37
3.2 Spin precession experiments . . . . .	41
3.3 Determination of the spin lifetime anisotropy . . . . .	43
3.3.1 Oblique spin precession . . . . .	44
3.3.2 Out-of-plane spin precession . . . . .	47
3.4 Characterization of the spin to charge interconversion . . . . .	48
3.5 Sample fabrication . . . . .	50
3.6 Instrumentation . . . . .	52
3.7 Electrical characterization . . . . .	53
References . . . . .	54
<b>4 Spin relaxation in graphene/TMDC van der Waals heterostructures</b>	<b>58</b>
4.1 Introduction . . . . .	58
4.2 Device design and measurement scheme . . . . .	59
4.3 Out-of-plane spin precession measurements in graphene (gr) and gr- /TMDC . . . . .	61
4.4 Oblique spin precision measurements in graphene . . . . .	64
4.5 Oblique spin precession measurements in gr/TMDC . . . . .	65
4.6 Model of the spin relaxation anisotropy in gr/TMDC . . . . .	67
4.7 Gate control of the spin relaxation . . . . .	69
4.8 Modeling the spin precession in an anisotropic medium . . . . .	73
4.8.1 Non-precessing spin component . . . . .	74
4.8.2 General solution: Out-of-plane spin precession . . . . .	74
4.8.3 General solution: Oblique spin precession . . . . .	77
References . . . . .	79
<b>5 Spin to charge interconversion in graphene/TMDC heterostructures</b>	<b>84</b>
5.1 Introduction . . . . .	84
5.2 Measurement scheme and electrical characterization . . . . .	85
5.3 Conventional non-local spin precession measurements . . . . .	88
5.4 Spin-to-charge interconversion measurements . . . . .	89
5.5 SGE and SHE efficiency . . . . .	91
5.6 Gate control of the ISHE and SGE at room temperature . . . . .	91
5.7 ISHE temperature dependence . . . . .	93
5.8 Bloch diffusion equations . . . . .	94
5.8.1 Solution of the BDE for out-of-plane magnetic fields . . . . .	94
5.8.2 Solution of BDE for in-plane magnetic fields . . . . .	96
5.8.3 Spin relaxation anisotropy . . . . .	97
5.8.4 Inverse spin Hall effect, ISHE . . . . .	98

5.8.5 Spin galvanic effect, SGE . . . . .	98
References . . . . .	98
<b>6 Conclusions and recommendations</b>	<b>102</b>
References . . . . .	105
<b>A Supplementary material of chapter 5</b>	<b>107</b>
References . . . . .	111
<b>B Spin transport in BLG and thermoelectrical measurements in gr/hBN</b>	<b>113</b>
B.1 Spin-orbit valve in bilayer graphene in proximity to a TMDC . . . . .	113
B.2 Thermoelectric measurements in fully encapsulated graphene . . . . .	115
References . . . . .	116
<b>C Recipes for the sample fabrication</b>	<b>118</b>
References . . . . .	119
<b>D Curriculum vitae</b>	<b>120</b>

# List of Figures

2.1	Atomic structure and reciprocal lattice of graphene . . . . .	14
2.2	Graphene energy dispersion . . . . .	15
2.3	Graphene density of states . . . . .	16
2.4	Atomic structure of TMDCs . . . . .	17
2.5	TMDCs energy dispersion . . . . .	18
2.6	Schematic of Elliott–Yafet and Dyakonov–Perel spin relaxation mechanisms . . . . .	21
2.7	Building vdW heterostructures . . . . .	23
2.8	Graphene/TMDC energy dispersion . . . . .	24
2.9	Effective magnetic fields acting in graphene/TMDC . . . . .	26
2.10	Schematic of spin to charge conversion . . . . .	27
2.11	Spin Hall conductivity in graphene/TMDCs . . . . .	29
2.12	Spin galvanic effect . . . . .	30
2.13	Spin galvanic in graphene/TMDCs . . . . .	31
3.1	Resistor problem of conventional spin valve . . . . .	39
3.2	Spin injection in the non-local geometry . . . . .	40
3.3	Spin valve measurement . . . . .	42
3.4	Schematic of the oblique and out-of-plane spin precession . . . . .	44
3.5	Spin precession line shapes in an anisotropic medium. . . . .	46
3.6	Schematic illustrating the measurement concept of the SHE and SGE . . . . .	49
3.7	Graphene Raman spectra . . . . .	50
3.8	Steps for fabrication of van der Waals heterostructures . . . . .	51
3.9	Instrumentation . . . . .	52
3.10	Back gate measurement . . . . .	54
4.1	Proximity-induced spin-orbit coupling and measurement scheme . . . . .	60
4.2	Anisotropic spin relaxation in gr/WS <sub>2</sub> . . . . .	62
4.3	Anisotropic spin relaxation in gr/(MoS <sub>2</sub> , WSe <sub>2</sub> ) . . . . .	63
4.4	Isotropic spin relaxation in graphene . . . . .	64
4.5	Spin precession measurements under oblique magnetic fields in gr/WS <sub>2</sub> . . . . .	66
4.6	Spin lifetime anisotropy ratio, $\zeta$ . . . . .	67
4.7	Picture of the spin relaxation anisotropy . . . . .	68
4.8	Electrical control of the anisotropy spin relaxation using the oblique spin precession protocol. . . . .	70



4.9	Electrical control of the anisotropy spin relaxation using the out of plane spin precession protocol . . . . .	71
4.10	Regions in a gr/TMDC device . . . . .	73
4.11	Modeling of the non-local signal for different anisotropy ratio $\zeta$ . . . . .	75
4.12	Fitting of out-of-plane spin precession . . . . .	82
4.13	Fitting of oblique spin precession . . . . .	83
5.1	Spin-to-charge interconversion in gr/TMDC measurement scheme . . . . .	86
5.2	TMDC electrical characterization . . . . .	87
5.3	Spin precession measurements in graphene and graphene/WS <sub>2</sub> . . . . .	88
5.4	ISHE and SGE measurements . . . . .	89
5.5	SHE and ISGE measurements . . . . .	90
5.6	Gate control of the inverse spin Hall and spin galvanic effects at room temperature . . . . .	92
5.7	Temperature dependence of the spin Hall effect . . . . .	93
5.8	Device main elements . . . . .	95
5.9	Characterization of the spin dynamics in the reference device . . . . .	96
6.1	Schematic of a spin-orbit valve device and a gr/TMDC device for SOT	104
A.1	SEM image of the device used in Chapter 5. . . . .	109
A.2	Charge transport measurements . . . . .	110
A.3	SHE measurements with F1 and F2. . . . .	110
A.4	Spin precession measurements of the sign change in the ISHE . . . . .	111
B.1	Dual-gated bilayer graphene/WSe <sub>2</sub> . . . . .	113
B.2	Spin precession measurements in bilayer graphene/WSe <sub>2</sub> . . . . .	114
B.3	Thermoelectric measurements in graphene/hBN devices at RT . . . . .	116
B.4	Thermoelectric measurements in graphene/hBN devices at 77K . . . . .	117

# List of Abbreviations

2D	Two dimensional
2DEG	Two dimensional electron gas
BDE	Bloch diffusion equations
BLG	Bilayer graphene
BR	Bychkov-Rasbha
Chap	Chapter
CNP	Charge neutrality point
DOS	Density of states
DP	Dyakonov-Perel
Eq	Equation
EY	Elliot-Yafet
F	Ferromagnetic
FET	Field-effect transistor
Fig	Figure
GMR	Giant magneto resistance
gr	Graphene
ISGE	Inverse spin galvanic effect
ISHE	Inverse spin Hall effect
iv	intervalley
KM	Kane-Male
N	Non-magnetic
nl	Non-local
PIA	Pseudospin inversion asymmetry
SCI	Spin to charge interconversion
Sec	Section
SGE	Spin galvanic effect
SHE	Spin Hall effect
SOC	Spin orbit coupling
SOF	Spin orbit field
TMDC	Transition metal dichalcogenide
TMR	Tunnel magneto resistance
vdW	Van der Waals
VZ	Valley-Zeeman

## Chapter 1

# Introduction

The study of how the charge and spin move and interact in solid-state systems has led to tremendous advances in modern technologies of information processing, computing, and data storage. The invention of the solid-state field-effect transistor (FET), a compact device able to switch on/off the output charge current, is a milestone in electronics. FETs paved the way for smaller and cheaper radios, calculators, and computers, having a tremendous impact on almost every aspect of modern life.

Despite the continuous efforts, the semiconductor industry is facing severe physical constraints on continued miniaturization and energy consumption reduction [1–3]. For example, the gate insulator thickness and the operating voltage could no longer be reduced along with other device dimensions. Further reduction in insulator thickness in FETs would result in undesirable increases in gate leakage current through quantum tunneling [4]. Furthermore, a reduction in the operative voltage would result in low output currents in the on-state or leaking currents in the off-state (when the operation voltage  $V_g < k_B T/e$ ). Similar constraints are applied to current solid-state memory devices since they depend on FETs to store the bits. For example, the static random access memory (SRAM) uses six FETs, and the dynamic random access memory (DRAM) uses one FET (and one capacitor) to store a bit [1, 3]. Such physical limitations demand new devices based on a new physical basis that can go beyond conventional electronics in terms of miniaturization and efficiency.

In this context, spintronics, which attempts to use the spin of an electron as the carrier's information is a rapidly emerging field of science and technology that has produced an enormous impact in the field of storage and it will most likely have a significant impact on the future of all aspects of electronics.

### 1.1 Spintronics

While electronics deals with the emission, flow, and control of the electron's charge, spintronics is a multidisciplinary field that aims for the control of the spin degree of freedom of the electrons in solid-state systems [5]. This thesis is within the field of spintronics, and in this text, spin stands mainly for the average spin of an ensemble

of electrons. The control of spin is then the control of the average spin of an ensemble of particles. Spintronics target the use of the spin degree of freedom as the information carrier to complement or replace conventional electronics. Spintronics has the potential advantages of non-volatility, increased data processing speed, decreased electric power consumption, and increased integration densities compared with traditional semiconductor devices [6, 7].

The first significant application of spintronics is in the data storage where the "bits," fundamental units of information, are encoded into magnetic domains in a recording medium [8]. The foundation of spintronics dates back to 1988 when A. Fert and P. Grünberg independently discovered the giant magnetoresistance (GMR) effect. GMR is a significant change in the resistance in thin ferromagnetic/non-magnetic (F/N) multilayers, which depends on the relative magnetic orientation of the F layers [9, 10]. A similar change in the resistance also occurs in thin F/insulator/F multilayers, a phenomenon termed tunnel magnetoresistance (TMR) [11, 12].

Spintronics moved quickly from fundamental studies to a device technology where the GMR and TMR are used in a vast number of applications. For example, the magnetic sensors in a hard disk drive [13], in micro-electro-mechanical systems (MEMs) and biosensors. These and other applications are discussed in Refs. [14, 15]. TMR is the basis for magnetic random access memories (MRAMs). MRAMs combine non-volatility with relatively high read and write speeds and unlimited endurance [8, 16].

For MRAMs, a crucial parameter is a stable, fast, and reliable writing of the magnetic information with low currents. New routes in this direction for MRAMs include the spin-transfer torque (STT) and the spin-orbit torque (SOT), where the magnetization orientation of a free magnetic layer is controlled by direct transfer of the spin angular momentum from a spin-polarized current. Such spin-polarized currents can be generated by a ferromagnet for STT, or via the spin-orbit coupling (SOC) for SOT. SOT possesses advantages over STT in terms of design, reduced power consumption, device speed operation and promises to be the second revolution in magnetic storage [17]. Intense research is being carried out to better understand the physics of SOC, which is the critical ingredient for the design of spintronic devices. In particular, studies seek pristine materials or laboratory-made materials, that enhance the generation of spin currents via the SOC mechanism. This novel direction of spintronics is usually called spin-orbitronics, and as ultimate goal aims to exploit the SOC of nonmagnetic materials to generate, detect or exploit spin-polarized currents.

In addition to the enormous impact of spintronics within magnetic storage technology, the motivation for the use of spin-polarized currents began with the proposal for a spin field-effect transistor (spin-FET) made by Datta and Das [18, 19]. The spin-FET proposed by Datta and Dass relies on the electrical ON/OFF switching of spin information, which propagates in an N channel. The control is achieved by tuning the strength of the SOC of the N material. The proposal of Datta and

Das faced considerable experimental challenges such as the efficient spin injection into a non-magnetic material capable of transporting the spin information over long distances, and of course, the electrical control of the spins as they propagate. This proposal motivated remarkable experimental advances that have demonstrated the spin injection in metals [20] and semiconductors [21]; however, the spin information was fading away in very short distances. The short spin lifetime, combined with the elusive control of the SOC, impeded the possible realization of a reliable spin-FET at room temperature. Nevertheless, the discovery of the two-dimensional (2D) materials opened the door to overcome such limitations.

## 1.2 Two-dimensional materials

Graphene is the perfect 2D electronic material possible in nature, since it is exactly one atom thick, and carrier transport is confined in this 2D layer. After the experimental isolation of graphene in 2004 [22], it has positioned as a promising material because of its prominent mechanical [23, 24], electrical [25, 26], and optical properties [27–29]. What makes graphene special from an electronic point of view is its linear energy dispersion with the valence and conduction band touching at the  $K$  points. Because of its peculiar relation between valence and conduction bands, graphene has allowed the observation of the Klein paradox [30–32], the Half-integer quantum Hall effect [33], the quantum Hall effect at room temperature [34–36], among other exotic phenomena [37–42].

Since the first experimental demonstration of spin injection in graphene at room temperature [43], a vast number of studies have shown the advantage of this material respect to ordinary metals or semiconductors [44–48]. Because of its intrinsic low SOC and lack of hyperfine interaction [25], spins can propagate over tens of microns [45, 46], much longer than in any other material. Such property enables the transmission of spin signals in complex multi-terminal device architectures [49]. Even though, we are still far from the predicted extremely long propagation lengths, which is still an open issue within the field [50, 51]. Other unique advantages of graphene over other materials are its superior carrier mobility together with a high gate tunability [47, 52, 53].

Beyond graphene there exist an increasing family of 2D materials going from insulators like hBN [54], semiconductors made of transition metal dichalcogenides (TMDCs) such as MoS<sub>2</sub> or WS<sub>2</sub> [55], superconductors as NbSe<sub>2</sub> [56], topological insulators like Bi<sub>2</sub>Te<sub>3</sub> [57], magnetic insulators such as CrI<sub>3</sub> [58, 59] or Cr<sub>2</sub>Ge<sub>2</sub>Te<sub>6</sub> [60], among many others [54, 61]. As with graphene, the crystal quality of the obtained monolayers is very high, and their properties are gate tunable and very different from those of their 3D source. For example, a monolayer MoS<sub>2</sub> has a direct bandgap, while its bulk has an indirect bandgap [62]. Monolayer CrI<sub>3</sub> is an Ising ferromagnet with out-of-plane spin orientation, while bilayer CrI<sub>3</sub> shows antiferromagnetic behavior [58, 59]. Each material on their own has very interesting properties, and they

can be combined in heterostructures forming a stack [61, 63]. Because of their strong in-plane sigma bonds they will preserve its structural stability [25, 63], such as its flatness, but the final material will result in a combination of all the properties of each material. Moreover, such properties can be controlled, for example, by sample design [64] or electrically [65]. A recent breakthrough discovery shows that such properties can also be controlled with the twist angle between the 2D materials. Two layers of graphene stacked one on top of the other with a relative angle of  $1.1^\circ$ , combined with their exceptional gate tunability, leads to superconductive and insulator faces in the same device [66, 67]. Such a degree of freedom is, so far, a unique property of two-dimensional materials.

As discussed in previous section SOC is an important effect that plays a crucial role in spintronics. The small SOC present in graphene is an advantage for the spin propagation, but at the same time it is a disadvantage for the control and generation of spins in graphene. However, 2D materials such as MoS<sub>2</sub> or WS<sub>2</sub> present a giant SOC mostly coming from their heavy atoms [68, 69]. Such SOC manifest through a spin splitting of the conduction and valence band, and a spin valley polarization. Recent theoretical proposals [70] and later experimental confirmations [71–73] showed that such SOC can be imprinted in graphene while preserving its linear band structure. In this thesis we focus on studying such imprinted spin orbit coupling in graphene and its consequences on the spin dynamics and on the generation of spin currents.

### 1.3 Spin–orbit coupling

The SOC or spin-orbit interaction, is an effect that is present in atoms and solids, such as 2D materials. SOC has a relativistic nature and couples the particle’s spin with its motion inside an electric potential. The energy of SOC in atomic physics is given by,

$$H_{\text{SO}} = \frac{\hbar}{4m_0^2c^2} \vec{\sigma} \cdot (\vec{p} \times \vec{E}(\vec{r})), \quad (1.1)$$

where  $\vec{\sigma}$  and  $\vec{p}$  are the electron’s spin and linear momentum, respectively, and  $\vec{E}(\vec{r})$  is the electric field generated by the electric potential from the nucleus. Here,  $\vec{E}(\vec{r})$  is Lorentz-transformed to a magnetic field in the rest frame of a moving electron, so it acts on the spin. In a hydrogen-like electric potential, the energy from the spin-orbit interaction  $E_{\text{SO}}$  is proportional to  $\sim Z^2$ , where  $Z$  is the atomic number.

In solids, different SOC terms can arise from different asymmetries of the system. For example, the Rashba SOC is produced when a structural inversion asymmetry is present (e.g., because interfaces or external electric field) [74, 75], additionally bulk inversion asymmetry gives rise to another SOC, usually term as Dresselhaus SOC [76].

We always can see the spin-orbit interaction as an effective magnetic field,  $B_{SO}$ , felt by the spins inside the lattice. For example, for the Rashba SOC, we can write [74, 75]:

$$E_{SO} = g\mu_B \sigma B_{SO} = \alpha |\vec{\sigma} \times \vec{k}|, \quad (1.2)$$

where  $\alpha$  is a constant that depends on the material and  $\vec{k}$  is the momentum of the electron inside the lattice. The effective magnetic field,  $B_{SO}$ , generated by the spin-orbit interaction, is commonly termed as spin-orbit field (SOF). Equation (1.2) shows how the strength and direction of SOC depend on the motion of the electron. An immediate consequence of the SOC is the lifting of the spin degeneracy. Another important consequence of the SOC, is that the spins continuously rotate around the SOF; thus, initially aligned spins can be randomized after traveling a certain length. This process is called the spin relaxation. The spin-flip length is defined as a  $180^\circ$  rotation of the spins [77], and it qualitatively indicates how strong is the SOC. For example, in graphene where the spin-flip length  $\sim 30 \mu\text{m}$  [46], the SOC is very small, whereas in materials like InAs the spin-flip length  $\sim 100 \text{ nm}$  [78] indicates a stronger SOC. The Rashba and Dresselhaus SOC follow different coupling between spin and momentum. The ensuing SOFs add up resulting in a complex helicities as in the case of GaAs [79].

Over the years, the SOC became a very influential effect, beyond being the dominant spin relaxation mechanism in semiconductors. One of the important proposals that launched the field of spintronics is the spin field-effect transistor proposed by Data-Dass [18, 80], which makes use of the SOC to switch ON/OFF a polarized current. This idea inspired other spin-transistors proposals like the one of Schliemann *et. al.* [81] based on the peculiar interplay between the Dresselhaus and the Rashba coupling in semiconductors lacking bulk inversion symmetry. SOC is responsible for the spin Hall effect (SHE) [82, 83], in which the spin of an electron influences its motion. The usefulness of the SHE is, for example, to generate a spin accumulation, which later can be used in many spintronic devices [84]. SOC is an important ingredient in spin-orbit qubits [85], quantum spin Hall effect [86], 3D topological insulators [87], Majorana fermions [88], among others [79].

In this context, SOC is of notable importance for the progression of spintronics, and the 2D materials offer new possibilities to use SOC in novel devices, where SOC can be tuned on-demand [89, 90] and in combination with other effects such as magnetism. One layer graphene is expected to be a topological insulator because the nature of its SOC [91], bilayer graphene encapsulated in two layers of TMDCs shows tunable fragile topology [64], graphene-TMDC heterostructures were used to fabricate devices that switch ON/OFF spin currents like a spin-transistor [92, 93]. With this motivation, the results presented in this thesis aim to contribute to the knowledge of SOC in graphene-based heterostructures, the role of valley degree of freedom, and its consequences for the manipulation and generation of spin currents.

## 1.4 Thesis outline

This thesis focuses on the enhancement of SOC into graphene by the proximity to transition metal dichalcogenides, materials that possess a high SOC. We study the consequences of the induced SOC and spin-valley coupling in the dynamics of the spins and in the spin generation via the spin Hall and spin galvanic effects. This dissertation is organized into 6 chapters as follows:

- In chapter 1, we introduce the field of spintronics, the 2D materials and the spin-orbit coupling which are the driving force of this study.
- In chapter 2, we present theoretical concepts used through the text. We describe the electronic properties of graphene and transition metal dichalcogenides that are appealing for spintronics and, thus, the present work. We explain the spin-orbit coupling with a particular focus on the spin relaxation and spin-charge interconversion in graphene and in graphene/transition metal dichalcogenides heterostructures.
- In chapter 3, we present different aspects of the methodology used in this thesis. We explain the experimental methods and protocols adopted, going from the spin injection and detection, describing the spin precession experiments and how to obtain information about the spin relaxation time, which we used as a fingerprint of the induced SOC in graphene. Based on spin precession experiments, we explain the protocols aimed at detecting spin-charge interconversion in such systems. This chapter also contains the techniques used to fabricate and characterize our samples.
- In chapter 4, we present the obtained results comprising the first objective of this thesis: the study of the spin dynamics in graphene with a SOC enhanced by proximity to a TMDC. Using the methods described in chapter 3, we observe that the spin lifetime changes over an order of magnitude depending on the spin orientation, indicating that the strong spin-valley coupling of the TMDC is imprinted in the graphene and felt by the propagating spins. Moreover, we show that such anisotropic spin relaxation can be electrically controlled.
- In chapter 5, we present the obtained results comprising the second objective of this thesis: the study of spin-to-charge interconversion in graphene driven by the proximity of a transition metal dichalcogenide. By performing spin precession experiments in appropriately designed Hall bars, described in chapter 3, we demonstrated strongly enhanced room-temperature spin-to-charge interconversion in graphene driven by the induced SOC in graphene.
- In chapter 6, we review the conclusions of the present work and discuss recommendations for future works.



## References

- [1] Theis, T. N. & Philip Wong, H. S. The End of Moore's Law: A New Beginning for Information Technology. *Comput. Sci. Eng.* **19**, 41–50 (2017).
- [2] Wong, H.-S. P. Beyond the conventional transistor. *IBM J. Res. Dev.* **46**, 133–168 (2002).
- [3] Theis, T. N. & Solomon, P. M. In quest of the “next switch”: Prospects for greatly reduced power dissipation in a successor to the silicon field-effect transistor. *Proc. IEEE* **98**, 2005–2014 (2010).
- [4] Chaturvedi, P. & Goyal, N. Effect of gate dielectric thickness on gate leakage in tunnel field effect transistor. In *2012 8th International Caribbean Conference on Devices, Circuits and Systems (ICCDACS)* (IEEE, 2012).
- [5] Žutić, I., Fabian, J. & Das Sarma, S. Spintronics: Fundamentals and applications. *Rev. Mod. Phys.* **76**, 323–410 (2004).
- [6] Wolf, S. A. Spintronics: A Spin-Based Electronics Vision for the Future. *Science* **294**, 1488–1495 (2001).
- [7] Wolf, S. A., Chtchelkanova, A. Y. & Treger, D. M. Spintronics—A retrospective and perspective. *IBM J. Res. Dev.* **50**, 101–110 (2006).
- [8] Chappert, C., Fert, A. & Van Dau, F. N. The emergence of spin electronics in data storage. *Nat. Mater.* **6**, 813–823 (2007).
- [9] Baibich, M. N. *et al.* Giant magnetoresistance of (001)fe/(001)cr magnetic superlattices. *Phys. Rev. Lett.* **61**, 2472–2475 (1988).
- [10] Binasch, G., Grünberg, P., Saurenbach, F. & Zinn, W. Enhanced magnetoresistance in layered magnetic structures with antiferromagnetic interlayer exchange. *Phys. Rev. B* **39**, 4828–4830 (1989).
- [11] Moodera, J. S., Kinder, L. R., Wong, T. M. & Meservey, R. Large magnetoresistance at room temperature in ferromagnetic thin film tunnel junctions. *Phys. Rev. Lett.* **74**, 3273–3276 (1995).
- [12] Parkin, S. S. P. *et al.* Giant tunnelling magnetoresistance at room temperature with mgo (100) tunnel barriers. *Nat. Mater.* **3**, 862–867 (2004).
- [13] Tsang, C. H. *et al.* Design, fabrication, and performance of spin-valve read heads for magnetic recording applications. *IBM J. Res. Dev.* **42**, 103–116 (1998).
- [14] Buschow, K. H. J. *Handbook of magnetic materials* (Elsevier, 2003).
- [15] Daughton, J. M. Gmr applications. *J. Magn. Magn. Mater.* **192**, 334–342 (1999).

- 
- [16] Akerman, J. APPLIED PHYSICS: Toward a universal memory. *Science* **308**, 508–510 (2005).
- [17] Torres, L. E. F. F., Roche, S. & Charlier, J.-C. *Introduction to graphene-based nanomaterials: from electronic structure to quantum transport* (Cambridge University Press, 2020).
- [18] Datta, S. & Das, B. Electronic analog of the electro-optic modulator. *Appl. Phys. Lett.* **56**, 665–667 (1990).
- [19] Chuang, P. *et al.* All-electric all-semiconductor spin field-effect transistors. *Nat. Nanotechnol.* **10**, 35–39 (2015).
- [20] Jedema, F. J., Heersche, H. B., Filip, a. T., Baselmans, J. J. a. & van Wees, B. J. Electrical detection of spin precession in a metallic mesoscopic spin valve. *Nature* **416**, 713–716 (2002).
- [21] Dash, S. P., Sharma, S., Patel, R. S., de Jong, M. P. & Jansen, R. Electrical creation of spin polarization in silicon at room temperature. *Nature* **462**, 491–494 (2009).
- [22] Novoselov, K. S. Electric field effect in atomically thin carbon films. *Science* **306**, 666–669 (2004).
- [23] Papageorgiou, D. G., Kinloch, I. A. & Young, R. J. Mechanical properties of graphene and graphene-based nanocomposites. *Prog. Mater. Sci.* **90**, 75–127 (2017).
- [24] Bunch, J. S. *et al.* Electromechanical resonators from graphene sheets. *Science* **315**, 490–493 (2007).
- [25] Neto, A. H. C. *et al.* The electronic properties of graphene. *Rev. Mod. Phys.* **81**, 109–162 (2009).
- [26] Das Sarma, S., Adam, S., Hwang, E. H. & Rossi, E. Electronic transport in two-dimensional graphene. *Rev. Mod. Phys.* **83**, 407–470 (2011).
- [27] Falkovsky, L. A. Optical properties of graphene. *J. Phys. Conf. Ser.* **129**, 012004 (2008).
- [28] Kuzmenko, A. B., van Heumen, E., Carbone, F. & van der Marel, D. Universal optical conductance of graphite. *Phys. Rev. Lett.* **100**, 117401 (2008).
- [29] Mak, K. F., Shan, J. & Heinz, T. F. Electronic structure of few-layer graphene: Experimental demonstration of strong dependence on stacking sequence. *Phys. Rev. Lett.* **104**, 176404 (2010).
- [30] Katsnelson, M. I., Novoselov, K. S. & Geim, A. K. Chiral tunnelling and the Klein paradox in graphene. *Nat. Phys.* **2**, 620–625 (2006).

- [31] Gorbachev, R. V., Mayorov, A. S., Savchenko, A. K., Horsell, D. W. & Guinea, F. Conductance of p-n-p graphene structures with “air-bridge” top gates. *Nano Lett.* **8**, 1995–1999 (2008).
- [32] Young, A. F. & Kim, P. Quantum interference and Klein tunnelling in graphene heterojunctions. *Nat. Phys.* **5**, 222–226 (2009).
- [33] Zhang, Y., Tan, Y.-W., Stormer, H. L. & Kim, P. Experimental observation of the quantum Hall effect and Berry’s phase in graphene. *Nature* **438**, 201–204 (2005).
- [34] Novoselov, K. S. *et al.* Room-temperature quantum Hall effect in graphene. *Science* **315**, 1379–1379 (2007).
- [35] Giesbers, A. J. M. *et al.* Quantum-Hall activation gaps in graphene. *Phys. Rev. Lett.* **99**, 206803 (2007).
- [36] Tzalenchuk, A. *et al.* Towards a quantum resistance standard based on epitaxial graphene. *Nat. Nanotechnol.* **5**, 186–189 (2010).
- [37] Yan, J., Zhang, Y., Kim, P. & Pinczuk, A. Electric field effect tuning of electron-phonon coupling in graphene. *Phys. Rev. Lett.* **98**, 166802 (2007).
- [38] Dean, C. R. *et al.* Hofstadter’s butterfly and the fractal quantum Hall effect in moiré superlattices. *Nature* **497**, 598–602 (2013).
- [39] Bolotin, K. I., Ghahari, F., Shulman, M. D., Stormer, H. L. & Kim, P. Observation of the fractional quantum Hall effect in graphene. *Nature* **462**, 196–199 (2009).
- [40] Yang, H. *et al.* Graphene barristor, a triode device with a gate-controlled Schottky barrier. *Science* **336**, 1140–1143 (2012).
- [41] Heersche, H. B., Jarillo-Herrero, P., Oostinga, J. B., Vandersypen, L. M. K. & Morpurgo, A. F. Bipolar supercurrent in graphene. *Nature* **446**, 56–59 (2007).
- [42] Wei, D. S. *et al.* Mach-Zehnder interferometry using spin- and valley-polarized quantum Hall edge states in graphene. *Sci. Adv.* **3**, e1700600 (2017).
- [43] Tombros, N., Jozsa, C., Popinciuc, M., Jonkman, H. T. & van Wees, B. J. Electronic spin transport and spin precession in single graphene layers at room temperature. *Nature* **448**, 571–574 (2007).
- [44] Han, W., Kawakami, R. K., Gmitra, M. & Fabian, J. Graphene spintronics. *Nat. Nanotechnol.* **9**, 794–807 (2014).
- [45] Zomer, P. J., Guimarães, M. H. D., Tombros, N. & van Wees, B. J. Long-distance spin transport in high-mobility graphene on hexagonal boron nitride. *Phys. Rev. B* **86**, 161416(R) (2012).
- [46] Drögeler, M. *et al.* Spin lifetimes exceeding 12 ns in graphene nonlocal spin valve devices. *Nano Lett.* **16**, 3533–3539 (2016).

- [47] Guimarães, M. *et al.* Controlling spin relaxation in hexagonal BN-encapsulated graphene with a transverse electric field. *Phys. Rev. Lett.* **113**, 086602 (2014).
- [48] Benítez, L. A. *et al.* Investigating the spin-orbit interaction in van der Waals heterostructures by means of the spin relaxation anisotropy. *APL Mater.* **7**, 120701 (2019).
- [49] Gebeyehu, Z. M. *et al.* Spin communication over 30  $\mu\text{m}$  long channels of chemical vapor deposited graphene on SiO<sub>2</sub>. *2D Mater.* **6**, 034003 (2019).
- [50] Roche, S. & Valenzuela, S. O. Graphene spintronics: puzzling controversies and challenges for spin manipulation. *J. Phys. D: Appl. Phys.* **47**, 094011 (2014).
- [51] Roche, S. *et al.* Graphene spintronics: the european flagship perspective. *2D Mater.* **2**, 030202 (2015).
- [52] Bolotin, K. I. *et al.* Ultrahigh electron mobility in suspended graphene. *Solid State Commun.* **146**, 351–355 (2008).
- [53] Dean, C. R. *et al.* Boron nitride substrates for high-quality graphene electronics. *Nat. Nanotechnol.* **5**, 722–726 (2010).
- [54] Novoselov, K. S. *et al.* Two-dimensional atomic crystals. *Proceedings of the National Academy of Sciences* **102**, 10451–10453 (2005).
- [55] Mak, K. F., Lee, C., Hone, J., Shan, J. & Heinz, T. F. Atomically thin MoS<sub>2</sub>: A new direct-gap semiconductor. *Phys. Rev. Lett.* **105**, 136805 (2010).
- [56] Yokoya, T. Fermi surface sheet-dependent superconductivity in 2H-NbSe<sub>2</sub>. *Science* **294**, 2518–2520 (2001).
- [57] Teweldebrhan, D., Goyal, V. & Balandin, A. A. Exfoliation and characterization of bismuth telluride atomic quintuples and quasi-two-dimensional crystals. *Nano Lett.* **10**, 1209–1218 (2010).
- [58] Huang, B. *et al.* Layer-dependent ferromagnetism in a van der Waals crystal down to the monolayer limit. *Nature* **546**, 270–273 (2017).
- [59] Huang, B. *et al.* Electrical control of 2D magnetism in bilayer CrI<sub>2</sub>. *Nat. Nanotechnol.* **13**, 544–548 (2018).
- [60] Gong, C. *et al.* Discovery of intrinsic ferromagnetism in two-dimensional van der Waals crystals. *Nature* **546**, 265–269 (2017).
- [61] Novoselov, K. S., Mishchenko, A., Carvalho, A. & Neto, A. H. C. 2D materials and van der Waals heterostructures. *Science* **353**, aac9439 (2016).
- [62] Splendiani, A. *et al.* Emerging photoluminescence in monolayer MoS<sub>2</sub>. *Nano Lett.* **10**, 1271–1275 (2010).

- [63] Geim, A. K. & Grigorieva, I. V. Van der Waals heterostructures. *Nature* **499**, 419–425 (2013).
- [64] Island, J. O. *et al.* Spin-orbit-driven band inversion in bilayer graphene by the van der Waals proximity effect. *Nature* **571**, 85–89 (2019).
- [65] Benítez, L. A. *et al.* Tunable room-temperature spin galvanic and spin Hall effects in van der Waals heterostructures. *Nat. Mater.* **19**, 170–175 (2020).
- [66] Cao, Y. *et al.* Unconventional superconductivity in magic-angle graphene superlattices. *Nature* **556**, 43–50 (2018).
- [67] Cao, Y. *et al.* Correlated insulator behaviour at half-filling in magic-angle graphene superlattices. *Nature* **556**, 80–84 (2018).
- [68] Kormányos, A. *et al.* Corrigendum: k.p theory for two-dimensional transition metal dichalcogenide semiconductors (2015 2D mater. 2 022001). *2D Mater.* **2**, 049501 (2015).
- [69] Cappelluti, E., Roldán, R., Silva-Guillén, J. A., Ordejón, P. & Guinea, F. Tight-binding model and direct-gap/indirect-gap transition in single-layer and multilayer  $\text{mos}_2$ . *Phys. Rev. B* **88**, 075409 (2013).
- [70] Gmitra, M. & Fabian, J. Graphene on transition-metal dichalcogenides: A platform for proximity spin-orbit physics and optospintronics. *Phys. Rev. B* **92**, 155403 (2015).
- [71] Völkl, T. *et al.* Magnetotransport in heterostructures of transition metal dichalcogenides and graphene. *Phys. Rev. B* **96**, 125405 (2017).
- [72] Wakamura, T. *et al.* Strong Anisotropic Spin-Orbit Interaction Induced in Graphene by Monolayer  $\text{WS}_2$ . *Phys. Rev. Lett.* **120**, 106802 (2018).
- [73] Zihlmann, S. *et al.* Large spin relaxation anisotropy and valley-zeeman spin-orbit coupling in  $\text{WSe}_2$ /graphene/h-BN heterostructures. *Phys. Rev. B* **97**, 075434 (2018).
- [74] Bychkov, Y. A. & Rashba, E. I. Oscillatory effects and the magnetic susceptibility of carriers in inversion layers. *J. Phys. C: Solid State Phys.* **17**, 6039–6045 (1984).
- [75] Edelstein, V. M. Spin polarization of conduction electrons induced by electric current in two-dimensional asymmetric electron systems. *Solid State Commun.* **73**, 233–235 (1990).
- [76] Dresselhaus, G. Spin-orbit coupling effects in zinc blende structures. *Phys. Rev.* **100**, 580 (1955).
- [77] Bass, J. & Pratt, W. P. Spin-diffusion lengths in metals and alloys, and spin-flipping at metal/metal interfaces: an experimentalist's critical review. *J. Phys.: Condens. Matter* **19**, 183201 (2007).

- [78] Herling, F. *et al.* Spin-orbit interaction in InAs/GaSb heterostructures quantified by weak antilocalization. *Phys. Rev. B* **95**, 155307 (2017).
- [79] Manchon, A., Koo, H. C., Nitta, J., Frolov, S. M. & Duine, R. A. New perspectives for rashba spin-orbit coupling. *Nat. Mater.* **14**, 871–882 (2015).
- [80] Datta, S. How we proposed the spin transistor. *Nature Electronics* **1**, 604–604 (2018).
- [81] Schliemann, J., Egues, J. C. & Loss, D. Nonballistic spin-field-effect transistor. *Phys. Rev. Lett.* **90**, 146801 (2003).
- [82] Kato, Y. K., Myers, R. C., Gossard, A. C. & Awschalom, D. D. Observation of the spin hall effect in semiconductors. *Science* **306**, 1910–1913 (2004).
- [83] Valenzuela, S. O. & Tinkham, M. Direct electronic measurement of the spin Hall effect. *Nature* **442**, 176–179 (2006).
- [84] Sinova, J., Valenzuela, S. O., Wunderlich, J., Back, C. H. & Jungwirth, T. Spin Hall effects. *Rev. Mod. Phys.* **87**, 1213–1260 (2015).
- [85] Nadj-Perge, S., Frolov, S. M., Bakkers, E. P. A. M. & Kouwenhoven, L. P. Spin-orbit qubit in a semiconductor nanowire. *Nature* **468**, 1084–1087 (2010).
- [86] König, M. *et al.* Quantum Spin Hall Insulator State in HgTe Quantum Wells. *Science* **318**, 766–770 (2007).
- [87] Hasan, M. Z. & Kane, C. L. Colloquium: Topological insulators. *Rev. Mod. Phys.* **82**, 3045–3067 (2010).
- [88] Mourik, V. *et al.* Signatures of majorana fermions in hybrid superconductor-semiconductor nanowire devices. *Science* **336**, 1003–1007 (2012).
- [89] Khoo, J. Y., Morpurgo, A. F. & Levitov, L. On-demand spin-orbit interaction from which-layer tunability in bilayer graphene. *Nano Lett.* **17**, 7003–7008 (2017).
- [90] Gmitra, M. & Fabian, J. Proximity effects in bilayer graphene on monolayer WSe<sub>2</sub> : Field-effect spin valley locking, spin-orbit valve, and spin transistor. *Phys. Rev. Lett.* **119**, 146401 (2017).
- [91] Kane, C. L. & Mele, E. J. Quantum Spin Hall Effect in Graphene. *Phys. Rev. Lett.* **95**, 226801 (2005).
- [92] Dankert, A. & Dash, S. P. Electrical gate control of spin current in van der Waals heterostructures at room temperature. *Nat. Commun.* **8**, 16093 (2017).
- [93] Yan, W. *et al.* A two-dimensional spin field-effect switch. *Nat. Commun.* **7**, 13372 (2016).

## Chapter 2

# Theoretical background

In this chapter, we describe the theoretical concepts used through the thesis. We start with the description of the electronic properties of graphene and transition metal dichalcogenides (Secs. 2.1 and 2.2, respectively). In Sec. 2.3, we discuss the spin-orbit coupling and the spin relaxation mechanism in graphene. Finally, as an essential tool and driving for the present results, we devote the Sec. 2.5 to proximity effects in graphene/TMDCs.

### 2.1 Electronic properties of graphene

Graphene is a two-dimensional allotrope of carbon atoms, which are arranged in a honeycomb lattice (Fig. 2.1). The stable and elastic structure of graphene is determined by strong  $\sigma$  bonds, which result from the  $sp^2$  hybridization of the  $s$ ,  $p_x$ , and  $p_y$  carbon's valence electrons.  $sp^2$  hybridization consists of mixing one  $2s$  with two  $2p$  orbitals, leading to the formation of three hybrid  $sp^2$  orbitals, with an angle between them of  $120^\circ$  and a C-C bonding length of  $a_0 = 1.42 \text{ \AA}$ . The unmixed  $p_z$  orbital forms  $\pi$  orbitals. The  $\sigma$  bands separation is  $\sim 12 \text{ eV}$  away from the Fermi energy, so their contribution to graphene's electronic properties is disregarded.  $\pi$  bands produce the graphene's valence and conduction bands. Graphite is a three-dimensional stack of graphene layers, its structure is maintained by the weak van der Waals forces between  $\pi$  bonds of adjacent graphene sheets.

The graphene lattice can be described as a triangular Bravais lattice with two atoms per unit cell (A and B) and the lattice vectors  $\vec{a}_1$  and  $\vec{a}_2$ , defined in terms of  $a_0$ :

$$\vec{a}_1 = \frac{a}{2} \begin{bmatrix} \sqrt{3} \\ 1 \end{bmatrix}; \vec{a}_2 = a \begin{bmatrix} \sqrt{3} \\ -1 \end{bmatrix} \text{ where } |\vec{a}_1| = |\vec{a}_2| = a = \sqrt{3}a_0. \quad (2.1)$$

The reciprocal lattice vectors  $\vec{b}_1, \vec{b}_2$  are obtained using the relations  $\vec{a}_1 \cdot \vec{b}_1 = 2\pi$ ,  $\vec{a}_1 \cdot \vec{b}_2 = 0$ , etc:

$$\vec{b}_1 = \frac{2\pi}{a} \begin{bmatrix} \frac{1}{\sqrt{3}} \\ 1 \end{bmatrix}; \vec{b}_2 = \frac{2\pi}{a} \begin{bmatrix} \frac{1}{\sqrt{3}} \\ -1 \end{bmatrix}. \quad (2.2)$$

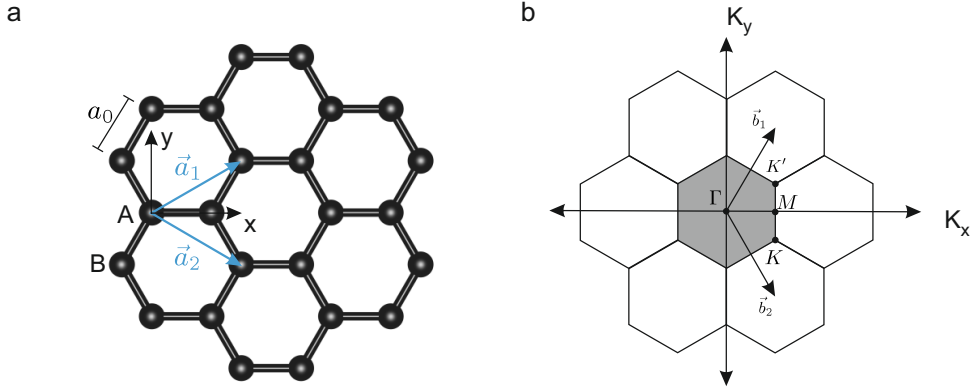


FIGURE 2.1: **a.** Atomic structure of graphene and lattice vectors  $\vec{a}_1$  and  $\vec{a}_2$ . The two atom-basis A, B marked. **b.** Reciprocal lattice of graphene with the reciprocal lattice vectors  $\vec{b}_1$  and  $\vec{b}_2$ . First Brillouin zone shaded and high symmetry points  $\Gamma$ ,  $K$  and  $M$  marked.

Graphene electronic dispersion relation has been widely studied using the tight-binding approximation, where the electrons are free to move only in the graphene's plane. Using this approximation, the result for the two-dimensional electronic dispersion relation is given by [1]:

$$E(k_x, k_y) = \pm \frac{t w(k_x, k_y)}{1 \pm s w(k_x, k_y)}, \quad (2.3)$$

with  $t = -3.033$  eV,  $s = 0.129$  eV, and

$$w(k_x, k_y) = \sqrt{1 + 4 \cos\left(\frac{\sqrt{3}k_x a}{2}\right) \cos\left(\frac{k_y a}{2}\right) + 4 \cos^2\left(\frac{k_y a}{2}\right)}. \quad (2.4)$$

Figure 2.2 shows that the graphene's valence and conduction bands coincide at the  $K$  points of the reciprocal space. The dispersion relation close to the  $K$  point can be approximated by:

$$E(k) \approx \pm t \frac{\sqrt{2}}{2} a k, \quad (2.5)$$

where  $k$  is the wave vector (pointing from  $K$  to a point in the vicinity of  $K$ ). Equation (2.5) confirms the conical dispersion relation in the region close to the  $K$  point (Fig. 2.2). The linear relation between the energy and the wave vector  $k$  in Eq. (2.5) displays the unique electronic properties of graphene; in particular the existence of massless electrons. The group velocity of electrons at the  $K$  (i.e. at the Fermi level) point can be easily evaluated  $v(k) = 1/\hbar |dE(k)/dk| = (\sqrt{3}a|t|)/(2\hbar)$ . Using  $t = -3.033$  eV [1] and  $a = 2.46$  Å, the group velocity is  $v(k) = v_F = 1.0 \times 10^6$  ms<sup>-1</sup>.  $v_F$  is the velocity of the electrons at the Fermi level. The value of  $v_F$  has been experimentally confirmed with angle-resolved photoemission spectroscopy (ARPES) [2]. The sections of the energy dispersion close to the  $K$  points are normally termed as "Dirac cones" because the tight-binding Hamiltonian for the electrons close to  $K$  using the linear dispersion approximation (Eq. (2.5) is mathematically identical to the



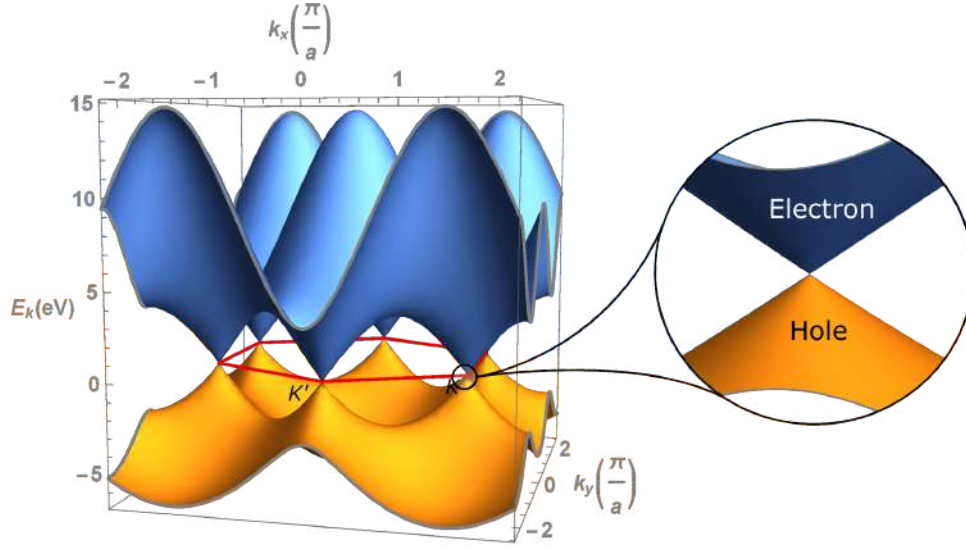


FIGURE 2.2: Graphene's energy dispersion. Plot of electron energy as a function of the wave vector  $k$  in the  $xy$  plane. The yellow and blue sections show the valence and conduction bands respectively. A zoom in the  $K$  point shows the Dirac cone, where valence and conduction bands touch with a zero-bandgap.

Dirac equation [3]. The Dirac equation is the relativistic invariant of the Schrödinger equation. However, in contrast to relativistic Dirac particles, low-energy excitation of graphene have a velocity  $v_F$  300 times smaller than the speed of light, the Pauli matrices operate on the sub-lattice degrees of freedom (pseudospin) instead on spin, and the relativistic particle wave function that accounts for the possibility of an antiparticle here describes holes and electrons.

### 2.1.1 Density of states of graphene

The density of states in graphene as a function of the wavevector  $k$  or energy has and unique behavior, unusually because it vanishes at the  $K$  point.

In a finite 2D box, the number of lattice points per unit area in  $k$ -space is  $(L/\pi)^2$ . The total number of states ( $N$ ) within a circle of radius  $k_0$  in the  $k$ -space is:

$$N(k_0) = 2 \times \frac{1}{4} \times \pi k_0^2 \times \left(\frac{L}{\pi}\right)^2, \quad (2.6)$$

Where the factor 2 accounts for the spin degeneracy, the fact that two electrons with opposite spins can occupy one quantum state. The factor  $1/4$  avoids counting states more than once. The factor  $\pi k_0^2$  is the area of the circle (see Fig. 2.3a). From Eq. (2.6) it is straight forward to derive an expression for the density of states  $D(k_0)dk$  available between  $k_0$  and  $k_0 + dk$ , per unit of area:

$$D(k_0)dk = \frac{1}{L^2} \frac{dN}{dk_0} dk = \frac{k_0}{\pi} dk. \quad (2.7)$$

It is convenient to define the density of states available between energy  $E$  and  $dE$  (see Fig. 2.3b). In graphene, given that  $E(k)$  is spherically symmetric around

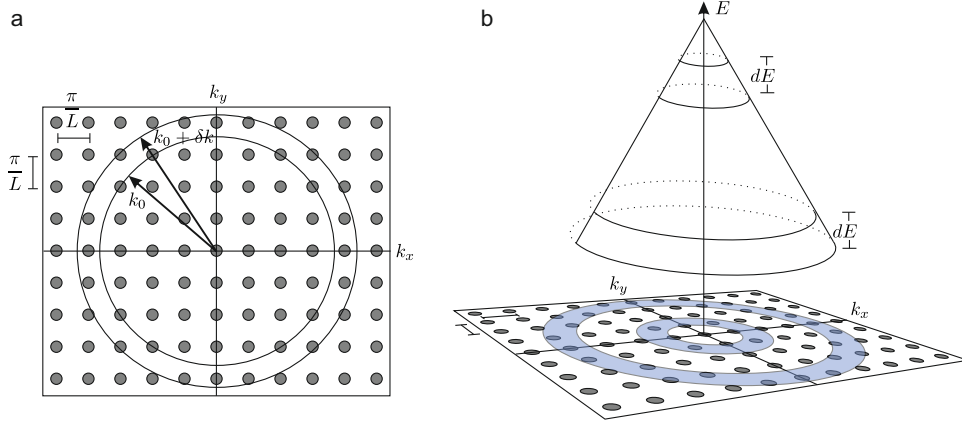


FIGURE 2.3: Graphene density of states. **a.** States for a particle with wavevector  $k_0$  and states between  $k_0$  and  $k_0 + \delta k$ .  $\pi/L$  is the distance between quantum states in the  $k$ -space. **b.** Density of states in graphene available within  $dE$  (shaded blue areas). The number of states in the interval  $dE$  drops to zero as the  $K$  point is approached. Further away from the  $K$  point, the number of available states increases. Adapted from [4].

the  $K$  point the density of states as a function of the energy and the wave vector are equivalents,  $D(E)|dE| = D(k_0)|dk|$ :

$$D(E)dE = D(k_0) \left| \frac{dE}{dk} \right|^{-1} dE = \frac{k_0}{\pi} \left| \frac{dE}{dk} \right|^{-1} dE. \quad (2.8)$$

From Eq. (2.8) it is straightforward to conclude that for  $k_0 \rightarrow 0$ ,  $D(E)dE \rightarrow 0$  which is also shown in Fig. 2.3.

Table 2.1 summarizes the expressions for the Fermi energy  $E_F$ , density of states  $D(E)$ , and density of states at the Fermi level  $D(E_F)$  for graphene as a function of the charge carrier density  $n$ , which denotes the number of charge carriers per unit of area that are filled up in the available quantum states. In general,  $n = \int D(E)f_0(E)dE$  where  $f_0(E)$  is the Fermi function, which in the limit of low temperatures is  $f_0(E) \approx \theta(E_F - E)$ ;  $\theta$  is the Heaviside step function. In this limit  $n = 2N/L^2$ , where  $N$  is given by Eq. (2.6). The factor 2 accounts for the valley degeneracy [5, 6].

$E_F$	$D(E)$	$D_F = D(E_F)$
$\hbar v_f \sqrt{\pi n}$	$\frac{2E}{\pi(\hbar v_f)^2}$	$\frac{\sqrt{n}}{\hbar v_f \sqrt{\pi}}$
$\sim 1.2 \times 10^{-4} \sqrt{n} \text{ [meV]}$	$\sim 1.8 \times 10^8 E \text{ [meV}^{-1} \text{ cm}^{-2}]$	$\sim 8.6 \times 10^3 \sqrt{n} \text{ [meV}^{-1} \text{ cm}^{-2}]$

TABLE 2.1: Graphene electronic characteristics.  $E_F$ ,  $D$ , and  $D_F$  are the Fermi energy  $E_F$ , density of states and density of states at the Fermi level.  $E$  is in meV unit and  $n$  is in  $\text{cm}^{-2}$  unit.

## 2.2 Two-dimensional transition metal dichalcogenides

Transition metal dichalcogenides (TMDCs) are semiconductors of the type  $\text{MX}_2$ , where M is a transition metal atom (such as Mo or W), and X is a chalcogen atom (such as S, Se or Te). TMDCs exist in different structural phases, the most common ones being the trigonal prismatic (2H) and octahedral (1T). The 2H phases correspond to an ABA stacking in which the X atoms in different atomic planes occupy the same position (Fig. 2.4). The 1T phases appear in an ABC order (Fig. 2.4) [7]. For semiconducting TMDCs such as  $\text{MoS}_2$ ,  $\text{MoSe}_2$ ,  $\text{WS}_2$  or  $\text{WSe}_2$ , the 2H phase is thermodynamically stable and the 1T is metastable [7–9]. Noticeable distortions that lower the periodicity can result in the formation of M-M bonds as it occurs in the dimerization of the 1T phase, which results in the 1T' phase (see Fig. 2.4), for example in semimetallic  $\text{WTe}_2$  [7]. In this thesis, we focus on semiconducting TMDC with the thermodynamically stable 2H phase. Thus whenever referring to a TMDC, we are referring to 2H-TMDC unless otherwise specified.

The crystal lattice of TMDCs consist in a triangular Bravais lattice with one X atom and one M atom per unit cell. As in the case of graphene, the Fermi level lies around the two inequivalent corners of the hexagonal Brillouin zone. Considering  $\text{MoS}_2$  as an example of a TMDC crystal, its energy dispersion from bulk to mono layer is shown in Fig. 2.5a. The positions of the valence and conduction bands change with decreasing thickness, in the limit of monolayer, an abrupt change from an indirect to a direct bandgap occurs [10]. Such a dramatic change is mediated by the contribution of the 3p<sub>z</sub> orbitals of sulfur atoms to the orbital composition of bulk and monolayer  $\text{MoS}_2$  [11]. Significant is that the valence and conduction states at the K point are mostly built up from Mo 4d-orbitals and are not affected by neighboring layers, so being not very sensitive to the number of layers [9, 11]. This property is common to the TMDCs (from group' 6) such as  $\text{WS}_2$ . First-principles calculations predict that the bandgap of bulk and monolayer  $\text{MoS}_2$  are 0.88 and 1.71 eV, respectively [7, 12].

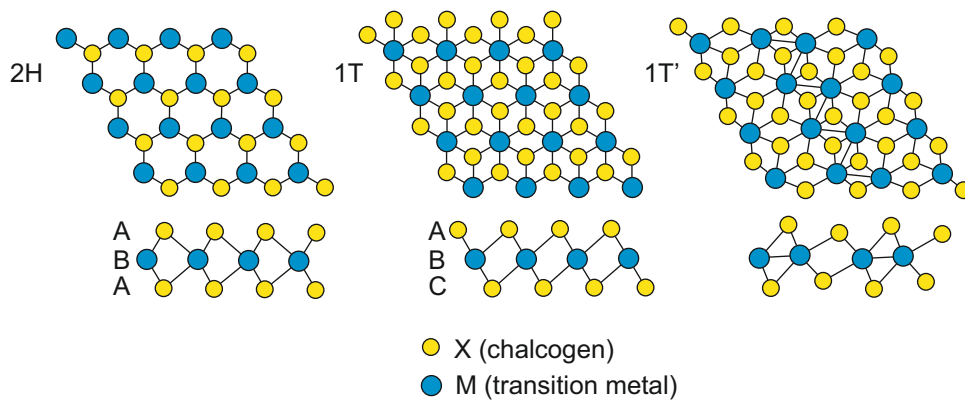


FIGURE 2.4: Top view (top panel) and side view (bottom panel) of the TMDC's atomic structure in its trigonal prismatic (2H), octahedral (1T) and dimerized (1T') phase .

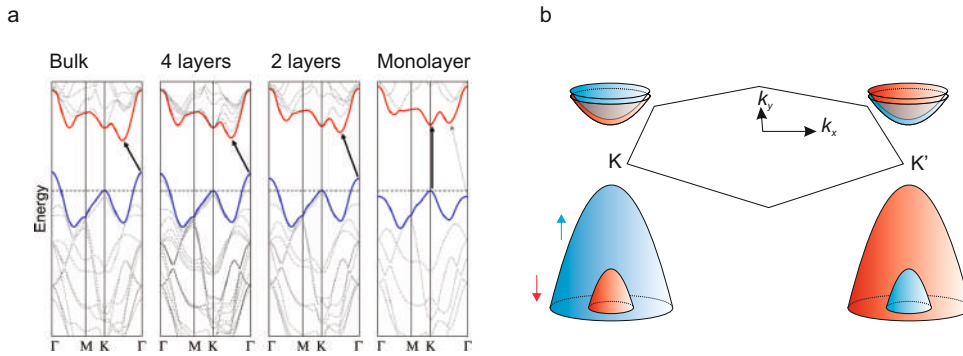


FIGURE 2.5: **a.** 2H-MoS<sub>2</sub> energy dispersion as a function of the number of layers. In the limit of monolayer an abrupt change from an indirect to a direct bandgap occurs. **b.** Schematic representation of the BZ and the band structure of monolayer 2H-MoS<sub>2</sub>, showing the spin splitting of the valence and conduction bands at the K and K' points. Blue and red colours indicate up and down spin polarization (up and down arrows). **a** from ref. [10]. Copyright 2010 American Chemical Society.

Monolayer TMDCs lack inversion symmetry, which, combined with the spin-orbit interaction, results in a splitting of the electronic bands, where the spin degeneracy of the conduction and valence is lifted at K and K' points [13] as shown schematically in Fig. 2.5b. This effect is particularly pronounced in the valence band, in which spin splitting values range from 0.15 eV in MoS<sub>2</sub> to 0.46 eV in WSe<sub>2</sub> [7, 14]. The conduction band is also split but the splitting energy is about an order of magnitude weaker than in the valence band. Remarkably, the splitting character of the conduction band is opposite between MoX<sub>2</sub> and WX<sub>2</sub> [13]. Because of time-reversal symmetry, the spin splitting of bands at K and K' is opposite. This property is referred to as spin–valley locking and implies that the valley polarization of charge carriers is directly translated into their spin polarization. This intrinsic property of TMDCs can, in principle, be imprinted in graphene by proximity-induced effects [15] and be used for smart-designing of spintronic devices, a subject that will be discussed in detail in Sec. 2.5.

### 2.3 Spin-orbit coupling in graphene

Even though SOC in pristine graphene is small; it leads to relevant consequences such as topological phases or, important for spintronics, it can also mediate the spin relaxation. When spin-orbit coupling in graphene is considered, it opens an orbital gap at the K points of the graphene BZ [16]. The magnitude of this gap has been predicted to be  $\sim 1 \mu\text{eV}$ , turning graphene from an ideal 2D semi-metal to a quantum spin Hall insulator [17]. However, it requires temperatures of 0.01 K to probe it [16]. The effective graphene Hamiltonian in the vicinity of the K points takes the form,

$$H = \hbar v_F (\tau_z \sigma_x k_x + \sigma_y k_y) + \Delta_{KM} \tau_z \sigma_z s_z + \Delta_{BR} (\tau_z \sigma_x s_y - \sigma_y s_x), \quad (2.9)$$

where  $\sigma_{x,y,z}$  are Pauli matrices describing states on the A (B) sublattices and  $\tau_z = \pm 1$  describes states at the K (K') points. The first term of Eq. (2.9) describes the gapless states with linear energy dispersion. The second term in Eq. (2.9) corresponds to the intrinsic SOC [17]. The  $\sigma_z \tau_z$  term is even under parity and odd under time reversal (interchanges between K and K'). The intrinsic SOC respects all of the symmetries of graphene. This term splits the bands in an energy of  $2\Delta_{KM}$ , where  $\Delta_{KM}$  is the intrinsic Kane-Mele parameter [17]. Models that capture SOC from  $\sigma$  and  $\pi$  mixing predict that  $\Delta_{KM} \sim 1 \mu\text{eV}$  [18, 19].  $\Delta_{KM}$  is enhanced when considering hybridization with d orbitals, leading to  $\Delta_{KM}$  from  $\sim 25 \mu\text{eV}$  to  $50 \mu\text{eV}$  [19]. A recent experiment demonstrated that  $\Delta_{KM} \sim 21 \mu\text{eV}$  employing electron-spin resonance on graphene [20].

The third term in Eq. (2.9) accounts for a commonly found extrinsic SOC, where  $\Delta_{BR}$  is the Bychkov-Rashba parameter [21]. This term is present when the mirror symmetry is broken e.g. by a perpendicular electric field or by interaction with a substrate. Contrary to the intrinsic SOC, the Bychkov-Rashba SOC term removes the spin degeneracy of the bands and favors to close the intrinsic spin-orbit gap [17]. Unlike in semiconductor heterostructures, the Bychkov-Rashba interaction in graphene does not depend on the magnitude of the electron momentum. First-principles calculations have estimated  $2\Delta_{BR}$  are  $\sim 10 \mu\text{eV}$  per V/nm [16] when an electric field is applied.

Corrugations in graphene, which can be induced by e.g., a rough substrate, generate new SOC terms. The origin of these new SOC can be explained by the change in the orientation of the orbitals due to curvatures in the graphene [18]. The curvature generates a Bychkov-Rashba type of SOC. From tight-binding models, estimates of the energy of this additional term are  $\sim 1.2 \text{ meV}$  [18].

Additional extrinsic SOC terms can arise from the environment surrounding graphene. Extra SOC is added to graphene when it is functionalized with hydrogen adatoms, which create a local out-of-plane induced distortion of the graphene lattice from  $sp^2$  to  $sp^3$ . This distortion leads to an enhancement of the SOC up to  $\sim 7 \text{ meV}$  [22]. First-principles calculations estimate a smaller enhancement of the SOC in hydrogenated graphene to  $\sim 0.33 \text{ meV}$  [23, 24]. Additional SOC emerges in decorated graphene with heavy metal atoms. Metallic atoms preserve the graphene  $sp^2$  bond while the SOC is enhanced due to tunneling of electrons from graphene to adatoms and back [23, 25].

The most appealing materials to enhanced SOC in graphene are probably layered semiconducting TMDCs since they have a large SOC, and at the same time, they can easily interact with graphene due to their 2D nature. Because they consist of atomically thin planes, their electrical, optical and spin properties can be enriched and tailored when they are stacked one on top of each other, in the same way than LEGO® blocks stacking. This thesis discusses the enhanced SOC in graphene by proximity to a TMDC, and its consequences in the transport, control and generation of spin currents in Section 2.5 and present results in Chaps. 4 and 5.

## 2.4 Spin relaxation in graphene

Extensive research in semiconductors and metallic systems has shown that SOC enables electric; and not just magnetic, control of the spin [26, 27]. But at the same time, the SOC mediates the spin relaxation, which limits the device performance. Thus, understanding the origin, nature and the interplay of SOC with the spin relaxation will open a door towards the efficient spin control. Two mechanisms of spin relaxation discussed in metals and semiconductors: the Elliot-Yafet [28, 29] and Dyakonov-Perel [30] mechanisms were initially adapted to understand the spin relaxation processes in graphene [31–33]. However, experimental results have not yet led to a conclusion which mechanism is responsible for limiting the spin relaxation, which was originally predicted to be orders of magnitude larger than the values reported so far [34].

The spin lifetime anisotropy  $\zeta$ , a parameter that quantifies the ratio between spin lifetimes for spins lying in the graphene plane ( $\tau_s^{\parallel}$ ) and pointing out of it ( $\tau_s^{\perp}$ ), can help discriminate between these relaxation mechanisms. In particular,  $\zeta$  is highly sensitive to the magnitude and orientation of existing spin-orbit fields (SOFs), if they drive the spin relaxation. For instance, for SOFs oriented in the graphene plane deriving from Rashba SOC, out-of-plane spins relax faster leading to  $\tau_s^{\perp} < \tau_s^{\parallel}$ , i.e.  $\zeta < 1$  [31, 35]. The relation is expected to change to  $\tau_s^{\perp} > \tau_s^{\parallel}$ , and consequently  $\zeta > 1$ , for spin relaxation driven by flexural distortions [36]. When there is no preferential direction in the spin relaxation, as in the case of spin relaxation driven by paramagnetic impurities or (random) gauge fields, the relaxation becomes isotropic with  $\tau_s^{\perp} = \tau_s^{\parallel}$ , so  $\zeta = 1$  [37, 38]. Given that the SOFs in graphene can be altered using compounds with large SOC, spin-relaxation anisotropy is a crucial parameter to investigate spin-orbit proximity effects and hence spin relaxation mechanism in graphene. A detail study and results on the anisotropic spin relaxation in graphene is presented in Chaps. 3 and 4.

### 2.4.1 Elliot–Yafet spin relaxation mechanism

The Elliot-Yafet (EY) spin relaxation mechanism is driven by spin flips during a scattering events with spin-conserving impurities, lattice defects, or phonons (Fig. 2.6). This is possible because the SOC produces electronic wave functions that are admixtures of the Pauli spin-up and spin-down states instead of Bloch states with well-defined spin polarization [33]. Since a spin-up electron has a small admixture amplitude of the Pauli spin-down spinor, then even a spin-conserving impurity or phonon scattering can induce a spin flip [32].

The EY spin relation establishes a linear relation between the spin relaxation time ( $\tau_s$ ) and momentum relaxation time ( $\tau_p$ ):

$$\tau_s = \frac{\tau_p}{b}, \quad (2.10)$$

where  $b$  is the spin-flip probability during a momentum relaxation event. In case of graphene  $1/b \approx \epsilon_F^2/\Delta^2$  where  $\epsilon_F$  is the Fermi energy and  $\Delta$  is the Rashba-like term. The intrinsic graphene SOC contribution is neglected in comparison to the Rashba-like coupling. The nature of the effective SOC in graphene and the vanishing gap between conduction and valence electrons, makes the ratio  $\tau_s/\tau_p$  depend strongly on the Fermi energy and hence the carrier concentration.

## 2.4.2 Dyakonov–Perel spin relaxation mechanism

The Dyakonov–Perel (DP) spin relaxation mechanism derives from spin precession between scattering events as it is shown schematically in Fig. 2.6 b. This mechanism is present for Rashba SOC, where the spin precession is mediated by an SOF oriented in plane  $\vec{B}_{\parallel} = \Delta_{RB}(\hat{\sigma} \times \hat{e}_z)/2$ ; where  $\hat{\sigma}$  correspond to Pauli matrices in sublattice space. This induced SOF changes direction during scattering resulting in a fluctuating magnetic field that depends on the momentum. The average spin orientation becomes random in a time [31]:

$$\tau_s = \frac{v_F}{\Delta_{RB}^2 \tau_p}, \quad (2.11)$$

which implies that within the DP mechanism, in contrast to EY case,  $\tau_s$  is inversely proportional to  $\tau_p$ . Additionally, given that the effective Rashba-field is oriented within the graphene plane, the out-of-plane spins relax faster than the in-plane spins. In fact, it has been proposed that if the spin relaxation in graphene is mediated by the DP mechanism, the spin relaxation should be anisotropic with a ratio  $\zeta = \tau_s^{\perp}/\tau_s^{\parallel} = 0.5$  [31, 32]. Such an anisotropic character with that given ratio  $\zeta$  has not been experimentally observed in graphene yet.

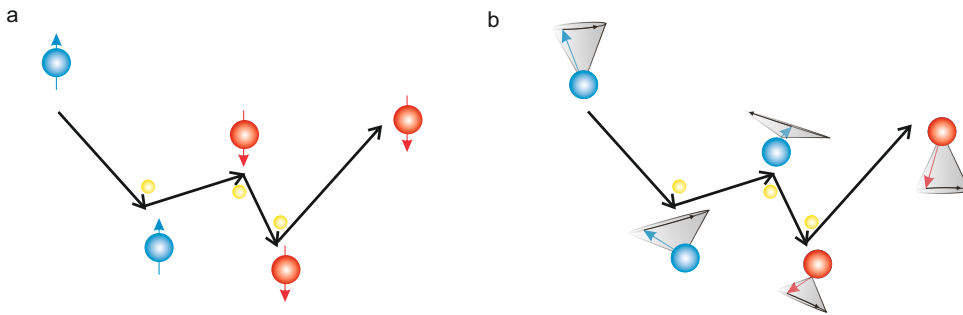


FIGURE 2.6: Schematic of **a.** Elliott–Yafet and **b.** Dyakonov–Perel spin relaxation mechanisms. The EY mechanism explains the spin relaxation by spin flips during scattering events (yellow dots), while the DP mechanism explains the spin relaxation by spin precession between scatters.

### 2.4.3 Specific spin relaxation mechanisms in graphene

The fact that none of the mechanisms described above explains the experimental observations in graphene, promoted the proposal of novel theories. These new mechanisms include the details of the SOC in graphene and the role of impurities and defects present in real graphene devices.

A particularly relevant proposal includes resonant scatterings of the spins with magnetic moments formed in graphene by the presence of vacancies or hydrogen-like adatoms. At the resonant energies, the carrier's spin precess at the impurity during a time comparable to the spin relaxation time. Then the spin-flip probability becomes equal for up and down [32] so the spins are randomized. Averaging over resonant energies that include thermal fluctuations, distribution of different defects, and electron-hole puddles, the spin relaxation time can be of 100 ps for just one ppm of magnetic moments. [37].

The resonant scattering spin relaxation can exist in combination with another spin relaxation mechanism driven by spin-pseudospin interaction. Here, the spin and the pseudospin are entangled by the SOC, which is caused by adatoms, ripples or even the substrate. The mixing between spin and pseudospin results in fast spin dephasing close to the charge neutrality point (CNP), where the entanglement is maximized. The spin relaxation time increases away from the CNP [39]. Such features are widely observed in experiments; however, if the spin relaxation is driven by pseudospin entanglement, a strict  $\zeta = 0.5$  should hold, in disagreement with the obtained results to date [34].

Lattice defects, strains, and curvature impact on the spin relaxation. Such effects have been captured by an induced effective gauge field. These gauge fields induce an effective magnetic field perpendicular to the graphene plane, which leads to a faster spin relaxation for spins oriented in-plane than for the spins oriented out-of-plane. The different spin relaxation times imply an anisotropic spin relaxation with  $\zeta > 1$ .

As exposed above, many theories have been proposed to explain the spin relaxation in graphene, which still remains an open issue within the research field. In this thesis, we explore the spin relaxation in graphene on hBN, which is supposed to be a suitable substrate for graphene (atomically flat and free from dangling bonds), results are present in Chapter 4. Very important is that SOC can be engineered in graphene via proximity effects. Such an advantage gives the freedom to tune SOC while keeping the attractive properties of graphene such as the ambipolar transport and the excellent carrier mobility. Proximity effects, its impact on spin relaxation, and spin control are of significant interest in this thesis. The theory of such phenomena is presented in the following section and experimental results are shown on Chapters 4 and 5.



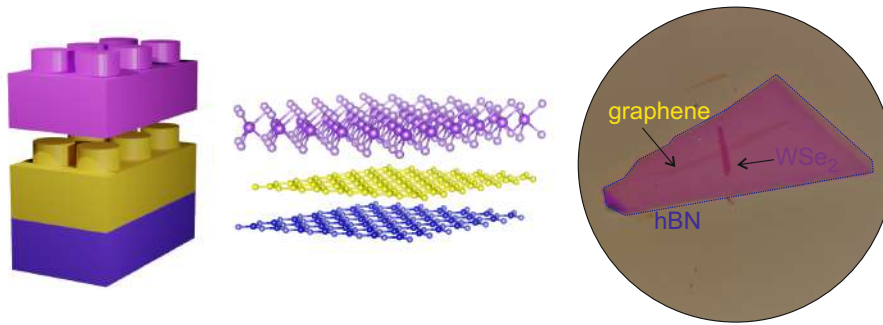


FIGURE 2.7: Cartoon representation of 2D crystals as LEGO® blocks (left panel). The construction of a plethora of 2D stackings forming new materials is possible, opening a door a new variety of phenomena. In the circle, an optical picture of a van der Waals heterostructure consisting of a  $\text{WSe}_2$  on top of a (bilayer) graphene flake, which is lying on an hBN substrate.

## 2.5 Proximity effects in graphene/TMDC heterostructures

Stacking atomically flat 2D materials in van der Waals (vdW) heterostructures have become a smart strategy to systematically design new artificial materials that combine the desired properties of each material. vdW heterostructures are commonly compared with building with one-atomic-thick (Fig. 2.7) LEGO® blocks. The stability of the heterostructure is provided by the in-plane stability of 2D crystals, whereas, van der Waals forces keep the stack together [40]. Properties are modified through proximity effects by which a proximitized material acquires characteristics that are absent in its pristine form (e. g., becoming superconductors, magnetic, or with an enhanced SOC [41]). Proximity effects can be intuitively understood from the well-known superconducting case, in which superconducting properties penetrate from a superconductor into an adjacent normal region over a characteristic length. In the same way, another property of a material can be transferred over a characteristic length into another region where it was initially absent. In 2D materials such as graphene or TMDCs, even short-range magnetic or SOC proximity effects can actively modify transport or optical properties.

When two or more materials are brought together, the inherent lack of inversion symmetry at interfaces yields to the formation of interfacial SOC [41]. A simple example is the Bychkov-Rashba SOC, which appears when graphene lies down on a substrate. When graphene is in proximity to a TMDC, the Dirac cone lies in the TMDC band gap, so the  $\pi$ -bands preserve their identity while acquiring a remarkably large SOC by proximity with the heavy atoms of the TMDC (thus the d orbitals of the heavy metal atoms). Generally, an effective symmetry-based Hamiltonian with graphene orbitals in the presence of pseudospin inversion symmetry breaking gives a good description of the proximity-induced changes in graphene's band structure. The effective-hamiltonian close to the K points is given by [15, 42],

$$\begin{aligned}
H = & \hbar v_F (\tau_z \sigma_x k_x + \sigma_y k_y) + \Delta_{KM} \tau_z \sigma_z s_z + \Delta_{BR} (\tau_z \sigma_x s_y - \sigma_y s_x) \\
& + \Delta_{st} \sigma_z \\
& + \left( \lambda_1^A (\sigma_z + 1) + \lambda_1^B (\sigma_z - 1) \right) \frac{\tau_z s_z}{2} \\
& + \frac{a}{2} \left( \lambda_{PIA}^A (\sigma_z + 1) + \lambda_{PIA}^B (\sigma_z - 1) \right) (k_x s_y - k_y s_x).
\end{aligned} \tag{2.12}$$

The first line in Eq. (2.12) is the graphene Hamiltonian described in Eq. (2.9) (Sec. 2.3) while the next three new terms arise as a result of the proximity with the TMDC. From these added terms, the first is the staggered potential  $\Delta_{st}$ , which describes the effective orbital energy difference on A and B sublattices of graphene in a TMDC. The second term is the sublattice-resolved intrinsic SOC, which acts on a given sublattice A and B.  $\lambda_1^{A/B}$  are the parameters for the intrinsic SOC for each subband. The last term is the pseudospin inversion asymmetry (PIA) SOC, which arises because sites that belong to the same sublattice see different local environments. The  $\lambda_{PIA}^{A/B}$  are the strength of the PIA SOC in each sublattice, and  $a \approx 2.6 \text{ \AA}$  is the graphene lattice constant.

There are three important modifications in the band structure of graphene as a consequence of the proximity effect with a TMDC, as shown in Fig. 2.8a. Firstly, the staggered potential opens an orbital gap at K points due to the breaking of the graphene pseudospin symmetry. Secondly, the intrinsic SOC lifts the spin degeneracy and imprint the spin valley locking at the K and K' points in graphene. Finally, the PIA and the Rashba terms are responsible for chiral spin textures away from the K and K' points. Figure 2.8b shows the calculated band structure of graphene on

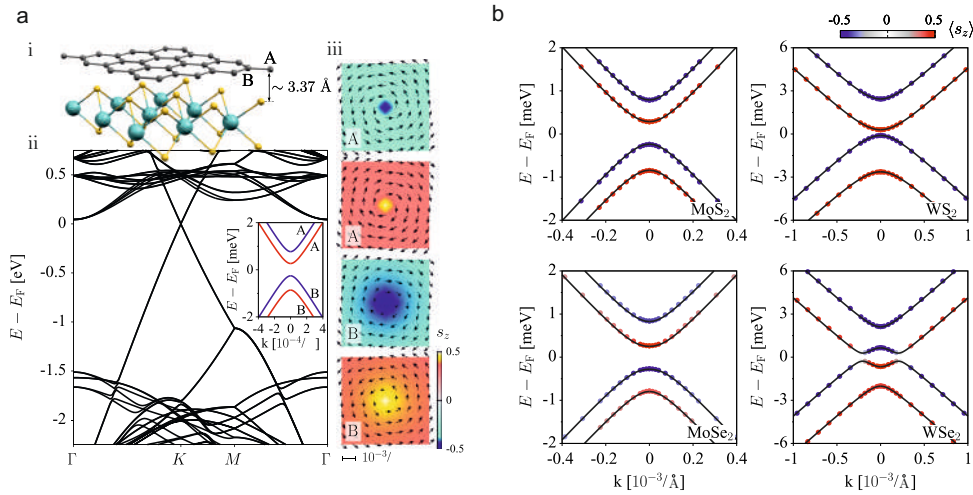


FIGURE 2.8: Graphene/TMDC energy dispersion. **a.** electronic and spin properties of graphene on MoS<sub>2</sub>. **i.** Supercell used for the ab-initio calculations. **ii.** Band structure along high symmetry points. In the inset a zoom to the of the low energy bands at the Fermi level at the K point. Bands with a up (down) spin are shown in red (blue). A and B indicates the sublattice character. **iii.** Spin texture in the vicinity of the K point. Away from K, the spins acquire a winding in-plane component, either clockwise or counterclockwise. **b.** Band structure for graphene on different TMDCs. **a** from ref. [15]. Copyright 2015 American Physical Society. **b** from ref. [42]. Copyright 2016 American Physical Society.

different TMDCs.

The spin splitting and the spin texture in the modified electronic states of graphene implies that the spin dynamics would likely differ for spins pointing in ( $\parallel$ ) and out of ( $\perp$ ) the graphene plane, leading to distinct spin lifetimes,  $\tau_s^\parallel$  and  $\tau_s^\perp$ . Indeed, realistic modelling and numerical simulations in graphene/WS<sub>2</sub>, which are presented in the next section, predict that the spin lifetime anisotropy ratio  $\zeta \equiv \tau_s^\perp/\tau_s^\parallel$  could reach values as large as a few hundreds, in the presence of intervalley scattering [43]. Quantification of  $\zeta$  can therefore provide unique insight into spin-valley coupling mechanisms. Experimental results unambiguously demonstrating the anisotropic spin relaxation in graphene/TMDCs are shown in Chap. 4. Additionally, the particular spin texture created in the modified graphene also leads to an enhanced spin-charge interconversion (SCI) by the spin Hall effect and the spin galvanic effect, as explained in subsec. 2.5.2.

### 2.5.1 Anisotropic spin relaxation in graphene/TMDCs

A direct consequence of the induced SOC and spin texture in graphene is the anisotropic spin relaxation, i.e., the spin relaxation time differs for spins pointing in- and out-of-the graphene plane. Here, we describe the current theoretical understanding of this phenomenon in graphene/TMDCs.

Recent theoretical studies have shown that in graphene/TMDCs, the spin relaxation time follows an inverse relation with the momentum relaxation time, suggesting a Dyakonov-Perel spin relaxation mechanism [43, 44]. However, because of the nature of the enhanced SOC in graphene, a different spin relaxation ratio  $\zeta$  has been proposed. Considering weak SOC, the Hamiltonian given by Eq. (2.12) is rewritten in the basis of  $H_0 = \hbar v_F(\tau_z \sigma_x k_x + \sigma_y k_y)$  and projected over the conduction and valence bands away from the Dirac point [43]:

$$\begin{aligned} H &= H_0 + \frac{1}{2} \hbar \vec{w}(t) \cdot \vec{s}, \\ \hbar w_x &= -2(ak\Delta_{\text{PIA}} \pm \Delta_{\text{BR}}) \sin \theta, \\ \hbar w_y &= 2(ak\Delta_{\text{PIA}} \pm \Delta_{\text{BR}}) \cos \theta, \\ \hbar w_z &= 2\tau_z \Delta_{\text{VZ}}, \end{aligned} \tag{2.13}$$

where  $k$  is the magnitude of the wave vector, and  $\pm$  accounts for the conduction (+) and valence (-) band.  $\vec{w}(t)$  contains the effects of the induced SOC, and it can be seen as an effective magnetic field, whose direction and strength are determined in its components (see schematics in Fig. 2.9)  $\Delta_{\text{PIA}} = (\lambda_{\text{PIA}}^{\text{A}} - \lambda_{\text{PIA}}^{\text{B}})/2$ , and  $\Delta_{\text{VZ}} = (\lambda_{\text{I}}^{\text{A}} - \lambda_{\text{I}}^{\text{B}})/2$ .  $\Delta_{\text{VZ}}$  is the valley-Zeeman term, which polarizes the graphene's spin sub-bands out-of-plane with opposite orientation in the K and K' points (valleys).

The time ( $t$ ) dependence of  $\vec{w}$  is produced by scattering events which change the momentum, thus they change the  $\theta = \theta(t)$  coordinate and may change the valley index  $\tau_z = \tau_z(t)$  of a given state. Because  $\omega_{x,y}(t)$  depends only on  $\theta$ , they randomize the spins during scattering according to the momentum relaxation time  $\tau_p$ . On the

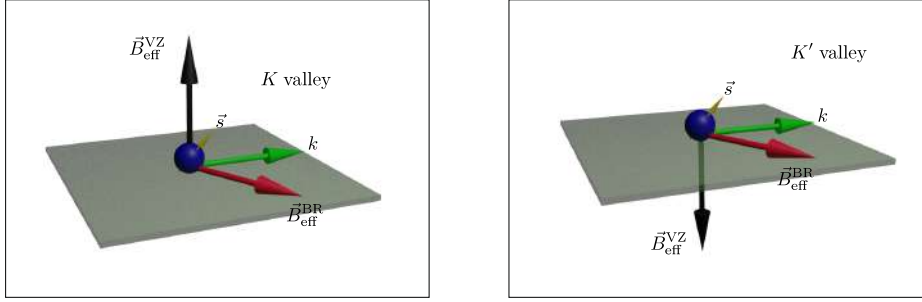


FIGURE 2.9: Effective magnetic fields acting in graphene/TMDC. The BR effective magnetic field  $\vec{B}_{\text{eff}}^{\text{BR}}$  points in-plane.  $k$  is the electron wave vector. The VZ effective magnetic field  $\vec{B}_{\text{eff}}^{\text{VZ}}$  lies perpendicular to the plane and it has opposite signs in K and K' valleys.

other hand,  $\omega_z$  depends only on the valley  $\tau_z$ , so this component randomizes the spins by the intervalley scattering time  $\tau_{iv}$  [43]. The relaxation rates of the out-of-plane and in-plane spins and its ratio are [43, 45]:

$$\begin{aligned}
 (\tau_s^\perp)^{-1} &= \left( \frac{2 a k \Delta_{\text{PIA}} \pm \Delta_{\text{BR}}}{\hbar} \right)^2 \tau_p, \\
 (\tau_s^\parallel)^{-1} &= \left( \frac{2 \Delta_{\text{VZ}}}{\hbar} \right)^2 \tau_{iv} + \frac{1}{2} (\tau_s^\perp)^{-1}, \\
 \zeta &= \frac{\tau_s^\perp}{\tau_s^\parallel} = \left( \frac{\Delta_{\text{VZ}}}{a k \Delta_{\text{PIA}} \pm \Delta_{\text{BR}}} \right)^2 \left( \frac{\tau_{iv}}{\tau_p} \right) + \frac{1}{2}.
 \end{aligned} \tag{2.14}$$

Intervalley scattering arises from short-range elastic scattering centers, e.g., structural defects in graphene, vacancies in the TMDC, or electron-hole puddles. Using DFT values of  $\Delta_{\text{BR}} = 0.56$  meV,  $\Delta_{\text{VZ}} = 1.2$  meV for graphene on WSe<sub>2</sub>, and ignoring the PIA term with  $\tau_{iv} \sim 5\tau_p$  the obtained anisotropy ratio is  $\sim 20$ . Thus, a large anisotropy should be an experimental fingerprint of SOC proximity effects and the spin-valley locking induced in graphene by TMDCs. However, in absence of intervalley scattering, the spin relaxation anisotropy ratio reduces to  $\zeta = 1/2$ . Therefore, the determination of  $\zeta$  provides information also on the type of scattering processes that are present. The experimental demonstration of the imprinted SOC and the spin-valley locking in graphene /TMDCs heterostructures is one of the objectives of this thesis, and its fully explained in Chap. 4.

Models that go beyond the DP motional narrowing regime of weak SOC predict more scenarios that depend on a competition between the Bychkov-Rashba and spin-valley interaction [44]. All these scenarios have a common experimentally accessible fingerprint, the spin relaxation anisotropy  $\zeta$ . Within these models, even in the absence of intervalley scattering, the intravalley scattering (momentum relaxation time) deviates  $\zeta$  from the usual 1/2. Considering intervalley scattering and going from weak SOC to well-resolved SOC, more scenarios for  $\zeta$  appear. In the limit of weak SOC, both approaches give good qualitative agreement with Eq. (2.14).

### 2.5.2 Spin to charge interconversion

SOC enables the generation and manipulation of spins solely by electric fields, and an easy way to understand it qualitatively is to recall that SOC is a relativity correction to the motion of a spin inside a potential. In the rest frame of an electron moving through a lattice, the external electric field (crystalline potential) is Lorentz transformed into a magnetic field that can act upon the spin of the electron. Using the SOC for manipulating electron spin circumvents the design complexities that are often associated with incorporating local magnetic fields into device architectures.

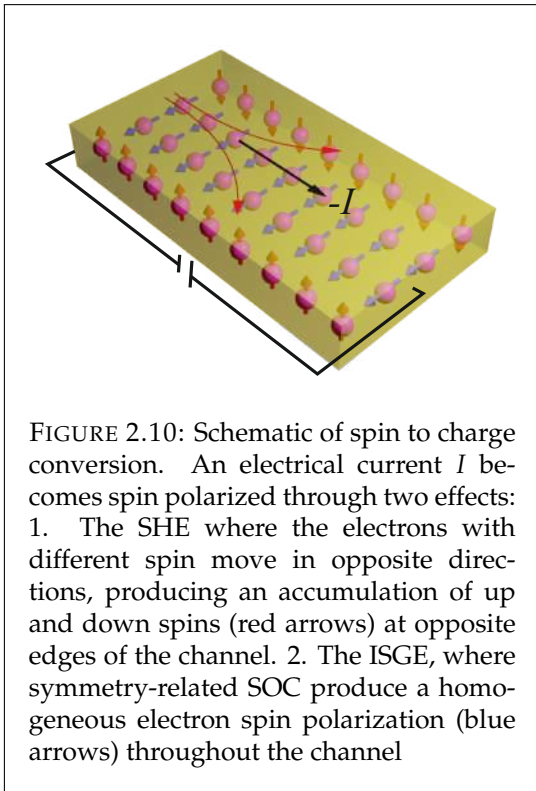


FIGURE 2.10: Schematic of spin to charge conversion. An electrical current  $I$  becomes spin polarized through two effects: 1. The SHE where the electrons with different spin move in opposite directions, producing an accumulation of up and down spins (red arrows) at opposite edges of the channel. 2. The ISGE, where symmetry-related SOC produce a homogeneous electron spin polarization (blue arrows) throughout the channel

The SOC generates spin polarization through two conceptually different processes: spin-dependent scattering and the acquisition of a geometric phase [46, 47]. The former idea was developed by Mott, who used the Dirac equation and calculated the spin-dependent skew scattering of relativistic electrons by a Coulomb potential produced by atomic nuclei, in which electrons with spin up and down are scattered in opposite trajectories [48]. Additionally, to skew scattering, SOC may modify the band structure lifting the spin degeneracy [49, 50]. This removal of spin degeneracy acts like an effective magnetic field that can be engineered into graphene. Such is the case of the effective valley-Zeeman field present in TMDCs and imprinted into graphene.

When an electric current flows through a semiconductor with SOC, spin polarization is generated by two complementary effects that often coexist: the spin Hall effect (SHE) and current-induced spin polarization, also known as the inverse spin galvanic effect (ISGE) or Rashba-Edelstein effect (REE). Figure 2.10 schematically represents the creation of a spin-polarized current during the flow of an electric current. Remarkably, both these phenomena are observed in a variety of standard semiconductor crystals, ranging from bulk (three-dimensional) systems to two-dimensional electron gases (2DEGs) [51], as well as, in metal/metal interfaces [52, 53]. Once a spin-polarized current is generated it can be further used e. g. for writing the magnetic information in magnetic random access memories [54].

## Spin Hall effect

The SHE arises when a current flows through a non-magnetic metal or semiconductor in the presence of SOC, generating an spin accumulation at the edges of the material (red arrows in Fig. 2.10). Its reciprocal phenomenon, the inverse spin Hall effect (ISHE), generates a charge current when a pure spin current flows in the transport channel. Even though the SHE prediction dates back to 1971 [55], it took over 30 years to have unambiguous experimental evidence of its existence using high-sensitivity scanning optical imaging techniques [56] and by pure electrical means later on [57]. Since then, the SHE has been extensively studied in metals and semiconductors [58].

The theories of the SHE have naturally emerged from the theory of the anomalous Hall effect (AHE). In the AHE, an electrical current flowing in a ferromagnet generates a transverse voltage due to the difference in the population of majority and minority carriers. The driving force behind the AHE and the SHE is the SOC, which selectively deflects spins up and down. The SHE does not generate a transverse voltage at the edge of the N material given that there is equal population of spins up and down.

The AHE, SHE, and ISHE originate from extrinsic disorder-related effects (the skew, the side jump), and an intrinsic mechanism which can be described in terms of the Berry phase effect in the crystal momentum space. The Berry phase is a geometric factor, in the sense that its contribution to the action depends on the trajectory in the momentum space but not on the rate of the motion along this trajectory.

### Intrinsic contribution to the SHE

The intrinsic contribution to the SHE depends exclusively on the band structure of the crystal. The Berry curvature of the Bloch bands produces an anomalous velocity term added to the standard Bloch band group velocity. Such a term, in the presence of an electric field, gives rise to a transverse conductivity ( $\sigma_{xy}$ ) for the AHE [59, 60], and pure spin current for the SHE [58]. Qualitatively, the Berry curvature can be considered as a particular magnetic field acting on the momentum space. However, unlike the magnetic field, the Berry curvature originates from a source. In electrodynamics, a magnetic field with such properties would originate from magnetic monopoles. Their analogs in Bloch bands are the points of exact crossings of band dispersion curves [59, 59, 60]. The integral of the Berry curvature over a closed manifold gives the so-called Chern number, which is a topological invariant of the band structure. The nontrivial topology is not special, as in the case of a quantum Hall system, but is generic in the presence of the SOC. In this sense, the SHE is a fingerprint of the band structure and very sensitive to the the Berry curvature (gauge field) [61].

Fig. 2.11a shows the calculated intrinsic SHE conductivity  $\sigma_{xy}^z$  for different graphene/TMDC heterostructures defined by the Hamiltonian given in Eq. (2.12).  $z$

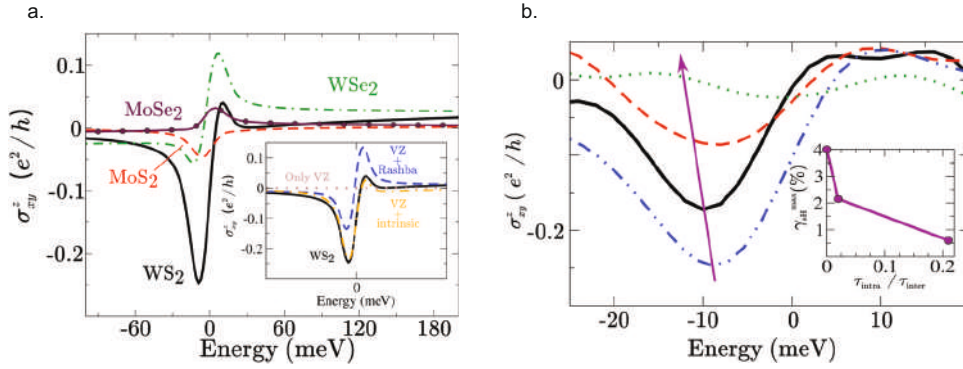


FIGURE 2.11: Spin Hall conductivity  $\sigma_{xy}^z$  in graphene/TMDCs as a function of the Fermi energy,  $z$ , accounts for the direction of spins. **a.** The calculated  $\sigma_{xy}^z$  for graphene on top of different TMDCs, shows that the graphene/WS<sub>2</sub> system maximizes the SHE signal compared to graphene on MoS<sub>2</sub>, WSe<sub>2</sub>, or MoSe<sub>2</sub>. Inset shows the calculated  $\sigma_{xy}^z$  for a different combination of SOC terms, only VZ in combination with Rashba or intrinsic SOC results in a finite transversal conductivity. **b.** Effect of inter-valley scattering in  $\sigma_{xy}^z$ . The solid black line, the dashed red line, and the dashed and dotted green line correspond to weak, intermediate and strong inter-valley scattering, respectively. Pristine spin Hall conductivity (dot-dashed blue line) is shown as a reference. The inset shows the scaling of the spin Hall angle with intervalley scattering strength. The inset shows the scaling of the spin Hall angle with intervalley scattering strength. **a** and **b** from [45]. Copyright 2018 The Royal Society of Chemistry.

stands for the direction of the spins. Fig. 2.11a shows that the higher  $\sigma_{xy}^z$  is achieved in graphene/WS<sub>2</sub> and that valley-Zeeman SOC alone does not lead to a spin Hall effect. Only valley-Zeeman SOC in combination with Rashba and intrinsic SOC lead to a finite spin Hall conductivity. Fig. 2.11b displays  $\sigma_{xy}^z$  for different disorder regimes, showing that disorder has a major impact on the spin Hall conductivity, leading to the suppression of the SHE.

### Extrinsic contribution to the SHE

Extrinsic mechanisms, associated to the problem of scattering on the smooth potential of an impurity, can be dominant for the SHE. The Mott-skew scattering occurs when an electron feels the impurity potential in the presence of SOC; the scattering results in different scattering angles for spin-up and spin-down electrons [62]. In the side-jump model, the scattering can produce a coordinate shift [59, 61], resulting in a lateral displacement of the electrons. Intrinsic contributions to the SHE or AHE are considered to arise from the spin-orbit coupling in the disorder potential only if the typical disorder broadening is larger than the splitting of the bands due to the spin-orbit coupling. Otherwise, the spin-orbit-coupled part of the wave packet formed by the Bloch electrons can also contribute [58].



### Spin galvanic effect

As mentioned before, the SHE is often accompanied by a bulk spin polarization generated by electron currents (blue arrows in Fig. 2.10). This effect in semiconductors with spin-orbit coupling was predicted in 1978 [63] and later theoretically analyzed in a two-dimensional electron gas (2DEG), in the presence of Dresselhaus [64] SOC, and Rashba SOC [65]. The current-induced spin polarization, which is the consequence of symmetry-allowed coupling between spin polarization and electrical current, may be referred to under different names.

The generation of current from a nonequilibrium spin polarization is called spin galvanic effect (SGE) or inverse Edelstein effect (IEE), both terms are equivalent. The reciprocal phenomenon of current-induced spin polarization is referred to as the inverse spin galvanic effect (ISGE) or the Rashba-Edelstein effect (REE).

For a 2DEG system, the linear dependence of the Rashba SOC with the electronic wave vector  $k$  results in the splitting into an inner and outer branches as shown in Fig. 2.12a *i*. The DOS for the inner and outer branches is different, but their sum equals the DOS for the case without SOI (Fig. 2.12a *ii*), the in-plane spin texture of each band is plotted in 2.12a *iii*. Under an applied in-plane electric field  $\vec{E}$  along the  $x$  direction, the Fermi contours, which have opposite helicity, are shifted resulting, in the repopulation of the spins. Although accumulated spin in the two Fermi contours is opposite, a nonzero spin density in the  $+y$  direction is generated because the total number of up spin is larger than that of down spin.

The ISGE is schematically represented in Fig. 2.12b *i*. When an in-plane spin accumulation is achieved in the system (e. g. by spin injection), the two Fermi contours are shifted in opposite directions, and a nonzero electric field is generated (Fig. 2.12b *ii*). This is the SGE, the reciprocal effect of the ISGE.

In the modified states of graphene by proximity with a TMDC, the ISGE can be understood in the same way, but with key differences. The first one comes from

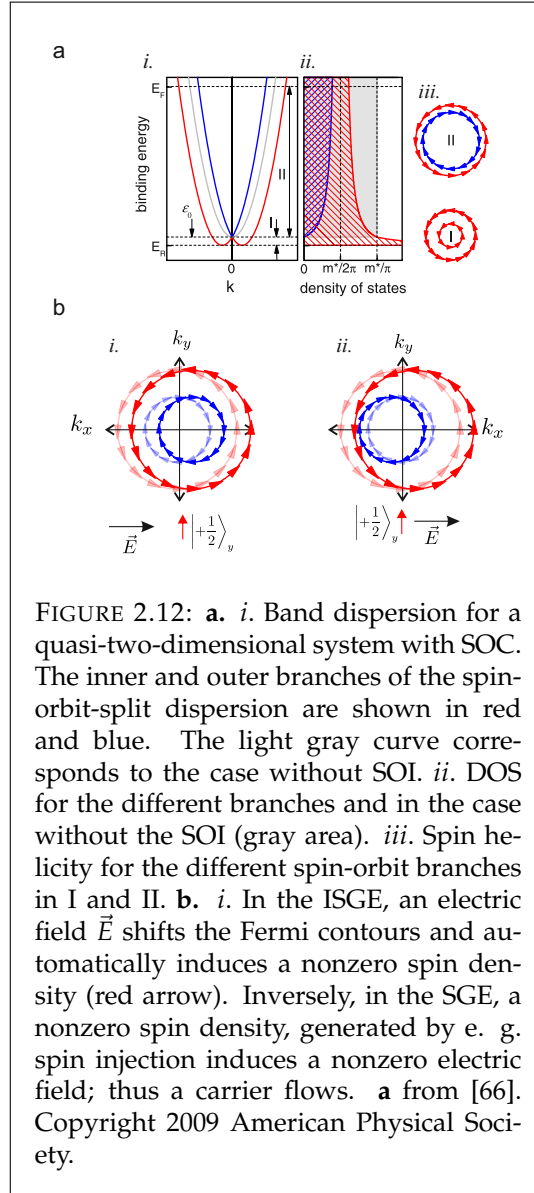


FIGURE 2.12: **a. i.** Band dispersion for a quasi-two-dimensional system with SOC. The inner and outer branches of the spin-orbit-split dispersion are shown in red and blue. The light gray curve corresponds to the case without SOI. **ii.** DOS for the different branches and in the case without the SOI (gray area). **iii.** Spin helicity for the different spin-orbit branches in I and II. **b. i.** In the ISGE, an electric field  $\vec{E}$  shifts the Fermi contours and automatically induces a nonzero spin density (red arrow). Inversely, in the SGE, a nonzero spin density, generated by e. g. spin injection induces a nonzero electric field; thus a carrier flows. **a** from [66]. Copyright 2009 American Physical Society.



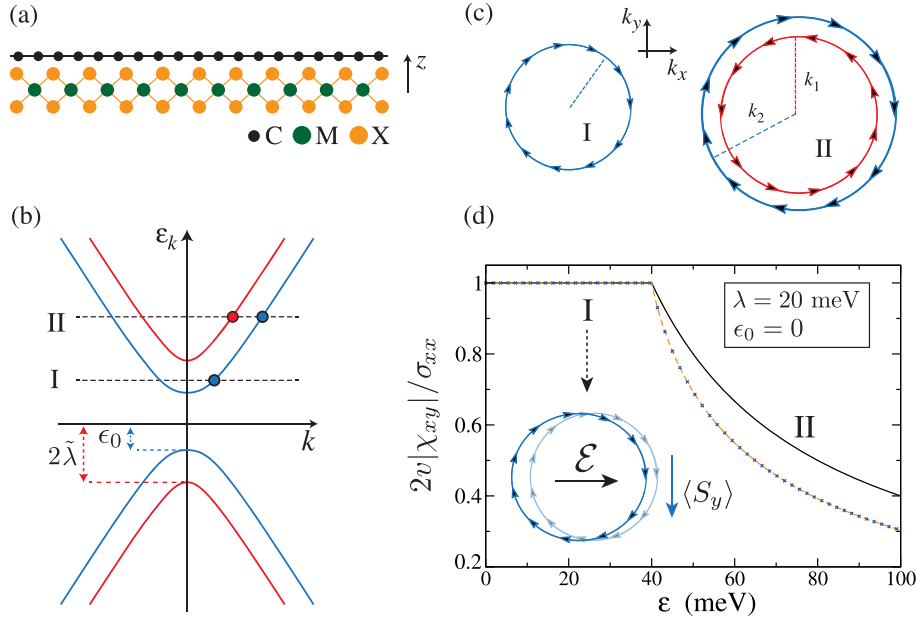


FIGURE 2.13: Spin galvanic in graphene/TMDCs heterostructures. **a.** Graphene/TMDC heterostructure. **b.** Spin orbit-split bands in the modified electronic states of graphene. **c.** Fermi contours of regions I and II in **b**, showing the well-defined spin-helicity of each spin-orbit branch. **d.** ISGE as a function of the Fermi energy, a remarkable efficient is achieved in I while it decreases algebraically at higher energies. **a**, **b**, **c**, **d** from [67]. Copyright 2017 American Physical Society.

the fact that the induced Rashba coupling in graphene does not depend on  $k$  as in a 2DEG, so the spin-orbit-splitting is not shifted in  $k$ . As described in Sec. 2.5, the spin spitting is mediated by the valley-Zeeman coupling. The second difference is that graphene/TMDC interfacial states are reminiscent of spin-momentum locking in topologically protected surface states, which leads to efficient spin-charge inter-conversion through SGE and ISGE [67].

The typical band structure with spin-split bands and opposite spin helicity is shown in Fig. 2.13b. The The spin texture of each band is [67]:

$$\langle s \rangle_{\alpha k} = -\xi \varrho(k) (\hat{k} \times \hat{z}) + m_{\alpha}^z(k) \hat{z}, \quad (2.15)$$

$\xi = \pm 1$  is the spin-helicity index. The first term describes the in-plane spin texture generated by the Rashba coupling and the second its out-of-plane tilting. Eq. (2.15) shows a remarkable  $k$  dependence in the spin texture, which in fact, is mediated by entanglement between spin and sublattice degrees of freedom [67].  $m_{\alpha}^z(k=0) = 1$ , and it decays to zero away from the Dirac point, while  $\varrho(k=0) = 0$  and it increases away from the Dirac point [67]. Time reversal symmetry imposes equivalent but opposite in- and out-of-plane spin polarization when changing sign of  $k$ , this leads to the same spin-helicity in the K and K' points. This definite spin helicity (Fig. 2.13b-c) is evocative of spin-momentum locking in topologically protected surface states, prompting efficient SGE [67]. The calculated efficiency is close

to unity when the Fermi level extends in the spin minority band, and it decays algebraically at higher electronic densities (Fig. 2.13d).

## References

- [1] Saito, R., Dresselhaus, G. & Dresselhaus, M. S. Trigonal warping effect of carbon nanotubes. *Phys. Rev. B* **61**, 2981 (2000).
- [2] Pletikosić, I. *et al.* Dirac cones and minigaps for graphene on Ir (111). *Phys. Rev. Lett.* **102**, 056808 (2009).
- [3] Torres, L. E. F. F., Roche, S. & Charlier, J.-C. *Introduction to graphene-based nanomaterials: from electronic structure to quantum transport* (Cambridge University Press, 2020).
- [4] Proctor, J. E., Armada, D. M. & Vijayaraghavan, A. *An introduction to graphene and carbon nanotubes* (CRC Press, 2017).
- [5] Das Sarma, S., Adam, S., Hwang, E. H. & Rossi, E. Electronic transport in two-dimensional graphene. *Rev. Mod. Phys.* **83**, 407–470 (2011).
- [6] Neto, A. H. C. *et al.* The electronic properties of graphene. *Rev. Mod. Phys.* **81**, 109–162 (2009).
- [7] Manzeli, S., Ovchinnikov, D., Pasquier, D., Yazyev, O. V. & Kis, A. 2D transition metal dichalcogenides. *Nat. Rev. Mater.* **2**, 17033 (2017).
- [8] Zhao, W. *et al.* Metastable MoS<sub>2</sub>: crystal structure, electronic band structure, synthetic approach and intriguing physical properties. *Chem.–Eur. J.* **24**, 15942–15954 (2018).
- [9] Samadi, M. *et al.* Group 6 transition metal dichalcogenide nanomaterials: synthesis, applications and future perspectives. *Nanoscale Horiz.* **3**, 90–204 (2018).
- [10] Splendiani, A. *et al.* Emerging photoluminescence in monolayer MoS<sub>2</sub>. *Nano Lett.* **10**, 1271–1275 (2010).
- [11] Cappelluti, E., Roldán, R., Silva-Guillén, J. A., Ordejón, P. & Guinea, F. Tight-binding model and direct-gap/indirect-gap transition in single-layer and multilayer MoS<sub>2</sub>. *Phys. Rev. B* **88**, 075409 (2013).
- [12] Hill, H. M., Rigosi, A. F., Rim, K. T., Flynn, G. W. & Heinz, T. F. Band alignment in MoS<sub>2</sub>/WS<sub>2</sub> transition metal dichalcogenide heterostructures probed by scanning tunneling microscopy and spectroscopy. *Nano Lett.* **16**, 4831–4837 (2016).
- [13] Kormányos, A. *et al.* Corrigendum: k.p theory for two-dimensional transition metal dichalcogenide semiconductors (2015 2D Mater. 2 022001). *2D Mater.* **2**, 049501 (2015).

- [14] Zhu, Z. Y., Cheng, Y. C. & Schwingenschlöggl, U. Giant spin-orbit-induced spin splitting in two-dimensional transition-metal dichalcogenide semiconductors. *Phys. Rev. B* **84**, 153402 (2011).
- [15] Gmitra, M. & Fabian, J. Graphene on transition-metal dichalcogenides: A platform for proximity spin-orbit physics and optospintronics. *Phys. Rev. B* **92**, 155403 (2015).
- [16] Gmitra, M., Konschuh, S., Ertler, C., Ambrosch-Draxl, C. & Fabian, J. Band-structure topologies of graphene: Spin-orbit coupling effects from first principles. *Phys. Rev. B* **80**, 235431 (2009).
- [17] Kane, C. L. & Mele, E. J. Quantum spin Hall effect in graphene. *Phys. Rev. Lett.* **95**, 226801 (2005).
- [18] Huertas-Hernando, D., Guinea, F. & Brataas, A. Spin-orbit coupling in curved graphene, fullerenes, nanotubes, and nanotube caps. *Phys. Rev. B - Condens. Matter Mater. Phys.* **74**, 155426 (2006).
- [19] Konschuh, S., Gmitra, M. & Fabian, J. Tight-binding theory of the spin-orbit coupling in graphene. *Phys. Rev. B* **82**, 245412 (2010).
- [20] Sichau, J. *et al.* Resonance microwave measurements of an intrinsic spin-orbit coupling gap in graphene: A possible indication of a topological state. *Phys. Rev. Lett.* **122**, 046403 (2019).
- [21] Rashba, E. I. Graphene with structure-induced spin-orbit coupling: Spin-polarized states, spin zero modes, and quantum Hall effect. *Phys. Rev. B* **79**, 161409 (2009).
- [22] Castro Neto, A. H. & Guinea, F. Impurity-induced spin-orbit coupling in graphene. *Phys. Rev. Lett.* **103**, 1–4 (2009).
- [23] Avsar, A. *et al.* Colloquium: Spintronics in graphene and other two-dimensional materials. *Rev. Mod. Phys.* **92**, 021003 (2020).
- [24] Gmitra, M., Kochan, D. & Fabian, J. Spin-orbit coupling in hydrogenated graphene. *Phys. Rev. Lett.* **110**, 1–5 (2013).
- [25] Marchenko, D. *et al.* Giant Rashba splitting in graphene due to hybridization with gold. *Nat. Commun.* **3**, 1232 (2012).
- [26] Žutić, I., Fabian, J. & Das Sarma, S. Spintronics: Fundamentals and applications. *Rev. Mod. Phys.* **76**, 323–410 (2004).
- [27] Fabian, J., Matos-Abiague, A., Ertler, C., Stano, P. & Žutić, I. Semiconductor spintronics. *Acta Phys. Slovaca. Rev. Tutorials* **57**, 1–9 (2007).

- [28] Elliott, R. J. Theory of the effect of spin-orbit coupling on magnetic resonance in some semiconductors. *Phys. Rev.* **96**, 266–279 (1954).
- [29] Yafet, Y. g factors and spin-lattice relaxation of conduction electrons. In Seitz, F. & Turnbull, D. (eds.) *Solid State Physics*, vol. 14, 1–98 (Academic Press, 1963).
- [30] Dyakonov, M. I. & Perel, V. I. Spin relaxation of conduction electrons in noncentrosymmetric semiconductors. *Soviet Physics Solid State* **13**, 3023–3026 (1972).
- [31] Huertas-Hernando, D., Guinea, F. & Brataas, A. Spin-orbit-mediated spin relaxation in graphene. *Phys. Rev. Lett.* **103**, 146801 (2009).
- [32] Han, W., Kawakami, R. K., Gmitra, M. & Fabian, J. Graphene spintronics. *Nat. Nanotechnol.* **9**, 794–807 (2014).
- [33] Ochoa, H., Neto, A. H. C. & Guinea, F. Elliot-Yafet mechanism in graphene. *Phys. Rev. Lett.* **108**, 206808 (2012).
- [34] Benítez, L. A. *et al.* Investigating the spin-orbit interaction in van der waals heterostructures by means of the spin relaxation anisotropy. *APL Mater.* **7**, 120701 (2019).
- [35] Ertler, C., Kunschuh, S., Gmitra, M. & Fabian, J. Electron spin relaxation in graphene: The role of the substrate. *Phys. Rev. B* **80**, 041405 (2009).
- [36] Fratini, S., Gosálbez-Martínez, D., Merodio Cámara, P. & Fernández-Rossier, J. Anisotropic intrinsic spin relaxation in graphene due to flexural distortions. *Phys. Rev. B* **88**, 115426 (2013).
- [37] Kochan, D., Gmitra, M. & Fabian, J. Spin relaxation mechanism in graphene: Resonant scattering by magnetic impurities. *Phys. Rev. Lett.* **112**, 116602 (2014).
- [38] Soriano, D. *et al.* Spin transport in hydrogenated graphene. *2D Mater.* **2**, 022002 (2015).
- [39] Tuan, D. V., Ortmann, F., Soriano, D., Valenzuela, S. O. & Roche, S. Pseudospin-driven spin relaxation mechanism in graphene. *Nat. Phys.* **10**, 857–863 (2014).
- [40] Geim, A. K. & Grigorieva, I. V. Van der Waals heterostructures. *Nature* **499**, 419–425 (2013).
- [41] Žutić, I., Matos-Abiague, A., Scharf, B., Dery, H. & Belashchenko, K. Proximitized materials. *Mater. Today* **22**, 85–107 (2019).
- [42] Gmitra, M., Kochan, D., Högl, P. & Fabian, J. Trivial and inverted Dirac bands and the emergence of quantum spin Hall states in graphene on transition-metal dichalcogenides. *Phys. Rev. B* **93**, 1–10 (2016).

- [43] Cummings, A. W., Garcia, J. H., Fabian, J. & Roche, S. Giant spin lifetime anisotropy in graphene induced by proximity effects. *Phys. Rev. Lett.* **119**, 1–7 (2017).
- [44] Offidani, M. & Ferreira, A. Microscopic theory of spin relaxation anisotropy in graphene with proximity-induced spin-orbit coupling. *Phys. Rev. B* **98**, 1–11 (2018).
- [45] Garcia, J. H., Vila, M., Cummings, A. W. & Roche, S. Spin transport in graphene/ transition metal dichalcogenide heterostructures. *Chem. Soc. Rev.* **47**, 3359–3379 (2018).
- [46] Fu, L., Kane, C. L. & Mele, E. J. Topological insulators in three dimensions. *Phys. Rev. Lett.* **98**, 106803 (2007).
- [47] Konig, M. *et al.* Quantum spin Hall insulator state in HgTe quantum wells. *Science* **318**, 766–770 (2007).
- [48] Mott, N. F. The scattering of fast electrons by atomic nuclei. *Proceedings of the Royal Society of London. Series A, Containing Papers of a Mathematical and Physical Character* **124**, 425–442 (1929).
- [49] Bychkov, Y. A. & Rashba, E. I. Oscillatory effects and the magnetic susceptibility of carriers in inversion layers. *J. Phys. C: Solid State Phys.* **17**, 6039–6045 (1984).
- [50] Dresselhaus, G. Spin-orbit coupling effects in zinc blende structures. *Phys. Rev.* **100**, 580 (1955).
- [51] Awschalom, D. & Samarth, N. Spintronics without magnetism. *Physics* **2**, 50 (2009).
- [52] Miron, I. M. *et al.* Perpendicular switching of a single ferromagnetic layer induced by in-plane current injection. *Nature* **476**, 189–193 (2011).
- [53] Liu, L. *et al.* Spin-torque switching with the giant spin Hall effect of tantalum. *Science* **336**, 555–558 (2012).
- [54] Manchon, A. *et al.* Current-induced spin-orbit torques in ferromagnetic and antiferromagnetic systems. *Rev. Mod. Phys.* **91**, 035004 (2019).
- [55] D'yakonov, M. I. & Perel, V. I. Possibility of orienting electron spins with current. *Soviet Journal of Experimental and Theoretical Physics Letters* **13**, 467 (1971).
- [56] Kato, Y. K., Myers, R. C., Gossard, A. C. & Awschalom, D. D. Observation of the spin Hall effect in semiconductors. *Science* **306**, 1910–1913 (2004).
- [57] Valenzuela, S. O. & Tinkham, M. Direct electronic measurement of the spin Hall effect. *Nature* **442**, 176–179 (2006).

- [58] Sinova, J., Valenzuela, S. O., Wunderlich, J., Back, C. H. & Jungwirth, T. Spin Hall effects. *Rev. Mod. Phys.* **87**, 1213–1260 (2015).
- [59] Sinitsyn, N. A. Semiclassical theories of the anomalous Hall effect. *J. Phys. Condens. Matter* **20**, 023201 (2008).
- [60] Jungwirth, T., Niu, Q. & MacDonald, A. H. Anomalous Hall effect in ferromagnetic semiconductors. *Phys. Rev. Lett.* 207208 (2002).
- [61] Nagaosa, N. Anomalous Hall effect –a new perspective–. *J. Phys. Soc. Japan* **75**, 042001 (2006).
- [62] Maekawa, S., Valenzuela, S. O., Saitoh, E. & Kimura, T. *Spin current*, vol. 22 (Oxford University Press, 2017).
- [63] Ivchenko, E. L. & Pikus, G. E. New photogalvanic effect in gyrotropic crystals. *JETP Lett.* **27**, 640–643 (1978).
- [64] Aronov, A. G. & Lyanda-Geller, Y. B. Mesoscopic spin polarization and nuclear electronic resonance. *Soviet Journal of Experimental and Theoretical Physics Letters* **52**, 10 (1990).
- [65] Edelstein, V. M. Spin polarization of conduction electrons induced by electric current in two-dimensional asymmetric electron systems. *Solid State Commun.* **73**, 233–235 (1990).
- [66] Nechaev, I. A. *et al.* Hole dynamics in a two-dimensional spin-orbit coupled electron system: Theoretical and experimental study of the Au(111) surface state. *Phys. Rev. B* **80**, 113402 (2009).
- [67] Offidani, M., Milletari, M., Raimondi, R. & Ferreira, A. Optimal charge-to-spin conversion in graphene on transition-metal dichalcogenides. *Phys. Rev. Lett.* **119**, 196801 (2017).

## Chapter 3

# Measurements protocols, device fabrication and characterization.

In this chapter, we describe the experimental methods and protocols used in this thesis. It starts with the description of spin injection and detection (Sec. 3.1), and then the spin precession experiments (Sec. 3.2). We introduce the concepts of out-of-plane and oblique spin precession measurements (Sec. 3.3), which are used to obtain information about the spin dynamics and possible anisotropic spin relaxations. Next, we describe how the spin precession measurements are adapted into a protocol to detect spin-charge interconversion in graphene/ TMDC devices (Sec. 3.4). Finally, the device fabrication and their characterization are described in Sec. 3.5.

### 3.1 Spin injection and detection in graphene lateral devices

In this thesis, the spin transport properties in graphene are studied in lateral devices using non-local techniques. The basic concept dates back to 1985 when Johnson and Silsbee experimentally demonstrated that an unequal density of spin-up and spin-down electrons could be generated and detected in non-magnetic materials using ferromagnets in a non-local configuration [1, 2]. But before describing a non-local spin valve, we introduce the "conventional" spin valve.

*Conventional spin valve.* A conventional spin-valve consists of a non-magnetic (N) material (e.g., Cu) contacted by ferromagnetic (F) source and drain leads (see Fig. 3.1). A voltage applied between the contacts generates a current ( $I$ ) that flows through the device. Experimental observations shows that when the magnetization of the F electrodes are in parallel alignment ( $\uparrow\uparrow$ ) the measured resistance ( $R^{\uparrow\uparrow}$ ) is lower than when their magnetization are in antiparallel alignment ( $R^{\uparrow\downarrow}$ );  $R^{\uparrow\uparrow} < R^{\uparrow\downarrow}$  [3, 4]. Such resistance dependence on whether the magnetization of F layers being parallel or anti-parallel is called the giant magneto-resistance (GMR). GMR opened a door for a wide number of applications, we discuss some of them in Chap. 1. Because

of its discovery, Albert Fert and Peter Grünberg were awarded the Nobel Prize in Physics in 2007 [5].

To understand why  $R^{\uparrow\uparrow} < R^{\uparrow\downarrow}$ , first, let us imagine the up and down DOS in N as two channels, like to lanes in a highway. Now, we make this postulate: when the magnetization of the F electrode is up, its interface resistance with the up-channel ( $r$ ) is lower than its interface resistance with the down-channel ( $R$ );  $R > r$  (we will explain the reason of this postulate later on). We present such a resistor model in Fig. 3.1a-b with:

$$R^{\uparrow\uparrow} = \frac{2 R r}{R + r} \text{ and } R^{\uparrow\downarrow} = \frac{R + r}{2}. \quad (3.1)$$

Eq. (3.1) clearly shows that  $R^{\uparrow\uparrow} < R^{\uparrow\downarrow}$  when  $r < R$ . The magnetoresistance of a spin valve can be defined as  $MR = (R^{\uparrow\downarrow} - R^{\uparrow\uparrow})/R^{\uparrow\uparrow}$ . Using Eqs. (3.1) MR can be rewritten as:

$$MR = \frac{P^2}{1 - P^2}; \quad P = \frac{R - r}{R + r}. \quad (3.2)$$

$P$  is the polarization of the F contact, a quantity that tells us how effective is the F electrode to get a high MR, the ideal would be a  $P \sim 1$ .

The electrochemical potential ( $\mu$ ) in the N material along its length can be easily obtained assuming independent channels using

$$I_{\text{up,dn}} = -\frac{\sigma A}{2e} \frac{d\mu_{\text{up,dn}}}{dx} \text{ and } \frac{dI_{\text{up,dn}}}{dx} = 0, \quad (3.3)$$

where  $\sigma$ ,  $A$ , and  $e$  are the channel conductivity (equal for up and down channels), its cross area, and the electron charge, respectively. The second equation in Eq. (3.3) establish a steady state. Because we assume independent channels for up and down spins in N, the chemical potential in N results in a line connecting the voltage drops at the interface. The voltage drops are proportional to  $r$  or  $R$  (see Fig. 3.1 a-b). However, in real situations, these different potentials try to equal, and to do so, the up and down spins flip until there is an equal potential between them; this is called the spin-flip process [6]. So the real chemical potential for the up and down channel looks like the dashed lines in Fig. 3.1a-b. To take into account the spin-flip process, the second term in Eq. (3.3) changes to [6]:

$$\frac{dI_{\text{up}}}{dx} = -\frac{dI_{\text{dn}}}{dx} = -K(\mu_{\text{up}} - \mu_{\text{dn}}), \quad (3.4)$$

where  $K$  constant of proportionality. Eq. (3.4) tells that if we consider a process that flips spins, the up and down channel are not independent anymore. From the first terms of Eq. (3.3) and using the Eq. (3.4) we get to the Valet-Fert equations [6]:

$$\frac{d^2\mu_{\text{up}}}{dx^2} = \frac{\mu_{\text{up}} - \mu_{\text{dn}}}{2\lambda_s^2} = -\frac{d^2\mu_{\text{dn}}}{dx^2}; \quad \lambda_s^2 = \frac{4eK}{\sigma A}. \quad (3.5)$$



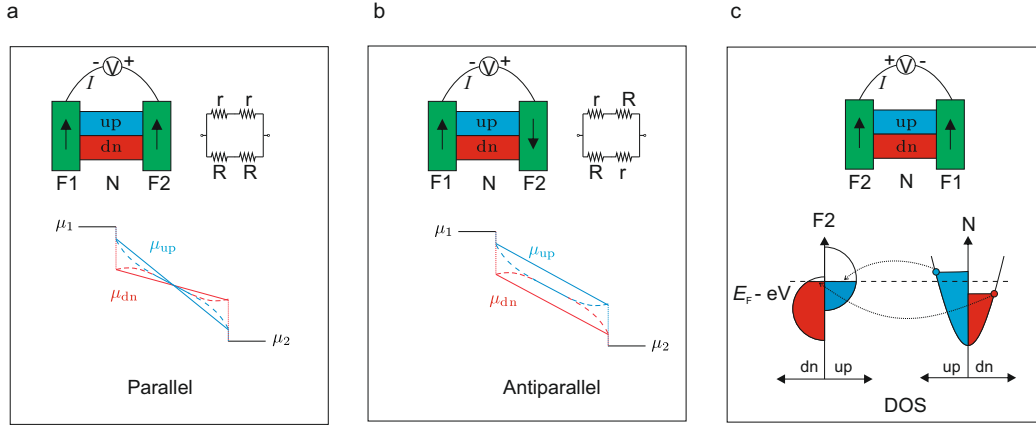


FIGURE 3.1: Top panel in **a** and **b**, conventional spin-valve consisting on a non-magnetic (N) conducting channel contacted by two ferromagnetic (F) electrodes. The electronic states in N can be seen as two channels, one for up-spins and one for down-spins (dn). A voltage ( $V$ ) between F generates a current ( $I$ ) that experiences different resistance ( $r < R$ ) with each channel in N. The bottom panel in **a** and **b** shows the electrochemical potential ( $\mu_{\text{up,dn}}$ ) in N considering no spin-flip process (continuous lines), and considering spin-flip process (dashed lines). **c**. Density of states (DOS) for F and N, a spin-up electron that jumps out from N finds a lot of states in F; thus, a low resistance ( $r$ ). A spin-down electron in N that jumps out from N to F finds a few states to fill; thus, a high resistance ( $R$ ).

$\lambda_s$  is termed as the spin diffusion length, and usually, is defined in terms of the spin lifetime  $\tau_s$ , time that takes to the spin to lose its initial state, and the diffusion constant  $D$ ;  $\lambda = \sqrt{D \tau_s}$ . From Eq. (3.5) we can define a fundamental concept called spin chemical potential  $\mu_s \equiv \mu_{\text{up}} - \mu_{\text{dn}}$ , also known as spin accumulation, and how it varies over the channel length:

$$\frac{d^2 \mu_s}{dx^2} = \frac{\mu_s}{\lambda_s^2}. \quad (3.6)$$

Eq. (3.6) is the spin diffusion equation. Note that the charge potential ( $\mu = (\mu_{\text{up}} + \mu_{\text{dn}})/2$ ) is given by the usual charge diffusion equation  $d^2 \mu / dx^2 = 0$ , and it is decoupled from the spin chemical potential. We can define now the spin current, which is  $I_s = I_{\text{up}} - I_{\text{dn}}$ .

So far, we described the consequences derived from the different interface resistances of the F electrode with the up and down-channel in the N material. To explain why this postulate is correct, we have to look at the density of states of the F and N materials. Because of the natural alignment of the spins in F, it has a net magnetization that can be seen as an internal magnetic field. Such an internal magnetic field is strong enough to split the DOS of the up and down-spins by an energy difference called "exchange energy." This means that at the Fermi level, there is a different DOS for up-spins and down-spins in F. On the contrary, in the N material, the up and down states are degenerate, which means they have the same energy even though they are different states. In the N material at the Fermi level, there is an equal number of DOS for up and down-spins. So if the F electrode is pointing upwards (see

Fig. 3.1 c), when an up-spin in N wants to jump out to F, it finds a lot of states to fill, so the resistance is low. But when a down-spin seeks to jump out to F, it sees very few states to fill, so the resistance is high.

*Non-local spin valve.* In a non-local spin-valve, the N channel extends out from the F contact as it is shown schematically in Fig. 3.2a. The current ( $I$ ) flowing through the different interface resistances generates different potential drops for up and down-spins (see Fig. 3.2b), creating a spin accumulation. Such spin accumulation ( $\mu_s$ ) diffuses out of the current loop, towards the right of F1.  $\mu_{\text{up}}$  and  $\mu_{\text{dn}}$  can be measured as a non-local voltage  $V_{\text{nl}}$  using the ferromagnetic F2 probe. This measurement is non-local in the sense that the voltage is measured out from the current loop. The distance  $L$  from F1 to F2 defines the channel length.

The potential at the probe (F2),  $V_{\text{nl}} = \mu_{\text{probe}}/e$ , will depend on the relative orientation of the F1 and F2 magnetization (parallel or antiparallel), and the interface resistance ( $r$ ,  $R$ ) of the up and down-channel with F2. A schematic diagram for the resistor model in the parallel and antiparallel configuration is shown in Fig. 3.2 c. The condition that at F2 no net current flows  $I_{\text{up}} + I_{\text{dn}} = 0$ , allow us to get the chemical potential at the probe:

$$\begin{aligned} \mu_{\text{probe}}^{\uparrow\uparrow} &= \frac{R\mu_{\text{up}} + r\mu_{\text{dn}}}{R + r} \\ \mu_{\text{probe}}^{\uparrow\downarrow} &= \frac{r\mu_{\text{up}} + R\mu_{\text{dn}}}{R + r} \end{aligned} \quad (3.7)$$

From Eqs. (3.7) we obtain that  $\Delta V_{\text{nl}} \equiv V_{\text{nl}}^{\uparrow\uparrow} - V_{\text{nl}}^{\uparrow\downarrow} = P_2 \mu_s / e$ . In simple words,  $\Delta V_{\text{nl}}$  is proportional to the spin accumulation.  $P_2$  is the contact polarization of F2.

The discussed process of spin injection and detection is general, and it applies to non-magnetic spin channels such as Al, Cu, Si, and of our particular interest, graphene. Graphene is a promising channel for spins because of its small SOC, the spin accumulation

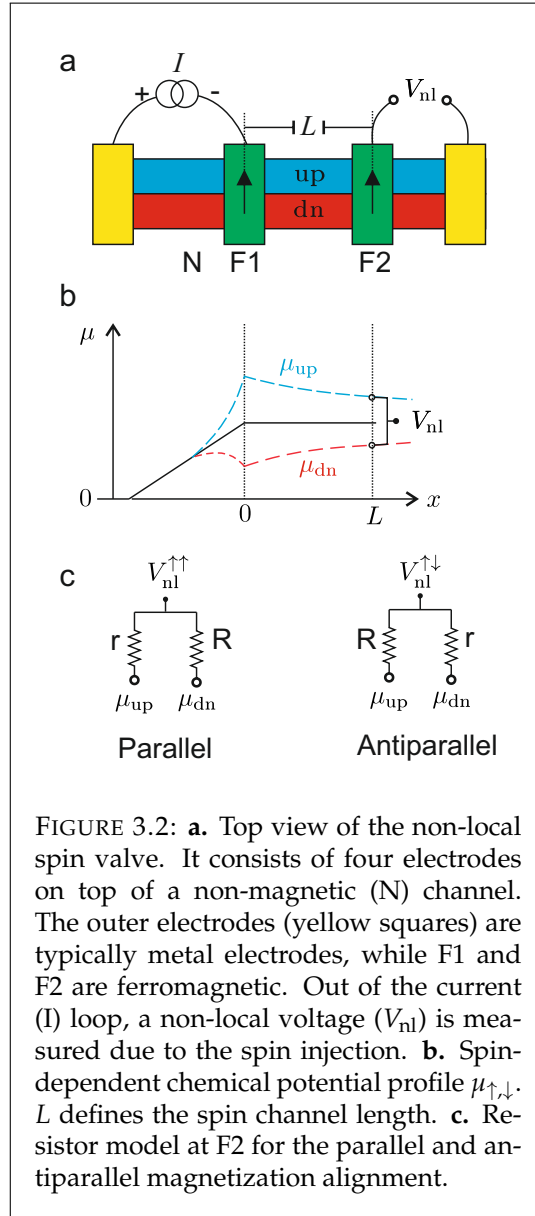


FIGURE 3.2: **a.** Top view of the non-local spin valve. It consists of four electrodes on top of a non-magnetic (N) channel. The outer electrodes (yellow squares) are typically metal electrodes, while F1 and F2 are ferromagnetic. Out of the current ( $I$ ) loop, a non-local voltage ( $V_{\text{nl}}$ ) is measured due to the spin injection. **b.** Spin-dependent chemical potential profile  $\mu_{\uparrow,\downarrow}$ .  $L$  defines the spin channel length. **c.** Resistor model at F2 for the parallel and antiparallel magnetization alignment.

can be sustained over  $\lambda_s \sim 30 \mu\text{m}$  [7],

much longer than in Al or Si with  $\lambda_s \sim 1$  and  $0.2 \mu\text{m}$  respectively [8, 9].

In practice, a restive (tunnel) barrier have to be introduced between the F and the graphene channel (or a general N channel). This barrier is a crucial element to avoid the conductivity mismatch problem, which tells that the spin injection capability decreases if the contact resistance is too low [10, 11]. Typical barriers include thin oxide layers such as  $\text{AlO}_x$ ,  $\text{MgO}$ ,  $\text{TiO}_x$ , or  $\text{SrO}$  [12–15], layered dielectrics such as hBN [16, 17], and amorphous carbon layers or fluorinated graphene [18, 19]. In all our graphene-based spin valves, we use  $\text{TiO}_x$  barrier; the fabrication details are presented in Sec. 3.5. Generally, graphene lateral spin devices are fabricated on an insulating layer on a highly conducting substrate (e.g.,  $\text{SiO}_2$  or hBN on p-doped Si). The graphene carrier density  $n$  can then be controlled by applying a back-gate voltage between the graphene and the conducting substrate (Sec. 3.7).

To experimentally measure the non-local resistance  $R_{\text{nl}} \equiv V_{\text{nl}}/I$  in the parallel and antiparallel alignment fo the F electrodes, we apply a magnetic field  $B_{\parallel}$  along the long axis of the F electrodes (schematic in Fig. 3.2a). The shape anisotropy of F creates a favorable energy term for magnetization along its long axis, so a small applied magnetic field in such direction is sufficient to reach the saturation magnetization. Through this thesis, the long axis of F is normally called the easy-axis. Because we intentionally define F1 and F2 with different widths, they have different coercive fields allowing us to set the parallel and the antiparallel configuration. A typical spin-valve measurement is shown in Fig. 3.2b. At high  $B_{\parallel}$  both F electrodes are pointing in the direction of  $B$  ( $\uparrow\uparrow$ ). But when  $B$  is reversed, the different coercive field in F1 and F2 makes that one of them switches its magnetization first. At this point, both electrodes are antiparallel ( $\uparrow\downarrow$ ), so an abrupt change of  $R_{\text{nl}}$  is measured. As the  $B$  increases, the second F electrode switches, so both electrodes are pointing parallel again ( $\downarrow\downarrow$ ). The difference in  $R_{\text{nl}}$  between the parallel and the antiparallel configuration,  $\Delta R_{\text{nl}} = R_{\text{nl}}^{\uparrow\uparrow} - R_{\text{nl}}^{\uparrow\downarrow} \propto \mu_s$ , is commonly called the non-local spin signal [20].

## 3.2 Spin precession experiments

Information about the spin relaxation length and the spin lifetime is typically obtained using (Hanle) spin precession experiments. Here, a magnetic field  $B_{\perp}$  is applied perpendicular to the substrate causing an in-plane spin precession as spins diffuse from F1 to F2 [1, 21]. The expression that gives the shape of a typical Hanle spin precession curve in the high contact resistance limit is,

$$R_{\text{nl}}(B) = \pm \frac{P_i P_d}{e^2 N A} \int_0^{\infty} \frac{1}{\sqrt{4\pi D_s t}} \exp\left[-\frac{L^2}{4D_s t}\right] \cos(\omega_L t) \exp(-t/\tau_s^{\parallel}) dt, \quad (3.8)$$

where the  $+(-)$  sign accounts for the parallel (antiparallel) configuration of injector and detector, and  $P_i$ ,  $P_d$ ,  $e$ ,  $N$  and  $A$  are the spin polarization of the injector

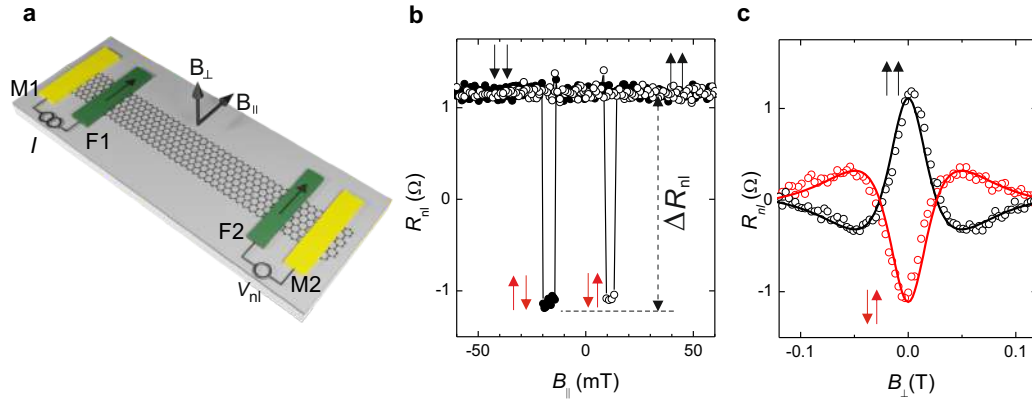


FIGURE 3.3: **a.** Schematic of the graphene spin-valve configuration measurement.  $B_{\parallel}$  indicate the direction of the magnetic field applied in the graphene's plane and parallel to the easy-axis of F1 and F2.  $B_{\perp}$  points out of the graphene's plane, and perpendicular to  $B_{\parallel}$ . **b.** Typical non-local spin resistance  $R_{nl}$  as function of the in-plane magnetic field  $B_{\parallel}$ . The sharp transitions from positive to negative  $R_{nl}$  mark the switching from parallel to antiparallel configuration between F1 and F2, as illustrated by the arrows.  $\Delta R_{nl}$  is the non-local spin signal. **c.** Spin precession measurements for parallel and antiparallel alignment of F1 and F2 magnetizations (symbols). Solid lines correspond to the fitting to Eq. (3.8) that allows the extraction of the spin parameters. For the shown example,  $\tau_s^{\parallel} = 0.21$  ns,  $D_s = 0.012$  m<sup>2</sup>s<sup>-1</sup> and  $\lambda_s^{\parallel} = 1.58$   $\mu$ m.

and the detector, the electron charge, the density of states at the Fermi energy and the contact area, respectively.  $D_s$  and  $\tau_s^{\parallel}$  stand for the spin diffusion constant and the spin lifetime while  $\lambda_s^{\parallel} = \sqrt{D_s \tau_s^{\parallel}}$  is the spin relaxation length. The Larmor frequency is given by  $\omega_L = \gamma_c B_{\perp}$ , with  $\gamma_c = g\mu_B/\hbar$ , where  $g$  is the gyromagnetic factor,  $\mu_B$  the Bohr magneton and  $\hbar$  the reduced Planck constant. The spin projection over the detector is captured in the term  $\cos(\omega_L t)$  whereas  $\frac{1}{\sqrt{4\pi D_s t}} \exp\left[-\frac{L^2}{4D_s t}\right]$  is the probability that the injected spins reach the detector in a time  $t$ , and  $\exp(-t/\tau_s^{\parallel})$  represents the effect of spin relaxation. Spin precession measurements for parallel and antiparallel configuration are shown in Fig. 3.3 (c). The spin signal is maximum at  $B = 0$  because the incoming spins are only pointing parallel to the magnetization of the detector. With increasing  $B$  the incoming spins rotate, so the signal which is sensitive only to the projection of the spin component parallel to its magnetization decreases. The signal is minimum when the spins reaching the detector are pointing antiparallel to its magnetization. The signal vanishes at large magnetic fields due to spin dephasing;  $\tau_s^{\parallel}$ ,  $D_s$ , and  $\lambda_s^{\parallel}$  are extracted by fitting the Hanle curve to Eq. (3.8).

Until 2016, most experiments used the configuration described above to determine spin relaxation properties. In this situation, spins precess in the plane of the spin channel, therefore, the extracted  $\tau_s^{\parallel}$  and  $\lambda_s^{\parallel}$  from fitting the Hanle curves (see Fig. 3.4c) correspond to the spin lifetime and spin relaxation length for spins oriented *in-plane* (thus the  $\parallel$  symbol). As discussed below (Sec. 3.3), Raes *et al.* demonstrated that the application of an oblique magnetic fields [22] or, alternatively, an

in-plane magnetic fields perpendicular to the magnetizations of F1, F2 [23] enable the determination of the spin lifetime  $\tau_s^\perp$  and spin relaxation lengths  $\lambda_s^\perp$  for spins oriented *out-of-plane*. The simplicity of the experimental approach with the lack of artifacts, which are present in other methods, has motivated its use in this thesis to gather information on the spin relaxation anisotropy and proximity-induced SOC in graphene/TMDC van der Waals heterostructures.

### 3.3 Determination of the spin lifetime anisotropy

As discussed in Sec. 2.4 of Chap. 2, the spin lifetime anisotropy  $\zeta$ , a parameter that quantifies the ratio between spin lifetimes for spins lying in the graphene plane ( $\tau_s^\parallel$ ) and pointing out of it ( $\tau_s^\perp$ ), is a fingerprint of the SOC, being highly sensitive to its magnitude and orientation. Thus, in this thesis we focus on the detection and quantification of such parameter to investigate the SOC in graphene and the induced SOC in graphene by the proximity to a TMDC.

The magnetization of the F electrodes on a typical device is oriented in-plane along their long axis due to magnetic shape-anisotropy (arrows in schematic Fig. 3.4 (a)). Therefore, spins are injected in the plane of the channel. The first reported method to determine the spin lifetime anisotropy in graphene uses a large  $B_\perp$  ( $> 1$  T) to tilt the magnetization of the F electrodes along the field direction in order to inject spins perpendicular to the graphene plane. The spin lifetime anisotropy  $\zeta$  is then extracted by comparing the spin signals when the injected spins are oriented in-plane ( $B_\perp = 0$ ) and perpendicular to it ( $B_\perp > 1$  T). The disadvantage of extracting  $\zeta$  with this method arises from the significant magnetoresistive effects that are present in graphene, which limits its range of validity to sufficiently large carrier concentrations  $n$  [24]. Therefore, alternative experimental approaches have been developed, which produce an out-of-plane spin population by spin precession and require much lower magnetic fields. Raes *et al.* discuss two approaches based on spin precession experiments under an oblique magnetic field [22] or under a magnetic field applied in the graphene plane and perpendicular to the F metal electrodes [23]. They focused on the oblique case because the significant rotation of the F electrodes magnetizations for in-plane fields generally complicates the data analysis and increases the uncertainty in the determination of  $\zeta$  [23]. However, shortly afterward Ghiasi *et al.* [25] and Benítez *et al.* [26] (published results of Chap. 4) implemented anisotropy measurements with in-plane magnetic fields in graphene-modified by the proximity of a TMDC, where the anisotropy is so large that it can still be readily visualized and quantified. In the following subsections, the characteristics of these methods are discussed in detail.

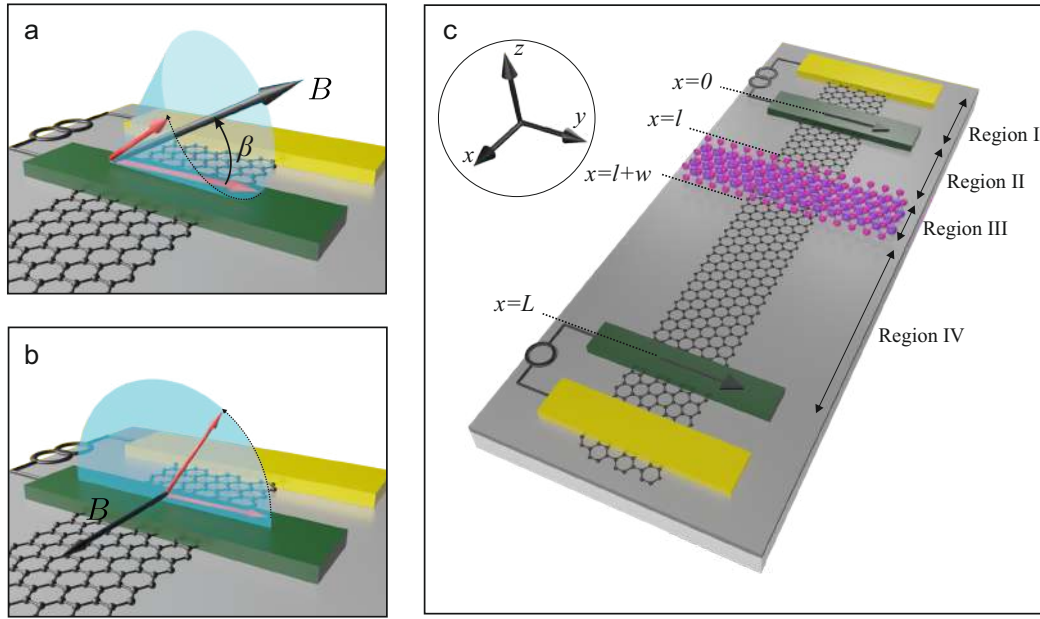


FIGURE 3.4: Determination of the spin relaxation anisotropy ratio  $\zeta$  by means of spin precession. **a.** Schematics of the oblique spin precession method. The magnetic field  $B$  is applied at an angle  $\beta$  in a plane that contains the easy-axis of the ferromagnetic injector (F1) and that is perpendicular to the substrate. **b.** Schematics of the out-of-plane spin precession method. The magnetic field  $B$  is applied in plane and perpendicular to the easy-axis of the ferromagnetic injector (F1). **c.** Illustration of a graphene-based lateral spin device with a non-homogeneous spin channel. Regions I, II and III indicate the pristine graphene channel while Region III is covered with a TMDC. As a spin diffuses from F1 to F2 under an oblique (a) or in-plane (b) magnetic field, it undergoes precession. As it approaches the TMDC, it gathers an out-of-plane component.

### 3.3.1 Oblique spin precession

#### Homogeneous spin channel

A schematic of the oblique spin precession method is shown in Fig. 3.4 (a). The magnetic field  $B$ , characterized by the angle  $\beta$ , is applied in a plane that contains the F metal electrode axis and is perpendicular to the substrate. The evolution of the spin density  $\vec{s}$  under an oblique magnetic field satisfies the one-dimensional steady-state Bloch equation,

$$D_s \nabla^2 \vec{s} - \gamma_c \vec{s} \times \vec{B} - \overline{\tau_s^{-1}} \cdot \vec{s} = 0, \quad (3.9)$$

where  $D_s$  is the spin diffusion constant,  $\overline{\tau_s^{-1}}$  is a  $3 \times 3$  tensor with entries  $\tau_s^{\parallel}$  and  $\tau_s^{\perp}$ .

The simplest approach to solve Eq. (3.9) is to transform the coordinates  $(e^x, e^y, e^z)$  to the rotated cartesian axis system characterized by unit vectors  $(e^x, e^{B^{\parallel}}, e^{B^{\perp}})$ . In the new coordinate system the applied magnetic field  $\vec{B} = (0, B, 0)$  can only induce precession to the spin population  $\vec{s} = (s^x, s^{B^{\parallel}}, s^{B^{\perp}})$  perpendicular to it. The solution of Eq. (3.9) for a homogeneous spin channel is described in detail in Ref. [23]. Refined models include contact induced spin relaxation due to the finite contact resistance [27] and inhomogeneous spin lifetimes in the graphene channel [25, 26].

The solution of Eq. (3.9) for different values of  $\zeta$  with  $B$  oriented at  $\beta = 45^\circ$  is shown in Fig. 3.5 (a). It is observed that at  $B \equiv B_d \sim 70$  mT the spin component perpendicular to  $B$  is fully dephased. For  $B > B_d$  the precessional motion is completely suppressed, thus  $R_{nl}$  saturates to the remanent non-precessional spin component that lies along the magnetic field direction. In this situation,  $R_{nl}$  at the F detector is given by  $R_{nl}^\beta = \bar{R}_{nl}(\zeta, \beta) \cos^2(\beta^*)$ , where  $\beta^* = \beta - \gamma(\beta, B)$  takes into consideration the tilting angle  $\gamma(\beta, B)$  of the magnetization of the F electrodes that results from the applied magnetic field, as calculated below. The factor  $\cos^2(\beta^*)$  accounts for the projection of the injected spins along the magnetic field direction and the subsequent projection along the easy-axis of the F metal detector. The term  $\bar{R}_{nl}(\zeta, \beta)$  is given by [22]

$$\bar{R}_{nl}(\zeta, \beta) = \sqrt{f(\zeta, \beta)} \exp \left[ -\frac{L}{\lambda_s^\parallel} \left( \sqrt{\frac{1}{f(\zeta, \beta)}} - 1 \right) \right] R_{nl}^0. \quad (3.10)$$

In this expression  $f(\zeta, \beta) = \left( \cos^2(\beta) + \frac{1}{\zeta} \sin^2(\beta) \right)^{-1}$  and  $R_{nl}^0$  is the value of the non-local resistance at  $B = 0$ . For the isotropic case, it is straightforward to verify that  $\bar{R}_{nl}(\zeta = 1, \beta)$  is independent of  $\beta$  and its value corresponds to  $\bar{R}_{nl}(\zeta = 1, \beta) = R_{nl}^0$ .

The tilt tangle  $\gamma$  of the F electrodes magnetizations can be calculated by considering the Stoner-Wolfarth model, which provides a good approximation for a coherent magnetization rotation at low  $B$ . The relationship between  $\gamma$  and  $\beta$  is given by the expression [28],

$$\gamma = \arcsin \left[ \frac{B \sin(\beta)}{B_s + B \cos(\beta)} \right], \quad (3.11)$$

where  $B_s$  is the saturation magnetic field. In the specific case of  $\beta = 90^\circ$ ,  $\gamma = \arcsin(B/B_s)$ . The functional dependence of  $\gamma$  with  $B$  is followed closely by experimental results on anisotropic multi-resistance and Hanle spin precession experiments, from which  $B_s$  is readily obtained [22].

A fundamental design parameter to correctly determine  $\zeta$  using Eq. (3.10) is the spin channel length  $L$ . In particular, a minimum  $L$  is required to observe complete dephasing of the spin component perpendicular to the magnetic field at sufficiently low  $B$ , typically  $B_d \sim 0.15$  T, thus avoiding magnetoresistance effects. Considering no contacts effects in the spin relaxation process, the contribution to the spin signal stemming from the spin component perpendicular to the magnetic field  $R_{nl}^\perp$  can be written as  $R_{nl}^\perp(B) \propto \exp(-L((B \gamma_c / 2D_s)^{1/2} - 1 / (D_s \tau_s^\parallel)^{1/2}))$  [27]. Defining a threshold value for the saturation such that  $R_{nl}^{sat} = 10^{-\eta} R_{nl}(B = 0)$ , the condition  $R_{nl}^\perp(B_d) \leq R_{nl}^{sat}$  establishes that  $L \geq \sqrt{\frac{2D_s}{B_d \gamma_c}} \eta \ln 10$ . Assuming high-quality devices with  $\lambda_s = 30 \mu\text{m}$ ,  $D_s = 0.075 \text{ m}^2\text{s}^{-1}$  and a saturation threshold  $10^{-\eta} = 10^{-3}$  [7, 27], the minimum channel length is  $L \approx 16 \mu\text{m}$  to achieve full dephasing at  $B_d = 0.15$  T.

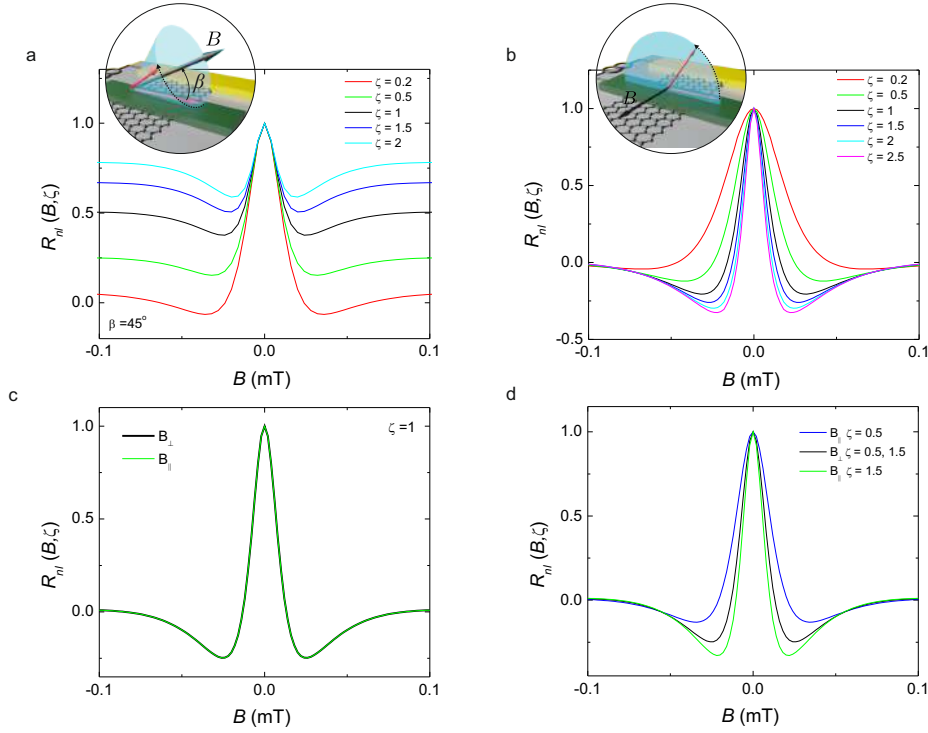


FIGURE 3.5: Spin precession line shapes  $R_{nl}(B, \zeta)$  obtained numerically using Eq. (3.9) in an anisotropic medium. **a.**  $R_{nl}(B, \zeta)$  for the oblique spin precession method at fixed  $\beta = 45^\circ$  for anisotropy ratios  $\zeta = 0.2, 0.5, 1.5, 2$ . The black line corresponds to the isotropic case ( $\zeta = 1$ ). As  $\zeta$  increases, the asymptotic value of the spin signal increases. **b.** Numerically extracted spin precession line shapes  $R_{nl}(B, \zeta)$  for the out-of-plane spin precession method for anisotropy ratios  $\zeta = 0.2, 0.5, 1.5, 2, 2.5$ . The black line corresponds to the isotropic case ( $\zeta = 1$ ). As  $\zeta$  decreases, the position of the minima shifts to higher magnetic fields.  $R_{nl}(B, \zeta)$  for magnetic fields applied out of plane ( $B_\perp$ ) and in plane ( $B_\parallel$ ) for the isotropic (**c**) and the anisotropic case (**d**). The perfect overlap between the two curves in (**c**) is a consequence of the isotropic spin relaxation, while in (**d**), the difference between  $R_{nl}$  for  $B_\perp$  and  $B_\parallel$  allows to easily identify the anisotropy nature of the spin transport. All the curves are normalized to their value at  $B = 0$  and are obtained for  $L = 7 \mu\text{m}$ ,  $D_s = 0.02 \text{ m}^2\text{s}^{-1}$ . The in-plane spin life time is constant in all curves  $\tau_s^\parallel = 0.5 \text{ ns}$  and only  $\tau_s^\perp$  is changed.

### Inhomogeneous spin channel

In the case of a non-uniform spin channel, Eqs. (3.8) and (3.10) are no longer valid to obtain the spin related parameters and  $\zeta$ . This is particularly relevant for heterostructures comprising graphene with other materials covering partially the spin channel (see Fig. 3.4 (c)). Here, the diffusive process is governed by Eq. (3.9) with boundary conditions,

$$\begin{aligned}
 x = 0 : \vec{s}_I &= \vec{s}_{II}; \partial_x \vec{s}_I - \partial_x \vec{s}_{II} = \vec{s}_0 \\
 x = l : \vec{s}_{II} &= \vec{s}_{III}; \partial_x \vec{s}_{II} = \partial_x \vec{s}_{III} \\
 x = w : \vec{s}_{III} &= \vec{s}_{IV}; \partial_x \vec{s}_{III} = \partial_x \vec{s}_{IV} \\
 x \rightarrow \pm\infty : \vec{s} &= 0,
 \end{aligned} \tag{3.12}$$



where I, II, and IV denote the pristine graphene and III the heterostructure region. Spins are injected in  $y$  direction  $\vec{s}_0 = (0, s_0, 0)$ , where  $s_0$  is a constant that depends on the injected electrical current and the contact polarization. Spin absorption effects are not taken into account in the given boundary conditions. The full study of the spin relaxation anisotropic in the non-homogeneous situation sketched in Fig. 3.4 (c) is fully explained in Chap. 4.

### 3.3.2 Out-of-plane spin precession

A schematics of the out-of-plane spin precession method is shown in Fig. 3.4 (b). Here, the magnetic field  $B$  is applied in plane and in a direction perpendicular to the easy-axis of the F metal electrodes. The precession occurs in a plane perpendicular to the substrate and containing the easy axis, thus probing both  $\tau_s^\perp$  and  $\tau_s^\parallel$ . The solution of Eq. (3.9) for this configuration is shown in Fig. 3.5 (b). For  $\zeta \gg 1$ ,  $R_{\text{nl}}$  strongly deviates from the isotropic case  $\zeta = 1$ , therefore a large anisotropy can be easily identified [25, 26, 29]. The magnitude of the minimum in  $R_{\text{nl}}$  corresponds to an average spin rotation angle of  $\pm\pi$ . When  $B$  increases spins start to acquire an out-of-plane component, which relaxes slower than the in plane one when  $\zeta > 1$ . Then, for an average spin rotation of  $\pm\pi$  and  $\zeta \gg 1$ ,  $R_{\text{nl}}$  can be larger than its value at  $B = 0$  (when spins are always in plane and the spin lifetime is short). In contrast, for  $\zeta < 1$  the out-of-plane spin component relaxes faster than the in-plane one, implying that the minimum in  $R_{\text{nl}}$  is less pronounced and can eventually disappear for  $\zeta \ll 1$ .

In addition, Fig. 3.5 (b) shows that the position of the minima, which occurs for a collective  $\pi$  spin precession, changes with  $\zeta$ . A spin contributes a precession angle  $\phi$  in a diffusion time  $t$  with a probability  $P(t)$ , such that  $t = \phi/\omega_L$ . Here  $P(t)$  is determined by the product of the diffusion-time distribution function and the probability that the spin has *not* flipped during  $t$ . The latter is proportional to  $\exp(-t/\tau_s)$ , resulting in a suppressed probability at long  $t$  or, equivalently, at large  $\phi$ . Such a suppression is more significant for short spin lifetimes, which implies that the collective spin precession angle for a given  $B$  will increase with longer spin lifetimes. This explains why the minima in Fig. 3.5 (b) develop at lower  $B$  as  $\zeta$  increases [23]. Figure 3.5 (c) compares  $R_{\text{nl}}$  when  $B$  is applied in-plane ( $B_\parallel$ , out-of-plane spin precession) and out-of-plane ( $B_\perp$ , in-plane spin precession) for the isotropic case  $\zeta = 1$ , where no differences are observed between the two configurations. These results are in stark contrast to those when  $\zeta \neq 1$ . In this case,  $R_{\text{nl}}$  clearly depends on the magnetic field orientation as shown in Fig. 3.5 (d). For out-of-plane spin precession,  $R_{\text{nl}}$  lies above (below) the in-plane spin precession lineshape when  $\zeta > 1$  ( $\zeta < 1$ ). Comparing the in-plane and the out-of-plane spin precession curves is a straightforward way to check the isotropic/anisotropic character of the system.

As explained in Secs. 3.2 and 3.3 precession measurements are an essential tool to obtain information about the spin relaxation time, which can be anisotropic, the spin diffusion constant and thus, the spin relaxation length. In the next section, we

explain a protocol based on spin precession measurements to demonstrate spin to charge interconversion in graphene/TMDC devices.

### 3.4 Characterization of the spin to charge interconversion

As explained in the Chap. 2 (Sec. 2.5), the enhanced SOC in graphene by proximity with a TMDC enables the generation of spin polarization through two coexisting processes: the spin Hall and the spin galvanic effects. In this section we thoroughly discuss how spin precession measurements can be used to electrically detect both the SHE and SGE. The experimental results associated to spin-charge interconversion (SCI) are presented in Chap 5.

The schematic of the proposed device and measurement scheme are shown in Fig. 3.6. A carefully designed experimental protocol based on non-local detection [8, 30, 31] combined with spin precession [32] allows us to isolate the proximity-induced SCI in the modified graphene (graphene/TMDC) from both spurious phenomena and competing SCI in the bulk of TMDC [33]. The device consists of a patterned graphene Hall cross with a TMDC flake along one of the arms and ferromagnetic injector/detector electrodes (F1) across the other (see Fig. 3.6 (a)). An applied electric field  $E$  along the graphene/TMDC arm, between electrodes E2 and E3, (and associated current  $I$ ) generates a spin current and spin accumulation due to the SHE (red arrows) and a non-equilibrium spin density conveyed by the ISGE (blue arrow, see Fig. 3.6 (a)). The spins, carrying information on the SHE and the ISGE, diffuse in the graphene and are detected by measuring the non-local voltage  $V_{nl}$  at F1 and E1. Alternatively, a spin current in graphene can be generated by applying  $I$  between the source F1 and the drain E1. In this case, the spin current and non-equilibrium spin density that reach the graphene(gr)-TMDC are converted into a voltage  $V_{nl}^{gr-TMDC}$  by the reciprocal effects.

For an applied current  $I$  along  $\hat{y}$  (Fig. 3.6 (a)), the spins generated by the SHE are polarized in the  $\hat{z}$  direction while those generated by the ISGE are in the  $\hat{x}$  direction. Because the ISGE and SHE spins are orthogonal, their contributions to  $V_{nl}$  can be readily separated using spin precession measurements.  $V_{nl}$  is proportional to the local spin accumulation projected along the detector magnetization  $\vec{M}_1$ . Due to magnetic shape anisotropy,  $\vec{M}_1$  tends to be aligned with the F1 length, which is set along  $\hat{y}$ , orthogonal to the spins generated by both the SHE and the ISGE (Fig. 3.6 (a)). Thus, at zero magnetic field,  $V_{nl} = 0$  since neither the SHE nor the ISGE contribute to  $V_{nl}$ .

For a low magnetic field  $B_z$  perpendicular to the graphene plane,  $V_{nl}$  solely depends on the ISGE. While the SHE spins are parallel to  $B_z$  and remain unaffected, the ISGE spins undergo precession. Because the ISGE spins are no longer perpendicular to  $\vec{M}_1$  when they reach F1,  $V_{nl} \neq 0$  (Fig. 3.6 (b)). In contrast, for an in-plane magnetic field  $B_x$ , the ISGE spins remain unaffected so that  $V_{nl}$  is solely dependent on the SHE (Fig. 3.6 (c)). Similar arguments apply to the ISHE and the SGE.

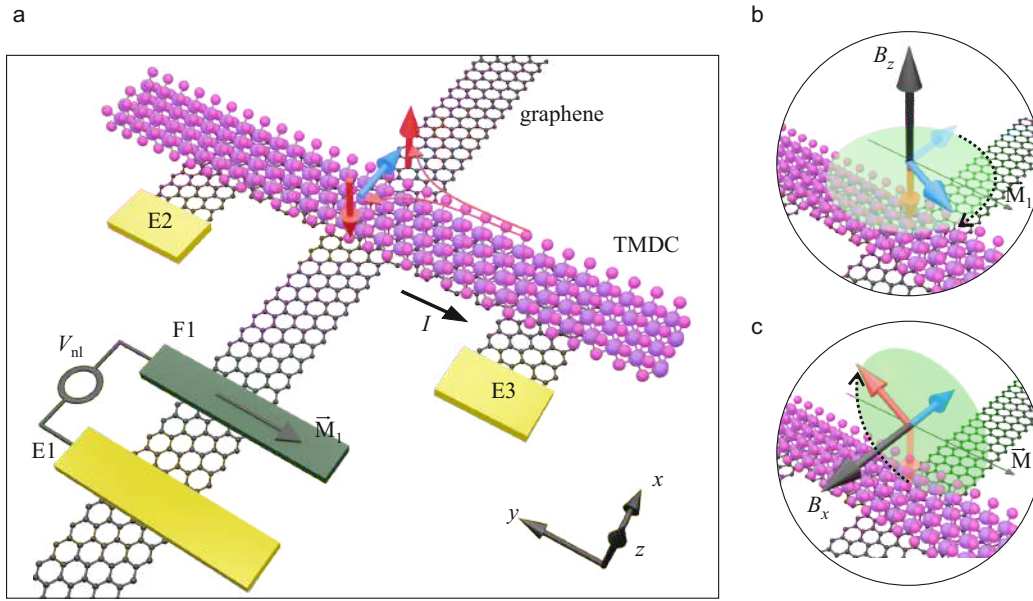


FIGURE 3.6: **a**. Schematics illustrating the measurement concept. The main elements of the device include a graphene Hall cross with a TMDC strip over one of the arms and a ferromagnet (F1) contacting the other. An injected current  $I$  between E2 and E3 (in  $\hat{y}$ ), along graphene-TMDC, induces a non-equilibrium spin density due to the ISGE with spins along  $\hat{x}$  (blue arrow). Spin accumulation with spins out of plane (along  $\hat{z}$ ) are generated by the SHE with opposite orientation at opposite edges of the graphene-TMDC (red arrows). The induced spins diffuse in graphene towards F1 and are detected non-locally by measuring  $V_{nl}$  between F1 and E1. At zero magnetic field  $V_{nl} = 0$ , as the ISGE and SHE spins are perpendicular to the F1 magnetization  $\vec{M}_1$ . **b**, ISGE detection. A magnetic field  $B_z$  induces spin precession on the ISGE generated spins (blue arrow), leading to a component along  $\vec{M}_1$  and  $V_{nl} \neq 0$ . The SHE spins (red arrow) do not contribute to  $V_{nl}$  as they are parallel to  $B_z$  and do not precess. **c**, SHE detection. Similar to **b**, a magnetic field  $B_x$  induces spin precession on the SHE generated spins leading to  $V_{nl} \neq 0$ . The ISGE spins do not precess and do not contribute to  $V_{nl}$ .

For the ISHE and SGE, an induced spin current and a spin density, respectively, generates a transverse voltage in the graphene/TMDC region. Such spin current (and spin density) is generated by applying  $I$  between the F1 and E1. At zero magnetic field, all the injected spins reach the graphene/TMDC along  $\hat{y}$ , so neither the ISHE nor the SGE generates a current. Hence  $V_{nl} = 0$  between E2 and E3. For a low magnetic field  $B_z$ , the injected spins undergo precession in the  $xy$  plane. When the spins enter the graphene- $WS_2$  region, their component along  $\hat{x}$  produces a  $V_{nl}$  in E2 and E3 that depends on the SGE. As no spin component along  $z$  is induced, the ISHE does not participate in the generation of a non-local voltage. In contrast, for a low magnetic field  $B_x$  the spins rotate in the  $yz$  plane. Hence, when they arrive to the graphene-TMDC region their  $\hat{z}$  component generates a current solely through the ISHE (thus,  $V_{nl} \neq 0$ ).

### 3.5 Sample fabrication

The sample fabrication starts with the mechanical exfoliation of graphene from highly-oriented pyrolytic graphite (SPI Supplies) onto a  $p$ -doped Si/SiO<sub>2</sub> substrate. The graphene flakes are selected by optical contrast after a previous calibration with Raman measurements. The most salient features of the Raman spectra for monolayer graphene is that the 2D band exhibits a sharp and symmetric single Lorentzian feature with a full width at half maximum (FWHM) of  $\sim 24 \text{ cm}^{-1}$  and centered at  $\sim 2700 \text{ cm}^{-1}$  [34]. While for bilayer graphene the 2D band exhibits a broader and asymmetric peak that can be fitted with four Lorentzian with a FWHM of  $\sim 24 \text{ cm}^{-1}$  [34].

In this thesis, the van der Waals graphene-TMDC heterostructures were fabricated using the dry viscoelastic stamping [35]. The transfer setup comprises an optical microscope with large working distance optical objectives (Nikon Eclipse Eclipse LV 100ND) and a three-axis micrometer stage (see schematic in Fig. 3.8a), which enable to accurately locate flakes for subsequent stacking. We can summarize the fabrication of van der Waals heterostructures in the following steps:

1. We prepare a stamp made of a small polydimethylsiloxane (PDMS) polymer on top of a glass slide. Details about the PDMS are in the appendix C.
2. The TMDC flakes are transferred onto the stamp by exfoliation with tape (see Fig. 3.8b)
3. The surface of the stamp is inspected under the optical microscope to select thin and narrow TMDC flakes due to their faint contrast under normal illumination

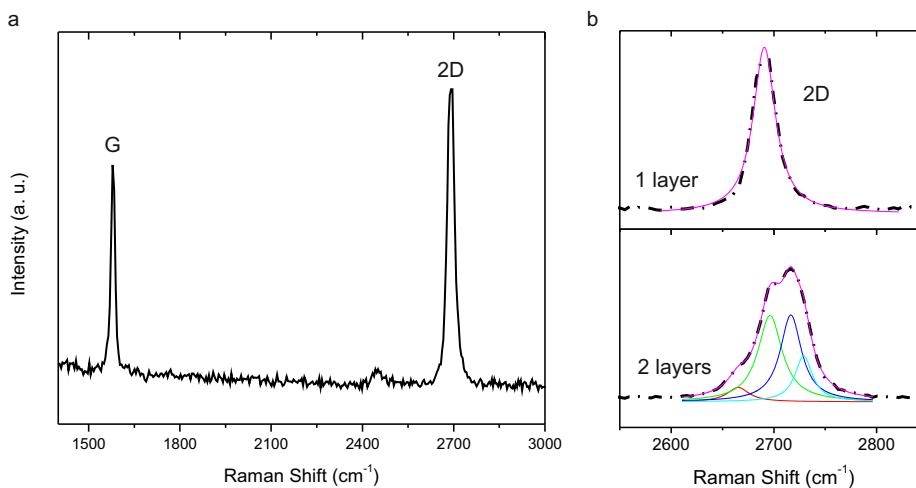


FIGURE 3.7: **a.** Graphene Raman spectra exhibiting the G band and 2D band which is described by one Lorentzian and a peak frequency of  $2691 \text{ cm}^{-1}$  showed in the top panel of **b.** In the bottom panel of **b.**, the measured 2D Raman band of bilayer graphene. The four fitted Lorentzian is also shown with peak frequencies at  $2665, 2696, 2716,$  and  $2728 \text{ cm}^{-1}$ .

4. The chosen TMDC flake on the stamp is aligned on top of the graphene target with the help of the micrometer stage, then it is pressed against the substrate and peeled off slowly, these steps are shown in Fig. 3.8b.

Figure 3.8c shows a color-enhanced optical image of a typical heterostructure used in this work to measure the spin properties in graphene/TMDC devices. The TMDC thickness is measured with Atomic Force Microscopy (AFM); the typical thickness is around  $\sim 20$  nm (Fig. 3.8d).

We use the described method because we can construct our heterostructures layer by layer from the bottom to the top without dissolving any polymer in each step. Our samples are not fully encapsulated between hBN; thus, we try to avoid as much as possible contact with solvents. Another method to fabricate heterostructures is usually called the "hot pick-up technique" [36]. This method differs from the one described above in constructing the stamp and in the fabrication steps. Here a

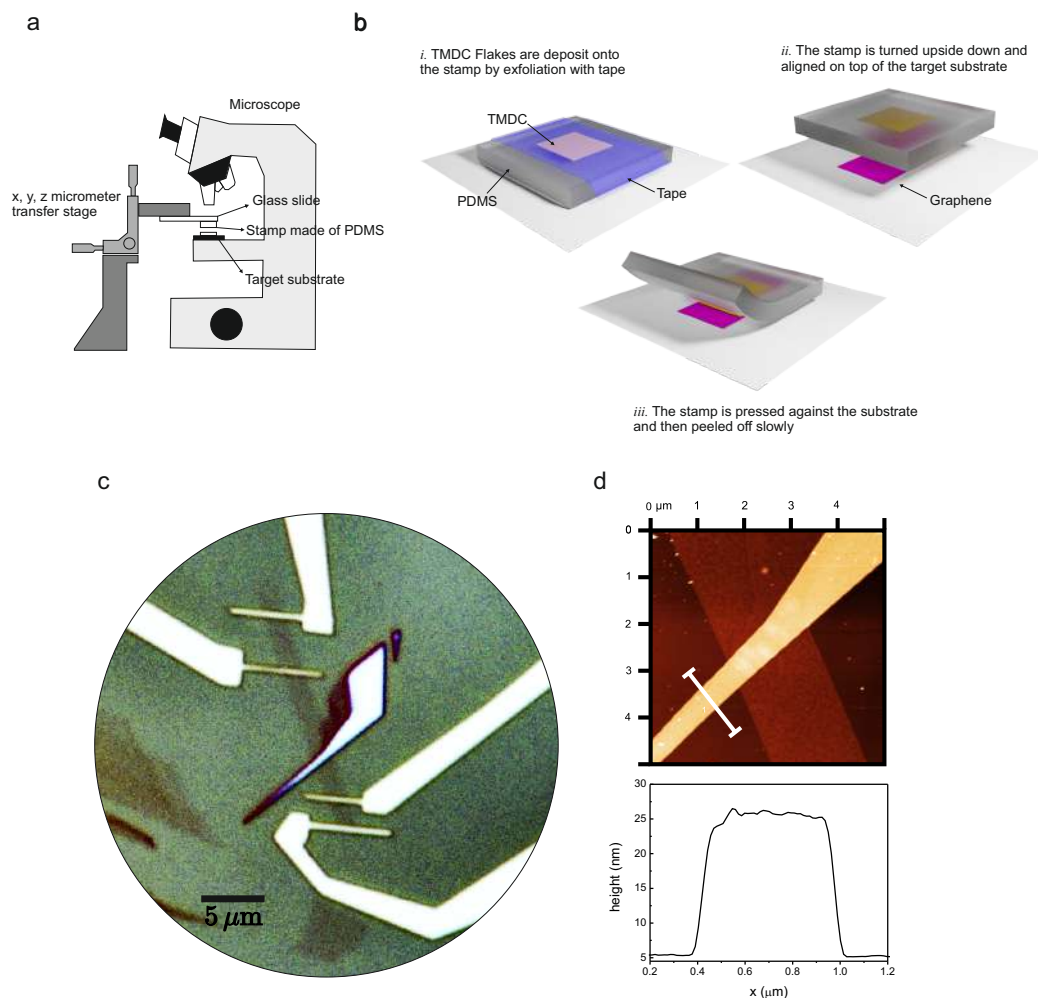


FIGURE 3.8: **a.** Schematic of the transfer setup. **b.** Steps involved in the transfer process. **c.** Color-enhanced optical picture of a typical device comprising monolayer graphene and a  $\text{WS}_2$  flake. **d.** In the top panel a zoom-in close to the  $\text{WS}_2$  using an AFM. In the bottom panel, the obtained height profile of the TMDC across the device bar showed in the top panel.

thin film of PC (or PPC) assists the picking up of the 2D crystals. This approach is handy to fabricate samples that are fully encapsulated. More details can be found in the appendix C.

The device contacts are defined using electron beam lithography (EBL). The choice of EBL over optical lithography is the adaptability of the structures with sub-10 nm resolution. In the EBL, an electron beam exposes the PMMA (other resin masks are also commonly used). The electron beam enhanced the solubility of the resist, enabling selective removal of the exposed regions (positive resist) of the polymer by immersing it in the solvent methyl isobutyl ketone, MIBK (development process). The exposure to an electron beam reduces the solubility in a negative resist, so they remain after the development process. For a detail lithography recipe see appendix C.

### 3.6 Instrumentation

We wired the device to a chip carrier that is placed in a cryostat. In one setup, a rack-and-pinion actuator is used to change the relative angle between the chip carrier and the homogenous applied magnetic field with a precision of  $0.2^\circ$ . In this setup, all the data were acquired at 300 K and under a pressure of  $10^{-6}$  Torr. For measurements at lower temperatures, the chip carrier was placed in a closed cycle cryostat system shown in Fig. 3.9. The cryostat is positioned between the poles of an electromagnet which can generate magnetic fields up to 0.7 T at 40 A. The device is connected to the sources and nanovoltmeters through an in-house made switching box.

The main components of the closed cycle refrigerator are the expander, compressor, vacuum shroud, and radiation shield (see Fig. 3.9a). The expander, commonly referred to as the cold finger, is where the refrigeration cycle takes place. It is connected to a compressor by two gas lines. One of the gas lines supplies high pressure helium gas to the expander, the other gas line returns low pressure helium gas from the expander. The refrigeration closed cycle starts with the opening of the high pressure path. This allows the high pressure helium gas to pass through the regenerating

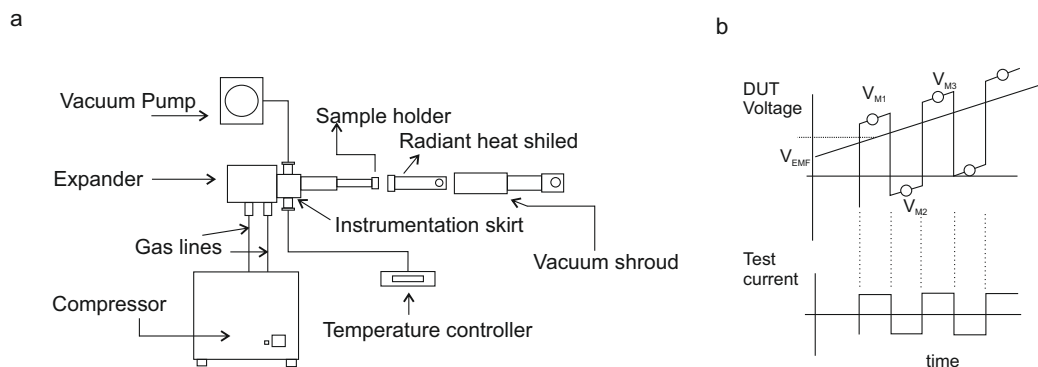


FIGURE 3.9: **a.** Closed cycle refrigerator components. **b.** Measurement proceed in the Delta mode.

material and into the expansion space. Then, the pressure moves the displacer, allowing the gas at the bottom to expand and cool. The rotation of the valve disk next opens the low pressure path, allowing the cold gas to flow through the regenerating material which removes heat from the system. Finally, the pressure differential returns the displacer to its original position, and the cycle is completed.

Electrical measurements were carried out using the current-reversal technique, commonly known as "delta" mode. We use the Keithley 6221 current source and 2182A nano voltmeter. In the delta mode, we alternate the current source polarity and read three voltage  $V_{M1}$ ,  $V_{M2}$ ,  $V_{M3}$  of Fig. 3.9b. The measured voltages contain, apart from the voltage drop ( $V$ ) coming from the device under test (DUT), a constant thermal voltage ( $V_{EMF}$ ) and a linearly changing thermoelectric voltage ( $\delta V$ ):

$$\begin{aligned} V_{M1} &= V_1 + V_{EMF} \\ V_{M2} &= -V_2 + V_{EMF} + \delta V \\ V_{M3} &= V_3 + V_{EMF} + 2\delta V \end{aligned} \quad (3.13)$$

To obtain the voltage in the DUT the voltages are added in the following way,

$$V = \frac{V_A - V_B}{2} = \frac{V_1 + V_3 - 2V_2}{4}; \text{ with } V_A = \frac{V_{M1} - V_{M2}}{2} \text{ \& } V_B = \frac{V_{M3} - V_{M2}}{2}. \quad (3.14)$$

This method eliminates constant and linearly changing thermoelectric voltages. In the delta method, each data point is the average of three voltage readings, and we typically repeat it 25 times, which results in  $3 \times 25$  times averaging for each point, thus the data resulting from the delta method has a low noise.

### 3.7 Electrical characterization

The first electrical characterization of our devices consists of measuring the electrical resistance. To do so, we apply a bias current and measure voltage drop along the channel. We can send the current and measure the voltage using two contacts (two points) or four contacts (four points) as it shown in Fig. 3.10 (inset). In our devices, normally the contact resistance in the  $\text{TiO}_2/\text{Co}$  electrodes are larger than 10 k $\Omega$ .

The number of electronic states in graphene that contributes to its electrical conductivity is tuned by changing the Fermi energy (Chap. 2). We use the field effect to electrically shift the Fermi energy in graphene and measure its effect on its resistance [37]. A back gate voltage ( $V_g$ ) applied in the configuration shown in Fig. 3.10 forms a capacitor with the  $\text{SiO}_2$  as the dielectric. The graphene and the heavily  $p^+$  doped Si compose the parallel plates. Because graphene has a finite density of states, the measured voltage between the plates is not purely electrostatic, but it contains the effect of the called quantum capacitance. The total capacitance is as if there are two capacitances in series: the capacitance of the  $\text{SiO}_2$  ( $C_{\text{SiO}_2}$ ) and the quantum capacitance ( $C_q$ ) related to the graphene's density of states. However, because we use a



thick SiO<sub>2</sub> dielectric (440 nm), the total capacitance is dominated by the oxide layer; thus, we ignore C<sub>q</sub> [38, 39]. The expression relating V<sub>g</sub> and C<sub>SiO<sub>2</sub></sub> is

$$V_g - V_{\text{CNP}} = \frac{en}{C_{\text{SiO}_2}}. \quad (3.15)$$

For 440 nm SiO<sub>2</sub> thickness, C<sub>SiO<sub>2</sub></sub>/e = 49 × 10<sup>9</sup> V<sup>-1</sup> cm<sup>-2</sup>. In the graphene's Dirac point (K point), the charge is neutral; this is called charge neutrality point (CNP). At the CNP, the resistance reaches a maximum, and in some devices, this may occur at certain V<sub>CNP</sub> ≠ 0 because of unintentional doping of the graphene sample during sample fabrication.

The total device resistance is given by

$$R = R_{\text{contact}} + \frac{N_{\text{sq}}}{e\mu n_{\text{tot}}}, \quad (3.16)$$

where R<sub>contact</sub> is the contact resistance (in four points measurements R<sub>contact</sub> = 0 Ω), μ is the carrier's mobility, N<sub>sq</sub> represents the number of squares of the gated area (N<sub>sq</sub> = channel length/channel width), and e is the electron charge. n<sub>tot</sub> is the total carrier density that can be approximated by [40]:

$$n_{\text{tot}} = \sqrt{n_0 + n(V_g)}, \quad (3.17)$$

where n<sub>0</sub> represents the residual carriers density at the minimum conductivity, Dirac point, and n(v<sub>g</sub>) is given by Eq. (3.15). For an ideal disorder-free graphene n<sub>0</sub> should be zero, however a n<sub>0</sub> ≠ 0 is generated by charged impurities [41].

By fitting the measured data using Eq. (3.16), we can extract the relevant parameters, n<sub>0</sub>, the average μ, and R<sub>contact</sub>. Fig. 3.10 shows a typical measurement of R versus V<sub>g</sub> (open circles) at room temperature, normally called "back-gate" measurement. The Eq. (3.16) (solid line) is used to fit the data. The modeling results agree well with the experimental data, the obtained residual concentration is n<sub>0</sub> = 2.8 × 10<sup>11</sup> cm<sup>-2</sup>, and the mobility μ = 6400 cm<sup>2</sup>/V s. The back-gate measurements are typically the first electrical characterization of our devices.

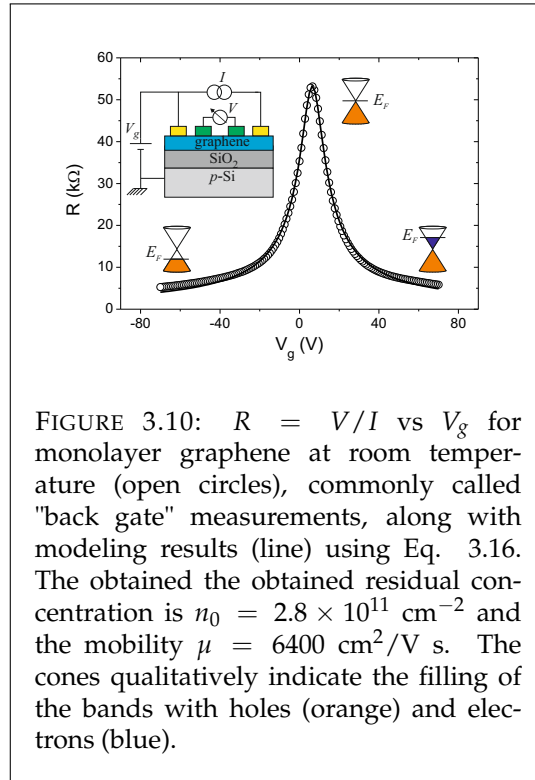


FIGURE 3.10:  $R = V/I$  vs  $V_g$  for monolayer graphene at room temperature (open circles), commonly called "back gate" measurements, along with modeling results (line) using Eq. 3.16. The obtained residual concentration is  $n_0 = 2.8 \times 10^{11} \text{ cm}^{-2}$  and the mobility  $\mu = 6400 \text{ cm}^2/\text{V s}$ . The cones qualitatively indicate the filling of the bands with holes (orange) and electrons (blue).



## References

- [1] Johnson, M. & Silsbee, R. H. Interfacial charge-spin coupling: Injection and detection of spin magnetization in metals. *Phys. Rev. Lett.* **55**, 1790–1793 (1985).
- [2] Johnson, M. & Silsbee, R. H. Spin-injection experiment. *Phys. Rev. B* **37**, 5326–5335 (1988).
- [3] Baibich, M. N. *et al.* Giant magnetoresistance of (001)fe/(001)cr magnetic superlattices. *Phys. Rev. Lett.* **61**, 2472–2475 (1988).
- [4] Binasch, G., Grünberg, P., Saurenbach, F. & Zinn, W. Enhanced magnetoresistance in layered magnetic structures with antiferromagnetic interlayer exchange. *Phys. Rev. B* **39**, 4828–4830 (1989).
- [5] NobelPrize.org. Nobel Media AB, . URL <https://www.nobelprize.org/prizes/physics/2007/press-release/>.
- [6] Valet, T. & Fert, A. Theory of the perpendicular magnetoresistance in magnetic multilayers. *Phys. Rev. B* **48**, 7099–7113 (1993).
- [7] Drögeler, M. *et al.* Spin lifetimes exceeding 12 ns in graphene nonlocal spin valve devices. *Nano Lett.* **16**, 3533–3539 (2016).
- [8] Valenzuela, S. O. & Tinkham, M. Direct electronic measurement of the spin Hall effect. *Nature* **442**, 176–179 (2006).
- [9] Dash, S. P., Sharma, S., Patel, R. S., de Jong, M. P. & Jansen, R. Electrical creation of spin polarization in silicon at room temperature. *Nature* **462**, 491–494 (2009).
- [10] Rashba, E. I. Theory of electrical spin injection: Tunnel contacts as a solution of the conductivity mismatch problem. *Phys. Rev. B* **62**, R16267–R16270 (2000).
- [11] Schmidt, G., Ferrand, D., Molenkamp, L. W., Filip, A. T. & van Wees, B. J. Fundamental obstacle for electrical spin injection from a ferromagnetic metal into a diffusive semiconductor. *Phys. Rev. B* **62**, R4790–R4793 (2000).
- [12] Tombros, N., Jozsa, C., Popinciuc, M., Jonkman, H. T. & van Wees, B. J. Electronic spin transport and spin precession in single graphene layers at room temperature. *Nature* **448**, 571–574 (2007).
- [13] Han, W. *et al.* Tunneling spin injection into single layer graphene. *Phys. Rev. Lett.* **105**, 167202 (2010).
- [14] Sierra, J. F. *et al.* Thermoelectric spin voltage in graphene. *Nature Nanotechnol.* **13**, 107–111 (2018).
- [15] Singh, S. *et al.* Strontium oxide tunnel barriers for high quality spin transport and large spin accumulation in graphene. *Nano Lett.* **17**, 7578–7585 (2017).

- [16] Kamalakar, M. V., Dankert, A., Bergsten, J., Ive, T. & Dash, S. P. Enhanced tunnel spin injection into graphene using chemical vapor deposited hexagonal boron nitride. *Sci. Rep.* **4**, 6146 (2014).
- [17] Gurram, M., Omar, S. & van Wees, B. J. Bias induced up to 100polarizations in ferromagnet/bilayer-hBN/graphene/hBN heterostructures. *Nature Commun.* **8**, 248 (2017).
- [18] Neumann, I., Costache, M. V., Bridoux, G., Sierra, J. F. & Valenzuela, S. O. Enhanced spin accumulation at room temperature in graphene spin valves with amorphous carbon interfacial layers. *App. Phys. Lett.* **103**, 112401 (2013).
- [19] Li, C. H., Robinson, J. T. & Jonker, B. T. Homoepitaxial tunnel barriers with functionalized graphene-on-graphene for charge and spin transport. *Nature Commun.* **5**, 3161 (2014).
- [20] Valenzuela, S. O. Nonlocal Electronic spin detection, spin accumulation and the spin Hall effect. *International Journal of Modern Physics B* **23**, 2413–2438 (2009).
- [21] Jedema, F. J., Heersche, H. B., Filip, a. T., Baselmans, J. J. a. & van Wees, B. J. Electrical detection of spin precession in a metallic mesoscopic spin valve. *Nature* **416**, 713–716 (2002).
- [22] Raes, B. *et al.* Determination of the spin-lifetime anisotropy in graphene using oblique spin precession. *Nature Commun.* **7**, 11444 (2016).
- [23] Raes, B. *et al.* Spin precession in anisotropic media. *Phys. Rev. B* **95**, 85403 (2017).
- [24] Guimarães, M. H. D. *et al.* Controlling Spin Relaxation in Hexagonal BN-Encapsulated Graphene with a Transverse Electric Field. *Phys. Rev. Lett.* **113**, 086602 (2014).
- [25] Ghiasi, T. S., Ingla-Aynés, J., Kaverzin, A. A. & van Wees, B. J. Large Proximity-Induced Spin Lifetime Anisotropy in Transition-Metal Dichalcogenide/Graphene Heterostructures. *Nano Lett.* **17**, 7528–7532 (2017).
- [26] Benítez, L. A. *et al.* Strongly anisotropic spin relaxation in graphene–transition metal dichalcogenide heterostructures at room temperature. *Nature Phys.* **14**, 303–308 (2018).
- [27] Zhu, T. & Kawakami, R. K. Modeling the oblique spin precession in lateral spin valves for accurate determination of the spin lifetime anisotropy: Effect of finite contact resistance and channel length. *Phys. Rev. B* **97**, 144413 (2018).
- [28] Blundell, S. *Magnetism in Condensed Matter* (Oxford University Press, USA, 2001).

- [29] Xu, J., Zhu, T., Luo, Y. K., Lu, Y.-M. & Kawakami, R. K. Strong and Tunable Spin-Lifetime Anisotropy in Dual-Gated Bilayer Graphene. *Phys. Rev. Lett.* **121**, 127703 (2018).
- [30] Valenzuela, S. O. & Tinkham, M. Electrical detection of spin currents: The spin-current induced Hall effect (invited). *J. Appl. Phys.* **101**, 09B103 (2007).
- [31] Kimura, T., Otani, Y., Sato, T., Takahashi, S. & Maekawa, S. Room-temperature reversible spin Hall effect. *Phys. Rev. Lett.* **98**, 156601 (2007).
- [32] Savero Torres, W. *et al.* Spin precession and spin Hall effect in monolayer graphene/Pt nanostructures. *2D Mater.* **4**, 041008 (2017).
- [33] Safeer, C. K. *et al.* Room-Temperature Spin Hall Effect in Graphene/MoS<sub>2</sub> van der Waals Heterostructures. *Nano Lett.* **19**, 1074–1082 (2019).
- [34] Malard, L. M., Pimenta, M. A., Dresselhaus, G. & Dresselhaus, M. S. Raman spectroscopy in graphene. *Phys. Rep.* **473**, 51–87 (2009).
- [35] Castellanos-Gomez, A. *et al.* Deterministic transfer of two-dimensional materials by all-dry viscoelastic stamping. *2D Mater.* **1**, 011002 (2014).
- [36] Pizzocchero, F. *et al.* The hot pick-up technique for batch assembly of van der waals heterostructures. *Nat. Commun.* **7**, 11894 (2016).
- [37] Novoselov, K. S. *et al.* Electric field effect in atomically thin carbon films. *Science* **306**, 666–669 (2004).
- [38] Chen, Z. & Appenzeller, J. Mobility extraction and quantum capacitance impact in high performance graphene field-effect transistor devices. In *2008 IEEE Int. Electron Devices Meet.*, L, 1–4 (IEEE, 2008).
- [39] Xia, J., Chen, F., Li, J. & Tao, N. Measurement of the quantum capacitance of graphene. *Nat. Nanotechnol.* **4**, 505–509 (2009).
- [40] Kim, S. *et al.* Realization of a high mobility dual-gated graphene field-effect transistor with Al<sub>2</sub>O<sub>3</sub> dielectric. *Appl. Phys. Lett.* **94**, 062107 (2009).
- [41] Adam, S., Hwang, E. H., Galitski, V. M. & Sarma, S. D. A self-consistent theory for graphene transport. *Proceedings of the National Academy of Sciences* **104**, 18392–18397 (2007).

## Chapter 4

# Spin relaxation in graphene/TMDC van der Waals heterostructures

This chapter contains the results regarding the study of spin dynamics in graphene with enhanced spin-orbit coupling (SOC) by proximity to a transition metal dichalcogenide (TMDC). Signatures of such an enhancement have recently been reported [1–4]. However, the nature of the spin relaxation in these systems remained unknown. Here, we unambiguously demonstrate anisotropic spin dynamics in heterostructures comprising graphene/TMDC, with TMDC being  $WS_2$ ,  $MoS_2$ , and  $WSe_2$ . By using out-of-plane and oblique spin precession (see Sec. 3.3), we show that the spin lifetime is largest when the spins point out of the graphene plane. We observe that the spin lifetime changes over an order of magnitude depending on the spin orientation, indicating that the strong spin-valley coupling of the TMDC is imprinted in the graphene and felt by the propagating spins. Moreover, we show that such anisotropic spin relaxation can be controlled. These findings provide a rich platform to explore coupled spin-valley phenomena and offer novel spin manipulation strategies in two-dimensional materials. The content of this chapter is mostly adapted from our original work published in *Nature Phys.* **14**, 303–308 (2018).

### 4.1 Introduction

First principle calculations shows that TMDCs can induce a large SOC in graphene in the meV range while preserving the graphene linear band structure [5, 6]. Enhancement of the SOC has been demonstrated using non-local charge transport and weak (anti-)localization measurements [1–4, 7], the most salient signature being a drastic reduction of the spin lifetime down to the picosecond range [2–4, 7]. In recent spin transport experiments, the spin sink effect in the TMDCs was used to modulate the transmission of pure spin currents. This enables the realization of a spin field-effect switch that changes between "on" and "off" by gate tuning [2, 4].

A further consequence of the proximity-induced SOC, which has not been addressed experimentally, is the strong spin-valley coupling [8–10] imprinted by the

TMDC to graphene. As represented in Fig. 4.1a, a band gap is present in the Dirac cone of graphene due to the breaking of pseudospin symmetry, while the SOC, combined with broken space inversion symmetry, removes the spin degeneracy of the conduction and valence bands [5, 6]. The spins in these bands tilt out of the graphene plane, with the out-of-plane component alternating from up to down as the energy of the bands increases, in a sequence that inverts between  $K$  and  $K'$ . Away from the  $K$  points a well-defined in-plane spin texture is present [6] (see Fig. 4.1a).

The complex spin texture present in graphene/TMDC implies that the spin dynamics would likely differ for spins pointing in ( $\parallel$ ) and out of ( $\perp$ ) the graphene plane, resulting in distinct spin lifetimes,  $\tau_s^{\parallel}$  and  $\tau_s^{\perp}$ . Indeed, realistic modelling and numerical simulations in graphene(gr)/WS<sub>2</sub> predict that the spin lifetime anisotropy ratio  $\zeta \equiv \tau_s^{\perp} / \tau_s^{\parallel}$  could reach values as large as a few hundreds, in the presence of intervalley scattering [11]. In other words, the recently proposed graphene/TMDC spin switch [2, 4] should actually behave as a filter for spin currents, with a transmission that depends on the orientation of the spins relative to the plane. Besides, quantification of  $\zeta$  can therefore provide unique insight to spin-valley coupling mechanisms and help elucidate the nature of the induced SOC [12, 13] in graphene by proximity to a TMDC.

The present chapter is organized as follows: in Sec. 4.2, we show the measurement method and the device design. More details about the used method are discussed in Chap. 3 (Sec. 3.3). In Sec. 4.3, we present spin out-of-plane precession measurements in graphene and graphene/TMDC devices using an in-plane magnetic field. The Secs. 4.4 and 4.5 are devoted to oblique spin precession measurements in graphene and graphene/TMDC devices, respectively. In Sec. 4.6 we discuss the origin of the anisotropy spin relaxation in graphene/TMDC heterostructures. In Sec. 4.7 we provide a study of the spin relaxation anisotropy as a function of an applied back-gate voltage. Finally, the Sec. 4.8 is devoted to the solutions of the spin-Bloch diffusion equations used to model the spin dynamics in our experiments.

## 4.2 Device design and measurement scheme

In Chap. 3 we explained that  $\zeta$  can readily be determined combining in-plane and out-of plane spin precession measurements [13, 14]. In order to reveal the spin-valley coupling in gr/TMDC, we implement such a technique using the device depicted in Figs. 4.1b-c. The measurements are based on the standard non-local spin injection and detection technique [15, 16]. A TMDC flake is placed over the graphene spin channel between the ferromagnetic injector (F1) and detector (F2) electrodes, creating a gr/TMDC van der Waals heterostructure (see Chap. 3 for fabrication details). The TMDC locally modifies the graphene band structure by proximity effect and, as a consequence, the spin diffusion. Considering that  $\tau_s^{\parallel}$  in the modified graphene region is expected to be in the range of a few ps [2, 11], the spin relaxation length should be in the submicron range. The width  $w$  of the TMDC flake is thus selected to

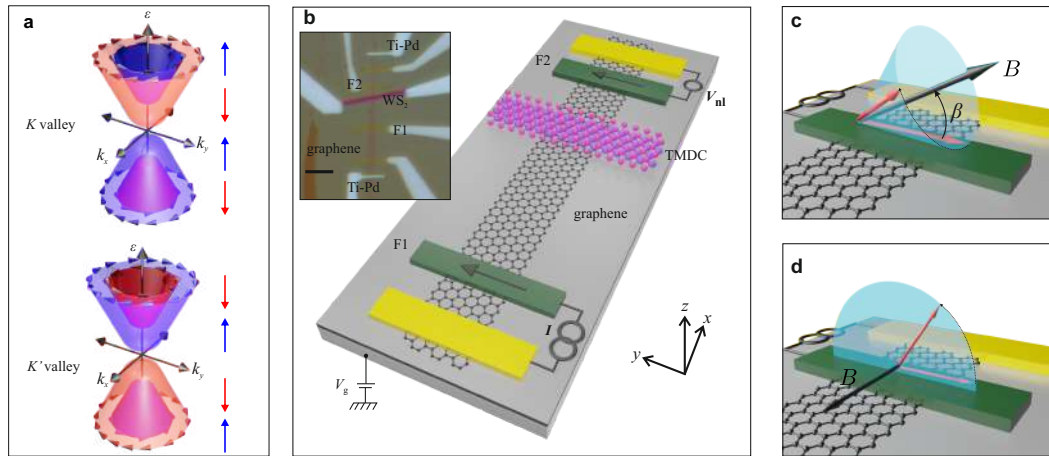


**FIGURE 4.1: Proximity-induced spin-orbit coupling and measurement scheme.** **a**, representation of the graphene (gr) electronic band structure in the vicinity of the K and K' valleys for gr/WS<sub>2</sub>. The colors and arrows represent the expectation value for the out-of-plane spin component, while the arrows in the Fermi contours represent the expected value for the in-plane spin component. **b**, schematics of the device design. The device consists of a graphene channel contacted with two ferromagnets (F1 and F2) and a transverse strip of WS<sub>2</sub> in between. A charge current through F1 injects spins having an orientation parallel to the F1 magnetization direction (black arrow in F1). Inset in **b**, enhanced-contrast optical image comprising one graphene–WS<sub>2</sub> device (Device 1) and two reference graphene devices enclosing it. The bar represents 5  $\mu\text{m}$ . **c**, oblique spin precession, where  $B$  is applied in a plane that contains the easy axis of the ferromagnetic electrodes and that is perpendicular to the substrate. **d**, Out-of-plane spin precession with in-plane  $B$  with  $B$  perpendicular to the length of F1 and F2. Spins precess in a plane perpendicular to the substrate. In **c** and **d**, the effective spin lifetime becomes sensitive to both parallel and perpendicular spin lifetimes,  $\tau_s^{\parallel}$  and  $\tau_s^{\perp}$ , and the spin relaxation anisotropy can be experimentally obtained.

be about one micrometre so as to avoid suppressing the spin population completely when spins are in-plane. The spin channel length  $L$ , which is defined as the distance between F1 and F2, is much longer than  $w$  (about 10  $\mu\text{m}$ ) to ensure that the spin precession response of the device can be studied at moderate magnetic fields [13, 14]. A gate voltage applied to the substrate ( $p^{++}$  Si/SiO<sub>2</sub>) is used to tune the graphene carrier density and the Fermi level in the TMDC [2, 4].

Owing to magnetic shape anisotropy, the magnetizations of F1 and F2 tend to remain in-plane. An out of plane magnetic field  $B$ , which causes spins to precess exclusively in plane, will sense  $\tau_s^{\parallel}$  only. In order to obtain information on  $\tau_s^{\perp}$ , we follow two strategies represented in Figs. 4.1 c-d. The strategies, which are described in Chap. 3, rely on the application of an oblique  $B$  characterized by an angle  $\beta$  (Fig. 4.1c) or an in-plane  $B$  transversal to the easy magnetization axes of F1/F2 (Fig. 4.1d). As represented by the red arrows, such magnetic fields cause the spins to precess out of the graphene plane as they diffuse towards the detector. The spin precession dynamics therefore becomes sensitive to both  $\tau_s^{\parallel}$  and  $\tau_s^{\perp}$ , and then  $\tau_s^{\perp}$  can be determined. If the spin lifetime in gr/WS<sub>2</sub> is anisotropic, the transmission of

the spins across this region will be modulated by  $B$ .

### 4.3 Out-of-plane spin precession measurements in graphene (gr) and gr/TMDC

In order to compare the spin transport in pristine graphene and in the gr/TMDC heterostructure, we study the spin dynamics in a reference device (pristine graphene), and in a gr/TMDC device. Both devices are fabricated in the same graphene flake (see Fig. 4.1b).

Figure 4.2 demonstrates the changes in the spin precession lineshape,  $R_{\text{nl}}$  vs  $B$ , induced by the presence of the TMDC = WS<sub>2</sub> in the spin channel. The non-local spin resistance  $R_{\text{nl}} = V_{\text{nl}}/I$  is determined from the non-local voltage  $V_{\text{nl}}$  at the detector F2 that is generated by a current  $I$  flowing at the injector F1 (Fig. 4.1c). Figures 4.2a to 4.2c show the measurements for a typical gr/WS<sub>2</sub> device. Figures 4.2d to 4.2f show the corresponding measurements in the reference graphene device. The data are acquired for parallel and antiparallel magnetization configurations of the spin injector and detector. Remarkably, the spin precession response in the two devices displays different behaviour.

Figures 4.2a and 4.2d present conventional spin precession measurements with an out-of-plane magnetic field. Even though spin precession is observed in both cases, the magnitude of the signal in Fig. 4.2a is two orders of magnitude smaller than in the reference device (Fig. 4.2d). Such a decrease indicates a large reduction of the in-plane spin relaxation length  $\lambda_s^{\parallel}$  in the gr/WS<sub>2</sub> region, as observed previously for MoS<sub>2</sub> [2].

Figures 4.2b and 4.2e present spin precession measurements for in-plane  $B$ , as shown in Fig. 4.1e. While the change in magnetic field configuration results in no significant variation in the reference device (compare Figs. 4.2d and 4.2e), the changes observed in the gr/WS<sub>2</sub> device are remarkable (see Figs. 4.2a and 4.2b). Figure 4.2b shows that, as  $|B|$  increases,  $|R_{\text{nl}}|$  becomes much larger than its value at  $B = 0$ . The anomalous enhancement of  $|R_{\text{nl}}|$  is a clear indication of anisotropic spin relaxation, with an out-of-plane spin relaxation length  $\lambda_s^{\perp}$  larger than  $\lambda_s^{\parallel}$  and thus  $\zeta > 1$ .

The slight difference between Figs. 4.2d and 4.2e is due to the tilting of the electrodes magnetization with  $B$ . In both experiments,  $B$  is perpendicular to the equilibrium magnetization at  $B = 0$ , however the tilting is more pronounced when  $B$  is oriented in-plane for which the shape anisotropy is smaller.

In an isotropic system,  $R_{\text{nl}}^{\pm} = [\pm g(B) \cos^2 \gamma + \sin^2 \gamma] R_{\text{nl},0}$  for initially parallel (+) and antiparallel (-) configurations of the F1/F2 magnetizations, with  $g(B)$  a function that captures the precession response,  $\gamma$  the tilting angle of the F1/F2 magnetizations and  $R_{\text{nl},0} = R_{\text{nl}}(B = 0)$ . By noting that  $\Delta R_{\text{nl}} = R_{\text{nl}}^+ - R_{\text{nl}}^- = 2g(B)R_{\text{nl},0} \cos^2 \gamma$ , it is evident that for an isotropic system and small  $\gamma$ ,  $\Delta R_{\text{nl}}$  is independent of the orientation of  $B$  (see details in Sec. 3.3). The obtained  $\Delta R_{\text{nl}}$  for the two  $B$  orientations

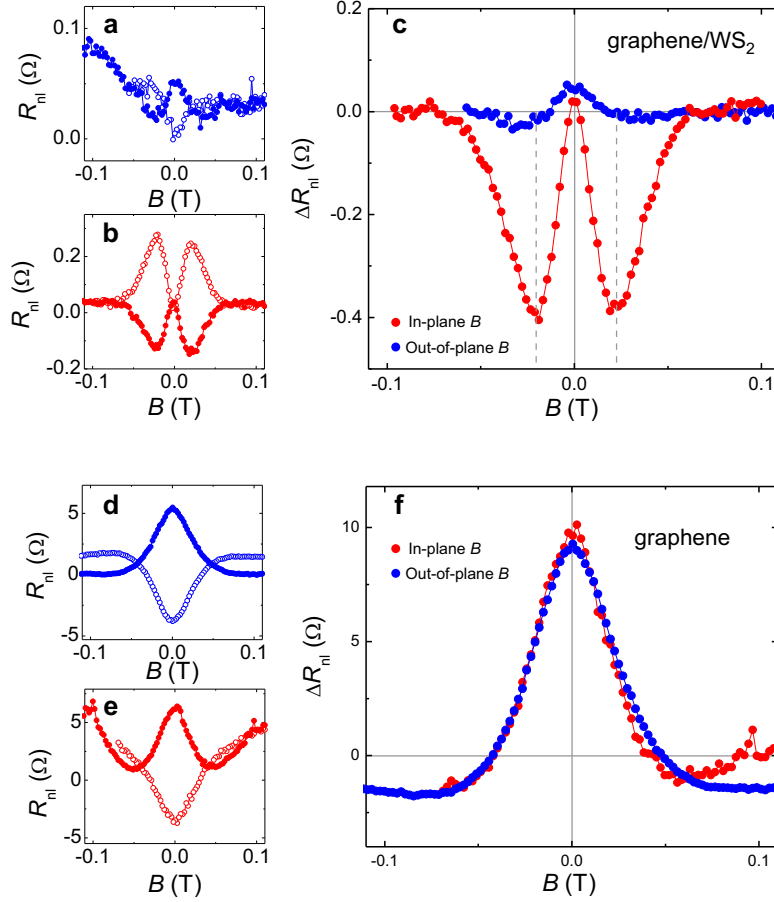


**FIGURE 4.2: Anisotropic spin relaxation in gr/WS<sub>2</sub>.** Non-local resistance  $R_{nl}$  versus  $B$  with different  $B$  orientation. The measurements in **a-c** are for a gr/WS<sub>2</sub> device while those in **d-f** are for a reference device in the same graphene flake. **a, d**, Standard spin precession measurements with  $B$  perpendicular to the substrate. Solid (open) symbols are for parallel (antiparallel) configurations of the magnetizations of F1 and F2 ( $R_{nl}^+$  and  $R_{nl}^-$ , respectively). The gr/WS<sub>2</sub> (**a**) and reference (**d**) show qualitatively the same response, although the magnitude of  $R_{nl}$  in the former is significantly smaller. **b, e**, Spin precession measurements with  $B$  in the graphene plane as represented in Fig. 4.1e. Solid and open symbols are for parallel and antiparallel configurations. The gr/WS<sub>2</sub> (**b**) and reference (**e**) display different behaviour.  $R_{nl}$  in the reference device does not vary with  $B$  orientation, neither in magnitude nor in the precession features. In the gr/WS<sub>2</sub> device  $R_{nl}$  increases in magnitude when spins rotate out of the graphene plane, rapidly changing sign;  $R_{nl}$  presents extrema at  $B \sim \pm 20$  mT with a magnitude that exceeds  $|R_{nl}(B = 0)|$ . **c, f**,  $\Delta R_{nl} = R_{nl}^+ - R_{nl}^-$  versus  $B$  as extracted from **a, b** and **d, e**. The blue (red) plots are for perpendicular (in-plane)  $B$ . The dashed lines in **c** mark the position of the extrema for the measurements with in-plane  $B$ .  $T = 300$  K;  $I = 2 \mu\text{A}$ .

are shown in Figs. 4.2c and 4.2f for the gr/WS<sub>2</sub> and the reference device, respectively. The nearly perfect overlap of the two curves in Fig. 4.2f is a consequence of the isotropic spin relaxation in graphene [13, 14]. The disparity of the curves in Fig. 4.2c demonstrates the highly anisotropic nature of the spin transport in gr/WS<sub>2</sub>. The extrema in  $R_{nl}$  in Fig. 4.2b are reached when the aggregate orientation of the



diffusing spins have rotated by  $\pi/2$  at the  $\text{WS}_2$  location. Because the diffusing spins reach first  $\text{WS}_2$  and later F2, the extrema occur at magnetic fields that are slightly larger than those at which  $R_{\text{nl}} = 0$  in the conventional spin precession measurements (dashed vertical lines in Fig. 4.2c).

The decrease in the magnitude of  $R_{\text{nl}}$  observed between Figs. 4.2c and 4.2a is systematically found in all of our devices. It is a direct consequence of the small spin relaxation length  $\lambda_s^{\parallel}$  in  $\text{gr}/\text{WS}_2$ , which can be determined by solving the diffusive Bloch equations (see Sec. 4.8). At  $B = 0$  the solution in  $z$ , along the graphene flake, for a specific region ( $r$ ) of the device has the general form  $A_r e^{z/\lambda_{s,r}} + B_r e^{-z/\lambda_{s,r}}$ , with  $A_r, B_r$  determined by the boundary conditions and  $\lambda_{s,r}$  the spin relaxation length. For  $\text{gr}/\text{WS}_2$   $\lambda_{s,r} = \lambda_s^{\parallel}$  and in graphene  $\lambda_{s,r} = \lambda_{s,\text{gr}}$ . The latter is extracted from conventional spin precession measurements (Fig. 4.2d) in the reference device. From the change in  $R_{\text{nl},0}$  between the  $\text{gr}/\text{WS}_2$  and reference devices,  $\lambda_s^{\parallel}$  is estimated to be about 0.2-0.4  $\mu\text{m}$ , which is significantly smaller than the typical  $\lambda_{s,\text{gr}} \sim 3\text{-}5 \mu\text{m}$ .

Figure 4.2 shows that the out-of-plane spin component is transmitted through  $\text{gr}/\text{WS}_2$  much more efficiently than the in-plane component. Thus,  $\text{gr}/\text{WS}_2$  acts as a filter with a transmission that depends on the spin orientation. Such a filter represents a new tool in spintronics to detect small variations in the orientation of spins arriving to it. From the data shown in Fig. 4.2, a difference in transmission of one order of magnitude is estimated by comparing the extrema in  $|R_{\text{nl}}|$  in the two  $B$  configurations.

In Fig. 4.3a and 4.3b we show similar anisotropic spin relaxation behavior when we replace  $\text{WS}_2$  by  $\text{MoS}_2$  and  $\text{WSe}_2$ , respectively. Moreover, such anisotropic spin relaxation has been also observed in  $\text{gr}/\text{MoSe}_2$  [17]. In the next two sections we use oblique spin precession measurements (see schematics in Fig. 4.1d) to quantify the anisotropy ratio,  $\zeta = \tau_s^{\perp} / \tau_s^{\parallel}$ , in graphene and graphene/TMDC devices.

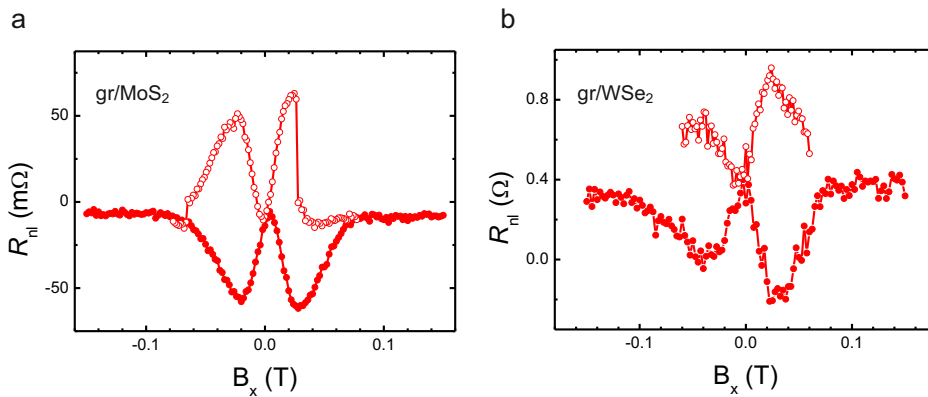


FIGURE 4.3: **Anisotropic spin relaxation in  $\text{gr}/(\text{MoS}_2, \text{WSe}_2)$**  **a** and **b**, spin precession measurements for in-plane  $B$  in  $\text{MoS}_2$  and  $\text{WSe}_2$  on graphene, respectively. The data are acquired at 77 K for parallel (filled circles) and antiparallel (open circles) magnetization of spin injector and detector. The carrier densities are  $n = -4.9 \times 10^{12} \text{ cm}^{-2}$  and  $n = -2.7 \times 10^{13} \text{ cm}^{-2}$  for **a** and **b** respectively.

#### 4.4 Oblique spin precision measurements in graphene

As display in Fig. 4.2f, the almost perfect overlap between the measurements with an out-of-plane and in-plane magnetic field, indicates isotropic spin relaxation in the reference device. Such results agree with previous observations on graphene/SiO<sub>2</sub> devices [13, 14]. To confirm the isotropic spin relaxation in our reference device, we measure the non-local resistance as a function of an oblique magnetic field. Additionally, we fabricated a device comprising graphene on a hexagonal boron nitride (hBN) substrate.

Figures 4.4a and 4.4b show typical spin precession measurements for a representative set of  $\beta$  values for graphene onto SiO<sub>2</sub> and hBN. In both cases  $\tau_s^{\parallel}$  is between 0.2 ns and 0.4 ns. When applying the oblique precession method, the precessional motion is suppressed at  $B_d \sim 0.1$  T for all  $\beta$  and the remanent non-local spin signal is independent of  $B$ . The remanent signal derives from the non-precessing spin component that lies along the  $B$  direction, whose magnitude  $R_{nl}^{\beta}$  depends on  $\beta$  as

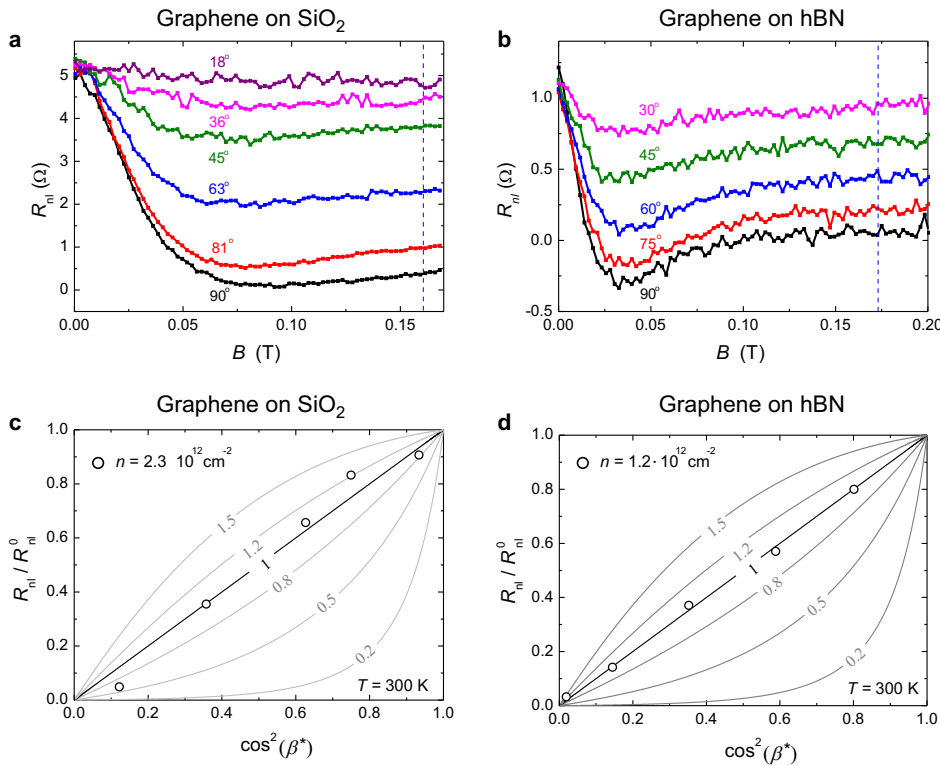


FIGURE 4.4: **Isotropic spin relaxation in graphene.** **a** and **b**, room temperature spin precession measurements for oblique magnetic fields  $B$  applied at different angles  $\beta$  in graphene on SiO<sub>2</sub> and hBN, respectively. The data are acquired for parallel magnetization configuration of spin injector and detector. The carrier densities are  $n = 2.3 \times 10^{12} \text{ cm}^{-2}$  and  $n = 1.2 \times 10^{12} \text{ cm}^{-2}$  respectively. **c** and **d**,  $R_{nl}$  normalized by  $R_{nl,0} = R_{nl}(B = 0)$  vs  $\cos^2(\beta^*)$  for graphene on SiO<sub>2</sub> and hBN, respectively. The values of  $R_{nl}$  are obtained at  $B$  marked by the vertical dashed blue line in **a** and **b**. The solid lines in **c** and **d** represent  $R_{nl}$  for the indicated value of  $\zeta$  calculated with Eq. 3.10, the black straight line corresponds to the isotropic case,  $\zeta = 1$ .

expected from Eq. (3.10). Figures 4.4c and 4.4d show  $R_{\text{nl}}$  at  $B$  marked by a vertical dashed line (see Figs. 4.4a and 4.4b) normalized to 1,  $R_{\text{nl}}^\beta/R_{\text{nl}}^0$ , as a function of  $\cos^2(\beta^*)$ .  $\beta^*$  accounts for the tilting angle of the injector and detector  $\beta^* = \beta - \gamma$  (see Sec. 3.3). From Eq. (3.10), for the isotropic case, *i.e.*  $\zeta = 1$ ,  $R_{\text{nl}}^\beta/R_{\text{nl}}^0 = \cos^2(\beta^*)$  so  $R_{\text{nl}}^\beta/R_{\text{nl}}^0$  as a function of  $\cos^2(\beta^*)$  results in a straight line with slope equal to one. For the anisotropic case,  $R_{\text{nl}}^\beta/R_{\text{nl}}^0$  lies above the straight line ( $\zeta > 1$ ) or below it ( $\zeta < 1$ ). Both for SiO<sub>2</sub> and hBN substrates, experimental results are in excellent agreement with  $\zeta \sim 1$ , thus,  $\tau_s^\parallel = \tau_s^\perp$ . Such result has been observed to be independently of  $n$  for graphene on SiO<sub>2</sub> [13, 14]. A more recent experiment in low-mobility CVD graphene on SiO<sub>2</sub> by Ringer *et al* [18] combines the oblique and out-of-plane spin precession experiments to extract  $\zeta$ , yielding  $\zeta \sim 0.9 - 0.7$ , with  $\tau_s^\parallel$  between 1.1 ns and 0.7 ns. However, measurements as a function of  $n$  and temperature in highest quality graphene devices and a careful analysis of the F magnetization with  $B$  in plane are still necessary.

## 4.5 Oblique spin precession measurements in gr/TMDC

Figure 4.5a shows spin precession measurements for a representative set of  $\beta$  values for a gr/WS<sub>2</sub> device, with F2 as injector. A back-gate voltage  $V_g = -15$  V is applied to suppress the spin absorption in WS<sub>2</sub>. It is observed that the diffusive broadening dephases the precessional motion at  $B_d \sim 0.12$  T. For  $B > B_d$ ,  $R_{\text{nl}}$  is nearly constant with increasing  $B$ , with a magnitude  $R_{\text{nl}}^\beta \equiv R_{\text{nl}}(B > B_d)$ . At  $\beta = 90^\circ$ , the response is similar to that found in conventional spin precession measurements in graphene (as in Fig. 4.2a). However, when  $B$  is tilted from the perpendicular orientation,  $R_{\text{nl}}^\beta$  increases anomalously, and even a few degrees tilt results in  $R_{\text{nl}}^\beta$  values that are larger than  $R_{\text{nl},0}$  even at small  $B$  (see, for example, the response at  $\beta = 85.5^\circ$ ). This is in stark contrast to the case of pristine graphene. Equivalent measurements for the reference device are shown in Fig. 4.4, there  $\zeta \approx 1$  and  $R_{\text{nl},0}$  is an upper limit for  $R_{\text{nl}}$ . As a comparison, Fig. 4.5b shows measurements as those in Fig. 4.5a with the role of F1 and F2 reversed.

The magnitude of  $R_{\text{nl}}^\beta \equiv R_{\text{nl}}(B > B_d)$  normalized to  $R_{\text{nl},0}$  is shown in Fig. 4.6a as a function of  $\cos^2(\beta - \gamma)$  both for the gr/WS<sub>2</sub> and the reference device (full and open symbols, respectively). The angle  $\gamma$  is calculated from the fittings to the spin precession in the reference device, using the conventional non-local spin precession method (see Sec. 3.3.1). The data for the gr/WS<sub>2</sub> and the reference devices were extracted from Fig. 4.5a and Fig. 4.4c, respectively. Consistent with the results in Fig. 4.2,  $\zeta \approx 1$  for the reference device, while  $\zeta \gg 1$  for gr/WS<sub>2</sub>.

The spin anisotropy ratio  $\zeta$  can be obtained from the in-plane and out-of-plane spin relaxation lengths as  $\zeta = (\lambda_s^\perp/\lambda_s^\parallel)^2$ . From  $\overline{R_{\text{nl}}^\beta} \sim 1.5 \Omega$  with  $\beta$  approaching  $90^\circ$  (Fig. 4.6b), we obtain  $\lambda_s^\perp \sim 1 \mu\text{m}$ , which combined with  $\lambda_s^\parallel \sim 0.3 \mu\text{m}$ , results in  $\zeta \approx 10$ . Assuming that the diffusion constant in gr/WS<sub>2</sub> is of similar magnitude to that in graphene,  $D \sim 0.03 \text{ m}^2\text{s}^{-1}$  then  $\tau_s^\parallel \sim 3 \text{ ps}$  and  $\tau_s^\perp \sim 30 \text{ ps}$ . Using

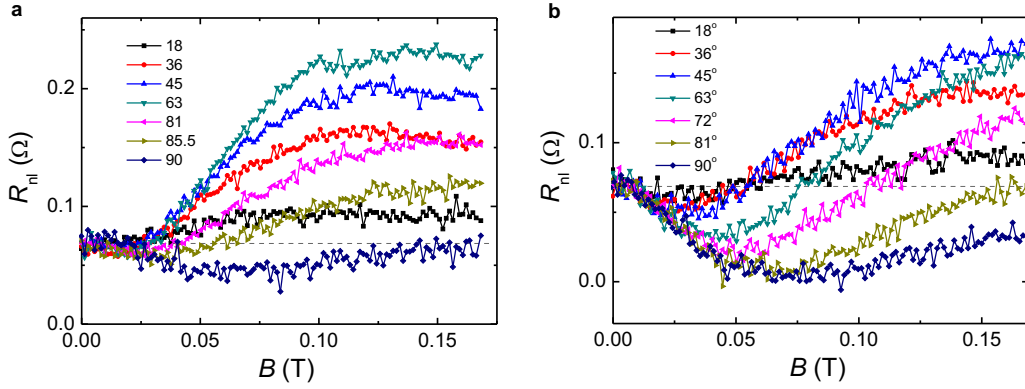


FIGURE 4.5: **Spin precession measurements under oblique magnetic fields in gr/WS<sub>2</sub>.** **a**, Representative subset of experimental spin precession curves for the indicated  $\beta$  as a function of  $B$ , when F2 is used as spin injector. The precession data are acquired after preparing a parallel magnetization configuration of F1 and F2. Dephasing of the precessing component is observed at  $B$  larger than  $\sim 0.12$  T. The horizontal dashed line is the non-local resistance at  $B = 0$ ,  $R_{\text{nl}}^0$ , which coincides with  $R_{\text{nl}}$  at  $\beta = 0^\circ$  in the parallel configuration. Similarly to Fig. 2b,  $R_{\text{nl}}$  surpasses  $R_{\text{nl}}^0$  as soon as the spins rotate out-of-plane. **b**, Representative subset of experimental spin precession curves for the indicated  $\beta$  at a function of  $B$  when F1 is used as spin injector. Because gr/WS<sub>2</sub> is close to the detector, dephasing of the precessing component is not achieved at its location and  $R_{\text{nl}}$  becomes dependent of  $B$  in the full  $B$  range.  $T = 300$  K,  $V_g = -15$  V and  $I = 2 \mu\text{A}$ .

these parameters we can directly estimate  $R_{\text{nl}}^\beta$  versus  $\cos^2(\beta - \gamma)$  (see Sec. 4.8). The results of the calculations are displayed in Fig. 4.6a (solid blue line), showing very good agreement with the experimental results, given that no adjustable parameters were used. Furthermore,  $R_{\text{nl}}^\beta$  for any given value of  $B$  can be found by solving the diffusive Bloch equation in the presence of an oblique magnetic field. We explore the solution of the Bloch equation in Sec. 4.8.

To find the origin of the anisotropy, the spin transport is studied as a function of the gate voltage  $V_g$ , which tunes the carrier density in both graphene and WS<sub>2</sub>. Figure 4.6b shows the obtained  $\overline{R_{\text{nl}}^\beta}$  versus  $\beta$  for different moderate values of  $V_g$ . Below a threshold gate voltage  $V_g^T \sim -5$  V,  $\overline{R_{\text{nl}}^\beta}$  barely varies with  $V_g$ . However an increasing signal at  $B = 0$  with lowering  $V_g$ , suggest an increasing  $\tau_s^\parallel$ . For  $V_g > V_g^T$ , a rapid reduction of  $\overline{R_{\text{nl}}^\beta}$  is observed for all values of  $\beta$ . For  $V_g > 10$  V, no spin signal can be detected when the spins are oriented in-plane; the spin signal is recovered as soon as the spin component out of plane is non zero, indicating that  $\zeta \gg 1$ . A detailed analysis of the spin anisotropy as a function of the external gate is shown in Sec. (4.7).

A strong modulation and vanishing of  $R_{\text{nl}}$  with the application of positive  $V_g$  were recently reported in gr/MoS<sub>2</sub> heterostructures [2, 4]. There, spins were oriented in-plane and the change in the spin transport properties was attributed to the gate tuning of the MoS<sub>2</sub> channel conductivity and associated modulation of the Schottky barrier at the MoS<sub>2</sub>/graphene interface [2, 4]. The inset of Fig. 4.6b shows the bias characteristics of our gr/WS<sub>2</sub> interface. The current  $I_{\text{ds}}$  is measured versus

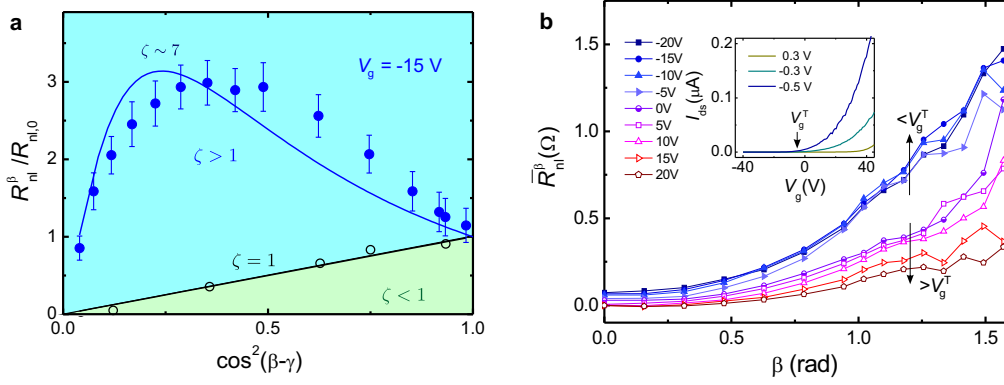


FIGURE 4.6: **Spin lifetime anisotropy ratio,  $\zeta$ .** **a**,  $R_{nl}^{\beta}$  normalized by  $R_{nl,0}$  as a function of  $\cos^2(\beta - \gamma)$ , with  $\gamma = \gamma(\beta, B)$ . The data represented by solid symbols are extracted from Fig. 4.5a at  $B = 0.16$  T. The error bars derive from the noise in Fig. 4.5a. The solid blue line represents the modeled response for an anisotropy ratio  $\zeta = 10$ . The data represented by open symbols are extracted from Fig. 4.4c and correspond to a reference device. In this case,  $\zeta \approx 1$ , as shown by the straight black line. **b**,  $\overline{R_{nl}^{\beta}}$  as a function of  $\beta$  for the indicated back-gate voltages  $V_g$ . For  $V_g < V_g^T \approx -5$  V,  $\overline{R_{nl}^{\beta}}$  is independent of  $V_g$  but decreases rapidly for  $V_g > V_g^T$ . Inset, Transfer characteristics  $I_{ds}$  versus  $V_g$  for different driving voltage  $V_{ds}$  in gr/WS<sub>2</sub>;  $V_g^T$  coincides with the back-gate voltage at which  $I_{ds}$  is observed.

$V_g$  when a voltage bias  $V_{ds}$  is applied across the gr/WS<sub>2</sub> interface. The response is very similar to that reported in Refs. [2, 4], with  $I_{ds}$  increasing sharply nearby  $V_g^T$ , suggesting that the reduction in the spin signal for  $V_g > V_g^T$  is due to a fast relaxation of spins as they enter WS<sub>2</sub>. Given that  $R_{nl}^{\beta}$  is measured at gate voltage below  $V_g^T$ , so the the carriers cannot enter WS<sub>2</sub>, confirms that the anisotropic spin relaxation must be due to proximity-induced SOC in graphene.

## 4.6 Model of the spin relaxation anisotropy in gr/TMDC

The induced Bychkov-Rashba (BR) and valley Zeeman (VZ) SOC can be seen as effective magnetic fields, which point in-plane and out-of-plane, respectively. The in-plane spin texture is always linearly dependent to the wave vector ( $\vec{k}$ ) and perpendicular to it, whereas the out-of-plane spin texture depends on the valley ( $\tau_z$ ), is maximum at  $k = 0$ , and decays to zero away from  $k = 0$  [6, 19]. In Fig. 4.7 we show such effective magnetic fields acting on a spin, in the K and K' valleys. On the one hand, the effective in-plane BR magnetic field ( $B_{eff}^{BR}$ ) induces precession to the out-of-plane spin component favoring it relaxation. Fluctuations of  $B_{eff}^{BR}$  are caused by intravalley scattering ( $\tau_p$ ) [11], see Fig. 4.7 (note that only intervalley scattering does not produce fluctuations to  $B_{eff}^{BR}$ ). Thus, the spin relaxation of the out-of-plane spins also depends on  $\tau_p$ . Since  $B_{eff}^{VZ}$  points in  $\hat{z}$ , it does not contribute to the spin relaxation of the out-of-plane spin component.

On the other hand,  $B_{eff}^{BR}$  also induces precession to the in-plane spin component that is perpendicular to  $B_{eff}^{BR}$ ; therefore, the in-plane spin relaxation will also depend

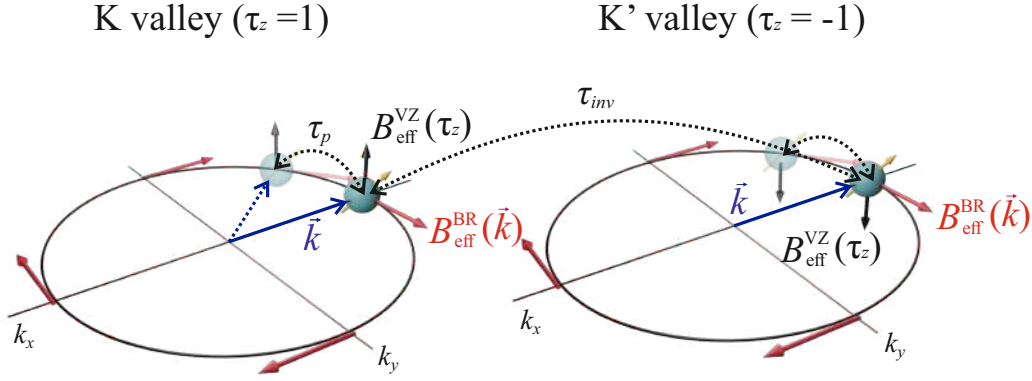


FIGURE 4.7: Picture of the spin relaxation anisotropy. A spin (yellow arrow in the blue sphere) moving inside a valley (K, K') with a wave vector  $\vec{k}$ , experiences the Bychkov-Rashba (BR) and valley Zeeman (VZ) SOC. Such SOC can be seen as effective magnetic fields  $B_{\text{eff}}^{\text{BR}}$ ,  $B_{\text{eff}}^{\text{VZ}}$ . Because the intervalley ( $\tau_{\text{inv}}$ ) and intravalley ( $\tau_p$ ) scattering, the spins feel fluctuating magnetic fields that are responsible for the spin relaxation (see main text).

on  $\tau_p$ . Additionally,  $B_{\text{eff}}^{\text{VZ}}$  will induce a rotation to the in-plane spins.  $B_{\text{eff}}^{\text{VZ}}$  direction switches between valleys (see Fig. 4.7). So, the intervalley scattering generates a fluctuating upwards/downwards  $B_{\text{eff}}^{\text{VZ}}$ . This situation recalls the spin resonance technique, where a relatively small oscillatory magnetic field flips a spin. In this technique, the spin flip process is efficient when the magnetic field frequency is in resonance with the spin precession frequency. Of course, the intervalley scattering produces a rather out-tone fluctuating  $B_{\text{eff}}^{\text{VZ}}$ , due to the intrinsic diffusive nature of the transport in our systems. However, as demonstrated by Cummings et al. [11], impurities of 0.1% (weak intervalley scattering) are enough to relax the in-plane spins effectively.

Spin dynamics modelling and numerical simulations have been used to compute  $\zeta$  in graphene interfaced with several TMDCs [11]. In the case of strong intervalley scattering,  $\zeta$  in gr/WS<sub>2</sub> was calculated to be between 20 to 200, with  $\tau_s^{\parallel} \sim 1$  ps and  $\tau_s^{\perp} \sim 20$  to 200 ps, while in the absence of intervalley scattering,  $\zeta$  decreases all the way down to 1/2, as expected with Rashba SOC, with  $\tau_s^{\parallel} \approx 2\tau_s^{\perp} \sim 10$  ps near the charge neutrality point. The large  $\zeta$  is therefore not only a fingerprint of SOC proximity effects induced by WS<sub>2</sub> but also indicates that intervalley scattering in our devices is the main spin relaxation mechanism in our gr/WS<sub>2</sub> heterostructures for the in-plane spins. The somewhat smaller  $\zeta$  found in the experiments can originate from a number of reasons, the most straightforward being that the intervalley scattering is stronger or the SOC weaker in our devices than the assumed in the model [11]. Moreover, the adopted parameters can also be sensitive to the number of layers in the TMDC or the specific supercells in the calculations [5, 6]. The model is developed for monolayer TMDCs; nevertheless, since the proximity effects are due to the TMDC layer that is adjacent to graphene, no dependence on the number of layers is expected, as long as the transport in graphene occurs in states within the

TMDC bandgap. There are other possibilities to explain the differences from the calculations, including the characteristics of the interface with graphene, and strain or twisting between the layers, which are currently not controlled in the experiments.

Because the obtained  $\lambda_s^\perp$  is similar to the width  $w$  of gr/WS<sub>2</sub>, our approach could become insensitive for large values of  $\zeta$ . However, calculations shown in Sec. 4.8 show that this limit has not been reached, in particular when  $B$  is tilted slightly from the perpendicular orientation. Another aspect to be considered is the relevance of intravalley scattering and how it compares with intervalley scattering. Our measurements are all carried out at room temperature, phonon scattering can increase the weight of intravalley scattering and effectively reduce the anisotropy.

The spin lifetime anisotropy therefore provides insight into the physics underpinning spin and valley dynamics. Our results show that the large SOC and spin-valley coupling in a semiconducting transition metal dichalcogenide, can be directly imprinted in graphene by proximity-induced effects. In addition, they open the door for novel approaches to control spin and valley information. The out-of-plane spin component propagates through graphene-TMDC much more efficiently than the in-plane component. Thus, graphene-TMDC acts as a filter with a transmission that depends on the effective orientation of the spins that reach it and that can vary over orders of magnitude. Such a filter represents a new tool in spintronics to detect small variations in the orientation of spins arriving at it. Interfacing graphene with TMDCs can also be utilized for direct electric-field tuning of the propagation of spins and for implementing spin-valleytronic and optospintronic [6, 20, 21] devices in which charge, spin and valley degrees of freedom can be simultaneously used [22], as previously proposed for TMDCs [23]. This represent a milestone for next-generation graphene-based electronics and computing.

## 4.7 Gate control of the spin relaxation

An evident question to answer is whether such anisotropic spin relaxation can be tuned via electrostatic gating. So we studied the gate dependence of the spin relaxation anisotropy in gr/WS<sub>2</sub> heterostructures in different devices, in which we were able to apply higher back-gate voltages. Figure 4.8a shows that indeed  $\zeta$  can be widely modulated. Data modeling in Fig. 4.8b shows that the change in  $\zeta$  is four fold, increasing monotonously between  $V_g$  equal to -30 and 30 V. The majority of the change occurs for negative  $V_g$ , when conduction between graphene and the TMDC is strongly suppressed and no spin absorption in the latter is expected (see Fig. 4.6). Such result demonstrates an unprecedented control of the spin dynamics in the gr/WS<sub>2</sub> devices at room temperature.

To elucidate the origin of the change in  $\zeta$ , it is necessary to investigate the back-gate dependence of  $\tau_s^\parallel$  and  $\tau_s^\perp$ . Figures 4.8c and 4.8d compare  $R_{nl}$  in the pristine graphene (reference) and the gr/WS<sub>2</sub> devices, respectively. As it is typical in pristine graphene,  $R_{nl}$  reaches a minimum at its charge neutrality point (CNP),  $V_g = V_{CNP} =$



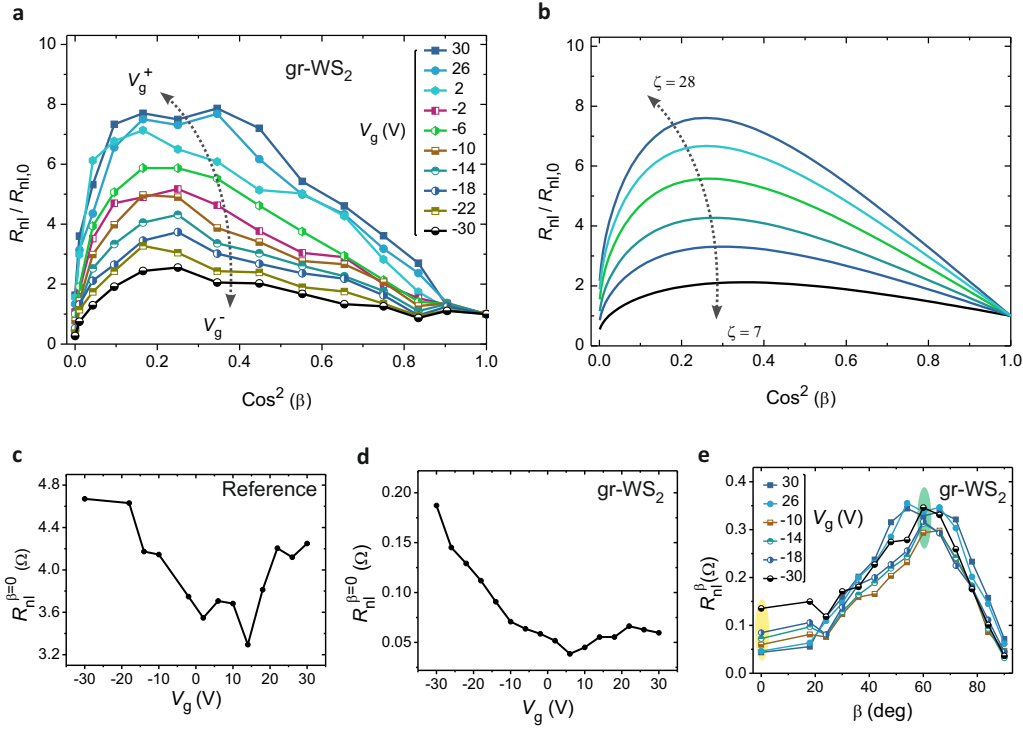


**FIGURE 4.8: Electrical control of the anisotropy spin relaxation using the oblique spin precession protocol.** **a.** Normalized  $R_{nl}(B = 140\text{mT})$  at its value at  $B = 0$ ,  $R_{nl,0}$ , vs  $\cos^2(\beta)$ , where  $\beta$  is the angle of the oblique  $B$ . The change in the curve shape with  $V_g$  is a clear sign of a variation in the anisotropy ratio  $\zeta$ .  $\zeta$  being larger when the curve is more pronounced at positive  $V_g^+$ . **b.** Set of close calculations to the experimental data (see Sec. 4.8 for details), showing a high modulation of  $\zeta$ . The used parameters are  $\zeta = 28, 26, 22, 18, 13, 7$  with  $\tau_s^{\parallel} = 5.6, 6, 6.8, 7.6, 8.6, 9.4$  ps. Taking  $D = 0.008 \text{ m}^2\text{s}^{-1}$  from the fitting to experimental data. **c** Gate dependence of the spin signal  $\Delta R_{nl}$  in the reference device.  $\Delta R_{nl}$  is minimum close to the charge neutrality point  $V_{\text{CNP}} = 10$  V and increases away from it. This suggest that  $\tau_s^{\parallel}$  in pristine graphene is minimum close to CNP and larger away from CNP. **d.**  $\Delta R_{nl}$  in the graphene-WS<sub>2</sub> device. Similar to the reference, the signal is minimum near CNP. But, conversely,  $\Delta R_{nl}$  scarcely changes for  $V_g > 10$  V indicating that  $\tau_s^{\parallel}$  remains constant when  $V_g > V_{\text{CNP}}$ . **e.**  $\Delta R_{nl}(B = 140\text{mT})$  angular dependence for a set of  $V_g$ . Significant signal change at  $\beta = 0^\circ$  as function of  $V_g$  is present (yellow mark).  $\Delta R_{nl}$  peaks near  $\beta = 60^\circ$  where spins have acquired a large out-of-plane component (green mark). Surprising  $\Delta R_{nl}$  at  $\beta \sim 60^\circ$  for  $V_g = -30$  V and  $V_g = 30$  V are very close, suggesting no change in  $\tau_s^{\perp}$  for those gates, but a clear variation in  $\tau_s^{\parallel}$  (related with the change in  $\Delta R_{nl}$  at  $\beta = 0^\circ$ ). Data acquired at RT.

10 V (Fig. 4.8c), which correlates with a minimum  $\tau_s$ . In contrast, in gr/WS<sub>2</sub>  $R_{nl}$  decreases as  $V_g$  approaches  $V_{\text{CNP}}$ , but then remains small for larger  $V_g$  (Fig. 4.8d). Because here the magnitude of  $R_{nl}$  is largely determined by  $\tau_s^{\parallel}$ , the results in Fig. 4.8c suggest a significant drop in  $\tau_s^{\parallel}$  between  $V_g = -30$  and 5 V, which is not fully recovered at larger positive  $V_g$ .

The behavior of  $R_{nl}$  in Fig. 4.8d has been ascribed to spin absorption in the TMDC, when the TMDC becomes conducting [2, 4]. However, when  $\beta$  is swept from  $0^\circ$  to  $90^\circ$  a more complex scenario is revealed. Figure 4.8e presents  $R_{nl}^{\beta}(B = 0.14 \text{ T})$



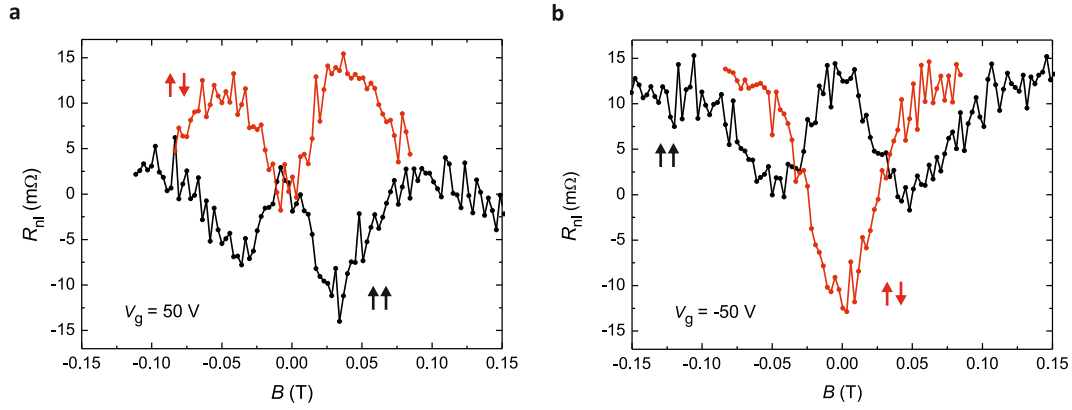


FIGURE 4.9: **Electrical control of the anisotropy spin relaxation using the out of plane spin precession protocol.** The measurements are carried out in the parallel (black) and antiparallel (red) configuration of F1 and F2. The back-gate voltage is set to  $V_g = 50$  V in **a** and  $V_g = -50$  V in **b**. The spin precession response is remarkable different in **a** and **b**. One hand, while at  $B = 0$ ,  $|R_{nl}|$  is minimum in **a**, is maximum in **b**. But while at  $B \sim 50$  mT,  $|R_{nl}|$  is maximum in **a**, is minimum in **b**.  $|R_{nl}|$  in **b** tends its initial value at  $B = 0$  due to the magnetization rotation of F, a typical behavior expected when  $\zeta \sim 1$ . Contrary, the curve shape in **a** is a clear fingerprint of  $\zeta > 1$ . Data acquired at room temperature.

vs  $\beta$  for a set of  $V_g$ .  $R_{nl}$  is observed to be maximum at  $\beta \sim 60^\circ$  for all  $V_g$ , with its value changing weakly from  $V_g = 30$  V (full blue squares) and  $V_g = -30$  V (half full black circles). On the other hand, the relative change of  $R_{nl}$  at  $\beta \sim 0^\circ$  is much larger. These observations suggest that the increase of  $\zeta$  with  $V_g$  is largely driven by a decrease in  $\tau_s^{\parallel}$ .

To further confirm the modulation of  $\zeta$  with  $V_g$ , we carried out spin precession experiments with an in-plane  $B$  using another gr/WS<sub>2</sub> device (Fig. 4.9). The measurements are acquired in the parallel (black) and antiparallel (red) configuration of the electrodes magnetizations. For  $\zeta \gg 1$ ,  $R_{nl}$  reaches its maximum magnitude when, due to precession, the spin point roughly perpendicular to the plane at the position of the TMDC. This behavior is observed in Fig. 4.9a, for  $V_g = 50$  V. The maximum value of  $|R_{nl}|$  is achieved at  $B \sim 0.05$  T. However, the spin precession response for large negative  $V_g$  is remarkably different. Figure 4.9b shows that, for  $V_g = -50$  V, the maximum of  $|R_{nl}|$  is observed at  $B = 0$ , an indication that the anisotropy, if any, is much weaker than for positive  $V_g$ . Indeed, for the parallel magnetization configuration,  $|R_{nl}|$  decreases until reaching a minimum at  $B \sim 0.05$  T. As  $|B|$  increases,  $|R_{nl}|$  increases again to its initial value at  $B = 0$ , when the magnetizations of the electrodes rotate and become parallel to  $B$ . Such a response is commonly observed in pristine graphene, for which  $\zeta \approx 1$ . Furthermore, the absolute magnitudes of  $|R_{nl}|$  at  $B \sim 0.05$  T are similar for  $V_g = \pm 50$  V. However,  $|R_{nl}|$  at  $B = 0$  is much larger for  $V_g = -50$  V than for  $V_g = 50$  V, where barely any signal is actually observed. This further supports the conclusion that the change in  $\zeta$  is largely ascribed to  $\tau_s^{\parallel}$ .

The control of the anisotropic spin relaxation has been reported experimentally in BLG, where it was proposed that  $\tau_s^{\perp}$  ( $\tau_s^{\parallel}$ ) increases with the out-of-plane  $\langle s_{\perp} \rangle$

(in-plane  $\langle s_{\parallel} \rangle$ ) spin polarization [24]. The same arguments could be applied to gr-TMDC systems in which  $\langle s_{\perp} \rangle$  spin texture is maximum when the wave vector  $k = 0$  and decays moving away from  $K$  and  $K'$  while  $\langle s_{\parallel} \rangle$  increases [5, 6, 19]. However, these expectations are at odds with results using realistic modelling in gr-TMDCs [11]. Theoretical modelling derived from first principles indicates that the anisotropy is mediated by the spin-valley locking, which is imprinted in graphene by the TMDC [11, 25]. Within this model,  $\tau_s^{\perp}$  follows the Dyakonov-Perel mechanism,  $(\tau_s^{\perp})^{-1} = [2(ak\Delta_{PIA} \pm \lambda_R)/\hbar]^2 \tau_p$ , with  $\tau_p$  the momentum relaxation time,  $k$  the wavenumber magnitude, and  $\lambda_R$  the strength of the Rashba SOC;  $\Delta_{PIA}$  is determined by the difference between the PIA SOC parameters in the two graphene sublattices [5]; the  $+$  and  $-$  signs are for the conduction and valence bands, respectively. On the other hand,  $\tau_s^{\parallel}$  includes contributions from both the intervalley scattering time  $\tau_{iv}$  and  $\tau_p$  as  $(\tau_s^{\parallel})^{-1} = (2\lambda_{vZ}/\hbar)^2 \tau_{iv} + (\tau_s^{\perp})^{-1}/2$ , with  $\lambda_{vZ}$  the valley-Zeeman SOC strength.

In materials with large PIA terms, an electron-hole asymmetry in  $\tau_s^{\perp}$  is expected. For gr-WS<sub>2</sub> ( $\Delta_{PIA} = 1.4$  meV,  $\lambda_R = 0.36$  meV),  $\tau_s^{\perp}$  (and  $\zeta$ ) is predicted to increase linearly on the hole side, away from the CNP, while  $\tau_s^{\parallel}$  stays roughly constant. This behaviour is opposite to our experimental observations. If the PIA term is ignored, then  $\zeta \approx (\lambda_{vZ}/\lambda_R)^2 (\tau_{iv}/\tau_p) + 1/2$ . Therefore, the decrease in  $\zeta$ , away from the CNP for hole conduction, could be ascribed to a suppression of  $\lambda_{vZ}$  and/or  $\tau_{iv}$  or to an enhancement of  $\tau_p$  and/or  $\lambda_R$  (or a combination of them).

Using an interband tunnelling picture to obtain the SOC, it has been proposed that  $\lambda_{vZ}$  decreases when moving away from the bottom of the TMDC conduction band [26]. Here the relevant energy scale (to observe changes in  $\lambda_{vZ}$ ) is the spin splitting in the conduction band of WS<sub>2</sub>, which is relatively small (25 meV for a monolayer, as opposed to 450 meV in the valence band) and well within our measurements. However, as shown in Ref. [11], which are supported by DFT calculations of the electronic structure [5],  $\zeta$  remains above 10 even for  $|n|$  larger than those in our experiments.

Alternatively, the effective SOC, and more specifically  $\lambda_R$ , could be modulated by  $V_g$ . Indeed, it has been shown that  $\lambda_R$  in WSe<sub>2</sub> exhibits a monotonic decrease as the transverse electric field increases [5]. A similar behaviour could be expected in WS<sub>2</sub> but, considering that a negative  $V_g$  results in a positive electric-field (according to the sign convention used in Ref. [5]), the experimental trend in Fig. 3 is opposite to that expected. Note that the PIA and valley-Zeeman SOC can also change with  $V_g$  [5], therefore adding another degree of complexity to the interpretation of  $\zeta$  vs.  $V_g$ .

Scattering and in-gap impurity or vacancy states can also play a role in modifying  $\zeta$ . A study on defected graphene suggests that, in multivalley systems,  $\tau_{iv}$  can be strongly modulated when the charge state of the defects are electrically tuned [27]. Moreover, it has been recently shown that sulphur vacancies in WS<sub>2</sub> correlate with in-gap states with very large SOC that are located below the WS<sub>2</sub> conduction

band [28]. The enhanced SOC due to vacancies could further account for the unexpectedly large spin-to-charge interconversion observed in gr-WS<sub>2</sub>, and the large SOC parameters extracted from it [1, 29]. Current understanding, which does not consider such vacancies, suggests that the spin Hall effect should be suppressed by intervalley scattering, rendering it incompatible with the observation of anisotropic spin relaxation [29] (see Chap. 5).

## 4.8 Modeling the spin precession in an anisotropic medium

As we mentioned in Chap. 3 (Sec. 3.3), in the case of a non-uniform spin channel, Eqs. (3.8) and (3.10) are no longer valid to obtain the spin related parameters and  $\zeta$ . This is particularly relevant in our heterostructures comprising graphene with the TMDC covering partially the spin channel (see Fig. 4.1c). Here, the diffusive process is described by the Bloch equations

$$D_s \nabla^2 \vec{\mu}_s - \gamma_c \vec{\mu}_s \times \vec{B} - \overline{\tau_s^{-1}} \cdot \vec{\mu}_s = 0, \quad (4.1)$$

where  $\vec{\mu}_s = (\mu_s^x, \mu_s^y, \mu_s^z)$ ,  $D_s$  is the spin diffusion constant, and

$$\overline{\tau_s^{-1}} = \begin{pmatrix} \tau_x^{-1} & 0 & 0 \\ 0 & \tau_y^{-1} & 0 \\ 0 & 0 & \tau_z^{-1} \end{pmatrix} \quad (4.2)$$

a diagonal matrix with  $\tau_x = \tau_y \equiv \tau_s^{\parallel}$  and  $\tau_z \equiv \tau_s^{\perp}$ .

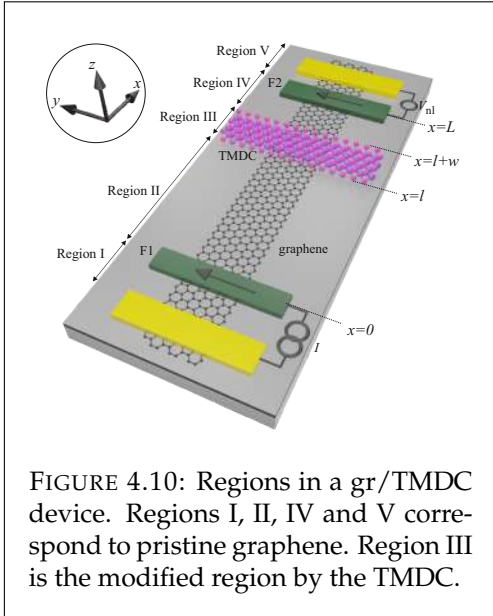


FIGURE 4.10: Regions in a gr/TMDC device. Regions I, II, IV and V correspond to pristine graphene. Region III is the modified region by the TMDC.

with boundary conditions:

$$\begin{aligned} x = 0 : \vec{\mu}_{sI} &= \vec{\mu}_{sII}; \vec{I}_{sI} - \vec{I}_{sII} = \vec{I}_{s0} + \vec{I}_{\text{abs.}} \\ x = l : \vec{\mu}_{sII} &= \vec{\mu}_{sIII}; \vec{I}_{sII} = \vec{I}_{sIII} \\ x = l + w : \vec{\mu}_{sIII} &= \vec{\mu}_{sIV}; \vec{I}_{sIII} = \vec{I}_{sIV} \\ x = L : \vec{\mu}_{sIV} &= \vec{\mu}_{sV}; \vec{I}_{sIV} = \vec{I}_{sV} + \vec{I}_{\text{abs.}} \\ x \rightarrow \pm\infty : \vec{\mu}_s &= 0, \end{aligned} \quad (4.3)$$

where I, II, IV and V denote the pristine graphene and III the heterostructure region (see Fig. 4.10).  $I_s$  is the spin current (see Sec. 3.1 in Chap. 3).  $I_{\text{abs}}$  accounts for the spin current absorbed by the F contacts,  $I_{\text{abs}} = \mu_s / \tilde{R}_F$ .  $\tilde{R}_F$  is the effective contact resistance  $\tilde{R}_F = R_c / (1 - P^2) + R_s / (1 - P^2)$ .  $R_s$  is the

F spin resistance  $R_s = \lambda_F \rho_F / A_F$  and  $R_c$  is the contact resistance.

Spins are injected in  $y$  direction  $\vec{I}_{s0} = (0, I_{s0}, 0)$ , where  $I_{s0}$  is a constant that depends on the injected electrical current and the contact polarization.

For the oblique magnetic field configuration  $\vec{B} = B(0, \cos \beta, \sin \beta)$ . For the in-plane magnetic field configuration  $\vec{B} = B(1, 0, 0)$ . In the former case, the solution at large fields can be approximated by that obtained with non-precessing spins along  $B$  [13] (see next subsec.). In the latter case, the problem reduces to a two dimensional problem because spin precession occurs in the  $x - y$  plane.

#### 4.8.1 Non-precessing spin component

In the limit of no spin precession, with the aggregate spin approximately in the direction of the magnetic field (defined by  $\beta$ ), the relaxation of the spin component along  $B$  proceeds with an effective lifetime  $\tau_s^\beta$  [13]. In this regime, the response of our devices (Figs. 4.5a and 4.6a) can be estimated by considering a distinct effective spin relaxation length in each regions. In the graphene regions we assume isotropic spin relaxation with  $\lambda_{s,gr}$  independent of  $\beta$ , while in the gr/WS<sub>2</sub> region we take  $\lambda_s^\beta \propto \sqrt{\tau_s^\beta}$ . We first obtain the response that would be observed if the spin signal was injected along  $B$ , which is represented by  $\overline{R_{nl}^\beta}$ . Thus  $\overline{R_{nl}^\beta}$  is found from the solution of the spin diffusion equations, which take the form  $A_r e^{z/\lambda_{s,r}} + B_r e^{-z/\lambda_{s,r}}$  with  $A_r, B_r$  determined by the boundary conditions and  $\lambda_{s,r} = \lambda_s^\beta, \lambda_{s,gr}$ :

$$\overline{R_{nl}^\beta} \propto \frac{2\lambda_{s,gr}^2 \lambda_s^\beta e^{w\left(\frac{1}{\lambda_{s,gr}} + \frac{1}{\lambda_s^\beta}\right)}}{(\lambda_{s,gr} + \lambda_s^\beta)^2 e^{\frac{2w}{\lambda_s^\beta}} - (\lambda_{s,gr} - \lambda_s^\beta)^2} e^{-\frac{L}{\lambda_{s,gr}}}. \quad (4.4)$$

To find  $\lambda_s^\beta$ , Eq. (4.4) is solved by taking  $\lambda_{s,gr}$  and  $\overline{R_{nl}^\beta}$  from the experiments. To find  $R_{nl}^\beta = \overline{R_{nl}^\beta} \cos^2(\beta - \gamma)$ ,  $\gamma$  is estimated as  $\gamma = \arcsin\left[\frac{\sin(\beta)}{\frac{B_s}{B} + \cos(\beta)}\right]$ , where  $B_s$  is the saturation field as extracted from spin precession measurements.

Figure 4.11 and the continuous line in Fig. 4.6a show the calculated  $R_{nl}^\beta$  normalized to the value at  $\beta = 0$ , which is equivalent to the value at  $B = 0$ . The calculations are made for the specified  $\zeta$  after assuming  $\lambda_s^{\beta-1} \approx \sqrt{\frac{1}{\lambda_s^\parallel} [\cos^2(\beta) + \frac{1}{\zeta} \sin^2(\beta)]}$  [13].  $R_{nl}^\beta$  increases with  $\zeta$  as long as  $\lambda_s^\perp = \lambda_s^\parallel \sqrt{\zeta}$  is not much larger than the gr/WS<sub>2</sub> width,  $w$ . That is, when  $\zeta \gg (w/\lambda_s^\parallel)^2$ ,  $R_{nl}^\beta$  becomes independent of  $\zeta$  because the relaxation of the spins when oriented out of plane becomes undetectable. The saturation occurs last for  $\beta \sim 90^\circ$  whereby the spins are barely tilted out-of-plane.

#### 4.8.2 General solution: Out-of-plane spin precession

When the magnetic field is applied in-plane along  $x$ ,  $\vec{B} = (B, 0, 0)$ , Eq. (4.1) can be written as,

$$D \frac{d^2}{dx^2} \begin{pmatrix} \mu_{sx} \\ \mu_{sy} \\ \mu_{sz} \end{pmatrix} - \begin{pmatrix} \tau_s^{\parallel-1} \\ \tau_s^{\parallel-1} \\ \tau_s^{\perp-1} \end{pmatrix} \begin{pmatrix} \mu_{sx} \\ \mu_{sy} \\ \mu_{sz} \end{pmatrix} + \omega \begin{pmatrix} 0 \\ \mu_{sz} \\ -\mu_{sy} \end{pmatrix} = 0. \quad (4.5)$$

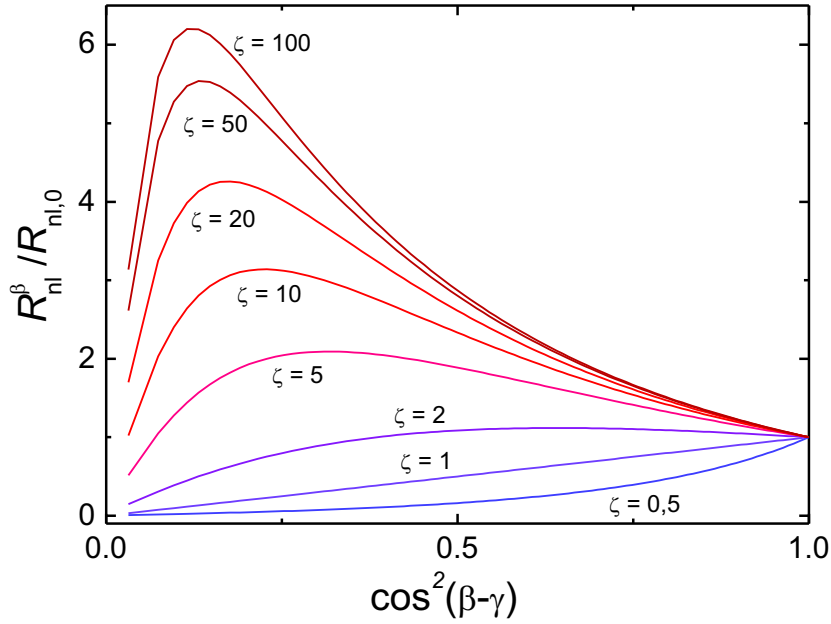


FIGURE 4.11: **Modeling of the anisotropy ratio  $\zeta$ .** Non precessing spin component  $R_{nl}^\beta = \overline{R_{nl}^\beta} \cos^2(\beta - \gamma)$  as a function of  $\cos^2(\beta - \gamma)$ ; here  $\lambda_{s,gr} = 3.5 \mu\text{m}$ ,  $\lambda_s = 0.29 \mu\text{m}$ , and  $w = 1 \mu\text{m}$ .

where  $\omega = \gamma_c B$ . The solution of Eq. (4.5) for z spin component is

$$\mu_{sz} = \eta \exp(\pm k_1 x), \quad k_1 = 1/\sqrt{D\tau_s^\perp}, \quad (4.6)$$

where  $\eta$  is a constant.

Assuming that  $\mu_{sy}$  and  $\mu_{sz}$  are proportional to  $\exp(-k_2 x)$ , Eq. (4.5) can be expressed as,

$$\begin{bmatrix} k_2^2 D - \tau_s^{\parallel -1} & \omega \\ -\omega & k_2^2 D - \tau_s^{\perp -1} \end{bmatrix} \begin{bmatrix} \mu_{sy,0} \\ \mu_{sz,0} \end{bmatrix} = \begin{bmatrix} 0 \\ 0 \end{bmatrix}, \quad (4.7)$$

where,  $\mu_{sy,0}$ ,  $\mu_{sz,0}$  are constants.

When  $\tau_s^\parallel < \tau_s^\perp$ , the following eigenvectors and eigenvalues are obtained,

$$\begin{aligned} \vec{v}_+ &= \begin{bmatrix} 1 \\ f_+ \end{bmatrix}, \quad \text{for } k_2^+ = \pm \sqrt{\frac{1}{2D} \left( \frac{1}{\tau_s^\parallel + \tau_s^\perp} + \sqrt{(\tau_s^{\parallel -1} - \tau_s^{\perp -1})^2 - 4\omega^2} \right)}, \\ \vec{v}_- &= \begin{bmatrix} f_- \\ 1 \end{bmatrix}, \quad \text{for } k_2^- = \pm \sqrt{\frac{1}{2D} \left( \frac{1}{\tau_s^\parallel + \tau_s^\perp} - \sqrt{(\tau_s^{\parallel -1} - \tau_s^{\perp -1})^2 - 4\omega^2} \right)}, \end{aligned} \quad (4.8)$$

with

$$f_\pm = \frac{\pm 2\omega}{\pm \tau_s^{\parallel -1} \mp \tau_s^{\perp -1} \pm \sqrt{(\tau_s^{\parallel -1} - \tau_s^{\perp -1})^2 - 4\omega^2}} \quad (4.9)$$

The solution of Eq. (4.5) is expressed as

$$(\mu_{s,y}, \mu_{s,z}) = c_1 \vec{v}_+ \exp(k_2^+ x) + c_2 \vec{v}_- \exp(k_2^- x) + c_3 \vec{v}_+ \exp(-k_2^+ x) + c_4 \vec{v}_- \exp(-k_2^- x). \quad (4.10)$$

where  $c_j, j = 1, 2, 3, 4$ , are determined with the boundary conditions.

The experimental spin lifetimes and the anisotropy ratio  $\zeta$  can be obtained from the spin precession measurements in the gr/WS<sub>2</sub> device. Here, the non-local resistance is given by

$$R_{\text{nl}} = \frac{P \mu_{s,y}^{\text{IV}}(L)}{e I}, \quad (4.11)$$

where  $\mu_{s,y}^{\text{IV}}$  is the spin density in region IV. Because in these experiments  $B$  is applied along  $x$ ,  $\mu_{s,y}^{\text{IV}}$  is given by Eq. (4.10) and can be expressed as

$$\mu_{s,y}^{\text{IV}} = \frac{e R_{\square} P I}{l_{\text{gr}}} h(\tau_s^{\parallel}, \zeta), \quad (4.12)$$

where  $l_{\text{gr}}$  and  $R_{\square}$  are the graphene width and its square resistance.  $h(\tau_s^{\parallel}, \zeta)$  is a function that captures the spin dynamics, taking as inputs  $\tau_s, D$ , which are known for the reference device. Thus,  $R_{\text{nl}}$  is expressed as

$$R_{\text{nl}} = \frac{P^2 R_{\square}}{l_{\text{gr}}} h(\tau_s^{\parallel}, \zeta). \quad (4.13)$$

Figure 4.12a shows the spin precession measurements within the out-of-plane spin precession protocol in gr/WS<sub>2</sub>. Figure 4.12b shows the fitting (solid line) to the experimental data (open squares) using Eq. (4.13). The sheet resistance  $R_{\square} = 1.3 \text{ k}\Omega$  is obtained from the back-gate measurements, using  $l_{\text{gr}} = 0.8 \text{ }\mu\text{m}$  and  $L = 5.3 \text{ }\mu\text{m}$ . The TMDC width is  $w = 0.6 \text{ }\mu\text{m}$ . The spin relaxation time and diffusion in graphene and the polarization of the electrodes can be obtained using the reference device,  $\tau_s = 0.51 \text{ ns}$ ,  $D = 0.03 \text{ m}^2/\text{s}$ ,  $P = 0.08$ . From the fitting  $\tau_s^{\parallel} = 5.5 \text{ ps}$  and  $\zeta = 12$ .

Figure 4.12c shows the calculated  $R_{\text{nl}}$  for different  $\zeta$  with  $\tau_s^{\parallel} = 5 \text{ ps}$  constant for all the curves. Here,  $P = 0.08$ ,  $L = 6 \text{ }\mu\text{m}$ ,  $w = 0.6 \text{ }\mu\text{m}$ ,  $D = 0.012 \text{ m}^2/\text{s}$ .  $\tau_{s,\text{gr}} = 0.26 \text{ ns}$ . The valleys in Fig. 4.12c are more pronounced as  $\zeta$  increases because the out-of-plane spins can pass the gr/TMDC region more efficiently (also discussed in Chap. 3, Sec. 3.3). Figure 4.12d shows the response of the calculated signal to the position of the TMDC respect to the injector,  $l$  (see inset in Fig. 4.12d). We use the same parameters in Fig. 4.12c with  $\zeta = 12$  for all the curves. Since the TMDC is narrow  $w = 0.6 \text{ }\mu\text{m}$ , the maximum response is achieved when the TMDC is close to half the channel length  $L$ . Here the spins have enough distance to achieve a  $90^\circ$  rotation and enter to the gr/TMDC region, and then, rotate again  $90^\circ$  to be detected.

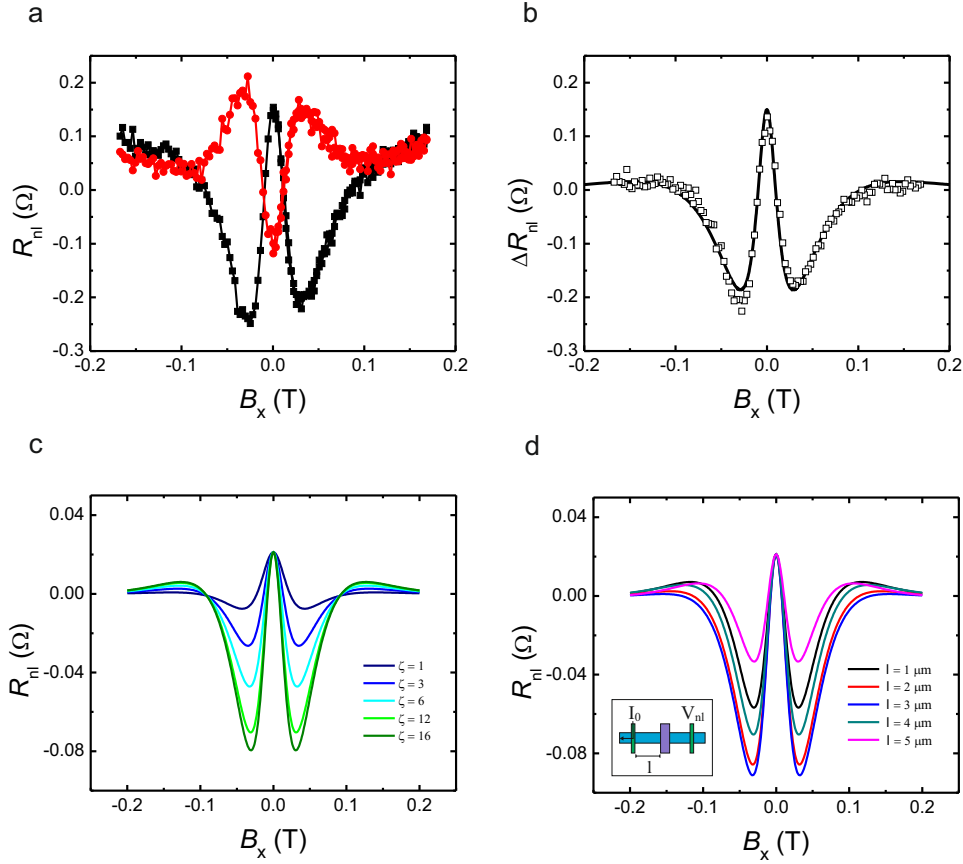


FIGURE 4.12: **Anisotropy ratio  $\zeta$ , out-of-plane spin precession.** **a.** Out-of-plane spin precession measurements in gr/WS<sub>2</sub> for the parallel (black) and antiparallel (red) configuration of the electrodes. **b.** Fitting to the spin signal  $\Delta R_{nl}$  obtained from **a** (open squares); here  $P = 0.08$ ,  $\tau_{s,gr} = 0.5$  ns,  $D = 0.015$  m<sup>2</sup>s<sup>-1</sup>, and the from the fitting  $\tau_s^{\parallel} = 5.5$  ps and  $\zeta = 12$ . **c.** Calculated signal response for different anisotropy ratios  $\zeta$  keeping constant  $\tau_s^{\parallel} = 5$  ps. The used parameters are:  $P = 0.08$ ,  $L = 6$   $\mu$ m,  $w = 0.6$   $\mu$ m,  $D = 0.012$  m<sup>2</sup>s<sup>-1</sup>.  $\tau_{s,gr} = 0.26$  ns. **d.** Calculated  $R_{nl}$  varying the position,  $l$ , of the TMDC (see inset). The used parameters are the ones for **c** with  $\zeta = 12$ .

### 4.8.3 General solution: Oblique spin precession

For oblique magnetic fields,  $\vec{B} = (0, B_y, B_x)$ , Eq. (4.5) can be written as

$$D \frac{d^2}{dx^2} \begin{pmatrix} \mu_{sx} \\ \mu_{sy} \\ \mu_{sz} \end{pmatrix} + \gamma_c \begin{pmatrix} \mu_{sy} B_z - \mu_{sz} B_y \\ -\mu_{sx} B_z \\ \mu_{sx} B_y \end{pmatrix} - \begin{pmatrix} \tau_s^{\parallel -1} \\ \tau_s^{\parallel -1} \\ \tau_s^{\perp -1} \end{pmatrix} \begin{pmatrix} \mu_{sx} \\ \mu_{sy} \\ \mu_{sz} \end{pmatrix} = 0. \quad (4.14)$$

Equation (4.14) can be expressed as,

$$D \begin{bmatrix} \mu_{sx}'' \\ \mu_{sy}'' \\ \mu_{sz}'' \end{bmatrix} - \begin{bmatrix} 1/\tau_s^{\parallel} & -\gamma_c B_z & \gamma_c B_y \\ \gamma_c B_z & 1/\tau_s^{\parallel} & 0 \\ -\gamma_c B_y & 0 & 1/\tau_s^{\perp} \end{bmatrix} \begin{bmatrix} \mu_{sx} \\ \mu_{sy} \\ \mu_{sz} \end{bmatrix} = \begin{bmatrix} 0 \\ 0 \\ 0 \end{bmatrix}, \quad (4.15)$$

where  $\mu_{s_i}'' = d^2\mu_{s_i}/dx^2$  with  $i = x, y, z$ .  $B_z = B \sin(\beta)$  and  $B_y = B \cos(\beta)$  are the out-of-plane and in-plane magnetic field components respectively. Equation (4.15) has the form  $D\vec{\mu}_s'' = A\vec{\mu}_s$ , with  $A$  being

$$A = \begin{bmatrix} 1/\tau_s^\parallel & -\gamma_c B_z & \gamma_c B_y \\ \gamma_c B_z & 1/\tau_s^\parallel & 0 \\ -\gamma_c B_y & 0 & 1/\tau_s^\perp \end{bmatrix}. \quad (4.16)$$

Assuming the solution of equation (4.15) has the form  $\vec{\mu}_s = e^{kx}\vec{v}$ , where  $k$  and  $\vec{v}$  are constants and vectors to determine, equation (4.15) becomes

$$(A - \lambda I)\vec{v} = 0, \quad (4.17)$$

where  $\lambda = Dk^2$  and  $I$  is the identity  $3 \times 3$  matrix. For each root of the characteristic polynomial of Eq. (4.17) there is a linearly independent solution of the form  $\vec{\mu}_s = e^{kx}\vec{v}$ . The general solution is a linear combination of each solution, thus,

$$\vec{\mu}_s = \sum_{n=1}^3 \left( c_n^+ e^{k_n^+ x} + c_n^- e^{k_n^- x} \right) \vec{v}_n. \quad (4.18)$$

Where  $k_n^\pm = \pm\sqrt{\lambda_n/D}$ .  $\lambda_n$  and  $\vec{v}_n$  are the eigenvalues and eigenvectors of  $A$ . The constants  $c_n^\pm$  are determined with the initial and boundary conditions of the system.

The device geometry is shown in Fig. 4.10. There are  $V$  distinct regions (I to V) with  $\tau_s^\perp = \tau_s^\parallel = \tau_s$  in I, II, IV, V, and  $\tau_s^\perp > \tau_s^\parallel$  in III. The boundary conditions are given by Eq (4.3). Briefly those conditions are: the continuity of  $\vec{\mu}_s$  and the spin current density  $\vec{i}_s \equiv -1/(eR_\square)d\vec{\mu}_s/dx$  everywhere except at the injection point  $x = 0$  and the detection point (if we consider spin abortion in the contacts), and  $\vec{\mu}_s \rightarrow 0$  for  $x \rightarrow \pm\infty$ . Here  $e$ ,  $R_\square$  are the electron charge and the graphene sheet resistance, respectively. The spins are injected along the  $y$  direction, with the spin current density  $i_0 = PI/l_{gr}$ , with  $I$  being the applied electrical current and  $l_{gr}$  the graphene width (Fig. S1). In this way, a set of 18 equations for 18 unknown constants is obtained. The non-local resistance is

$$R_{nl} = \frac{P \mu_{s,y}^{IV}(L)}{eI}, \quad (4.19)$$

with  $\mu_{s,y}$  given by Eq. (4.18).

Figure 4.13a shows oblique spin precession measurements in a gr/WS<sub>2</sub> device for a set of  $\beta$  angles with F detector close to the TMDC, here  $V_g = -30$  V. The curve shape strongly depends on  $\beta$  and  $B$ . The fact that for some  $\beta$  ( $\beta = 60$  i.e.) the signal  $R_{nl}$  ( $B \sim 0.14$  mT) is larger than its initial value at  $B = 0$  is a clear indication of the anisotropy nature of the spin relaxation with  $\tau_s^\perp > \tau_s^\parallel$ . In the case that  $B$  is oriented at  $\beta = 90^\circ$  the precession remains in-plane. This measurement can be used to get  $\tau_{s,gr}$  and  $D_s$ . For pristine graphene  $\tau_{s,gr} = 0.26$  ns is obtained, resulting in a spin relaxation length  $\lambda_s = \sqrt{D_s\tau_s} = 1.4$   $\mu\text{m}$ . A contact polarization  $P \approx 10\%$  is



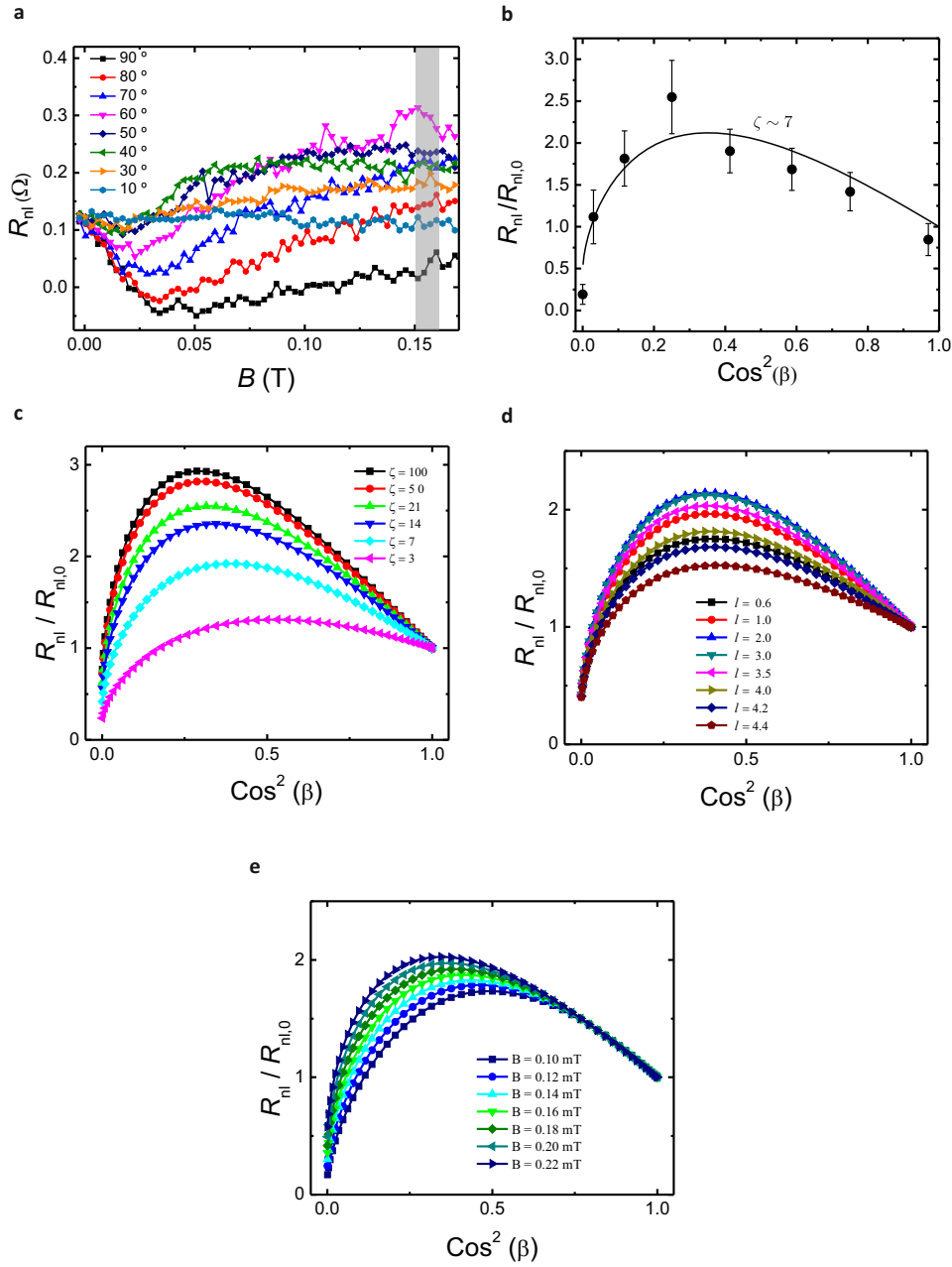


FIGURE 4.13: **Anisotropy ratio  $\zeta$ , oblique spin precession.** **a.** Set of measurements in gr/WS<sub>2</sub> for different oblique  $B$  characterized by  $\beta$ . **b.** Fitting to the normalized  $R_{nl}$  obtained from **a** (black dots). Here,  $\zeta \sim 7$  with  $\tau_s^{\parallel} = 9.4$  ps. **c.** Calculated signal response for different anisotropy ratios  $\zeta$  keeping constant  $\tau_s^{\parallel} = 9.4$  ps. The used parameters are:  $P = 0.08$ ,  $L = 5.3 \mu\text{m}$ ,  $l = 3.8 \mu\text{m}$ ,  $w = 0.6 \mu\text{m}$ ,  $D = 0.008 \text{ m}^2\text{s}^{-1}$ .  $\tau_{s,gr} = 0.26$  ns. **d.**  $R_{nl}$  varying the position,  $l$ , of the TMDC. The used parameters are the ones for **c** with  $\zeta = 7$ . **e.** Normalized  $R_{nl}$  obtained at different  $B$ . The used parameters are the same that in **a** with  $\zeta = 7$ .

assumed the same for F1 and F2. The  $\tau_s^{\parallel}$  in the graphene-WS<sub>2</sub> region can be obtained from Eq. (4.19) and the value of  $R_{nl}$  at  $\beta = 0^\circ$  which is estimated to be  $\tau_s^{\parallel} = 9.4$  ps when  $V_g = -30$  V.

Once  $\tau_s^{\parallel}$  is determined,  $\zeta$  is obtained from the  $R_{nl}$  signal at  $B > 0.14$  mT (gray area in Fig. 4.13a). Typically, at this  $B$  value the spin precession is suppressed in

pristine graphene NLSVs with  $\tau_{s,gr}$  in the order of hundreds of ps and large enough channels. In this case, only the spin component that is parallel to  $B$  contributes to the signal and it is proportional to the  $\cos^2(\beta)$ . The latter accounts for the projection of the injected spins over  $B$  and the subsequent projection over the detector. However, when  $\tau_s^{\parallel}$  and  $\tau_s^{\perp}$  are in the order of few ps a higher magnetic field is needed to observe a full spin precession. Hence, spin dephasing occurs at  $B \gg 0.14$  T. In this case, to accurately determine  $\zeta$  from  $R_{nl}$  ( $B = 0.14$  T) the spin dynamics is modelled by the Eq. (4.19), which is the solution to the Bloch equations for any  $B$  value. Figure 4.13b shows with black dots the normalized  $R_{nl}$  vs  $\cos^2(\beta)$ . The magnitude of  $R_{nl}$  is extracted from Fig. 4.13a at  $B$  value marked by the gray area. The continuous line in Fig. 4.13b shows the calculated  $R_{nl}/R_{nl,0}$  for  $\zeta = 7$ , which displays an excellent agreement with the data within the experimental error. Since  $\tau_s^{\parallel}$  was previously determined the only adjustable parameter is  $\zeta$ .

Given that Eq. 4.19 is calculated by any value of magnetic field, at difference of Eq. (4.4) where we assume no spin precession, we modeled the the normalized  $R_{nl}$  in different scenarios. Figure 4.13c shows the anisotropy ratio  $\zeta = \tau_s^{\perp}/\tau_s^{\parallel}$  dependence when  $\tau_s^{\parallel}$  is keep constant. The used parameters are  $\tau_{s,gr} = 0.2$  ns, TMDC width  $w = 0.6 \mu\text{m}$ ,  $D = 0.008 \text{ m}^2 \text{ s}^{-1}$ , channel length  $L = 5.3 \mu\text{m}$ , TMDC position respect to the injector  $l = 3.8 \mu\text{m}$ .

When  $\zeta$  increases the curves start to overlap, making us nonsensitive to large changes in  $\tau_s^{\perp}$ . This can be explained because at  $\zeta = 100$ ,  $\lambda_s^{\perp} \sim 5 \mu\text{m}$ , which is more than five times larger the TMDC width  $w = 0.6 \mu\text{m}$ .

Figure 4.13d shows the response of the normalized  $R_{nl}$  to the TMDC position respect to the injector, we have keep the parameters from Fig. 4.13b with  $\zeta = 7$ . The signal is larger when the TMDC approximates from the injector to the middle of the channel length. Which agrees with the measurements in Fig. 4.5. When TMDC was close to the injector, the signal seemed to saturate at lower  $B$  than when the TMDC was far from it.

Finally, Fig. 4.13e shows the normalized  $R_{nl}$  obtained at different magnetic fields. The parameters used are the same in Fig. 4.13c with  $\zeta = 7$ . The curve shape clearly depends on the value at which  $R_{nl}$  is obtained, with the peak moving towards  $\sim 60^\circ$  at larger values of  $B$ .

## References

- [1] Avsar, A. *et al.* Spin-orbit proximity effect in graphene. *Nat. Commun.* **5**, 4875 (2014).
- [2] Dankert, A. & Dash, S. P. Electrical gate control of spin current in van der waals heterostructures at room temperature. *Nat. Commun.* **8**, 16093 (2017).
- [3] Wang, Z. *et al.* Strong interface-induced spin-orbit interaction in graphene on  $\text{WS}_2$ . *Nat. Commun.* **6**, 8339 (2015).

- 
- [4] Yan, W. *et al.* A two-dimensional spin field-effect switch. *Nat. Commun.* **7**, 13372 (2016).
- [5] Gmitra, M., Kochan, D., Högl, P. & Fabian, J. Trivial and inverted Dirac bands and the emergence of quantum spin Hall states in graphene on transition-metal dichalcogenides. *Phys. Rev. B* **93**, 155104 (2016).
- [6] Gmitra, M. & Fabian, J. Graphene on transition-metal dichalcogenides: A platform for proximity spin-orbit physics and optospintronics. *Phys. Rev. B* **92**, 155403 (2015).
- [7] Wang, Z. *et al.* Origin and magnitude of ‘designer’ spin-orbit interaction in graphene on semiconducting transition metal dichalcogenides. *Phys. Rev. X* **6**, 041020 (2016).
- [8] Wang, Q. H., Kalantar-Zadeh, K., Kis, A., Coleman, J. N. & Strano, M. S. Electronics and optoelectronics of two-dimensional transition metal dichalcogenides. *Nat. Nanotechnol.* **7**, 699–712 (2012).
- [9] Xiao, D., Liu, G.-B., Feng, W., Xu, X. & Yao, W. Coupled spin and valley physics in monolayers of MoS<sub>2</sub> and other group-VI dichalcogenides. *Phys. Rev. Lett.* **108**, 196802 (2012).
- [10] Rivera, P. *et al.* Valley-polarized exciton dynamics in a 2D semiconductor heterostructure. *Science* **351**, 688–691 (2016).
- [11] Cummings, A. W., Garcia, J. H., Fabian, J. & Roche, S. Giant spin lifetime anisotropy in graphene induced by proximity effects. *Phys. Rev. Lett.* **119**, 10972 (2017).
- [12] Han, W., Kawakami, R. K., Gmitra, M. & Fabian, J. Graphene spintronics. *Nature Nanotech.* **9**, 794 (2014).
- [13] Raes, B. *et al.* Determination of the spin-lifetime anisotropy in graphene using oblique spin precession. *Nat. Commun.* **7**, 13372 (2016).
- [14] Raes, B. *et al.* Spin precession in anisotropic media. *Phys. Rev. B* **95**, 085403 (2017).
- [15] Johnson, M. & Silsbee, R. H. Interfacial charge-spin coupling: Injection and detection of spin magnetization in metals. *Phys. Rev. Lett.* **55**, 1790 (1985).
- [16] Jedema, F. J., Filip, A. T. & van Wees, B. J. Electrical spin injection and accumulation at room temperature in an all-metal mesoscopic spin valve. *Nature* **410**, 345–348 (2001).
- [17] Ghiasi, T. S., Ingla-Aynés, J., Kaverzin, A. A. & van Wees, B. J. Large proximity-induced spin lifetime anisotropy in transition-metal dichalcogenide/graphene heterostructures. *Nano Lett.* **17**, 7528–7532 (2017).

- [18] Ringer, S. *et al.* Measuring anisotropic spin relaxation in graphene. *Phys. Rev. B* **97**, 205439 (2018).
- [19] Offidani, M., Milletari, M., Raimondi, R. & Ferreira, A. Optimal charge-to-spin conversion in graphene on transition-metal dichalcogenides. *Phys. Rev. Lett.* **119**, 196801 (2017).
- [20] Luo, Y. K. *et al.* Opto-valleytronic spin injection in monolayer MoS<sub>2</sub>/few-layer graphene hybrid spin valves. *Nano Lett.* **17**, 3877–3883 (2017).
- [21] Avsar, A. *et al.* Optospintronics in graphene via proximity coupling. *ACS Nano* **11**, 11678–11686 (2017).
- [22] Gmitra, M. & Fabian, J. Proximity effects in bilayer graphene on monolayer WSe<sub>2</sub> : Field-effect spin valley locking, spin-orbit valve, and spin transistor. *Phys. Rev. Lett.* **119**, 146401 (2017).
- [23] Ye, Y. *et al.* Electrical generation and control of the valley carriers in a monolayer transition metal dichalcogenide. *Nat. Nanotechnol.* **11**, 598–602 (2016).
- [24] Xu, J., Zhu, T., Luo, Y. K., Lu, Y.-M. & Kawakami, R. K. Strong and tunable spin-lifetime anisotropy in dual-gated bilayer graphene. *Phys. Rev. Lett.* **121**, 127703 (2018).
- [25] Offidani, M. & Ferreira, A. Microscopic theory of spin relaxation anisotropy in graphene with proximity-induced spin-orbit coupling. *Phys. Rev. B* **98**, 245408 (2018).
- [26] David, A., Rakyta, P., Kormányos, A. & Burkard, G. Induced spin-orbit coupling in twisted graphene–transition metal dichalcogenide heterobilayers: Twistronics meets spintronics. *Phys. Rev. B* **100**, 085412 (2019).
- [27] Yan, B. *et al.* Electrical control of intervalley scattering in graphene via the charge state of defects. *Phys. Rev. B* **93**, 041407(R) (2016).
- [28] Schuler, B. *et al.* Large spin-orbit splitting of deep in-gap defect states of engineered sulfur vacancies in monolayer WS<sub>2</sub>. *Phys. Rev. Lett.* **123**, 076801 (2019).
- [29] Benítez, L. A. *et al.* Tunable room-temperature spin galvanic and spin hall effects in van der waals heterostructures. *Nat. Mater.* **19**, 170–175 (2020).

## Chapter 5

# Spin to charge interconversion in graphene/TMDC heterostructures

In this chapter, we demonstrate strongly enhanced room-temperature spin-to-charge interconversion in graphene driven by the proximity of  $WS_2$ . By performing spin precession experiments in Hall bars, we separate the contributions of the spin Hall and the spin galvanic effects. Remarkably, their corresponding conversion efficiencies can be tailored by electrostatic gating in magnitude and sign, peaking nearby the charge neutrality point with an equivalent magnitude that is comparable to the largest efficiencies reported to date. Such electric-field tunability provides a building block for spin generation free from magnetic materials and for ultra-compact magnetic memory technologies. The content of this chapter is adapted from our original work published in *Nat. Mater.* **19**, 170–175 (2020).

### 5.1 Introduction

While classical spintronics relies on the generation and manipulation of spin-polarized currents using ferromagnetic materials, the emerging field of spin orbitronics is driven by the interconversion of spin and charge currents by means of the spin-orbit coupling (SOC) [1–4]. In the spin Hall effect (SHE) and in the inverse spin galvanic effect (ISGE), a charge current generates a transverse spin current and a non-equilibrium spin density, respectively, that can manipulate the magnetization of ferromagnets in non-volatile memory technologies [1, 5]. Their reciprocals, the inverse SHE (ISHE) and the SGE, convert spin currents and spin densities, respectively, into a charge current [6, 7] that can be utilized in logic devices [8]. Various classes of materials are being investigated for such purposes, including metals, oxides and topological insulators [1–4, 9, 10]. Two-dimensional (2D) atomic crystals constitute a unique platform to engineer novel functionalities in the limit of ultra-compact device architectures [11–14]. Because they consist of atomically thin planes,

their electrical, optical and spin properties can be enriched and tailored by proximity effects. In recent years, magnetic correlations and strong SOC have been successfully imprinted onto graphene and observed at room temperature [15–19]. When graphene is in proximity to a transition metal dichalcogenide (TMDC), it preserves its electronic properties while acquiring a complex spin texture, with out-of-plane and winding in-plane components (Fig. 5.1a), that results in anisotropic spin dynamics [17, 20–23]. Theoretical studies further suggest that the unique nature of the proximity-induced SOI can enhance the graphene spin-to-charge interconversion (SCI) efficiency [24–26]. The observation of the SHE was originally reported in graphene decorated with adatoms and in contact with  $WS_2$  [27]. However, follow-up studies question the interpretation of the experiments and the spin-related character of the signals [28–31]. More recently, the ISHE was observed in heterostructures comprising multilayer graphene and  $MoS_2$  [32]. Even though the observation of the ISHE is unequivocal, it is not possible to discriminate between proximity-induced SCI in graphene or in the bulk of  $MoS_2$  because  $MoS_2$  is believed to be conductive [32]. In this chapter, we demonstrate SCI in graphene/TMDC carefully designed devices that allow us to determine that the TMDC is insulating, demonstrating that the transport occurs in graphene and that the SGE and SHE originate from proximity effects. We show that, the SGE and SHE are tuneable with Fermi energy and the conversion efficiency can change sign, which implies that the generated spin density can be controlled in orientation and magnitude with electrostatic gating.

The present chapter is organized as follows: in Sec. 5.2, we show the measurement method and the device design, as well as electrical characterization measurements in graphene and graphene/ $WS_2$ . More details about the used method are discussed in Chap. 3 (Sec. 3.4). In Sec. 5.3, we present conventional spin precession measurements used to fully characterize the spin dynamics in graphene/ $WS_2$  heterostructure as well as in the pristine graphene reference device. In Sec. 5.4, we present the spin precession measurements associated with the SHE, SGE, and their reciprocal effects, and in Sec. 5.5 we discuss the efficiencies of such effects. In Sec. 5.6, we present a carrier dependence study of the SGE and ISHE, and in Sec. 5.7 we provide a temperature study of the ISHE as a function of the carrier density. Finally, in Sec. 5.8, we describe the solutions of the spin-Bloch diffusion equations used to model the spin precession response in our measurements.

## 5.2 Measurement scheme and electrical characterization

To probe the SCI in graphene/TMDC heterostructures we implement the protocol described in Sec. 3.4 of Chap. 3. Figure 5.1b and 5.1c displays the measurement scheme and optical image of a typical device, respectively. (See Chap. 3 for fabrication details). The device consists of a patterned graphene Hall cross with a  $WS_2$  flake along one of the arms and ferromagnetic injector/detector electrodes (F1, F2, F3) across the other. An electric field  $E$  along the graphene/ $WS_2$  arm generates a spin

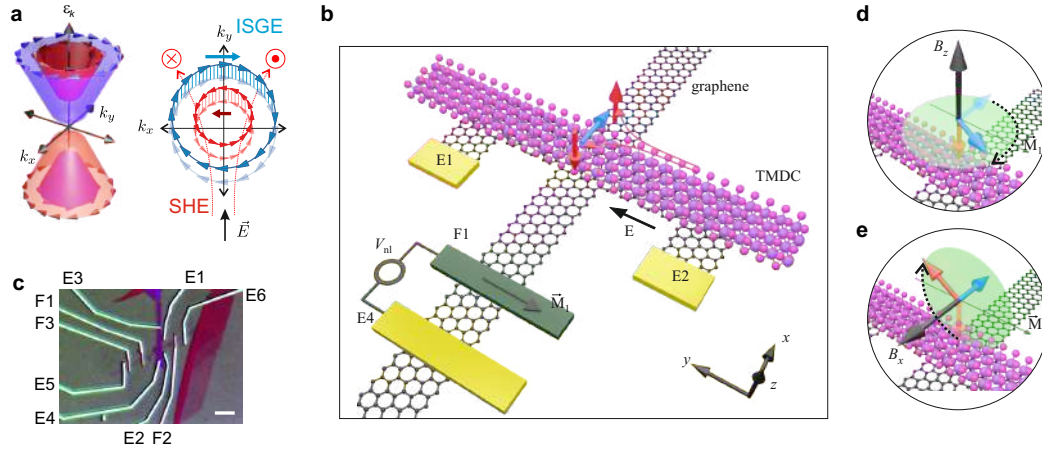


**FIGURE 5.1: Spin-to-charge interconversion in graphene/TMDC measurement scheme.** **a**, Left: Sketch of the energy bands  $\epsilon_k$  versus the wave vectors  $k_x, k_y$  showing the graphene/TMDC spin-split bands with opposite spin helicity. Right: In an applied electric field  $E$ , the ISGE generates a net non-equilibrium spin density (the blue arrow larger than the red arrow) due to the different Fermi contour sizes. **b** Schematics illustrating the measurement concept. The main elements of the device include a graphene Hall cross with a TMDC strip over one of the arms and a ferromagnet (F1) contacting the other. A current  $I$  generated by  $E$  in  $\hat{y}$ , along graphene-TMDC, induces a non-equilibrium spin density due to the ISGE with spins along  $\hat{x}$  (blue arrow, see **a**). Spin accumulation with spins out of plane (along  $\hat{z}$ ) are generated by the SHE with opposite orientation at opposite edges of the graphene/TMDC (red arrows). The induced spins diffuse in graphene towards F1 and are detected by measuring  $V_{\text{nl}} = V_{\text{nl}}^+ - V_{\text{nl}}^-$ . **c**, Optical image of a device with TMDC = WS<sub>2</sub>. Besides F1 and the Hall cross, the device comprises additional ferromagnetic electrodes (F2, F3) and contacts to graphene (E1, E2) and the WS<sub>2</sub> (E3, E4). The scale bar represents 5  $\mu\text{m}$ . The additional contacts are used to characterize the spin transport in graphene (F3 and F1), the spin relaxation anisotropy in graphene/WS<sub>2</sub> and the conductivity of graphene/WS<sub>2</sub> and of WS<sub>2</sub> (E1-E4). **d**, ISGE detection. A magnetic field  $B_z$  induces spin precession on the ISGE generated spins (blue arrow), leading to a component along  $\mathbf{M}_1$  and  $V_{\text{nl}} \neq 0$ . The SHE spins (red arrow) do not contribute to  $V_{\text{nl}}$  as they are parallel to  $B_z$  and do not precess. **e**, SHE detection. Similar to **d**, a magnetic field  $B_x$  induces spin precession on the SHE generated spins leading to  $V_{\text{nl}} \neq 0$ . The ISGE spins do not precess and do not contribute to  $V_{\text{nl}}$ .

current and spin accumulation due to the SHE (red arrows) and a non-equilibrium spin density conveyed by the ISGE (blue arrow, see Fig. 5.1a). The spins, carrying information on the SHE and the ISGE, diffuse in the graphene and are detected by measuring the non-local voltage  $V_{\text{nl}}^{\text{F}}$  at F1. Alternatively, a spin current in graphene can be generated by applying  $I$  in F1. In this case, the spin current and non-equilibrium spin density that reach the graphene(gr)/WS<sub>2</sub> are converted into a voltage  $V_{\text{nl}}^{\text{gr-WS}_2}$  by the reciprocal effects.

Electrodes F1 and F2 are equivalent and either of them can be used to investigate the SCI. In addition, F2 and F3 (in combination with F1) are used to independently characterize the spin dynamics in both the pristine graphene and the graphene/WS<sub>2</sub> [17].

The out-of-plane and in-plane spin relaxation lengths in gr/WS<sub>2</sub>,  $\lambda_s^\perp$  and  $\lambda_s^\parallel$ , are about one-micrometre and few-hundred nanometres, respectively [17]. Thus, the width  $l_w$  of the WS<sub>2</sub> flake is selected to be  $l_w \sim 1 \mu\text{m}$  to simultaneously detect the

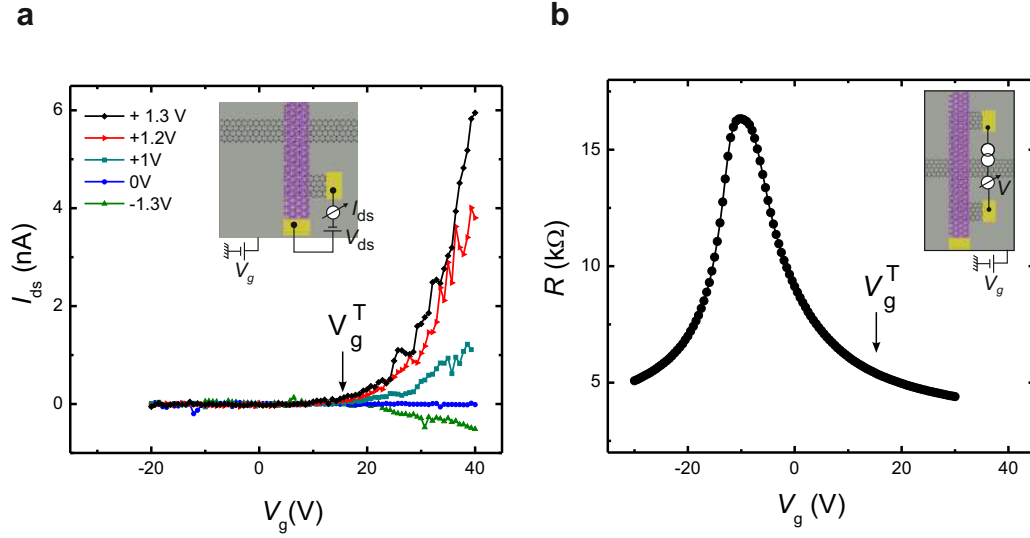


FIGURE 5.2: **Sample electrical characterization.** **a**, Transfer characteristics  $I_{ds}$  versus  $V_g$  for different bias voltage  $V_{ds}$  in gr/WS<sub>2</sub>;  $V_g^T$  indicates the back-gate voltage at which  $I_{ds}$  is first observed. **b**, Resistance  $R$  vs.  $V_g$  along gr/WS<sub>2</sub>. The charge neutrality point is located at  $V_g \approx -10$  V, well below  $V_g^T$ . Measurements performed at 200 K.

spin Hall and spin galvanic effects [1]. Sufficiently large distances from the WS<sub>2</sub> to F1 and F2 ensure large-angle spin precession at low magnetic fields, for which the magnetization of the electrodes  $\mathbf{M}_{1,2}$  remain unaffected [33, 34]. A back-gate voltage  $V_g$  is applied to the SiO<sub>2</sub>/ $p^{++}$ -Si substrate to tune the carrier density of both the graphene and WS<sub>2</sub>.

The generated spins by the SHE and the ISGE are orthogonal with each other and with the easy-axis magnetization  $\mathbf{M}_1$  of the detector. Thus, as explained in the Sec. 3.4 of Chap. 3, we can separate their contributions to the non-local voltage  $V_{nl}$  using spin precession measurements with different magnetic field configurations. For magnetic fields along the  $z$  direction ( $B_z$ ) the ISGE spins undergo precession, while the SHE spins remain unaffected (Fig. 5.1d). In this case  $V_{nl}$  solely depends on the ISGE. In contrast, for an in-plane magnetic field  $B_x$ , the ISGE spins remain unaffected so that  $V_{nl}$  is solely dependent on the SHE (Fig. 5.1e).

For the spin transport to occur only in the modified graphene, it is crucial to verify the insulating character of WS<sub>2</sub>. Otherwise, a current in WS<sub>2</sub> could generate both out-of-plane and in-plane spins through the SHE in WS<sub>2</sub>, which can be mistaken with those associated with proximity effects. Alternatively, in the case of reciprocal effects, WS<sub>2</sub> could act as a spin sink [35, 36] and the absorbed spin current could then lead to a measurable charge current (and voltage) through the ISHE in WS<sub>2</sub> [32]. Figure 5.2a shows the current  $I_{ds}$  versus  $V_g$  when a constant bias voltage  $V_{ds}$  is applied across the graphene/WS<sub>2</sub> interface.  $I_{ds}$  increases sharply at  $V_g^T \sim 12$  V, marking the onset above which WS<sub>2</sub> becomes conducting. Therefore, in order to avoid spin transfer to (from) WS<sub>2</sub>, SCI measurements are acquired at  $V_g < V_g^T$ . Figure 5.2b shows the gate-dependent resistance  $R$  of the gr/WS<sub>2</sub>. The fact that the modified graphene is



$n$ -doped with  $V_g^{\text{CNP}} = -10 \text{ V} < V_g^{\text{T}}$  allows us to investigate the proximity-induced SCI for both electron and hole transport.

### 5.3 Conventional non-local spin precession measurements

Typical non-local spin precession measurements  $r_{\text{nl}} = V_{\text{nl}}^{\downarrow\uparrow, \uparrow\uparrow} / I$  in pristine graphene are presented in Figures 5.3a and 5.3b. Measurements are performed for antiparallel ( $\downarrow\uparrow$ ) and parallel ( $\uparrow\uparrow$ ) configurations of  $\mathbf{M}_{1,3}$  versus  $B_x$  (Fig. 5.3a) and  $B_z$  (Fig. 5.3b). In these measurements, we apply a current  $I$  between F1 and E6 and detect the non-local voltage  $V_{\text{nl}}$  between F3 and E5. From the measurements with  $B_z$ , we extract the spin lifetime  $\tau_s = 0.11 \text{ ns}$ , diffusion constant  $D = 0.03 \text{ m}^2/\text{Vs}$  in pristine graphene and the polarization  $P = 0.08$  of the ferromagnetic electrodes (see Chap. 3 for details about how to get those spin parameters).

With the measurements in Fig. 5.3a, the rotation of the electrodes magnetization can also be obtained [7]. This is particularly relevant for SGE experiments when the magnetic field is applied along  $\hat{x}$ .

Figure 5.3c shows the spin precession response in the gr/WS<sub>2</sub> device when the magnetic field is applied in  $\hat{x}$ . The results highlight the anisotropic character of the spin transport [17]. As  $B_x$  increases, the corresponding  $r_{\text{nl}}$  becomes much larger than its value at  $B = 0$ , which demonstrates that the spin lifetime for spins in the plane

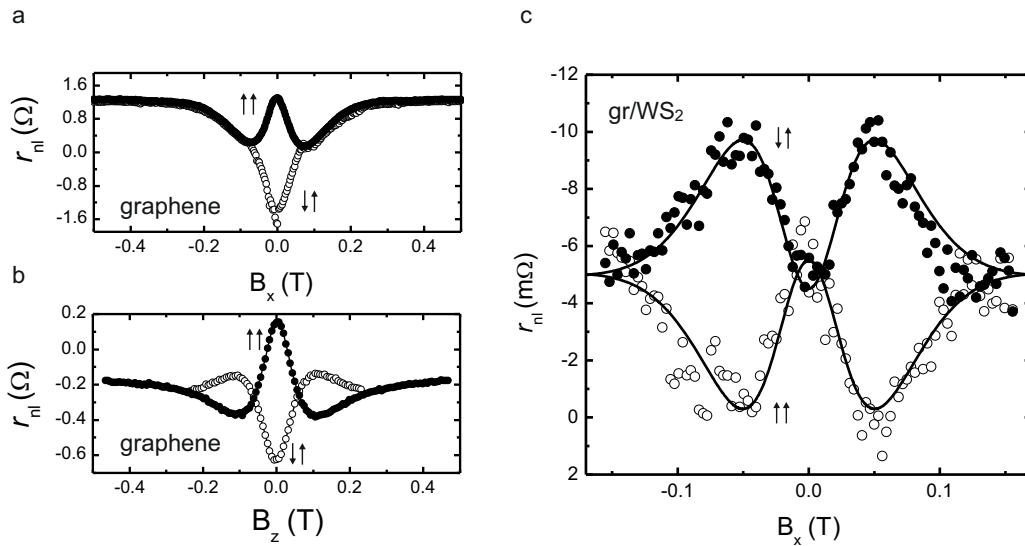


FIGURE 5.3: **Spin precession measurements in graphene and graphene/WS<sub>2</sub>.** **a**, non-local spin signal  $r_{\text{nl}}$  vs.  $B_x$  in the graphene reference device with F1 and F3 as spin injector and detector electrodes for antiparallel (open symbols) and parallel (solid symbols) configuration of the electrodes magnetizations. **b**, as in **a** with a magnetic field oriented in  $\hat{z}$ ,  $B_z$ . **c**, as in **a** in the gr/WS<sub>2</sub> device, using F1 and F2. The signal becomes larger when  $B_x \neq 0$  than at  $B_x = 0$ , indicating a large spin relaxation anisotropy in gr/WS<sub>2</sub> with long spin lifetimes out of the graphene plane. Solid line is the fitting to  $\Delta r_{\text{nl}}$  to the solution of the anisotropic spin diffusion equations, where  $\tau_s^{\parallel} = (6 \pm 1) \text{ ps}$  and  $\zeta = 8 \pm 3$  are obtained (Sec. 5.8). Measurements in **a**, **b**, **c** are performed at 200 K.

of graphene/WS<sub>2</sub>,  $\tau_s^{\parallel}$ , is much smaller than that for spins pointing out of plane,  $\tau_s^{\perp}$ . Modelling the spin diffusion in the graphene and the gr/WS<sub>2</sub>, with the parameters obtained from Fig. 5.3b, yields  $\tau_s^{\parallel} = (6 \pm 1)$  ps and  $\tau_s^{\perp} = (52 \pm 10)$  ps while the anisotropy ratio, defined as  $\zeta = \tau_s^{\perp}/\tau_s^{\parallel}$  is  $\zeta = 8 \pm 3$ .

## 5.4 Spin-to-charge interconversion measurements

Representative spin precession measurements in the ISHE and SGE configurations are shown in Figs. 5.4a and 5.4b, respectively. In the ISHE configuration, the non-local resistance  $R_{nl}^{\downarrow,\uparrow} = V_{nl}^{\downarrow,\uparrow}/I$  is measured with the magnetic field  $B_x$  oriented along

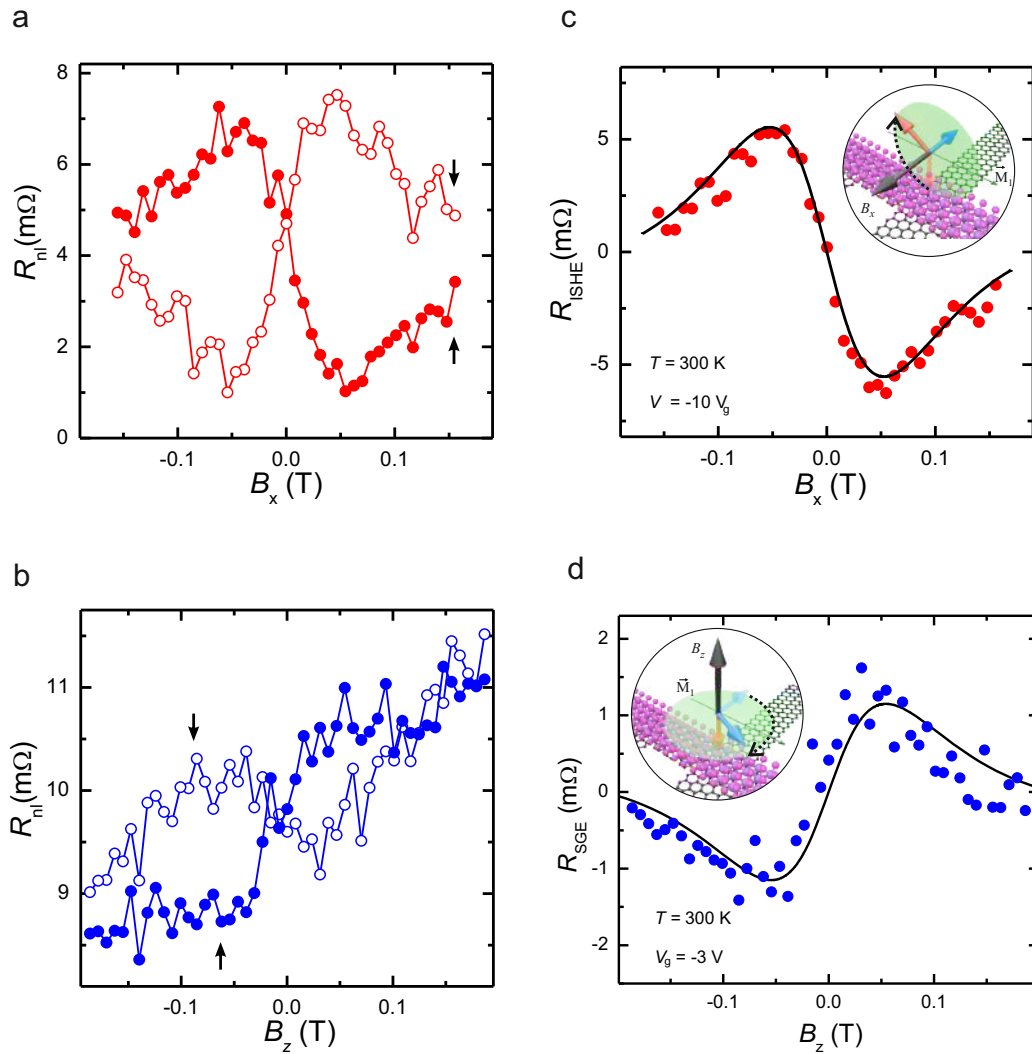


FIGURE 5.4: **ISHE and SGE measurements.** **a**, representative room-temperature non-local measurements in the ISHE configuration.  $R_{nl}^{\downarrow,\uparrow}$  vs.  $B_x$  for  $M_1$  antiparallel ( $\downarrow$ , open symbols) and parallel ( $\uparrow$ , solid symbols) to  $\hat{y}$ . **b**, as in **a** in the SGE measurement configuration. **c**,  $R_{ISHE} = (R_{nl}^{\uparrow} - R_{nl}^{\downarrow})$ . The inset shows the ISHE configuration. **d**, as **c** in the SGE configuration. Solid lines in **c** and **d** are fittings to the solution of the anisotropic spin diffusion equations (See Secs. 5.5 and 5.8).

$\hat{x}$ . In the SGE configuration  $R_{\text{nl}}$  is measured with  $B_z$  oriented along  $\hat{z}$ . The orientation of  $\mathbf{M}_1$  ( $\uparrow$ ,  $\downarrow$ ) is prepared prior to the measurements by applying a magnetic field along  $\hat{y}$  with a magnitude exceeding the coercive field of the spin injector F1. The current  $I$  is applied at F1 and  $V_{\text{nl}}^{\downarrow,\uparrow}$  measured in the graphene across the graphene/WS<sub>2</sub> arm, between E1 and E2. The inversion of the magnetic-field dependence when  $\mathbf{M}_1$  reverses demonstrates the spin-related origin of the signal. Figs. 5.4c and 5.4d show  $\Delta R_{\text{nl}} \equiv R_{\text{nl}}^{\uparrow} - R_{\text{nl}}^{\downarrow}$ . By calculating the difference between  $R_{\text{nl}}^{\uparrow}$  and  $R_{\text{nl}}^{\downarrow}$ , any non-spin related component in  $V_{\text{nl}}^{\downarrow,\uparrow}$  is eliminated.

The data in Figs. 5.4c and 5.4d exhibit an antisymmetric spin precession lineshape. The spins injected by F1 are parallel to  $\hat{y}$  and, consequently, only when the magnetic field generates a  $\hat{z}$  ( $\hat{x}$ ) spin component, a nonzero  $R_{\text{ISHE}}$  ( $R_{\text{SGE}}$ ) is detected. At low magnetic fields  $R_{\text{ISHE}}$  and  $R_{\text{SGE}}$  are approximately linear; they reach maximum magnitude at about  $\pm 50$  mT and then decrease. The extrema in  $R_{\text{ISHE}}$  and  $R_{\text{SGE}}$  indicate an aggregate spin precession angle of  $\pi/2$  when reaching the Hall cross. The asymptotic decrease to zero at larger magnetic fields ( $> 50$  mT) is associated to spin dephasing [37].

The device structure shown in Fig. 5.1b allows us to measure the ISHE and the SGE effects, but also their reciprocals, the spin Hall (SHE) and the inverse spin galvanic effects (ISGE), which are shown in Fig. 5.5. Even though, the focus has been on the ISHE and SGE, for which systematic measurements were performed, it is important to verify that the SHE and ISGE can also be observed.

In the next Sec. we provide a study of the SCI efficiencies obtained from the spin precession lineshapes in Figs. 5.4c and 5.4d. To reduce the number of unknown parameters, we use the spin transport characterization, described in Sec. 5.3, outside and inside the graphene/WS<sub>2</sub> region.

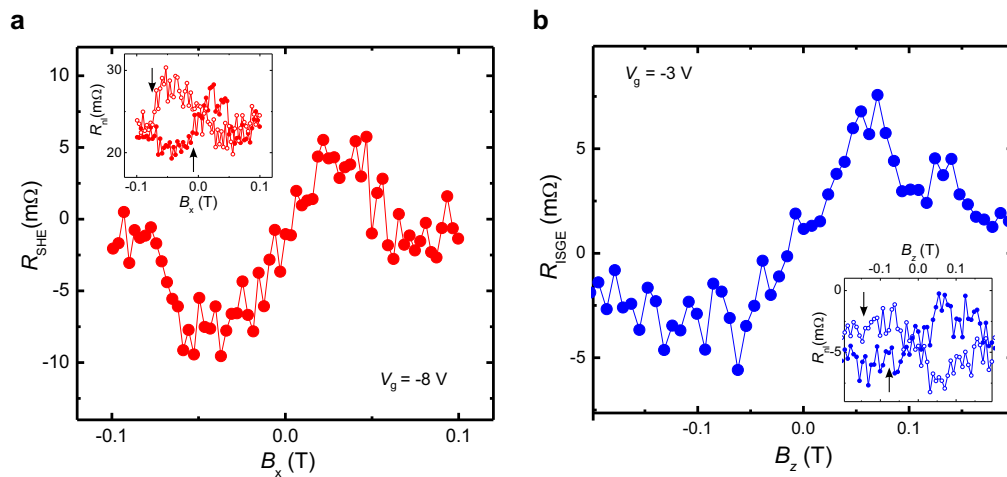


FIGURE 5.5: **SHE and ISGE measurements.** **a**, Representative spin Hall effect signal. Current  $I$  is injected between E2 and E3 and  $V_{\text{nl}}$  measured at F1.  $V_g = -8$  V;  $T = 300$  K. **b**, Representative inverse spin galvanic effect signal.  $I$  is applied between E1 and E1 and  $V_{\text{nl}}$  measured at F2.  $V_g = -3$  V;  $T = 200$  K.

## 5.5 SGE and SHE efficiency

The spin and spin-current densities can be calculated, at any position, from the analytical solution of the Bloch diffusion equation (Sec. 5.8). At this point, the spin precession lineshapes in Figs. 5.4c and 5.4d can be inferred from the spin current density  $j_s^z$  associated to the spins projected in  $\hat{z}$  (ISHE) and the in-plane component of the spin density in  $\hat{x}$  (SGE) in the graphene/WS<sub>2</sub> region (Fig. 5.1b). The only unknown parameters are scaling factors associated to the SCI efficiencies (Sec. 5.8). The ISHE is quantified by the spin Hall angle  $\theta_{\text{SHE}}$ , which measures the conversion from  $j_s^z$  to a charge current density  $j_c^y$  [1]. In the case of the SGE, where a spin density is converted into  $j_c^y$ , several figures of merit have been proposed. In our experiments, the spin density leading to  $R_{\text{SGE}}$  derives directly from the spin current density  $j_s^x$ . Therefore, it is possible to adopt an SGE equivalent to  $\theta_{\text{SHE}}$ , namely  $\alpha_{\text{SGE}} \equiv j_c^y / j_s^x$ . Because the latter conversion is from a 2D spin current into a 2D charge current,  $\alpha_{\text{SGE}}$  is dimensionless. This contrasts with the commonly used inverse Edelstein effect length  $\lambda_{\text{IEE}}$ , which quantifies the SGE conversion efficiency from a three-dimensional spin current into a 2D charge current and has the dimension of a length [38].

The solid lines in Figs. 5.4c and 5.4d are fits to the data from which room-temperature  $\theta_{\text{SHE}} \approx 0.3\%$ , and  $\alpha_{\text{SGE}} \approx 0.1\%$  are estimated. The agreement between the model and experiment is excellent considering that only one adjustable (scaling) parameter is used. For comparison purposes, one can convert  $\alpha_{\text{SGE}}$  and  $\theta_{\text{SHE}}$  into an equivalent efficiency  $\lambda_{\text{IEE}}$  through  $\lambda_{\text{IEE}}^{\text{SGE}} = \alpha_{\text{SGE}} \lambda_s^{\parallel} \approx 0.42$  nm and  $\lambda_{\text{IEE}}^{\text{SHE}} = \theta_{\text{SHE}} \lambda_s^{\perp} \approx 3.75$  nm, where  $\lambda_s^{\parallel} = 420$  nm and  $\lambda_s^{\perp} = 1.25$   $\mu\text{m}$  are the in-plane and out-of-plane spin relaxation lengths in graphene/WS<sub>2</sub>. Remarkably, these values compare very favourably with those estimated for heavy metals as  $\theta_{\text{SHE}} \lambda_s^{\text{M}}$  ( $\lambda_s^{\text{M}}$  the metal spin diffusion length), yielding 0.2 nm for Pt, 0.3 nm for Ta and 0.43 nm for W [39]. Furthermore,  $\lambda_{\text{IEE}}^{\text{SHE}}$  is larger than the  $\lambda_{\text{IEE}}$  reported for any material at room temperature, being one order of magnitude larger than in Bi/Ag interfaces,  $\lambda_{\text{IEE}} = 0.2 - 0.33$  nm [38], and almost twice  $\lambda_{\text{IEE}} = 2.1$  nm in the topological insulator  $\alpha$ -Sn [40].

## 5.6 Gate control of the ISHE and SGE at room temperature

The ISGE and SGE can also be investigated when  $\mathbf{M}_1$  rotates towards  $\hat{x}$  with sufficiently large  $B_x$  [7, 41]. As observed in Fig. 5.3a, the magnetization rotation is evident for  $B_x > 0.2$  T, with  $\mathbf{M}_1$  (and  $\mathbf{M}_3$ ) becoming fully aligned with  $B_x$  for  $|B_x| > 0.3$  T. Therefore, in the configuration of the SHE (Fig. 5.1a) a broad step in  $R_{\text{nl}}$  is expected for  $B_x$  between -0.3 and 0.3 T due to the SGE contribution. Figure 5.6a shows  $R_{\text{nl}}$  versus  $B_x$  for three representative  $V_g$ : at the CNP ( $V_g = -10$  V) and for electron ( $V_g = -3$  V) and hole ( $V_g = -13$  V) conduction. The SGE signal is clearly observed together with the spin precession response associated to the ISHE (Fig. 5.4a). The

solid lines represent  $M_{1,x}$ , the projected  $\mathbf{M}_1$  along  $\hat{x}$ , which is obtained using measurements as in Fig. 5.3a [7]. The agreement between the field-dependence of  $M_{1,x}$  and the SGE step is excellent. Note that the contribution of the conventional Hall effect induced by stray magnetic fields from the rotating  $\mathbf{M}_1$  follows the same dependence [42]. Nevertheless, such a contribution is suppressed in our device design by using a narrow graphene flake and by placing F1 sufficiently far from the Hall cross region. Most important, the magnitude of the SGE extracted from these measurements matches with that obtained by spin precession experiments (Fig. 5.4d), enabling to confidently discard any artifacts associated to stray magnetic fields.

The results in Fig. 5.6a suggest that the ISHE and the SGE follow distinct carrier density dependence. While a SHE signal is clearly distinguished at the CNP, the SGE signal changes sign between electrons and holes, becoming zero at the CNP. Figure 5.6b represents the room-temperature magnitude of the ISHE and SGE versus  $V_g$ . The SGE is quantified by the step height,  $R_{\text{SGE}}^* \equiv R_{\text{nl}}(0.4 \text{ T}) - R_{\text{nl}}(-0.4 \text{ T})$  and the ISHE by the subtraction  $R_{\text{ISHE}}^*$  between the values of  $R_{\text{ISHE}}$  at its two extrema (see Fig. 3a). It is observed that  $V_g$  has a dramatic influence in the SCI.  $R_{\text{ISHE}}^*$  displays a sharp peak with its maximum located nearby the CNP. In contrast,  $R_{\text{SGE}}^*$  is highly asymmetric about the CNP, changing sign between electrons and holes, as concluded

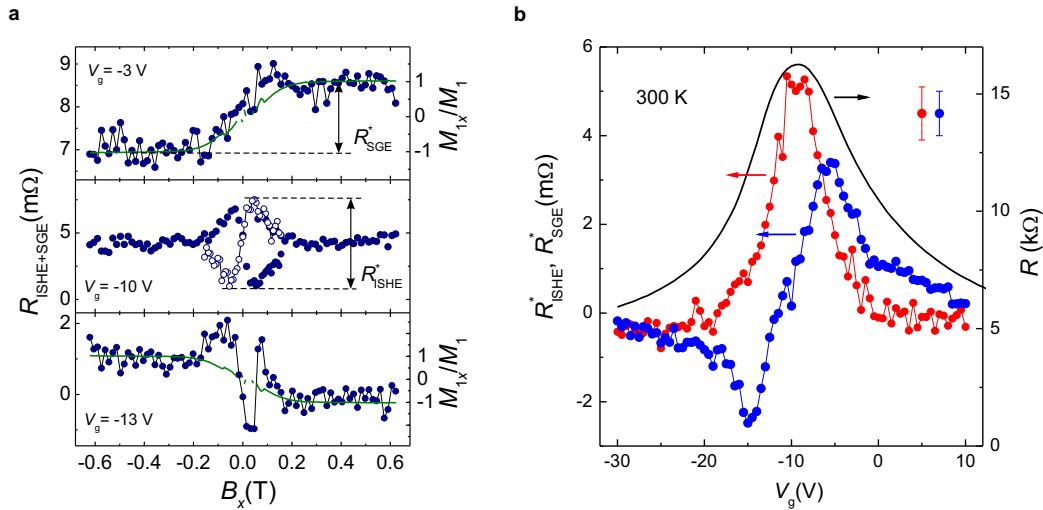
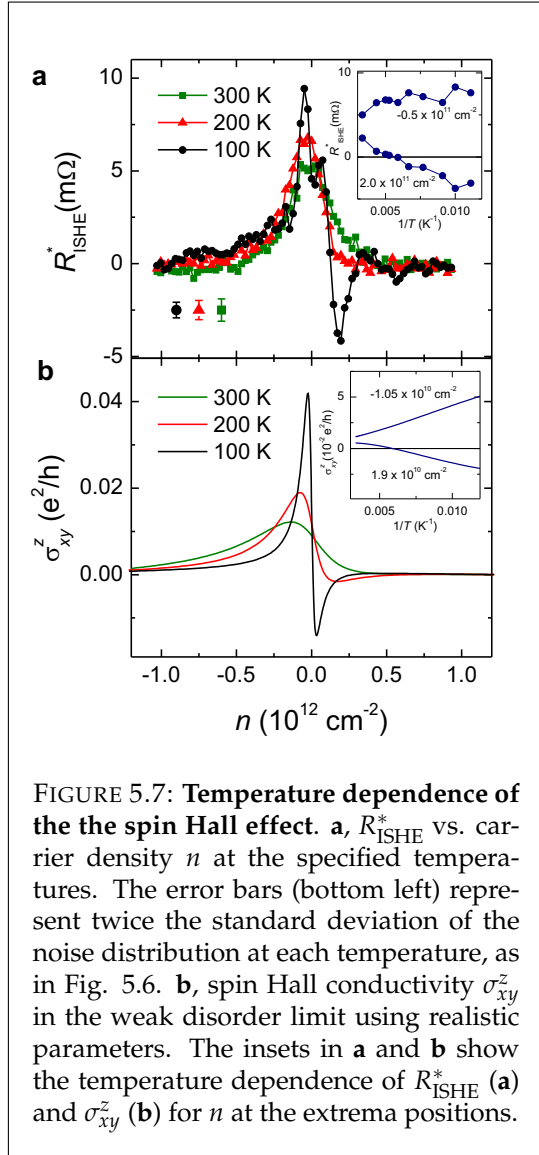


**FIGURE 5.6: Gate control of the inverse spin Hall and spin galvanic effects at room temperature.** **a**, Non-local resistance  $R_{\text{nl}}$  vs  $B_x$  at selected gate voltages  $V_g$  showing the ISHE precession response at low magnetic fields and the step feature associated to the SGE. The latter is observed when the magnetic field is large enough to rotate  $\mathbf{M}_1$  and generate a component along  $\hat{x}$ ,  $M_{1,x}$ . The normalized  $M_{1,x}$  (sine of the rotation angle) is extracted from spin precession measurements as in Fig. 5.3a [7] and represented with green lines. In the hole side ( $V_g = -13 \text{ V}$ ), the jump in the ISHE signal at  $\sim 50 \text{ mT}$  originates from the magnetization switching of the detector as  $B_x$  is swept from negative to positive values. **b**, Spin-to-charge interconversion for the ISHE (red) and the SGE (blue) as a function of  $V_g$ . The corresponding conversion efficiencies are quantified with  $R_{\text{ISHE}}^*$  and  $R_{\text{SGE}}^*$  as defined in **a**.  $R$  vs  $V_g$  is shown as a reference (solid black line). The error bars (top right) represent twice the standard deviation of the noise distribution in **a**; it is largest for  $R_{\text{ISHE}}^*$  because of the added uncertainty in the determination of the extrema location.

from Fig. 5.6a.

The sign change in  $R_{\text{SGE}}^*$  stems from the change in the nature of the carriers, as the winding of the spin texture is symmetrical about the CNP [21, 25]. This further confirms our interpretation of the signal as originating from the SGE [25].

## 5.7 ISHE temperature dependence



features using parameters that are within a factor two of those obtained by density functional theory [21, 24], including the relative magnitude of the positive and negative extrema, their approximate width and the temperature  $T \sim 200$  K at which the sign change is observed (Fig. 5.7 Insets). Although the temperature dependence of  $R_{\text{ISHE}}^*$  is highly non-trivial,  $R_{\text{ISHE}}^*$  varies roughly as  $1/T$  nearby the extrema (Inset Fig. 5.7a), which is also well reproduced by the calculations (Inset Fig. 5.7b).

Theoretical calculations for graphene/WS<sub>2</sub> suggest that  $R_{\text{ISHE}}$  also changes sign nearby the CNP with a behavior qualitatively similar to that of  $R_{\text{SGE}}$ . However, the magnitude of  $R_{\text{ISHE}}$  is expected to be much larger for holes than for electrons [24]. As a consequence, the smearing effect resulting from the presence of charge puddles and thermal broadening might suppress the extremum in the electron side, leaving only the dominant hole peak by the CNP. The results in Fig. 5.7a, showing  $R_{\text{ISHE}}^*$  versus  $n$  as the temperature  $T$  decreases, indicate that this hypothesis is likely. Indeed,  $R_{\text{ISHE}}^*$  at room temperature presents an incipient electron-hole asymmetry, with a more sharp decrease for electron conduction. At 200 K, the decrease becomes steeper as thermal broadening is reduced. At 100 K a negative minimum at  $n = 5 \times 10^{11} \text{ cm}^{-2}$  becomes fully developed.

Figure 5.7b shows the computed spin Hall conductivity  $\sigma_{xy}^{\text{SHE}}$  in the weak disorder limit [24] (see Annex A). Notably, the theoretical model describes qualitatively all of the experimental fea-

The tendency for saturation in  $R_{\text{ISHE}}^*$  at low  $T$  for hole conduction, which is not observed in the model, could indicate the presence of charge puddles or other types of impurities and defects.

## 5.8 Bloch diffusion equations

The one-dimensional steady-state Bloch diffusion equation (BDE) is used to calculate the spin density  $\vec{\mu}_s$  over the channel as function of the spin relaxation time in the graphene plane ( $\tau_s^{\parallel}$ ) and out of the graphene plane ( $\tau_s^{\perp}$ ),

$$D \frac{d^2 \vec{\mu}_s}{dx^2} + \gamma_c \vec{\mu}_s \times \vec{B} - \overline{\tau_s^{-1}} \cdot \vec{\mu}_s = 0. \quad (5.1)$$

The three components of  $\vec{\mu}_s$  describe the spin density projected along the corresponding Cartesian axes.  $D$  is the spin diffusion constant,  $\gamma_c = 2\mu_B/\hbar$  is the electron gyromagnetic ratio with  $\mu_B$  and  $\hbar$  the Bohr magneton and the reduced Planck constant, respectively.  $\overline{\tau_s^{-1}}$  is a  $3 \times 3$  diagonal matrix containing the spin relaxation times.

Within this model the spin transport in the device is characterized by means of spin precession measurements with a magnetic field oriented in the  $z$  and the  $x$  direction (Fig. 5.4 and 5.3) as described. The solution with and in-plane ( $x$ ) magnetic field was explained in Sec. 4.8 of Chap. 4. The solution with an out of plane  $B$  is sketched in Subsec. 5.8.1.

With the spin dynamics in the device fully characterized,  $\vec{\mu}_s$  is calculated at any position and therefore, the spin and spin-current densities that generate the SGE and ISHE. By comparing the calculated SGE and ISHE with the measured signals, the SCI efficiencies are obtained. This approach is described in Subsec. 5.8.4 and 5.8.5.

### 5.8.1 Solution of the BDE for out-of-plane magnetic fields

Following the procedure in Chap. 4. For out-of-plane magnetic fields,  $\vec{B} = (0, 0, B)$ , Eq. (5.1) can be written as

$$D \frac{d^2}{dx^2} \begin{pmatrix} \mu_{sx} \\ \mu_{sy} \\ \mu_{sz} \end{pmatrix} - \begin{pmatrix} \tau_s^{\parallel -1} \\ \tau_s^{\parallel -1} \\ \tau_s^{\perp -1} \end{pmatrix} \begin{pmatrix} \mu_{sx} \\ \mu_{sy} \\ \mu_{sz} \end{pmatrix} + \omega \begin{pmatrix} \mu_{sy} \\ -\mu_{sx} \\ 0 \end{pmatrix} = 0, \quad (5.2)$$

where  $\omega = \gamma_c B$ . The solution of Eq. (5.2) for  $z$  spin component is

$$\mu_{sz} = \eta \exp(\pm k_1 x), \quad k_1 = 1/\sqrt{D\tau_s^{\perp}}, \quad (5.3)$$



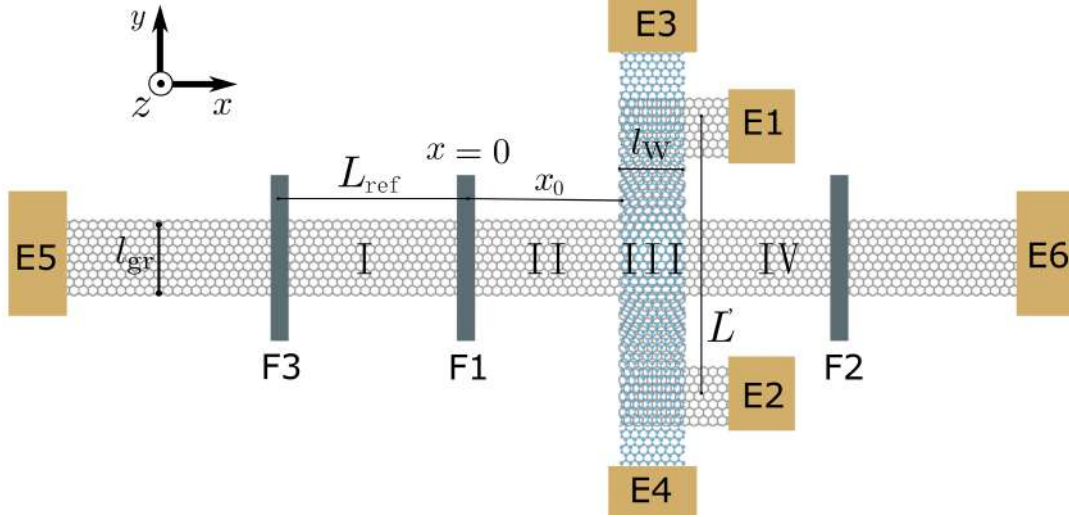


FIGURE 5.8: **SCI device main elements.** The device comprises a graphene Hall cross and normal metal (E1-E6) and ferromagnetic (F1-F3) electrodes. The TMDC is placed on top of one of the Hall-cross arms and F1-F3 patterned on top of the other. The electrodes are used to fully characterize the charge and spin transport properties of each device element. The shown notation for the dimensions and device regions (I-IV) are used when modelling the spin dynamics in the device.

where  $\eta$  is a constant. Making the guess that  $s_x$  and  $s_y$  are proportional to  $\exp(-k_2 x)$ , Eq. (5.2) can be written as,

$$\begin{bmatrix} k_2^2 D - \tau_s^{\parallel -1} & \omega \\ -\omega & k_2^2 D - \tau_s^{\parallel -1} \end{bmatrix} \begin{bmatrix} \mu_{s_x,0} \\ \mu_{s_y,0} \end{bmatrix} = \begin{bmatrix} 0 \\ 0 \end{bmatrix}, \quad (5.4)$$

where  $\mu_{s_x,0}, \mu_{s_y,0}$  are constants.

The eigenvectors ( $\vec{v}_{\pm}$ ) and eigenvalues ( $k_2^{\pm}$ ) are,

$$\begin{aligned} \vec{v}_+ &= \begin{bmatrix} 1 \\ i \end{bmatrix}, \text{ for } k_2^+ = \pm \sqrt{\frac{1}{\tau_s^{\parallel} D} + i \frac{\omega}{D}}, \\ \vec{v}_- &= \begin{bmatrix} 1 \\ -i \end{bmatrix}, \text{ for } k_2^- = \pm \sqrt{\frac{1}{\tau_s^{\parallel} D} - i \frac{\omega}{D}}, \end{aligned} \quad (5.5)$$

with  $i = \sqrt{-1}$ . In this basis of eigenvectors the solution to Eq. (5.2) is given by

$$(\mu_{s_x}, \mu_{s_y}) = a_1 \vec{v}_+ \exp(k_2^+ x) + a_2 \vec{v}_- \exp(k_2^- x) + a_3 \vec{v}_+ \exp(-k_2^+ x) + a_4 \vec{v}_- \exp(-k_2^- x). \quad (5.6)$$

where  $a_j, j = 1, 2, 3, 4$ , are determined by the boundary conditions.

The device geometry is shown in Fig. 5.8. There are four distinct regions (I to IV) with  $\tau_s^{\perp} = \tau_s^{\parallel} = \tau_s$  in I, II, IV, and  $\tau_s^{\perp} > \tau_s^{\parallel}$  in III [17, 23]. The boundary conditions are set by the continuity of  $\vec{\mu}_s$  and the spin current density  $\vec{j}_s \equiv -1/(e R_{\square}) d\vec{\mu}_s/dx$  everywhere except at the injection point  $x = 0$  and by  $\vec{\mu}_s \rightarrow 0$  for  $x \rightarrow \pm\infty$ . Here  $e$ ,



$R_{\square}$  are the electron charge and the graphene sheet resistance, respectively. The spins are injected along the  $y$  direction, with the spin current density  $j_0 = P I / l_{\text{gr}}$ , with  $I$  the applied electrical current and  $l_{\text{gr}}$  the graphene width (Fig. S1). In this way, a set of 12 equations for 12 unknown constants is obtained, which is solved analytically using the software Mathematica  $\text{\textcircled{R}}$ .

For the reference device, comprising F1 and F3,  $\tau_s^{\parallel} = \tau_s^{\perp} = \tau_s$ . Assuming the polarization of the detector equal to that of the injector, the non-local resistance is,

$$r_{\text{nl}} = \frac{P S_y^I}{e I_0} = \frac{P^2 R_{\square}}{4 l_{\text{gr}}} \left( \frac{e^{-L_{\text{ref}} \sqrt{\frac{1-i\tau_s w}{D\tau_s}}}}{\sqrt{\frac{1-i\tau_s w}{D\tau_s}}} + \text{h.c.} \right), \quad (5.7)$$

where h.c is Hermitian conjugate. The spin lifetimes in Fig. 5.9a are obtained by fitting the experimental data in Fig 5.9b to Eq. (5.7). The device parameters are,  $l_{\text{gr}} = 1 \mu\text{m}$ ,  $L_{\text{ref}} = 4 \mu\text{m}$ . Taking  $R_{\square} = 1.6 \text{ k}\Omega$  at  $n = -0.5 \times 10^{11} \text{ cm}^{-2}$ , the extracted F polarization is  $P=0.08$ .

### 5.8.2 Solution of BDE for in-plane magnetic fields

The solution for  $\vec{B} = (B, 0, 0)$  was presented in Sec. 4.8 of Chap. 4. Here we recall those solution to calculate  $\vec{\mu}_s$  at any position of the channel.

The solution of Eq. (5.1) is expressed as

$$(\mu_{s_y}, \mu_{s_z}) = c_1 \vec{v}_+ \exp(k_2^+ x) + c_2 \vec{v}_- \exp(k_2^- x) + c_3 \vec{v}_+ \exp(-k_2^+ x) + c_4 \vec{v}_- \exp(-k_2^- x), \quad (5.8)$$

where,

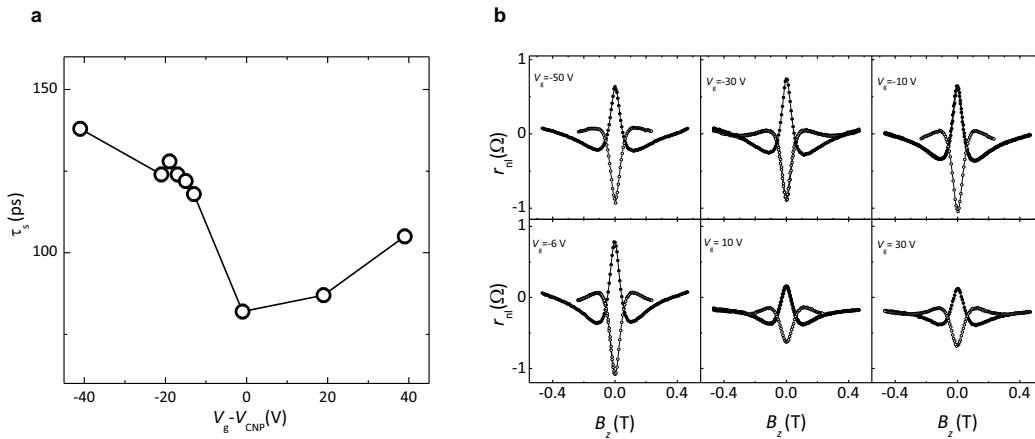


FIGURE 5.9: **Characterization of the spin dynamics in the reference device.** **a**, Representative spin precession measurements between F1 and F3 for parallel (solid symbols) and antiparallel (open symbols) F1-F3 magnetization orientation at the specified gate voltages  $V_g$ . **b**, Extracted spin lifetimes versus  $V_g$  as obtained from steady-state Bloch diffusion equations.

$$\begin{aligned} \vec{v}_+ &= \begin{bmatrix} 1 \\ f_+ \end{bmatrix}, \text{ for } k_2^+ = \pm \sqrt{\frac{1}{2D} \left( \frac{1}{\tau_s^\parallel + \tau_s^\perp} + \sqrt{(\tau_s^{\parallel -1} - \tau_s^{\perp -1})^2 - 4\omega^2} \right)}, \\ \vec{v}_- &= \begin{bmatrix} f_- \\ 1 \end{bmatrix}, \text{ for } k_2^- = \pm \sqrt{\frac{1}{2D} \left( \frac{1}{\tau_s^\parallel + \tau_s^\perp} - \sqrt{(\tau_s^{\parallel -1} - \tau_s^{\perp -1})^2 - 4\omega^2} \right)}, \end{aligned} \quad (5.9)$$

with

$$f_\pm = \frac{\pm 2\omega}{\pm \tau_s^{\parallel -1} \mp \tau_s^{\perp -1} \pm \sqrt{(\tau_s^{\parallel -1} - \tau_s^{\perp -1})^2 - 4\omega^2}} \quad (5.10)$$

### 5.8.3 Spin relaxation anisotropy

The experimental spin lifetimes and the anisotropy ratio  $\zeta$  are obtained from the spin precession measurements in the graphene/WS<sub>2</sub> device (Fig. 5.3c). Here, the non-local resistance is given by

$$r_{\text{nl}} = \frac{P\mu_{s_y}^{\text{IV}}(L)}{eI}, \quad (5.11)$$

where  $\mu_{s_y}^{\text{IV}}$  is the spin density in region IV. Because in these experiments  $B$  is applied along  $x$ ,  $\mu_{s_y}^{\text{IV}}$  is given by Eq. (5.8) and can be expressed as

$$\mu_{s_y}^{\text{IV}} = \frac{eR_\square PI}{l_{\text{gr}}} h(\tau_s^\parallel, \zeta), \quad (5.12)$$

where  $h(\tau_s^\parallel, \zeta)$  is a function that captures the spin dynamics, taking as inputs  $\tau_s$ ,  $D$ , which are known for the reference device.

The measured  $r_{\text{nl}}$  is somewhat smaller than the typical signals reported in similar systems (Chap. 4). This stems in part from the diffusion of spins towards the graphene/WS<sub>2</sub> arm, which is not taken into account in our one dimensional model. To consider the additional relaxation path, an effective injector polarization  $P = \varepsilon P$  is introduced with  $\varepsilon < 1$ . Thus,  $r_{\text{nl}}$  is expressed as

$$r_{\text{nl}} = \frac{\varepsilon P^2 R_\square}{l_{\text{gr}}} h(\tau_s^\parallel, \zeta). \quad (5.13)$$

Figure 5.3c shows the fitting (solid line) to the experimental data (open and closed circles) using Eq. (5.13). The sheet resistance  $R_\square = 1.3 \text{ k}\Omega$  is obtained from the data in Fig. 5.2b using  $l_{\text{gr}} = 1 \text{ }\mu\text{m}$  and  $L' = 9.7 \text{ }\mu\text{m}$ . The spin relaxation time and diffusion in graphene and the polarization of the electrodes are obtained using the reference device,  $\tau_s = 0.11 \text{ ns}$ ,  $D = 0.03 \text{ m}^2/\text{Vs}$ ,  $P = 0.08$ . From the fitting  $\tau_s^\parallel = (6 \pm 1) \text{ ps}$  and  $\zeta = 8 \pm 3$  are extracted with  $\varepsilon = 0.5 \pm 0.1$ .

### 5.8.4 Inverse spin Hall effect, ISHE

A spin current density with spins projected along the  $z$  direction  $j_{s,z}^{\text{III}}$  in the graphene/TMDC region (III) generates a charge current density  $j_c^y$  that is detected as a  $R_{\text{ISHE}} = V_{\text{ISHE}}/I$  due to the ISHE. The conversion efficiency is related with the spin Hall angle  $\theta_{\text{SHE}} = |j_c^y|/|j_{s,z}^{\text{III}}|$ . The charge density current is  $j_c^y = V_{\text{ISHE}}/(R_a l_w)$ , where  $R_a$  is the resistance of the region where  $j_s^{\text{III}}$  generates  $V_{\text{ISHE}}$ .

$$|j_{s,z}^{\text{III}}| = \frac{1}{e l_w R_{\square}} \int_{x_0}^{x_0+l_w} \frac{d\mu_{s,z}^{\text{III}}(x)}{dx} dx = \frac{\Delta\mu_{s,z}^{\text{III}}}{e l_w R_{\square}}, \quad (5.14)$$

The spin density  $s_z^{\text{III}}(x)$  is given by Eq. (5.8) and  $\Delta s_z^{\text{III}} = s_z^{\text{III}}(x_0 + l_w) - s_z^{\text{III}}(x_0)$ . Note that  $\Delta s_z^{\text{III}}$  captures the spin dynamics in the system, including the fact that in the graphene/WS<sub>2</sub> region  $\tau_s^{\parallel} \neq \tau_s^{\perp}$ .  $\theta_{\text{SHE}}$  is then expressed as

$$\theta_{\text{SHE}} = \frac{|j_c^y|}{|j_{s,z}^{\text{III}}|} = \frac{e R_{\square} I R_{\text{ISHE}}}{R_a \Delta\mu_{s,z}^{\text{III}}}. \quad (5.15)$$

The solid line in Fig. 5.4c represents the scaled Eq. (5.15) resulting in  $\theta_{\text{SHE}} \sim 0.19\%$ . Similarly to the anisotropy measurements, the one dimensional model does not consider the spin diffusion towards the graphene/WS<sub>2</sub> arms. However, the effect of such diffusion can readily be taken into account by considering the projected spin current along  $x$  that generates  $V_{\text{ISHE}}$ , which is approximately  $\overline{j_s^{\text{III}}}/\pi \int_0^{\pi} \sin \phi d\phi = \overline{j_s^{\text{III}}}/2$ . Therefore, the spin Hall angle must be corrected by a factor  $\pi/2$  and thus  $\theta_{\text{SHE}} \sim 0.3\%$ .

### 5.8.5 Spin galvanic effect, SGE

In the SGE experiments, the spin density leading to the charge current density results directly from the spin current density  $j_{s,x}^{\text{III}}$ . Therefore, it is possible to adopt an SGE efficiency, namely  $\alpha_{\text{SGE}} = |j_c^y|/|j_{s,x}^{\text{III}}|$ , that is analogous to the spin Hall angle. The key difference compared to the analysis for ISHE is that here  $j_{s,x}^{\text{III}}$  is the spin current density for the spins projected in the  $x$  direction,

$$\alpha_{\text{SGE}} = \frac{|j_c^y|}{|j_{s,x}^{\text{III}}|} = \frac{e R_{\square} I R_{\text{SGE}}}{R_a \Delta\mu_{s,x}^{\text{III}}}. \quad (5.16)$$

As with the ISHE, by using independently measured properties of the device,  $\alpha_{\text{SGE}}$  remains as the only fitting parameter for  $R_{\text{SGE}}$ , appearing as a scaling factor. Figure 5.4 represents the scaled Eq. (5.16) from which  $\alpha_{\text{SGE}} \sim 0.1\%$  is extracted.

Similar results are obtained using a simplified approach by disregarding spin precession within the TMDC and adapting the results in Ref. [37] for the two-dimensional limit of the SHE material.

## References

- [1] Sinova, J., Valenzuela, S. O., Wunderlich, J., Back, C. & Jungwirth, T. Spin Hall effects. *Rev. Mod. Phys.* **87**, 1213–1260 (2015).
- [2] Manchon, A., Koo, H. C., Nitta, J., Frolov, S. M. & Duine, R. A. New perspectives for Rashba spin–orbit coupling. *Nat. Mater.* **14**, 871–882 (2015).
- [3] Soumyanarayanan, A., Reyren, N., Fert, A. & Panagopoulos, C. Emergent phenomena induced by spin–orbit coupling at surfaces and interfaces. *Nature* **539**, 509–517 (2016).
- [4] Sander, D. *et al.* The 2017 magnetism roadmap. *J. Phys. D: Appl. Phys.* **50**, 363001 (2017).
- [5] Garello, K. *et al.* SOT-MRAM 300MM integration for low power and ultrafast embedded memories. In *2018 IEEE Symposium on VLSI Circuits*, 81–82 (IEEE, 2018).
- [6] Ganichev, S. D. *et al.* Spin-galvanic effect. *Nature* **417**, 153–156 (2002).
- [7] Valenzuela, S. O. & Tinkham, M. Direct electronic measurement of the spin Hall effect. *Nature* **442**, 176–179 (2006).
- [8] Manipatruni, S. *et al.* Scalable energy-efficient magnetoelectric spin–orbit logic. *Nature* **565**, 35–42 (2018).
- [9] Manchon, A. *et al.* Current-induced spin-orbit torques in ferromagnetic and antiferromagnetic systems. *Rev. Mod. Phys.* **91**, 035004 (2019).
- [10] Bibes, M. & Barthelemy, A. Oxide spintronics. *IEEE Transactions on Electron Devices* **54**, 1003–1023 (2007).
- [11] Geim, A. K. & Grigorieva, I. V. Van der Waals heterostructures. *Nature* **499**, 419–425 (2013).
- [12] Han, W., Kawakami, R. K., Gmitra, M. & Fabian, J. Graphene Spintronics. *Nat. Nanotechnol.* **9**, 794–807 (2014).
- [13] Roche, S. *et al.* Graphene spintronics: The European flagship perspective. *2D Mater.* **2**, 030202 (2015).
- [14] Novoselov, K. S., Mishchenko, A., Carvalho, A. & Neto, A. H. C. 2D materials and van der Waals heterostructures. *Science* **353**, aac9439 (2016).
- [15] Wang, Z., Tang, C., Sachs, R., Barlas, Y. & Shi, J. Proximity-induced ferromagnetism in graphene revealed by the anomalous Hall effect. *Phys. Rev. Lett.* **114**, 016603 (2015).

- 
- [16] Leutenantsmeyer, J. C., Kaverzin, A. A., Wojtaszek, M. & van Wees, B. J. Proximity induced room temperature ferromagnetism in graphene probed with spin currents. *2D Mater.* **4**, 014001 (2016).
- [17] Benítez, L. A. *et al.* Strongly anisotropic spin relaxation in graphene–transition metal dichalcogenide heterostructures at room temperature. *Nat. Phys.* **14**, 303–308 (2017).
- [18] Mendes, J. B. S. *et al.* Spin-current to charge-current conversion and magnetoresistance in a hybrid structure of graphene and Yttrium Iron Garnet. *Phys. Rev. Lett.* **115**, 226601 (2015).
- [19] Dushenko, S. *et al.* Gate-tunable spin-charge conversion and the role of spin-orbit interaction in graphene. *Phys. Rev. Lett.* **116**, 106602 (2016).
- [20] Gmitra, M. & Fabian, J. Graphene on transition-metal dichalcogenides: A platform for proximity spin-orbit physics and optospintronics. *Phys. Rev. B* **92**, 155403 (2015).
- [21] Gmitra, M., Kochan, D., Högl, P. & Fabian, J. Trivial and inverted Dirac bands and the emergence of quantum spin Hall states in graphene on transition-metal dichalcogenides. *Phys. Rev. B* **93**, 155104 (2016).
- [22] Cummings, A. W., Garcia, J. H., Fabian, J. & Roche, S. Giant spin lifetime anisotropy in graphene induced by proximity effects. *Phys. Rev. Lett.* **119**, 206601 (2017).
- [23] Ghiasi, T. S., Ingla-Aynés, J., Kaverzin, A. A. & van Wees, B. J. Large proximity-induced spin lifetime anisotropy in transition-metal dichalcogenide/graphene heterostructures. *Nano Lett.* **17**, 7528–7532 (2017).
- [24] Garcia, J. H., Cummings, A. W. & Roche, S. Spin Hall effect and weak antilocalization in graphene/transition metal dichalcogenide heterostructures. *Nano Lett.* **17**, 5078–5083 (2017).
- [25] Offidani, M., Milletari, M., Raimondi, R. & Ferreira, A. Optimal charge-to-spin conversion in graphene on transition-metal dichalcogenides. *Phys. Rev. Lett.* **119**, 0196801 (2017).
- [26] Milletari, M., Offidani, M., Ferreira, A. & Raimondi, R. Covariant conservation laws and the spin Hall effect in Dirac-Rashba systems. *Phys. Rev. Lett.* **119**, 246801 (2017).
- [27] Avsar, A. *et al.* Spin–orbit proximity effect in graphene. *Nat. Commun.* **5**, 4875 (2014).
- [28] Kaverzin, A. A. & van Wees, B. J. Electron transport nonlocality in monolayer graphene modified with hydrogen silsesquioxane polymerization. *Phys. Rev. B* **91**, 165412 (2015).

- [29] Wang, Y., Cai, X., Reutt-Robey, J. & Fuhrer, M. S. Neutral-current Hall effects in disordered graphene. *Phys. Rev. B* **92**, 161411(R) (2015).
- [30] Tuan, D. V. *et al.* Spin Hall effect and origins of nonlocal resistance in adatom-decorated graphene. *Phys. Rev. Lett.* **117**, 176602 (2016).
- [31] Ribeiro, M., Power, S. R., Roche, S., Hueso, L. E. & Casanova, F. Scale-invariant large nonlocality in polycrystalline graphene. *Nat. Commun.* **8**, 2198 (2017).
- [32] Safeer, C. K. *et al.* Room-temperature spin Hall effect in graphene/MoS<sub>2</sub> van der waals heterostructures. *Nano Lett.* **19**, 1074–1082 (2019).
- [33] Raes, B. *et al.* Determination of the spin-lifetime anisotropy in graphene using oblique spin precession. *Nat. Commun* **7**, 11444 (2016).
- [34] Raes, B. *et al.* Spin precession in anisotropic media. *Phys. Rev. B* **95**, 085403 (2017).
- [35] Yan, W. *et al.* A two-dimensional spin field-effect switch. *Nat. Commun.* **7**, 13372 (2016).
- [36] Dankert, A. & Dash, S. P. Electrical gate control of spin current in van der waals heterostructures at room temperature. *Nat. Commun.* **8**, 16093 (2017).
- [37] Savero Torres, W. *et al.* Spin precession and spin Hall effect in monolayer graphene/Pt nanostructures. *2D Mater.* **4**, 041008 (2017).
- [38] Sánchez, J. C. R. *et al.* Spin-to-charge conversion using Rashba coupling at the interface between non-magnetic materials. *Nat. Commun.* **4**, 1944 (2013).
- [39] Lesne, E. *et al.* Highly efficient and tunable spin-to-charge conversion through Rashba coupling at oxide interfaces. *Nat. Mater.* **15**, 1261–1266 (2016).
- [40] Rojas-Sánchez, J.-C. *et al.* Spin to charge conversion at room temperature by spin pumping into a new type of topological insulator:  $\alpha$ -sn films. *Phys. Rev. Lett.* **116**, 096602 (2016).
- [41] Kimura, T., Otani, Y., Sato, T., Takahashi, S. & Maekawa, S. Erratum: Room-temperature reversible spin Hall effect [phys. rev. lett.98, 156601 (2007)]. *Phys. Rev. Lett.* **98**, 156601 (2007).
- [42] Ghiasi, T. S., Kaverzin, A. A., Blah, P. J. & van Wees, B. J. Charge-to-spin conversion by the Rashba–edelstein effect in two-dimensional van der waals heterostructures up to room temperature. *Nano Lett.* **19**, 5959–5966 (2019).

## Chapter 6

# Conclusions and recommendations

Graphene spintronics is a vivid research field, which is continuously seeking for the understanding of fundamental phenomena that may lead to future novel devices. Spin-orbit coupling, as mentioned during this thesis, is a powerful tool that enables the electrical control of spins in graphene/TMDC devices. The study performed in this thesis goes in the direction of contributing to a better understanding of the physics underpinning SOC in graphene. The obtained results allowed us to obtain several relevant contributions to the field:

- We demonstrated anisotropic spin relaxation in graphene/TMDC van der Waals heterostructures at room temperatures. Such anisotropic character is characterized by the anisotropy ratio  $\zeta = \tau_s^{\parallel} / \tau_s^{\perp}$ . The anisotropic nature of the spin relaxation is a direct consequence of the imprinted spin-orbit coupling and the spin valley locking in graphene by the TMDC.
- We observed a fast in-plane spin relaxation, which is in the order of a few ps ( $\sim 5$  ps), such an efficient in-plane spin relaxation is presumably mediated by intervalley scattering. The out-plane-spins relax around ten times slower than the in-plane. Thus, graphene/TMDC acts as a filter with a transmission that depends on the spin orientation.
- We showed that the spin dynamics in graphene/WS<sub>2</sub> heterostructures can be modulated by electrically gating. The behavior goes from anisotropic to nearly isotropic spin relaxation when the applied back-gate voltage goes from 50 V to -50 V. Far away from the charge neutrality point, the out-of-plane spin texture is expected to get reduced; thus, even in the presence of intervalley scattering, the in-plane spins relax less.

The obtained results provide insight into the physics underpinning spin and valley dynamics, and open a door for novel approaches to control spin and valley information.

- We have demonstrated for the first time simultaneous room-temperature SHE and SGE induced in graphene by proximity of a WS<sub>2</sub>. Each effect is detected in separate experiments and is established by spin precession measurements. The devices and experimental protocols were carefully developed so that the

interpretation is self-evident and does not require any sophisticated modelling. We showed that the TMDC is insulating, demonstrating that the transport occurs in the modified graphene, thus the SGE and SHE originate from proximity effects.

- We observed that the SHE and SGE present remarkable tunability in magnitude and sign, peaking nearby the CNP and decreasing rapidly away from it. In our experiments, the SHE (SGE) efficiency is the only fitting parameter. Other parameters characterizing the spin dynamics are extracted from complementary experiments. The obtained spin-to-charge conversion efficiencies can be more than one order of magnitude larger than originally predicted for intrinsic effects, indicating that current understanding is still incomplete. Theoretical results, which consider only intrinsic effects, are compatible with the experimental  $\theta_{\text{SHE}}$  only for weak intervalley scattering while yielding an  $\alpha_{\text{SGE}}$  that is at least one order of magnitude smaller than the experimental value.
- We demonstrated that the charge-to-spin conversion coexists with large spin relaxation anisotropy. Experiments in the same device show that the spin lifetime for spins pointing out of plane is several times larger than for spins pointing in plane. Notably, such anisotropy is incompatible with intrinsic mechanisms; together with the large efficiency of the spin-to-charge conversion, it suggests the presence of additional extrinsic contributions, which have yet to be identified. Within the recent theory, a large SHE has been deemed incompatible with anisotropic spin relaxation because it signals the presence of intervalley scattering, which effectively reduces the mass of the carriers and leads to the suppression of the SHE. A larger localized SOC can be mediated by localized defects, such as sulfur vacancies in  $\text{WS}_2$ , while  $\theta_{\text{SHE}}$  could be enhanced by resonant scattering as it has been proposed for metallic adatoms.

Because of the seeking for a complete control of the spins in gr/TMDC systems is still a challenge, we present the following recommendations for future works:

The results present in Chap. 4 demonstrate that the spin relaxation anisotropy in graphene/TMDC heterostructures is a fingerprint of the SOC present in graphene. Such SOC can be tuned by electrostatic gating, resulting in a tunable spin dynamics. However, in graphene/TMDC systems, the imprinted SOC is always present in graphene and felt by the propagating spins. Recent theoretical works have anticipated that in bilayer graphene (BLG) on TMDC substrates, a complete ON/OFF of the imprinted SOC can be fulfilled. The BLG/TMDC systems have an environment with a spatially inhomogeneous SOC, high only on the layer adjacent to the TMDC. In such a scenario, carriers can be shifted between layers with strong and weak SOC by applying a transverse electric field [1, 2]. This renders the SOC strength felt by the carriers strongly dependent on the which-layer they propagate. Such behavior



establishes a highly efficient field-effect spin-orbit valve, making BLG/TMDC a potential platform for a field-effect spin transistor.

In principle, in BLG/TMDC systems, we can experimentally probe the spin-orbit valve using spin precession measurements in non-local spin-valve devices. Suppose that by electrostatic gating, we tune the SOC and the Fermi level in the conduction band of the BLG. In that case, we should observe a fast relaxation of the in-plane spins together with a highly anisotropic spin relaxation. On the contrary, if we can tune the SOC in the valence band of the BLG while keeping the Fermi level in the conduction band, the spins can travel easily with no extra relaxation driven by the imprinted SOC. Such signatures will constitute a direct observation of a spin-orbit valve with an ON/OFF of the SOC. In appendix B, we present some preliminary results of spin transport measurements in BLG/TMDC systems

At the same time, it is important to notice that thermal gradients can affect the propagation of the spins in our devices. Previous studies done at the group showed that hot carriers, created by thermal gradients, can enhance the graphene spin signal close to the CNP [3]. Such gradients can be more pronounced in samples with high electronic mobilities, where the created hot carriers can reach longer distances than in the common SiO<sub>2</sub> [4]. We started to perform thermometric measurements in high-mobility samples comprising graphene on an hBN substrate (appendix B); however, spin transport measurements on those devices are still required.

Another important point to address experimentally is the SOC's control via the twisted angle between gr and the TMDC [5, 6]. Such experiments would demand a novel experimental approach that could allow us to vary the twist angle systematically. In graphene/hBN heterostructures, e. g, it is predicted to find a remarkable change in  $\zeta$  due to the presence of a twist angle [7]. It is also desirable spin transport studies in gr/TMDC at shallow temperatures where the intervalley scattering

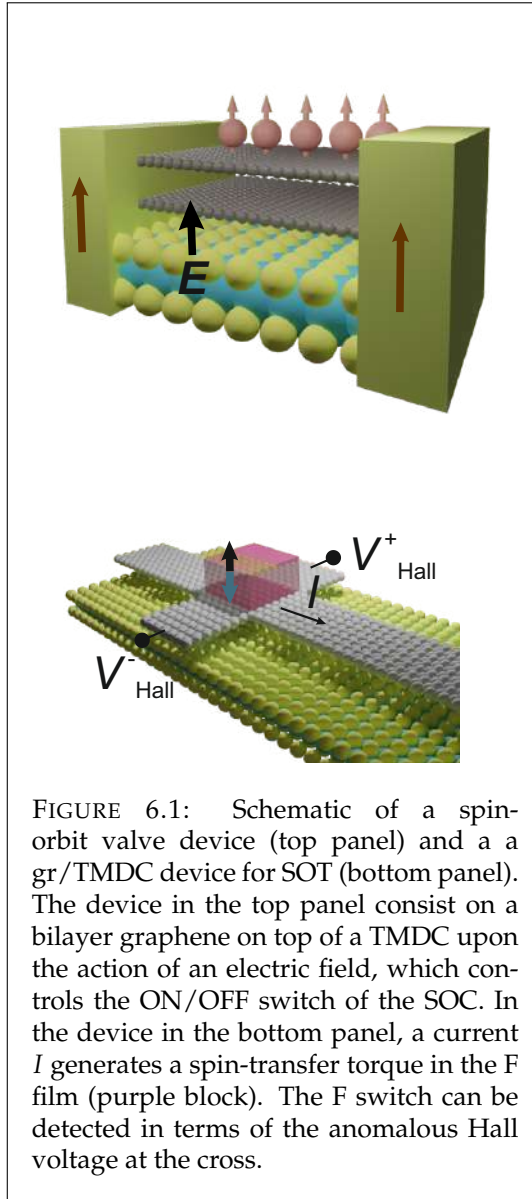


FIGURE 6.1: Schematic of a spin-orbit valve device (top panel) and a gr/TMDC device for SOT (bottom panel). The device in the top panel consist on a bilayer graphene on top of a TMDC upon the action of an electric field, which controls the ON/OFF switch of the SOC. In the device in the bottom panel, a current  $I$  generates a spin-transfer torque in the F film (purple block). The F switch can be detected in terms of the anomalous Hall voltage at the cross.

is strongly reduced.

Regarding our spin-to-charge interconversion studies, an immediate application is to explore the possibility of switching the magnetization of an F layer in a gr/WS<sub>2</sub> by the SOT. One possible experiment could be the one displayed in Fig. 6.1 where an electrical current flowing through the modified graphene generates an in-plane and out-of-plane spin accumulation underneath the FM layer, which can be transferred to the FM, causing it switches [8]. This device would have the advantages of the excellent and tunable graphene electrical properties combined with the SOC coming from the TMDC.

It has recently been shown spin-to-charge interconversion in gr heterostructures with different semiconducting TMDCs, like MoS<sub>2</sub> [9], WSe<sub>2</sub> [10], or WS<sub>2</sub> (this thesis, and also [11, 12]). Additionally, experiments with semimetallic TMDCs are gaining attention due to the promising results [13–15] and theoretical predictions [16].

Finally, another strong candidate to explore spin to charge interconversion is the dual gated bilayer graphene. Recently, it was shown that upon the action of an electric field, the system acquires a strong spin-Valley coupling, leading to an anisotropic spin relaxation [17, 18]. Such spin-valley coupling can allow, in principle, a nonvanishing spin Hall conductivity mediated by a skew scattering [19] (theoretical calculations show that in a pure Rashba system, the spin-Hall conductivity is null [19]).

## References

- [1] Khoo, J. Y., Morpurgo, A. F. & Levitov, L. On-demand spin-orbit interaction from which-layer tunability in bilayer graphene. *Nano Lett.* **17**, 7003–7008 (2017).
- [2] Gmitra, M. & Fabian, J. Proximity effects in bilayer graphene on monolayer WSe<sub>2</sub>: Field-effect spin valley locking, spin-orbit valve, and spin transistor. *Phys. Rev. Lett.* **119**, 146401 (2017).
- [3] Sierra, J. F. *et al.* Thermoelectric spin voltage in graphene. *Nat. Nanotechnol.* **13**, 107–111 (2017).
- [4] Sierra, J. F., Neumann, I., Costache, M. V. & Valenzuela, S. O. Hot-carrier seebeck effect: Diffusion and remote detection of hot carriers in graphene. *Nano Lett.* **15**, 4000–4005 (2015).
- [5] Li, Y. & Koshino, M. Twist-angle dependence of the proximity spin-orbit coupling in graphene on transition-metal dichalcogenides. *Phys. Rev. B* **99**, 075438 (2019).
- [6] David, A., Rakyta, P., Kormányos, A. & Burkard, G. Induced spin-orbit coupling in twisted graphene-transition metal dichalcogenide heterobilayers: Twistronics meets spintronics. *Phys. Rev. B* **100**, 085412 (2019).

- [7] Zollner, K., Gmitra, M. & Fabian, J. Heterostructures of graphene and hBN: Electronic, spin-orbit, and spin relaxation properties from first principles. *Phys. Rev. B* **99**, 125151 (2019).
- [8] Miron, I. M. *et al.* Perpendicular switching of a single ferromagnetic layer induced by in-plane current injection. *Nature* **476**, 189–193 (2011).
- [9] Safeer, C. K. *et al.* Room-temperature spin hall effect in graphene/MoS<sub>2</sub> van der waals heterostructures. *Nano Lett.* **19**, 1074–1082 (2019).
- [10] Herling, F. *et al.* Gate tunability of highly efficient spin-to-charge conversion by spin hall effect in graphene proximitized with WSe<sub>2</sub>. *APL Materials* **8**, 071103 (2020).
- [11] Benítez, L. A. *et al.* Tunable room-temperature spin galvanic and spin hall effects in van der waals heterostructures. *Nat. Mater.* **19**, 170–175 (2020).
- [12] Ghiasi, T. S., Kaverzin, A. A., Blah, P. J. & van Wees, B. J. Charge-to-spin conversion by the Rashba–edelstein effect in two-dimensional van der waals heterostructures up to room temperature. *Nano Lett.* **19**, 5959–5966 (2019).
- [13] Safeer, C. K. *et al.* Large multidirectional spin-to-charge conversion in low-symmetry semimetal MoTe<sub>2</sub> at room temperature. *Nano Lett.* **19**, 8758–8766 (2019).
- [14] Zhao, B. *et al.* Unconventional charge-spin conversion in weyl-semimetal WTe<sub>2</sub>. *Adv. Mater.* **32**, 2000818 (2020).
- [15] Hoque, A. M., Khokhriakov, D., Karpiak, B. & Dash, S. P. Charge-spin conversion in layered semimetal TaTe<sub>2</sub> and spin injection in van der Waals heterostructures. *Phys. Rev. Research* **2**, 033204 (2020).
- [16] Vila, M. *et al.* Charge-to-spin interconversion in low-symmetry topological materials. *ArXiv* [2007.02053](https://arxiv.org/abs/2007.02053).
- [17] Leutenantsmeyer, J. C., Ingla-Aynés, J., Fabian, J. & van Wees, B. J. Observation of spin-valley-coupling-induced large spin-lifetime anisotropy in bilayer graphene. *Phys. Rev. Lett.* **121**, 127702 (2018).
- [18] Xu, J., Zhu, T., Luo, Y. K., Lu, Y.-M. & Kawakami, R. K. Strong and tunable spin-lifetime anisotropy in dual-gated bilayer graphene. *Phys. Rev. Lett.* **121**, 127703 (2018).
- [19] Milletari, M., Offidani, M., Ferreira, A. & Raimondi, R. Covariant conservation laws and the spin hall effect in dirac-rashba systems. *Phys. Rev. Lett.* **119**, 246801 (2017).

## Appendix A

# Supplementary material of chapter 5

### Theoretical calculation of the spin Hall conductivity

The quantum simulations (Fig. 5.7b) were developed by José H. García, thus the analysis present in this section.

The electronic properties of clean graphene are well described by a Dirac's Hamiltonian [1],

$$H_{\text{gr}} = \hbar v_{\text{F}}(\tau_z \sigma_x k_x + \sigma_y k_y), \quad (\text{A.1})$$

with  $v_{\text{F}} \approx 10^6$  the Fermi velocity,  $\tau_z = \pm 1$ , and  $\sigma_\alpha$  with  $\alpha = x, y, z$ , the Pauli matrices acting on the pseudospin subspace. This Hamiltonian generates a linear dispersion relation at two inequivalent points of the Brillouin zone, K and K', which are described by choosing  $\tau_z = 1$  or  $-1$ , respectively. The proximity with a WS<sub>2</sub> monolayer modifies the electronic properties of graphene due to a combination of the periodic potential, originating from the interaction between the two different layers, and a weak hybridization between the carbon and the tungsten atoms. This combination opens a small electronic gap and imprints in graphene an effective spin-orbit coupling (SOC); both effects can be captured by the following Hamiltonian [2],

$$H_{\text{gr}} = H_{\text{gr}} + \Delta \sigma_z + (\lambda_{\text{I}} s_z + \lambda_{\text{VZ}} s_0) \tau_z \sigma_z + \lambda_{\text{R}} (\tau_z \sigma_x s_y - \sigma_y s_x), \quad (\text{A.2})$$

where the first term is the Hamiltonian for pristine graphene, the second term opens an energy gap in the spectrum of magnitude  $\Delta$ , the third term is composed by the intrinsic and a valley-Zeeman SOC of strengths  $\lambda_{\text{I}}$  and  $\lambda_{\text{VZ}}$ , respectively, and the last term is the Rashba SOC with magnitude  $\lambda_{\text{R}}$ .

To model the experimental results, the Hamiltonian in Eq. (A.2) was parameterized from *ab-initio* calculations and the set of parameters for WS<sub>2</sub> as reported in Table I. The table includes the parameters extracted from density functional theorem (DFT) [2] and those used to better match the experimental features, which are about a factor two larger.

There is another type of SOC that is predicted by DFT, referred as PIA [2], but depends linearly with the momentum and, therefore, does not contribute nearby the

	$v_F$ (nm/fs)	$\Delta$ (meV)	$\lambda_I$ (meV)	$\lambda_{VZ}$ (meV)	$\lambda_R$ (meV)
<i>ab-initio</i>	0.8463	1.31	0.095	-1.115	0.36
Effective parameters	0.8463	2.62	-0.19	-2.230	0.0

TABLE A.1: Table of parameters used for the model in Eq. (A.2). The first row corresponds to the parameters extracted from DFT in Ref. [2], the second row corresponds to the parameters used in our calculations to simulate the experimental curves.

charge neutrality point. Additionally, although the Rashba interaction is essential for the ISGE, its contribution to the SHE is small and is also neglected [3, 4]. Within these approximations, the following dispersion relation is obtained analytically,

$$\varepsilon(k, \tau_z, s_z) = s\lambda_{VZ} \pm \sqrt{\hbar(v_F k)^2 + (\Delta - \tau_z s_z \lambda_I)^2}. \quad (\text{A.3})$$

where there are four independent Dirac cones defined by  $\tau_z = \pm 1$  and  $s_z = \pm 1$ . The spin Hall conductivity  $\sigma_{xy}^z$  is calculated by summing the individual contributions of each cone. Each contribution can be computed analytically at zero temperature by following the procedure described in Refs. [5, 6], resulting in the following expression,

$$\sigma_{xy}^z(\varepsilon_F) = \frac{e^2}{2h} \sum_{s_z, \tau_z = \pm 1} \tau_z \left[ \frac{(\Delta + s\tau_z \lambda_I) \theta(|\Delta + s_z \tau_z \lambda_I| - |\varepsilon_F - \tau_z s_z \lambda|)}{\sqrt{(\Delta + s_z \tau_z \lambda_I)^2 + (\varepsilon_F - \tau_z s_z \lambda)^2}} + \theta(-|\Delta + s_z \tau_z \lambda_I| + |\varepsilon_F - \tau_z s_z \lambda|) \right]. \quad (\text{A.4})$$

States both *at* and *below* the Fermi level contribute to  $\sigma_{xy}^z$ . Therefore, to obtain the temperature the following integral needs to be computed,

$$\sigma_{xy}^z(\mu, T) = \int_{-\infty}^{\infty} f(\varepsilon - \mu, T) K(\varepsilon) d\varepsilon, \quad (\text{A.5})$$

where  $f(\mu, T)$  is the Fermi-Dirac distribution at temperature  $T$  and chemical potential  $\mu$ , and  $K(H, \varepsilon)$  the integration kernel that can be derived from the Kubo-Bastin formula [7, 8]. At zero temperature, the upper integration limit is set by the Fermi-Dirac distribution, and therefore, one can use the second fundamental theorem of calculus to determine the value of  $K(\varepsilon)$  in terms of the conductivity at zero temperature,

$$\frac{d\sigma_{xy}^z(\varepsilon_F, 0)}{d\varepsilon_F} = \frac{d}{d\varepsilon_F} \int_{-\infty}^{\varepsilon_F} K(\varepsilon) d\varepsilon = K(\varepsilon_F). \quad (\text{A.6})$$

Finally, the finite temperature  $\sigma_{xy}^z$  presented in the Main Text is obtained as follows,

$$\sigma_{xy}^z(\mu, T) = \int_{-\infty}^{\infty} f(\varepsilon - \mu, T) \frac{d\sigma_{xy}^z(\varepsilon, 0)}{d\varepsilon} d\varepsilon. \quad (\text{A.7})$$

Within this model, the asymmetric behavior with Fermi energy in Fig. 4 (main

text), which is more prominent at low temperatures, can be explained through symmetry arguments regarding the Berry phases at the four Dirac cones of the system (spin up K, spin down K, spin up K', spin down K'). In the absence of SOC, these four cones are degenerate, and any possible Berry phase from each of them is compensated by another due to time-reversal symmetry. However, this degeneracy is lifted by the valley-Zeeman effect induced in graphene due to proximity with the TMDC [see Fig. 1b in [3]], leaving only two cones (spin up K, spin down K' for instance). Due to inversion and time-reversal symmetries, these cones must have opposite Berry phase and opposite spins, leading to a non-vanishing spin Hall conductivity close to the charge neutrality point, with opposite signs for electrons and holes as deduced using similar symmetry arguments. The presence of intrinsic SOC of the Kane-Mele type produces an additional asymmetry in the splitting at the conduction and valence bands, also leading to asymmetric spin transport [5]. The combination of these two terms therefore results in spin-hall-conductivity peaks having opposite sign and different magnitude for electrons and holes.

When thermal broadening is considered, the peaks merge into a single peak. The sign of the spin Hall conductivity at high temperature is ultimately determined by the sign of the original peak with the largest magnitude.

*Note:* In Ref. [8] the graphene is considered to be on top of the TMDC, using a sign convention that is different from that of the experiments (Fig. 5.7 Main Text). This explains the opposite sign in the  $\sigma_{xy}^z$  that was calculated originally [8], even though the parameters that are assumed in those calculations are similar to those used in the present work.

## SEM image of the device used to measure the spin-charge interconversion

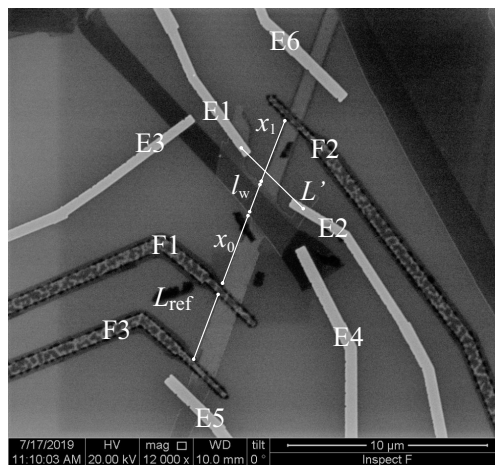


FIGURE A.1: SEM image of the device used in Chapter 5, where  $L_{ref} = 3.8$ ,  $x_0 = 4.2$ ,  $l_w = 1.3$ ,  $x_1 = 4$  and  $L' = 4.5 \mu\text{m}$ .

## Charge transport measurements

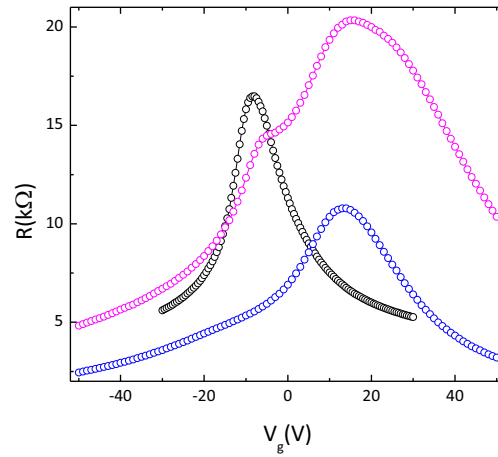


FIGURE A.2: RT charge transport properties in different regions of the device. The blue and magenta curves correspond to the resistance measured when we measure between F3 and F1 (reference channel) and between F1 and F2, respectively. In both situations the current flows from E5 to E6. The black curve is the two-terminal resistance measured in the modified graphene region, between E1 and E2. In this region graphene is covered by the TMD, reducing its exposure during the nanofabrication process thus the different doping level in this region.

## Measurement of spin Hall signals obtained with the spin injector F1 and F2

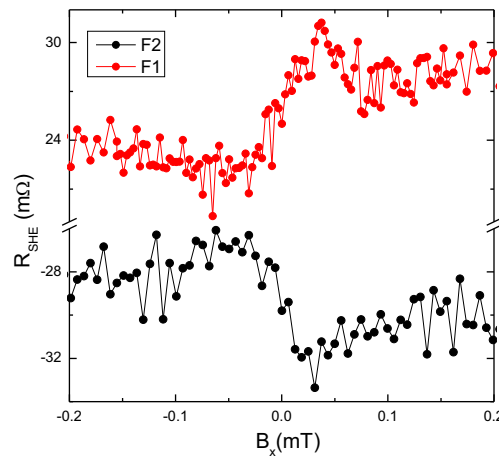


FIGURE A.3: RT SHE measurements at  $V_g = -6$  V using F1 (red) and F2 (black) as spin detectors. In prior the measurements, F1 and F2 are aligned along  $\hat{y}$ . The mirror behavior displayed by the SHE signal verifies the spin-related origin of the signal.

## Measurement of inverse spin Hall at 100 K

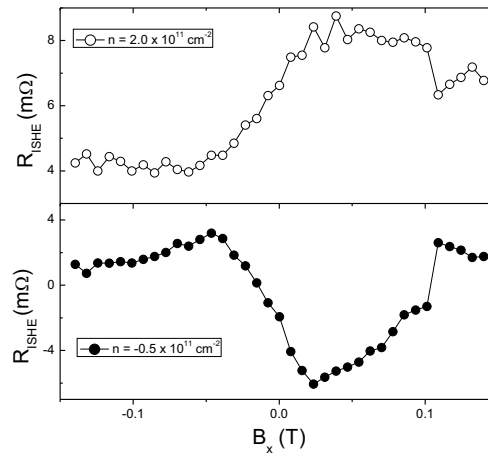


FIGURE A.4: Spin precession measurements in the ISHE configuration using F1 as spin detector at 100 K for the extrema positions showed in Fig. 5.7. The measurements were obtained saturating F1 and F2 in  $\hat{y}$  and sweeping  $B_x$  from negative to positive. The reverse response of the signal in the two extrema confirm the sign change of the spin hall angle.

## References

- [1] Neto, A. H. C., Guinea, F., Peres, N. M. R., Novoselov, K. S. & Geim, A. K. The electronic properties of graphene. *Reviews of Modern Physics* **81**, 109–162 (2009).
- [2] Gmitra, M., Kochan, D., Högl, P. & Fabian, J. Trivial and inverted dirac bands and the emergence of quantum spin hall states in graphene on transition-metal dichalcogenides. *Phys. Rev. B* **93**, 155104 (2016).
- [3] Garcia, J. H., Vila, M., Cummings, A. W. & Roche, S. Spin transport in graphene/transition metal dichalcogenide heterostructures. *Chem. Soc. Rev.* **47**, 3359–3379 (2018).
- [4] Safeer, C. K. *et al.* Room-temperature spin hall effect in graphene/MoS2 van der waals heterostructures. *Nano Lett.* **19**, 1074–1082 (2019).
- [5] Dyrdał, A., Dugaev, V. K. & Barnaś, J. Spin hall effect in a system of dirac fermions in the honeycomb lattice with intrinsic and rashba spin-orbit interaction. *Phys. Rev. B* **80** (2009).
- [6] Sinitsyn, N. A., Hill, J. E., Min, H., Sinova, J. & MacDonald, A. H. Charge and spin hall conductivity in metallic graphene. *Phys. Rev. Lett.* **97** (2006).
- [7] Bastin, A., Lewiner, C., Betbeder-Matibet, O. & Nozieres, P. Quantum oscillations of the hall effect of a fermion gas with random impurity scattering. *Solid State Commun.* **9**, iii (1971).



- 
- [8] Garcia, J. H., Cummings, A. W. & Roche, S. Spin hall effect and weak antilocalization in graphene/transition metal dichalcogenide heterostructures. *Nano Lett.* **17**, 5078–5083 (2017).

## Appendix B

# Spin transport in BLG and thermoelectrical measurements in gr/hBN

### B.1 Spin-orbit valve in bilayer graphene in proximity to a TMDC

In principle, in BLG/TMDC systems, we can experimentally probe the spin-orbit valve using spin precession measurements in non-local spin-valve devices (see Chap. 6). We fabricated spin-devices comprising hBN/BLG/WSe<sub>2</sub> on top of a SiO<sub>2</sub>/p-Si

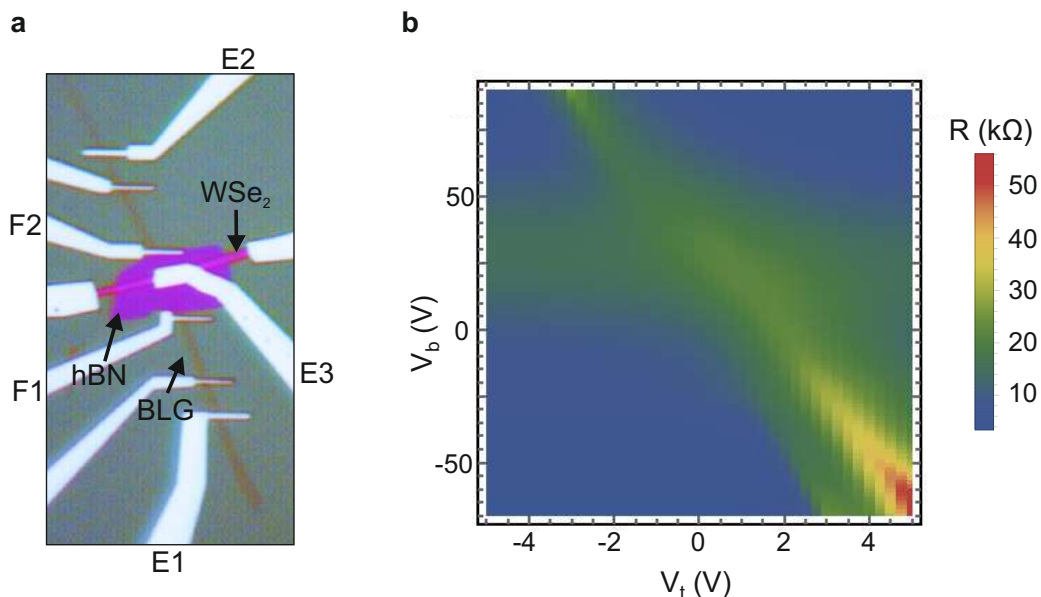


FIGURE B.1: **Dual-gated bilayer graphene/WSe<sub>2</sub>**. **a**, optical picture of a spin-device comprising a BLG/WSe<sub>2</sub>/hBN heterostructure. E1, E2 and E3 are metallic electrodes while F1 and F2 are spin-sensitive electrodes. **b**, BLG/WSe<sub>2</sub> electrical resistance as a function of top and back gate voltages ( $V_t$ ,  $V_b$ ). The resistance peaks at  $V_b^0 \approx 40$  V and  $V_t \approx 0.3$  V, correspond to an offset coming from an environmental doping. Data acquired at 77 K

substrate (see Fig. B.1a). The  $p$ -Si is used to globally back-gate the device. An electrode on top of the hBN (E3 in Fig. B.1) is used to locally top-gate the heterostructure, allowing us to control the applied transverse electric field and the carrier density  $n$ .

The top and back gate voltages ( $V_t$  and  $V_b$ ) induce the displacement fields  $D_t = -\epsilon_t(V_t - V_t^0)/d_t$  and  $D_b = +\epsilon_b(V_b - V_b^0)/d_b$ , respectively. Here  $\epsilon$  and  $d$  are the dielectric constant and thickness of the dielectric layer, and  $V^0$  is the effective offset voltage due to initial environmental induced carrier doping. Upon electrical gating, the difference  $\delta D = D_b - D_t$  induces a shift of the Fermi energy, thus a net carrier density  $n$ . The average of the two,  $\bar{D} = (D_b + D_t)/2$ , drives the inversion of the BLG/TMDC conduction and valence bands. Fig. B.1b shows the resistance drop measured at 77 K between the contacts F1 and F2 as a function of  $V_t$  and  $V_g$ . The peaks in the resistance curve identify the CNPs. The narrow peak, whose position follows  $V_b + aV_t = b$  (with  $a$  and  $b$  positive constants), marks the CNP of the BLG covered by the top gate. The increased peak resistance is the result of a gap opening. The broad peak at  $V_b^0 \sim 40V$ , whose position is independent of  $V_t$ , marks the CNP of the BLG that is not covered by the top gate.

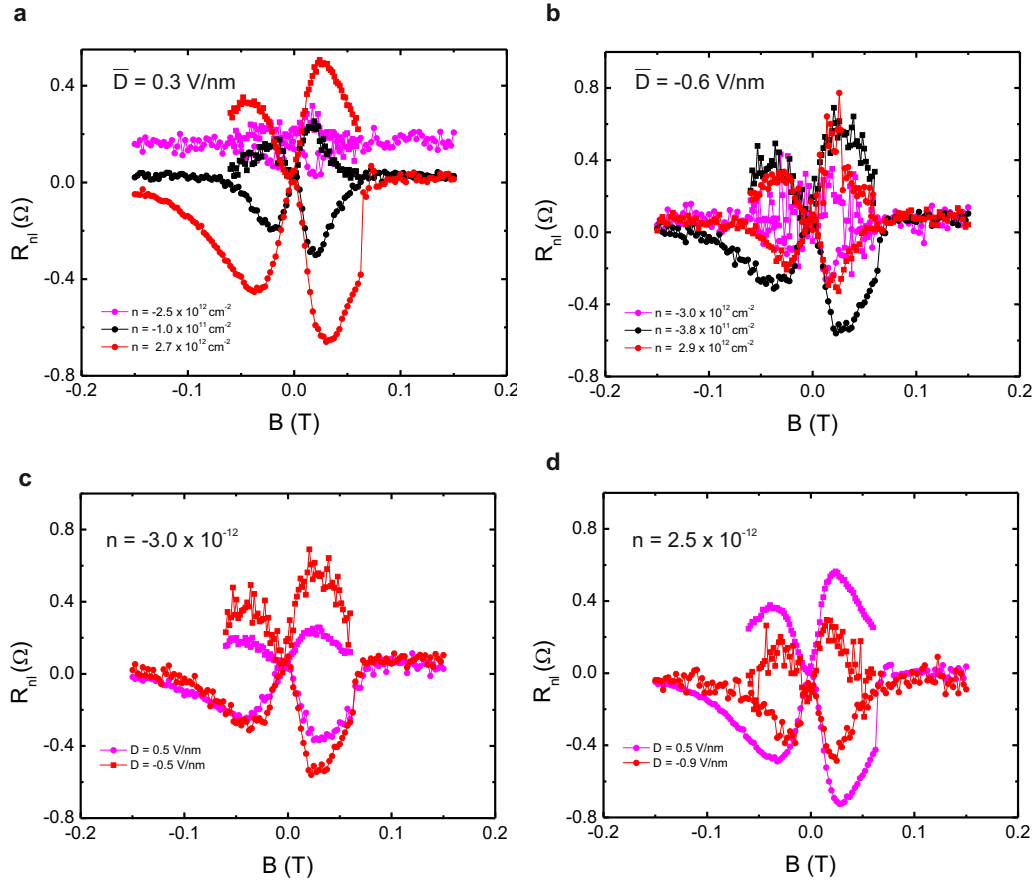


FIGURE B.2: Spin precession measurements in bilayer graphene/WSe<sub>2</sub> applying an in-plane magnetic field. In **a**, **b**, we show a set of measurement in which we keep constant the displacement field  $\bar{D}$  and we change the doping level. In **c**, **d**, we maintain fixed the carrier density  $n$  and changed  $\bar{D}$ .

Turning our attention to spin transport, we performed non-local spin precession measurements with an in-plane magnetic field in the device shown in Fig. B.2a at 77 K. Fig. B.2a, b shows a set of spin transport signal  $R_{nl}$  as a function of different charge densities for two constant positive and negative  $\bar{D}$ . The  $n$  values correspond to the CNP, hole and electron transport regime. The measurements are obtained in the parallel (circles) and antiparallel (squares) magnetic configuration of the electrodes. In Fig. B.2c, d we show the spin precession response for two constant carrier densities and different displacement fields  $\bar{D}$ .

First, we observe that no matter the applied  $\bar{D}$  and the doping level, the signal at  $B = 0$  T is close to zero, increasing with  $B$  and reaching a maximum at  $B \sim 30$  mT. Such behavior is a typical response of an anisotropic spin dynamics with  $\tau_s^{\parallel} < \tau_s^{\perp}$ . Fig. B.2a, b indicates that the spin SOC is always present in our devices, contrary to what we expected. We observe a modulation in the curve shapes, probably caused by changes in the spin parameters in the BLG [1, 2] or due to modulation of the SOC. However, we do not observe any signs of an ON/OFF switching of the SOC, as proposed in Ref. [3], even though, it was recently confirmed using capacitance measurements at 50 mK [4]. The temperature broadening and the charge puddles most likely present in our sample hampered the spin-orbit valve's observation. New spin transport measurements close to the CNP in cleaner devices, e.g., using hBN as a substrate, and at lower temperatures, are still required.

## B.2 Thermoelectric measurements in fully encapsulated graphene

Besides spin transport phenomena, we started to study thermoelectric effects in lateral devices based on graphene and the interaction between spin and heat currents. We fabricated high quality graphene device fully encapsulated with hBN with the aim to characterize their thermoelectric response and the presence of hot carriers, and in a near future study its effects on the spin propagation.

A device sketch is shown in Fig. B.3a. There, a bias current  $I_{dc}$  is applied between the metallic electrodes E1 and E2 is used to generate hot carriers, which diffuse along the graphene channel, building thermal gradients which can be as large as hundreds of K between the injector and the detector. By measuring the non local voltage  $V_{nl}$  in the remote detector (between E3 and E4) as a function of the bias current it is possible to identify the presence of hot carriers in the system.

We start by estimating the thermopower (Seebeck Coefficient) of our devices from the square resistance  $R$  vs. the gate voltage  $V_g$  (Fig. B.3b), using the Mott relation:

$$S_{\text{Mott}} = \frac{\pi^2 k_B T}{3e} \left. \frac{d \ln R}{\mu} \right|_{\mu=\mu_F}, \quad (\text{B.1})$$

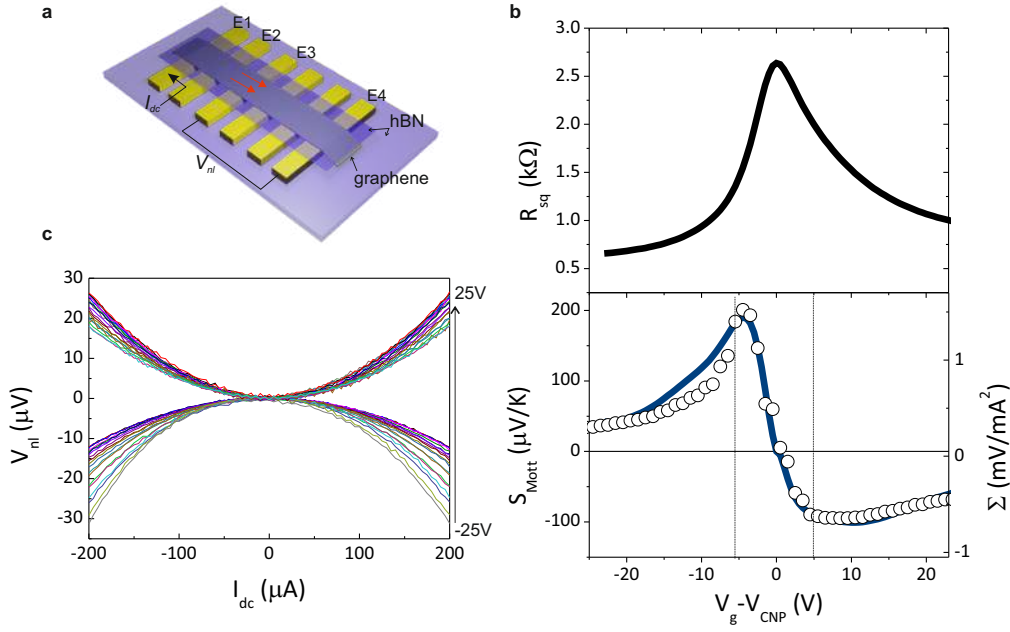


FIGURE B.3: **Thermoelectric measurements in graphene/hBN devices at RT.** **a**, schematic representation of the device under test. **b**, In the top panel the measured square resistance  $R_{sq}$  as a function of the gate voltage  $V_g$ . In the bottom panel the calculated Seebeck coefficient using Eq. (B.1), and the quadratic fitting coefficient  $V_{nl} = \Sigma I_{dc}$  (obtained from **c**). **c**, Non-local thermoelectric response  $V_{nl}$  vs the injected current  $I_{dc}$ . Data acquired at RT.

with  $e$ ,  $k_B$  the electron's charge and the Boltzman constant, respectively.  $\mu$  refers to the chemical potential. To compare  $S_{Mott}$  with the actual thermoelectric response of the device we measured  $V_{nl}$  vs  $I_{dc}$  in the heater. Figure B.3c shows the results at room temperature. Owing to the nature of the carriers in the system, we observe a change from an upward to a downward response with the gate voltage  $V_g$ , as expected from a thermoelectric effect. In addition, it is observed that  $V_{nl} = -\Sigma I_{dc}$ , which indicates Joule dissipation in the device.

As compared to room temperature, at 77 K we observe an increase of the non-local signals and hot carrier propagation at remote distances as large as  $6 \mu\text{m}$  from the injection point. While at low injected powers the response appears to be associated to Joule dissipation, when the current  $I_{dc}$  (i.e with the injected power) is increased, we immediately observe a scaling between  $V_{nl}$  and  $I_{dc}$  which points out to the presence of hot carriers with a cooling mechanism dominated by supercollisions. We finally observe deviations from the simple supercollision model at higher powers that might be ascribed to a coupling of carrier in the graphene with (optical) phonon modes in the hexagonal boron nitride substrate. Nevertheless, more systematic thermometric measurements on cleaner devices and on graphene/WSe<sub>2</sub> devices, where the mobility can surpass the upper phonon-limited room-temperature mobility of graphene [5] are of great interest. In particular, high quality devices would enable to access the hydrodynamic regime, where strong interactions lead to viscous, fluid-like, charge flow.

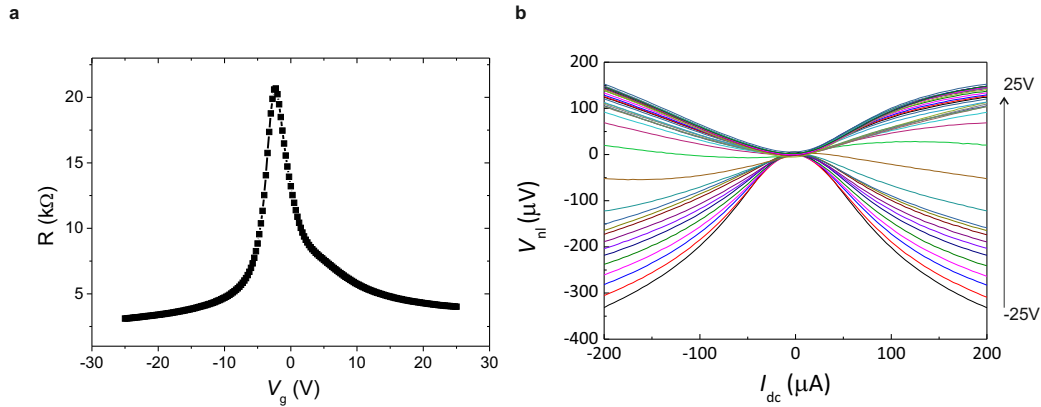


FIGURE B.4: **Thermoelectric measurements in graphene/hBN devices at 77K.** **a**, Graphene resistance as a function of the back gate voltage. **b**, Non-local thermoelectric response  $V_{nl}$  vs the injected current  $I_{dc}$ . Data acquired at RT, at  $|I_{dc}| > 75 \mu A$  a deviation from the quadratic response is observed.

## References

- [1] Leutenantsmeyer, J. C., Ingla-Aynés, J., Fabian, J. & van Wees, B. J. Observation of spin-valley-coupling-induced large spin-lifetime anisotropy in bilayer graphene. *Phys. Rev. Lett.* **121**, 127702 (2018).
- [2] Xu, J., Zhu, T., Luo, Y. K., Lu, Y.-M. & Kawakami, R. K. Strong and tunable spin-lifetime anisotropy in dual-gated bilayer graphene. *Phys. Rev. Lett.* **121**, 127703 (2018).
- [3] Gmitra, M. & Fabian, J. Proximity effects in bilayer graphene on monolayer  $WSe_2$ : Field-effect spin valley locking, spin-orbit valve, and spin transistor. *Phys. Rev. Lett.* **119**, 146401 (2017).
- [4] Island, J. O. *et al.* Spin-orbit-driven band inversion in bilayer graphene by the van der Waals proximity effect. *Nature* **571**, 85–89 (2019).
- [5] Banszerus, L. *et al.* Extraordinary high room-temperature carrier mobility in graphene- $WSe_2$  heterostructures. *arXiv: 1909.09523*.

## Appendix C

# Recipes for the sample fabrication

### Fabrication of graphene devices on a Si-Substrate

Here we itemize the steps followed for the fabrication of our devices

- Oxygen plasma cleaning of the 440 nm  $\text{SiO}_2/p^{++}\text{Si}$  substrates at a power of 400 W for around 10 min.
- Mechanical exfoliation of graphene from Highly oriented pyrolytic graphite (HOPG). We use the blue tape SPV-224PR-MJ, which is a PVC base surface protective tape from Nitto.
- Spin-coating: 1 layer of MMA A2 and PMMA A4 at 5000 rpm for 40 s followed by bake out at 180°C for 1.5 min and 5 min, respectively
- The contacts were designed using Klayout Editor
- Most of the devices were fabricated at the cleanroom of the Institute of Microelectronics of Barcelona (IMB-CNM) using the RAITH 150 (TWO) dedicated electron beam lithography system. The EBL parameters were: dose factor of 1.4 and a step size of 10/20 nm for the contacts/markers with a beam aperture of 20  $\mu\text{m}$ . For extensive features such as the bond pads, we use a step size of 100 nm and a dose of 1.6 with a beam aperture of 120  $\mu\text{m}$ .
- We use Methyl isobutyl ketone (MIBK) mixed isopropyl alcohol (1:3) as a developer for the MMA and PMMA electron beam lithography resist. We immerse the chip with the resist into MIBK for  $\sim 1$  min 30 sec while shaking it.
- The metalization was done through the physical vapor deposition technique. We use the E-Beam evaporator ATC-8E Orion, manufactured by AJA International Inc. For the insulator barrier, we evaporate 4 nm of Ti at a rate of  $\sim 0.2$   $\text{\AA}/\text{s}$  in an environment of  $10^{-8}$  Torr. We introduce  $\text{O}_2$  to the main chamber until we reach a base pressure of  $10^{-1}$  Torr. We kept such pressure for 30 min. We repeated the process one more time to get an 8 nm thick  $\text{TiO}_x$ . Next, we deposited typically 30 nm of Co ( $\sim 0.8$   $\text{\AA}/\text{s}$ ).

For the metallic electrodes, we deposited first a 1 nm Ti film followed by 35 nm of Pd ( $\sim 1 \text{ \AA/s}$ ).

- For the lift-off, we immersed the chip in room temperature acetone for a couple of minutes.

## Fabrication of graphene based heterostructures

For the fabrication of heterostructures, we use the dry viscoelastic method described in Chap. 3 and adapted from *2D Mater.* **1**, 011002 (2014). We always used either the Highly purified "Free-Gel" laminated onto a flexible substrate or the WF FILM Gel-Bonded to metalized polyester substrate from Gel-Pack®. We usually used the X4 retention level.

During the development of this thesis, we adopt different methods to fabricate heterostructures. Although, all the devices present in this thesis are made using the dry viscoelastic stamping, we have also used the "dry transfer" method to encapsulate graphene onto hBN fully. To do so, we fabricated a stamp made of PDMS and a thin film of Poly(propylene carbonate), PPC. We used the commercially available PPC from Sigma-Aldrich®, and we diluted to a density of 0.1 g/ml using acetone as solvent. A thin film of PPC was obtained using spin-coating ( $2000 \text{ rpm} \times 40 \text{ s}$ ). Prior the spin-coating the PDMS was treated with oxygen plasma during  $\sim 10 \text{ s}$  with a power of 200 W. The "dry transfer" process is well described in *Science*. **342**, 614 (2013). For our devices, we note that no heating was necessary to pick-up the hBN flakes and later the graphene. To release the stack, we heat the stamp in contact with the target to a temperature of  $90 \text{ }^\circ\text{C}$ . The process is similar when Polycarbonate (PC) is used instead of PPC. However, when using PC the successful rate of picking up a flake seems to increase if the substrate is always heated. A promising technique to fabricate heterostructures is described in *Nano Lett.* **17**, 11, 6961 (2017). The technique consists of an assisted pick-up for capillary forces.

After assembling, the stacks are annealed for 1 hour at  $500 \text{ }^\circ\text{C}$  in a high vacuum ( $10^{-8} \text{ Torr}$ ).

For the spin-charge interconversion experiments, large-area monolayer graphene is selected. The van der Waals heterostructure is fabricated using the steps described above. After assembling, the stacks are annealed for 1 hour at  $500 \text{ }^\circ\text{C}$  in a high vacuum ( $10^{-8} \text{ Torr}$ ). Annealing removes contamination between the layers as well as the remaining residues from the transfer process. The heterostructure is coated with a poly(methyl methacrylate) (PMMA) resin mask and patterned into a Hall crossbar using electron-beam lithography (EBL), followed by oxygen plasma etching with 200 W power for about 30 s. The oxygen plasma etching was done using the microwave plasma system 210 from PVA TePla Inc. The resin is then removed with acetone.



## Appendix D

# Curriculum vitae



## LUIS ANTONIO BENITEZ MORENO

- 🕒 Date of birth: 28<sup>th</sup> August 1990
- 📍 Address: Universitat Autònoma de Barcelona, Edifici ICN2, Av. de Serragalliners, s/n. 08193, Barcelona, Spain.
- ☎ Phone number: +34 692360647
- ✉ Email address: [an.benitez7@gmail.com](mailto:an.benitez7@gmail.com)
- 🇨🇴🇪🇸 Nationality: Colombian and Spanish

---

### EDUCATION

#### Doctoral Student

1<sup>st</sup> May 2016 – Present

*Catalan Institute of Nanoscience and Nanotechnology (ICN2) & Autonomous University of Barcelona (UAB), Spain.*

#### Master in science physics

2014 – 2015

*Instituto Balseiro (IB), Argentina.*

Thesis: “Exact Kohn-Sham potential for strongly correlated finite systems.”  
Supervisor: Dr. César R. Proetto.

#### Bachelor degree in physics

2007 – 2013

*Nariño University (UDENAR), Colombia.*

Thesis: “Statistical methods for image processing: Random Walks, diffusion and Potts model”  
Supervisor: Dr. Alejandro Pérez Riascos.  
Honors: Bachelor award-winning thesis.

### AWARDS AND FELLOWSHIPS

- Doctoral fellowship sponsored by the Ministry of Economy and Business. Spain. 2016 – Present
- Master fellowship sponsored by the National Atomic Energy Commission, Argentina. 2014 – 2015  
*The fellowship was granted after I passed a selection exam among other candidates from South America.*
- Mention of Honor. Nariño University, Colombia. 2014  
*Mention was given to students with grade points averages not less to 4.2/5, who have not repeated any course during the full Bachelor and to those who have an award-winning thesis.*

- Outstanding student award, Nariño University, Colombia. 2012  
*I obtained the highest grade point among 396 students who obtained the highest grades in their corresponding courses.*
- Honors in 8/10 semesters during my bachelor. 2007-2013

## PUBLICATIONS

Torres, W.S., Sierra, J.F., **Benítez, L.A.**, Bonell, F., García, J.H., Roche, S. and Valenzuela, S.O. “Magnetism, spin dynamics, and quantum transport in two-dimensional systems”. *MRS Bulletin*. **45**, 357-365 (2020). DOI: [10.1557/mrs.2020.121](https://doi.org/10.1557/mrs.2020.121)

**L. Antonio Benítez**, Williams Savero Torres, Juan F. Sierra, Marius V. Costache and Sergio O. Valenzuela. “Gate-tunable spin anisotropy in graphene – WS<sub>2</sub> heterostructures at room temperature”. *Under preparation*.

**L. Antonio Benítez †‡**, Williams Savero Torres †‡, Juan F. Sierra, Matias Timmermans, Jose H. Garcia, Stephan Roche, Marius V. Costache and Sergio O. Valenzuela †. “Tuneable room-temperature spin-to-charge conversion in van der Waal heterostructures”. *Nat. Mater.* **19**, 170–175 (2020). †: Equal contributing authors. ‡: Corresponding authors. DOI: [10.1038/s41563-019-0575-1](https://doi.org/10.1038/s41563-019-0575-1), arXiv: [1908.07868](https://arxiv.org/abs/1908.07868).

**L. Antonio Benítez †**, Juan F. Sierra †, Williams Savero Torres, Matias Timmermans, Marius V. Costache and Sergio O. Valenzuela †. “Investigating the spin-orbit interaction in van der Waals heterostructures by means of the spin relaxation anisotropy”. *APL Materials* **7**, 120701 (2019). †: Corresponding authors.

**L. Antonio Benítez †**, Juan F. Sierra ‡, Williams Savero Torres ‡, Aloïs Arrighi, Frédéric Bonell, Marius V. Costache and Sergio O Valenzuela†. “Strongly anisotropic spin relaxation in graphene–transition metal dichalcogenide heterostructures at room temperature”. *Nat. Phys.* **14**, 303–308 (2018). †: Equal contributing authors. ‡: Corresponding authors. DOI: [10.1038/s41567-017-0019-2](https://doi.org/10.1038/s41567-017-0019-2), arXiv: [1710.11568](https://arxiv.org/abs/1710.11568).

Williams Savero Torres, Juan F. Sierra, **L. Antonio Benítez**, Frédéric Bonell, Marius V. Costache, Sergio O. Valenzuela. “Spin precession and spin Hall effect in monolayer graphene/Pt nanostructures”. *2D Mater.* **4**, 041008 (2017). DOI: [10.1088/2053-1583/aa8823](https://doi.org/10.1088/2053-1583/aa8823), arXiv: [1709.01854v1](https://arxiv.org/abs/1709.01854v1)

**Antonio Benítez** and César R. Proetto †. “Kohn-Sham potential for a strongly correlated finite system with fractional occupancy.” *Phys. Rev. A* **94**, 052506 (2016). †: Corresponding authors. DOI: [10.1103/PhysRevA.94.052506](https://doi.org/10.1103/PhysRevA.94.052506), arXiv: [1609.07674](https://arxiv.org/abs/1609.07674)

Google scholar profile: [L. Antonio Benítez](https://scholar.google.com/citations?user=L-Antonio-Benitez)

## PRESENTATIONS AND SEMINARS

- “Spin-orbit phenomena in proximitized graphene.” February 25<sup>th</sup>, 2020. MIT, Boston, USA. [Invited seminar](#).
- “Spin-orbit phenomena in proximitized graphene.” February 24<sup>th</sup>, 2020. Harvard, Boston, USA. [Invited seminar](#).
- “Gate-tunable spin anisotropy in graphene – WS<sub>2</sub> heterostructures at room temperature.” Graphene for US. February 20<sup>th</sup> – 21<sup>st</sup>, 2020. New York, USA. [Oral contribution](#).
- “Tunable room-temperature spin galvanic (SGE) and spin Hall effects (SHE) in proximitized graphene.” Graphene & 2DM Singapore Summit. November 25<sup>th</sup> – 28<sup>th</sup>, 2019. Singapore. [Oral contribution](#).
- “Spin relaxation anisotropy and spin-to-charge conversion in graphene/TMDC lateral devices.” 4th Graphene and 2D heterostructures Workshop. October 24<sup>th</sup> – 25<sup>th</sup>, 2019. Budapest, Hungary. [Invited talk](#).

- “Gate-tunable spin anisotropy in graphene – WS2 heterostructures at room temperature.” Graphene Conference. June 25<sup>th</sup> – 28<sup>th</sup>, 2019. Rome, Italy. Poster contribution.
- “Strongly anisotropic spin relaxation in graphene–transition metal dichalcogenide heterostructures at room temperature.” JEMS 2018 – The Joint European Magnetic Symposia. September 3<sup>th</sup> – 7<sup>th</sup>, 2018. Mainz, Germany. Oral contribution.
- “Strongly anisotropic spin relaxation in graphene–transition metal dichalcogenide heterostructures at room temperature.” Graphene Conference. June 26<sup>th</sup>– 29<sup>th</sup>, 2018. Dresden, Germany. Oral contribution.
- “Isotropic spin relaxation in graphene on hexagonal boron nitride.” Graphene Conference. March 28<sup>th</sup> -31<sup>st</sup>, 2017. Barcelona, Spain. Poster contribution.

## SKILLS

- Device fabrication / characterization:
  - Exfoliation of different layered materials (TMDCs, hBN, Graphene).
  - Fabrication of van der Waals heterostructures using dry transfer techniques. In particular, I built (from scratch) a transfer system in my host group.
  - Electron-beam lithography, oxygen plasma etching, reactive ion etching, atomic force microscopy characterization, scanning electron microscopy, electron beam evaporation.
- Electrical characterization:
  - Magnetotransport.
  - Spin transport using non-local detection.
  - Measurements at cryogenic temperatures (using N-flow and 10K cryogen-free cryostats).
- Programming:
  - Python, Mathematica.
- Theory:
  - Solid background in theory of solids and in density functional theory (DFT).